Dissertation

submitted to the
Combined Facilities for the Natural Sciences and for Mathematics
of the Ruperto-Carola University of Heidelberg, Germany
for the degree of
Doctor of Natural Sciences

Put forward by
M. Sc. Dimitri Probst
born in Zatobolsk, Kazakhstan
Oral examination: 11.07.2018

Continuum Modeling of Cell Contractility

Referees: Prof. Dr. Ulrich Schwarz
Prof. Dr. Heinz Horner

Continuum Modeling of Cell Contractility

Biological cells generate mechanical forces to sense and interact with neighboring cells and the extracellular environment. In this thesis, I combine traction force microscopy, viscoelastic continuum models, finite element simulations and homogenization techniques to demonstrate how contractility on the cellular level emerges from the force-generating actomyosin cytoskeleton. These theoretical approaches are complemented by a series of collaborations with experimental groups that investigate the actomyosin system in different biological systems. For stress fibers, we find a transition from elastic to fluid behavior at a typical timescale of tens of minutes. For small yet strong spreading platelets, we estimate intracellular stresses in the kilopascal range. For epithelial monolayers, I show that the propagation of mechanical forces defines the territories for leader cell formation. Homogenization is used to demonstrate how intracellular polarization determines traction forces, and that stress fibers are characterized by negative compressibility, a property which defines mechanical metamaterials.

Kontinuumsmodellierung zellulärer Kontraktilität

Biologische Zellen erzeugen mechanische Kräfte, um andere Zellen und die extrazelluläre Umgebung zu ertasten und um mit ihnen wechselzuwirken. In dieser Arbeit verknüpfe ich Zellkraftmikroskopie, viskoelastische Kontinuumsmodelle, Finite-Elemente-Simulationen und Homogenisierungsmethoden, um zu zeigen, wie Kontraktilität auf der Zellebene aus dem krafterzeugenden Aktomyosin-Zytoskelett entsteht. Diese theoretischen Ansätze werden durch verschiedene Zusammenarbeiten mit experimentellen Gruppen ergänzt, die das Aktomyosin-System in unterschiedlichen biologischen Systemen untersuchen. Für Stressfasern finden wir auf einer charakteristischen Zeitskala von einigen Zehnerminuten einen Übergang von elastischem zu fluidem Verhalten. Für kleine und trotzdem starke Blutplättchen, die sich auf einer Unterlage ausbreiten, schätzen wir intrazellulären Spannungen im Kilopascalbereich. Für Epithelschichten zeige ich, dass die Ausbreitung mechanischer Kräfte die Territorien für die Ausbildung von Führungszellen definiert. Homogenisierung wird angewandt, um zu zeigen, wie intrazelluläre Polarisierung Zellkräfte bestimmt, und dass sich Stressfasern durch eine negative Kompressibilität auszeichnen, eine Eigenschaft, die mechanische Metamaterialien definiert.

Contents

1 Introduction

The adult human body is composed of roughly 10^{13} cells and its fate essentially depends on how these cells move and reproduce. Even a small imbalance in the context of cell locomotion and reproduction can lead to incurable diseases like cancer. The last two decades of research have progressively revealed that not only biochemical signaling but also physical forces affect the decisions about these processes at the level of each single cell. In particular, physical forces have been identified to play a key role in many physiological processes like organogenesis and wound healing [*Iskratsch et al.*, 2014]. These forces can act from the exterior on a cell, but often they are generated by the cell itself by means of a highly complex contractile apparatus, the so-called actin cytoskeleton (CSK). For instance, cells exert contractile forces to feel the mechanical properties of their environment. These are then fed back into the cell as chemical signal and allow the cell to make decisions thereupon, a process which is called mechanotransduction [*Paluch et al.*, 2015]. This shows that the quantification of cellular forces and their linkage to the underlying molecular mechanisms is not only an inevitable step in the search for new treatment methods, but also bears potential to uncover fundamental design principles of the actin CSK.
This thesis contributes to the disclosure of this linkage by demonstrating how the force production on the cellular level arises from the composition of the actin CSK. This is accomplished by a theoretical investigation which is subdivided into the three parts, such that, overall, a top-down approach is established to gain insight into this multiscale biological problem. These three parts determine the structure of this thesis.
First, we will apply traction force microscopy (TFM) to quantify cellular traction forces [*Style et al.*, 2014; *Schwarz and Soiné*, 2015]. Briefly speaking, TFM uses elasticity theory to estimate forces from the deformation induced by cells adhering to a soft substrate. Since elasticity theory is of long-ranged nature, any noise signal in the deformation pattern distorts the traction force pattern. A mathematical method, the so-called regularization, is then needed to eliminate the noise efficiently while preserving the force signal. In this context, we will benchmark existing regularization algorithms based on artificial data sets. This will serve as a basis for a robust estimation of cellular traction forces in the remainder of this thesis.
Second, we make use of the cellular force patterns and the dynamics of cellular force production to constrain a continuum model, which allows to determine material features of cells. Cells are known to exhibit both an elastic behavior, which allows them to resist abrupt external forces, and a viscous behavior, which facilitates processes like cell growth, movement and reproduction. The exact manifestation of these contributions strongly depends on factors like the predominant regulatory mechanism. In the course of this thesis, an adhering cell is described by a viscoelastic sheet coupled to a viscoelastic foundation while contractility is introduced as thermoelastic stress [*Edwards and Schwarz*, 2011]. The

model is validated by data from a series of collaborations with experimental groups that investigate the actin CSK in different biological systems. We will find that the theoretical approach captures the contractile behavior of cells on multiple spatial scales, ranging from subcellular actin bundles via single cells to cell colonies. Yet, each biological system comes with a different type and variety of measurement data and, therefore, challenges a different aspect of the model.
Third, we use the information about both the material features at the level of single cells and the architecture of the actin CSK to infer physical characteristics at the molecular level. We adapt a mathematical approach, the so-called asymptotic homogenization, to the dynamics of our continuum model to establish a relation between these two levels [*Bensoussan et al.*, 1978; *Sánchez-Palencia*, 1980]. The molecular model is represented as a continuum with rapidly varying material features while the cell level constitutes a coarse-grained continuum equivalent thereof. Experimental data will allow to constrain parameters on both scales and estimate experimentally yet not probed properties of the actin CSK. The homogenized continuum model will be finally used to link the intracellular organization of the actin CSK to the spatial distribution of traction forces induced by adhering cells.
In the remainder of this chapter, we will start in Section 1.1 with a description of the underlying biological entities and processes which are required for accomplishing force generation in cells. We will then, in Section 1.2, discuss classical and advanced techniques to quantify cellular forces on different spatial scales. Section 1.3 will summarize physical models which aim at capturing the dynamics and effects of force generation in cells and, with this, allow to gain a deeper understanding of the involved biological mechanisms. We will conclude this chapter in Section 1.4 with the outline of this manuscript.

1.1 The Cytoskeleton

In the following section, we will introduce the subsystems of the cellular cytoskeleton (CSK). In particular, we will focus on the different forms of appearance of the force-generating actin CSK and discuss the structure, functionality, distribution and regulation of myosin II motor proteins, which conduct the contraction of the actin CSK. We will conclude this section by a brief description of how single cells are mechanically embedded both into the extracellular environment and into a layer of cells.

1.1.1 Cytoskeleton subsystems

The cellular CSK accomplishes mechanical interactions within the cell and at the interface of the cell and its environment by means of a dense mesh of polymer networks consisting of diverse types of filaments, molecular motor proteins as well as crosslinking and regulatory molecules. It is composed of three main subsystems: the actin CSK, intermediate filaments and microtubules. Each of the three subsystems interacts via various types of active and passive crosslinkers, but each subsystem comes with its own mechanical properties, which allow them to specialize on different functions within the cell. Further, they all have in

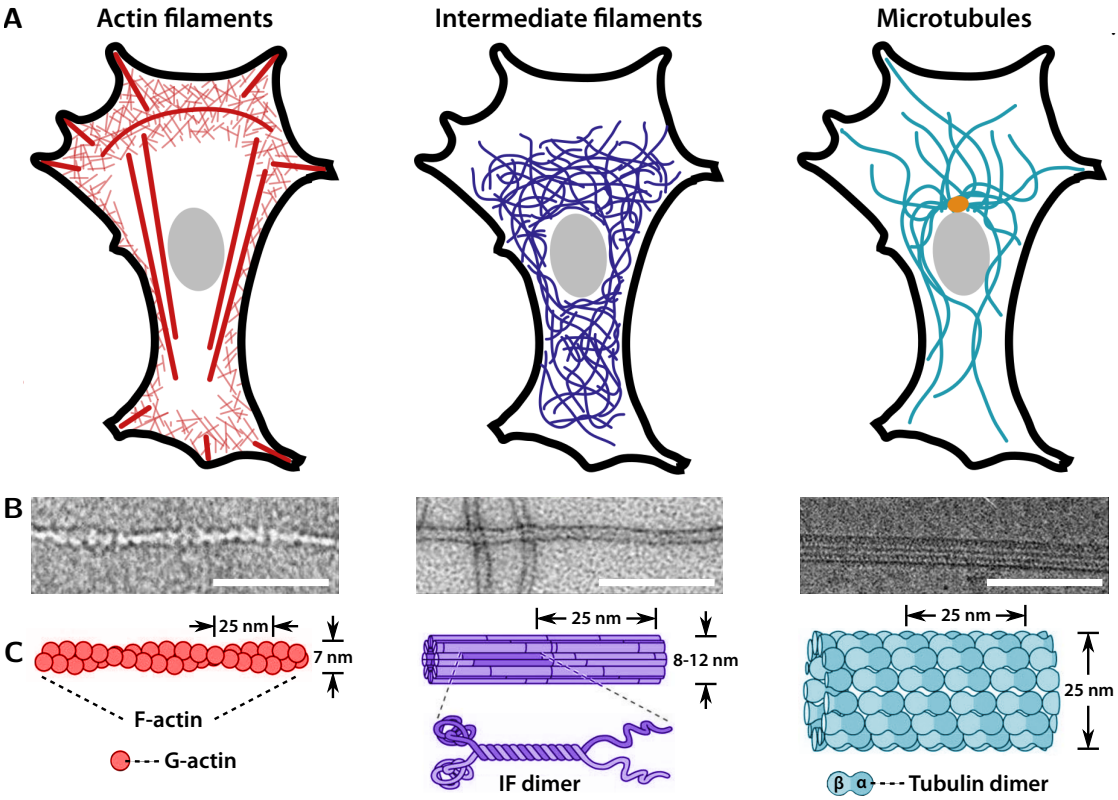

Figure 1.1: The individual cytoskeleton subsystems and their molecular constituents. **(A)** Simplified sketch of the three different cytoskeleton subsystems. The actin cytoskeleton consists of both polymer networks and fibers. Intermediate filaments are the most flexible filaments. They form large polymer networks which span the whole cell. Microtubules are rigid hollow cylinders which originate at the cell nucleus (*grey*) and also span the whole cell. All three cytoskeleton subsystems interact via diverse active and passive crosslinkers. **(B)** Exemplar SEM micrographs of the three filamentous structures. Scale bars are 100 nm. **(C)** Schematic drawing of the filamentous building blocks of the corresponding subsystem, ranging from the thin actin filament to the thick microtubule. Both actin filaments and microtubules are polar and consist of globular subunits. Intermediate filaments are nonpolar and are composed of fibrous subunits. Figures adapted from: **A**, *Huber et al.* [2015]; **B**, *Alberts et al.* [2007]; **C**, *Purves et al.* [2003].

common that they consist of small protein subunits which cohere by weak noncovalent bonds and dynamically polymerize and depolymerize.
We will now closer investigate the actin CSK, which provides the force-generating machinery of the cell. For reasons of completeness, we will also briefly address the properties and function of intermediate filaments and microtubules.

Actin cytoskeleton The actin CSK is the contractile system which is mainly composed of the filamentous structure protein actin and the molecular motor protein myosin II [*Alberts et al.*, 2014]. Actin is a central constituent of the CSK in all eucaryotic cells. The structure protein exists in the cell either as monomeric globular G-actin or polymerized as the filamentous F-actin, comprising a double-stranded right-handed helix of cross-section diameter 7 nm and a pitch of about 70 nm (see Figure 1.1). Actin filaments are polar and semiflexible, comprising a typical persistence length of 10 μm [*Huber et al.*, 2015]. They polymerize on a time scale of milliseconds, which allows actin networks a rapid adaptation to mechanical changes in the cellular environment [*Pollard*, 1986]. Typical turnover times of actin networks are in the range of minutes.

Actin filaments have two essential functions in the cell: They stabilize the cellular shape and, either via de-/polymerization or via myosin-driven contraction, change the cell shape and generate a directed movement of the cell. The particular function is predetermined by the location of the filament within the cell and the present concentrations of active and passive crosslinking and capping proteins in this region, as illustrated in Figure 1.2A and B. In general, one can distinguish between two different forms of appearance of actin structures in cells: Networks and linear bundles [*Blanchoin et al.*, 2014].

Actin networks can be further classified into crosslinked and branched networks. Two prominent examples are the actin cortex and the lamellipodium. The actin cortex is situated underneath the cell membrane and provides for its mechanical stability by means of a dense actin mesh crosslinked by both active crosslinkers like myosin II and passive crosslinking proteins like α-actinin. The lamellipodium is a mixture of polymerizing branched actin network at its front and contractile network at its back and is also located at the cell membrane. By polymerizing against the membrane, it allows to change the cell shape and, with this, defines the leading edge of the cell. In contrast to the cell cortex, the predominant crosslinker and growth factor is the Arp2/3 complex, which establishes a tree-like branching structure of the network. Capping proteins then allow to terminate the growth of single actin branches.

Actin bundles can be classified into either parallel or antiparallel bundles. Stress fibers (SFs) are typical examples for antiparallel actin bundles, comprising a number of $10 - 30$ actin filaments arranged in an antiparallel fashion. The dynamics of SFs are determined by both the active crosslinker myosin II and passive crosslinkers like α-actinin. Based on their location in the actin CSK, their exact composition and coupling to the extracellular environment, SFs can either be ventral SFs, dorsal SFs or transverse arcs [*Hotulainen and Lappalainen*, 2006].

Both ventral SFs and transverse arcs have in common that they exhibit a sarcomeric structure of myosin-occupied and myosin-free regions, similar to the sarcomeric architecture found in muscle cells, while dorsal SFs remain passive [*Burnette et al.*, 2014]. Ventral SFs are the strongest SFs entailing typical contractile forces of about 10 nN, which are transduced at both ends to the extracellular matrix via focal adhesions [*Burridge and Wittchen*, 2013]. Apart from the mechanical sensing and signaling function, they provide the contraction of the rear end of the cell while the cell is migrating. A more complete parametric characterization of ventral SFs is given in Chapter 7.

Dorsal SFs originate from newly generated focal adhesions at the front of the cell and

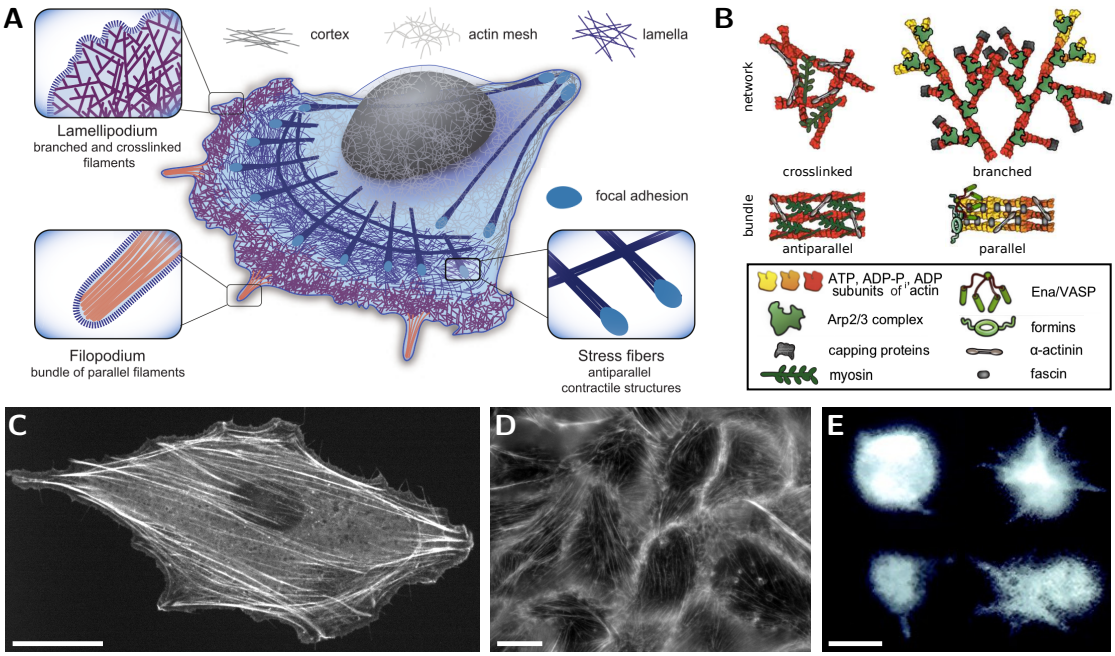

Figure 1.2: The actin cytoskeleton, its diverse forms of appearance and its anchoring to the extracellular matrix. **(A)** Depending on the location within the cell and the local concentration of crosslinking proteins, the structure of the actin cytoskeleton varies. **(B)** Detailed local structure of the actin cytoskeleton and the involved crosslinking and capping proteins. **(C)** Actin-stained mouse embryo fibroblast. Stress fibers are the most dominant cytoskeletal components of the (spread) fibroblasts. **(D)** Actin-stained epithelial layer of MDCK cells. Here, both stress fibers and actin cortex are the predominant structures. **(E)** Actin-stained human blood platelets. Platelets exhibit a characteristic central clot of actin and filopodia. Scale bars are: **C-D**, 10 μm; **E**, 2 μm. Figures adapted from: **A**, *Letort et al.* [2015]; **B**, *Blanchoin et al.* [2014]; **C**, courtesy of Patrick Oakes, University of Rochester; **D**, courtesy of Medhavi Vishwakarma, MPI Stuttgart; **E**, *Li et al.* [2002].

polymerize backwards, with this initiating a new generation of ventral SFs in a migrating cell [*Burridge and Guilluy*, 2016]. *Tojkander et al.* [2012] present a hypothetical model, how a single ventral SF might be formed from the fusion of two dorsal SFs and a single transverse arc. In contrast to the lamellipodium, the assembly of dorsal SFs is determined by the growth factor formin.

Transverse arcs are oriented parallel to the leading edge and only comprise indirect connections to the focal adhesions via ventral and dorsal SFs. Their assembly differs from those of the other types of SFs. As the lamellipodium proceeds, the polymerized actin branches are pushing against the cell membrane which, as a result, exerts a counterforce compelling a retrograde flow of the actin branches. When hitting a focal adhesion, the flow is hindered, the dendritic network breaks and is contracted by means of myosin motors yielding a linear bundle structure [*Burnette et al.*, 2011]. As Figures 1.2C and

D illustrate, SFs are the predominant actin structures in fibroblasts and epithelial cells, respectively.
Typical examples for parallel actin bundles are filopodia, which are dense finger-like protrusions mostly located at the leading edge of the cell. Their assembly is mediated by the crosslinker fascin and growth factors like formin and Ena/VASP. Their task is associated with spreading, migration and sensing. Filopodia are often found e.g. in spreading blood platelets (see Figure 1.2E).
Cellular contractility is established by myosin II motor proteins, which not only exist in muscle cells, but also in non-muscle cells, such as fibroblasts, epithelial cells or blood platelets. Myosin, in general, is a family of motor proteins in eucaryotic cells, of which each class is associated with different tasks within the cell [*Alberts et al.*, 2014]. A single myosin II molecule is a polar hexamer which can be subdivided into a head, neck and tail domain (see Figure 1.3A and B). Heads and tail are composed of two coiled-coiled heavy chains, while the neck of each head is entwined by two smaller light chains, namely the essential and regulatory light chain, which are both bound non-covalently to the heavy chain. The essential light chain supports the structure of the molecular motor, while the regulatory light chain regulates the activity of the motor head.
In non-muscle cells, myosin II exists in three different isoforms, of which myosin IIA and IIB are known as the fast and slow isoform [*Beach et al.*, 2014; *Stam et al.*, 2015]. Both types of myosin II assemble into bipolar filaments of $10 - 30$ motor heads in total, also known as minifilaments, comprising a typical length of about 300 nm (see Figure 1.3A and B). In muscle cells, the number of motor heads per filament is about ten times higher. When interacting with actin filaments, myosin filaments can translate chemical energy in terms of ATP into motion via so-called cross-bridge cycling [*Alberts et al.*, 2014]. Figure 1.3C illustrated a sketch of a single cross-bridge cycle. Binding of ATP leads to the dissociation of the motor head from the actin filament and changes the inclination angle of the neck. Hydrolysis of ATP to ADP and phosphate enforces again an association of the motor head and the actin filament, but now to a different actin monomer at a distance of about 11 nm [*Finer et al.*, 1994]. Dissociation of both ADP and phosphate provokes a power stroke, i.e. the neck attains its original inclination angle, and a consequent movement of the actin filament in the direction of its minus, also known as pointed, end. Thus, without changing the structure and composition of the actin filament, the myosin filament can generate contractile forces when attached to actin at both of its ends.
Beach et al. [2014] used SIM to visualize the location of single myosin II filaments in non-muscle cells by attaching fluorescent markers to both head and tail regions of the myosin filaments (see Figure 1.3D). One finds that the distribution of myosin II filaments is very sparse and that filaments are predominantly arranged along SFs in a sarcomeric manner. Remarkably, myosin II filaments of neighboring SFs often form stack-like structures in the direction perpendicular to the SFs, as the insets of Figure 1.3D indicate (see also *Hu et al.* [2017]).
The activity of myosin II filaments is regulated by diverse signal transduction pathways. For example, minifilaments directly react upon external physical forces, as has been shown in experiments by *Luo et al.* [2013] in which cells were locally deformed and a correlated increase of the concentration of minifilaments in the cell cortex was observed.

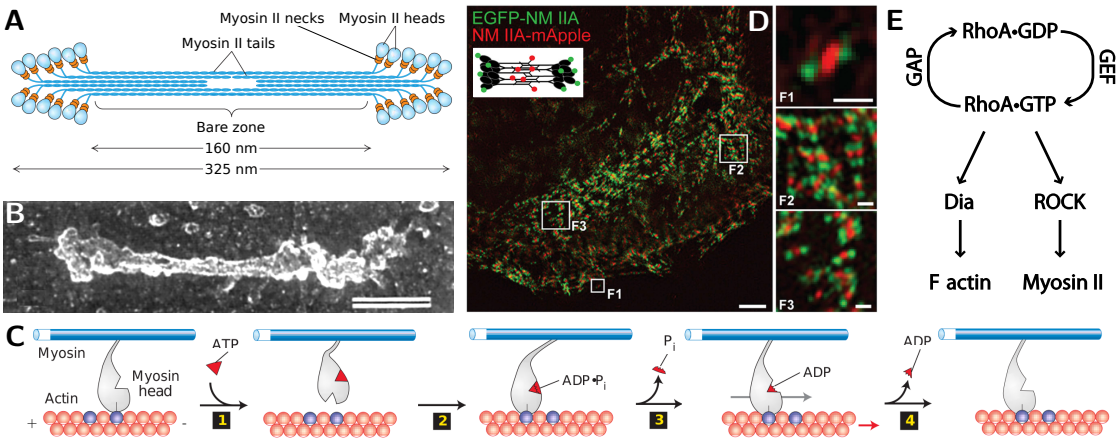

Figure 1.3: Structure, functionality, distribution and regulation of non-muscle myosin II motor proteins. **(A)** A myosin monomer is, in general, composed of a head, neck and tail region. Myosin II proteins form dimers, which further assemble into bipolar filaments of $10 - 30$ proteins in total. **(B)** SEM micrograph of a myosin II filament. **(C)** By sliding along an actin filament, the myosin II protein generates force. For more details, see main text. **(D)** Distribution of individual myosin II filaments visualized by means of SIM. Myosin II filaments are mostly located along stress fibers. Neighboring myosin filaments form stack structures perpendicular to the actin bundles. **(E)** Simplified RhoA signaling pathway. In its activated form, RhoA promotes both actin polymerization and myosin activation. Scale bars are: **B**, 100 nm; **D**, 2 μm for main figure, 300 nm for insets. Figures adapted from: **A,C**, *Lodish et al.* [2004]; **B**, *Verkhovsky and Borisy* [1993]; **D**, *Beach et al.* [2014]; **E**, *Oakes et al.* [2017].

One of the most prominent signal transduction pathways is assigned to the regulatory pathway directed by the small GTPase RhoA (see Figure 1.3E). In its active GTP-bound state, it activates its effectors Rho-associated coiled-coil containing protein kinase, or ROCK, and Diaphanous-related formin, or Dia, which themselves trigger the activation of the myosin II and the polymerization of actin, respectively. In its low energy form, which ensues after hydrolysis of the GTP by means of GTP-activating proteins (GAPs), RhoA and its downstream effectors remain inactive until the GTPase is activated again by a Guanine nucleotide exchange factor (GEF), which is predominantly located in the cell plasma.
In *in vitro* experiments, the activity and effects of RhoA is usually analyzed via addition of drugs. For example, *Ridley and Hall* [1992] could show that the activity of RhoA has a strong effect on the assembly of focal adhesions and SFs. Recently developed techniques by *Valon et al.* [2015] or *Wagner and Glotzer* [2016] allow the activation of the RhoA pathway by an optogenetic recruitment of GEFs to the cell membrane, where RhoA is anchored. We will further discuss these techniques in Chapters 3 and 4.

Intermediate filaments Intermediate filaments are not part of the cytoskeleton in all eucaryotic cells. They consist of fibrous protein dimers which exhibit a resistive rope-like

organization [*Purves et al.*, 2003]. By spanning the whole cell, they mechanically stabilize the cell and, in particular, endow the cell with a high tear strength. However, intermediate filaments do not actively participate in cellular contraction. As their name suggests, their cross-section diameter of $8 - 12\,\mathrm{nm}$ is larger than those of actin filaments, but smaller than the diameter of microtubules (see Figure 1.1). Intermediate filaments are non-polar and less dynamic with a typical network turnover time in the range of hours, but more flexible than other cytoskeletal filaments with a persistence length smaller than $1\,\mu\mathrm{m}$ [*Huber et al.*, 2015]. For a detailed review on intermediate filaments, the reader is e.g. referred to *Herrmann et al.* [2007].

Microtubules Microtubules are present in all animal cells. They are long, rigid and hollow cylinders with a persistence length of about 1 mm, a typical length of tens of micrometers and a diameter of about 25 nm [*Alberts et al.*, 2014]. Typical turnover times of microtubule networks lie in the range of minutes [*Huber et al.*, 2015]. As Figure 1.1 illustrates, microtubules are composed of polar tubulin dimers, which in turn compose polar filaments. These originate at the so-called centrosome in the vicinity of the cell nucleus with the plus end growing in the direction of the cell membrane. Their major role is the directed intracellular transport of vesicles towards and away from the nucleus which is established by the two specialized motor proteins dynein and kinesin, respectively [*Welte*, 2004]. Another task which is ascribed to microtubules is the formation of the mitotic spindle during the process of cell division. An extensive review on microtubules can be found e.g. in *Akhmanova and Steinmetz* [2015].

1.1.2 Mechanical Cell-Matrix and Cell-Cell Interactions

Animal cells usually do not have a stable cell wall, as is typical for plant cells. Instead they are surrounded by either adjacent cells or the extracellular matrix (ECM), of which the latter occupies the largest part of the tissue volume [*Alberts et al.*, 2014]. The ECM consists of a sparse network of fibrous proteins, like collagen, fibronectin or vitronectin, and large polysaccharide-protein complexes, also known as proteoglycans (see Figure 1.4A). The ECM acts as a substrate in which cells can adhere and interact, but also supports the path finding of migrating cells in processes like embryogenesis and tissue repair [*Rozario and DeSimone*, 2010]. In particular, mesenchymal stem cells have been shown to be extremely sensitive to the stiffness of the surrounding ECM, with the ECM acting as a guide for differentiation [*Engler et al.*, 2006]: For example, soft matrices in the range of 100 Pa, mimicking brain tissue, trigger the development of neurons. Stiffer matrices, which mimic muscle (10 kPa) or collagenous bone tissue (1 MPa), commence the differentiation to muscle or bone cells, respectively. At the same time, cells are also able to remodel the architecture of the ECM by exerting contractile forces, which are then transduced to the ECM via focal adhesions, as in the case of tumorigenesis [*Wolf et al.*, 2007]. The process of converting mechanical stimuli, such as ECM rigidity, structural composition and external stresses into chemical signals to regulate cell behavior is known as mechanotransduction [*Iskratsch et al.*, 2014].

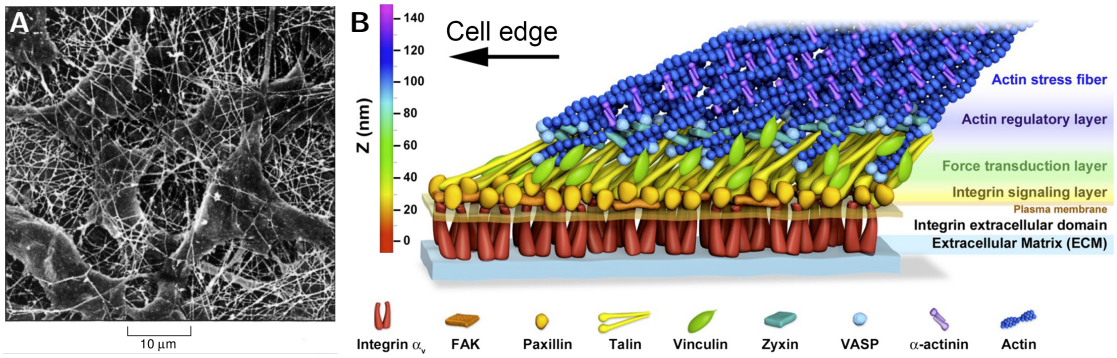

Figure 1.4: The extracellular matrix and cell-matrix interaction. **(A)** Fibroblast cells embedded in a sparse extracellular matrix of collagen fibers. **(B)** Molecular composition of a focal adhesion (FA). FAs is hierarchically structured into the actin regulatory layer, force transduction layer and integrin signaling layer. Both actin flow speed and traction force magnitude peak in the vicinity of the distal FA tip. Figures adapted from: **A**, *Alberts et al.* [2014]; **B**, *Kanchanawong et al.* [2010].

In the following, we will outline the structure and function of focal adhesions and adherens junctions, which constitute the mechanical interface of a cell with the ECM or with neighboring cells, respectively.

Focal Adhesions The mechanical interaction of the force-generating actin CSK and ECM molecules like collagen or fibronectin is mediated via focal adhesions (FAs), which are clusters of integrin proteins and attached ligands (see Figure 1.4B). Integrins are transmembrane proteins which bind to specific amino acid sequences of ECM proteins. They are heterodimers, consisting of an α- and β-subunit, which have both an intra- and extracellular domain. More than 150 different proteins are further involved in connecting integrins to actin bundles, with each protein coupled to different functional pathways [*Zaidel-Bar et al.*, 2004].
FAs are known to be highly dynamic, maturing and degrading in a force-dependent manner [*Wolfenson et al.*, 2011]. *Balaban et al.* [2001] showed, by measuring forces of cells attached to adhesive islands, that the local forces transduced by FAs correlate with the area of the FAs, yielding a constant stress in FAs of $5.5 \pm 2\,{}^{\mathrm{nN}}/_{\mu\mathrm{m}^2}$. The study by *Trichet et al.* [2012] further revealed that this constant depends on the stiffness of the substrate the cell adheres to.
In migrating cells, early FAs, also known as focal complexes, are developed upon protrusion of the lamellipodium. During retraction of the lamellipodium, most of these focal complexes disappear. Only a few residual complexes grow into stable adhesions, which is promoted by the recruitment of stabilizing proteins [*Zaidel-Bar et al.*, 2003]. These adhesions remain stable during migration until they are reached by the rear end of the cell, whereupon they detach and disassemble.
It has to be noted that the inclination angle of the SF in the vicinity of the FA, indicated

by Figure 1.4, is not true to scale. Indeed, a recently developed experimental method based on a combination of metal-induced energy transfer and FRET allow to determine an inclination angle for ventral stress fibers in a range of about 0.2 ° [*Chizhik et al.*, 2018]. This suggests that stress fibers rather shearing the extracellular surface than producing normal forces.

Adherens Junctions In a collectively migrating cell layer, like an epithelial sheet during the process of wound closure, the actin CSK of adjacent cells is mechanically coupled via so-called adherens junctions [*Hartsock and Nelson*, 2008]. Adherens junctions are mainly composed of the proteins cadherin and catenin, which provide the mechanotransduction between adjacent cells. Cadherins are almost completely located at the outside of the cell membrane and form calcium-dependent homodimers with cadherins of adjacent cells. Catenin proteins are attached to the cadherins at the inside of the cell membrane and connect these to individual actin filaments. Usually, adherens junctions appear as bonds encircling the cell and thus allow tight connections to adjacent cells (see Figure 1.2). Thus, on natural conditions epithelial sheets effectively form large super-cells [*Ladoux et al.*, 2016].

1.2 Quantification of Cellular Contractility

After introducing the force-generating processes and force-transducing proteins in cells, we will now provide an overview of classical and advanced methods to measure cellular forces on different spatial scales. In particular, we will consider methods which allow to quantify forces either exerted by single molecular motors, by actin bundles or by spread cells. We will further classify methods into multi-scale and single-scale methods. For a more detailed overview on force quantification techniques in mechanobiology, the reader is referred to recent reviews by *Polacheck and Chen* [2016], *Sugimura et al.* [2016] or *Roca-Cusachs et al.* [2017].

1.2.1 Multi-Scale Force Quantification Methods

Multi-scale force quantification methods have in common that they allow to measure cellular forces on multiple spatial scales with one single measurement. We will afford a closer insight into two-dimensional traction force microscopy (TFM), which is both the most prominent technique and the standard method used for cellular force quantification in the course of this manuscript. Thereafter, we will briefly review other multi-scale force quantification methods.

Two-Dimensional Traction Force Microscopy In the original experiment conducted by *Dembo and Wang* [1999], as sketched in Figure 1.5A and, in more detail, in Figure 1.6A, cells are placed on top of a flat elastic hydrogel substrate of known stiffness, whose spatial dimensions exceed those of the cell, such that it can be considered as a semi-infinite half space. The substrate is made of a dense polymer network, such as Polyacrylamide (PAA)

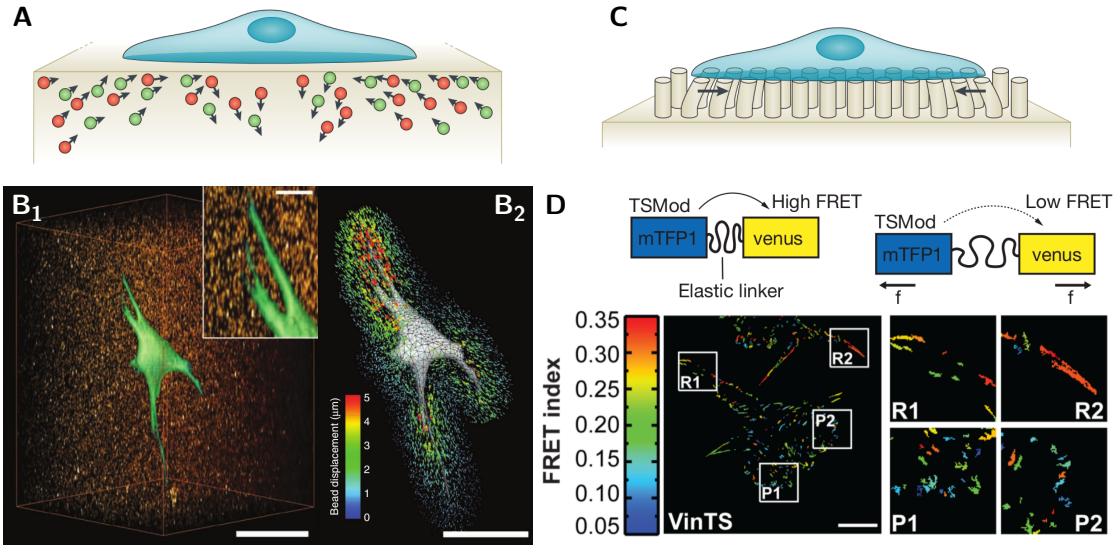

Figure 1.5: Classical and modern multi-scale force quantification methods in mechanobiology. **(A)** Two- and 2.5-dimensional traction force microscopy. **(B)** Three-dimensional traction force microscopy. **(C)** Micropillar array. **(D)** Molecular force sensors. Scale bars are: **B**, 50 μm; **D**, 20 μm. Figures adapted from: **A,C**, *Iskratsch et al.* [2014]; **B**, *Legant et al.* [2010]; **D**, *Grashoff et al.* [2010].

or Polydimethylsiloxan (PDMS), whereas the mesh size of the polymer network determines the substrate stiffness. The elastic substrate is further coated with a glycoprotein usually found in the ECM, such as fibronectin or collagen. This allows the cell to spread on top of the substrate, synthesize its contractile cytoskeleton, whose contractile dynamics are then transduced to the substrate via focal adhesions. As a result, the displacement of the substrate provides information about the forces the cells exerts. To capture the displacements of the substrate, fluorescent sub-micron sized beads, usually made of latex or similar materials, are embedded close to the surface of the substrate and their position is registered, usually via a confocal microscope. After the acquisition of the displaced image, the cell is detached from the substrate by means of proteases such as trypsin. The substrate displacement is then the difference between the bead positions of the displaced and relaxed gel.

Usually, cells adopt a flat shape on the substrate, exerting forces predominantly in the xy-plane (see Section 1.1.2). Therefore, in the first versions of TFM, displacements in vertical direction were neglected. To compute forces from displacements, *Dembo and Wang* [1999] used the Green's function $\mathbf{G}$ for a flat elastic half space, also known as Boussinesq solution [*Landau and Lifshitz*, 1986], which relates traction stresses $\mathbf{t}$ and displacements $\mathbf{u}$ via the convolution integral

$$\mathbf{u}(\mathbf{x}) = \int \mathbf{G}(\mathbf{x}, \mathbf{x}')\, \mathbf{t}(\mathbf{x}')\, \mathrm{d}\mathbf{x}' . \tag{1.1}$$

The traction stresses $\mathbf{t}$ result from inverting the equation, which *Dembo and Wang* [1999]

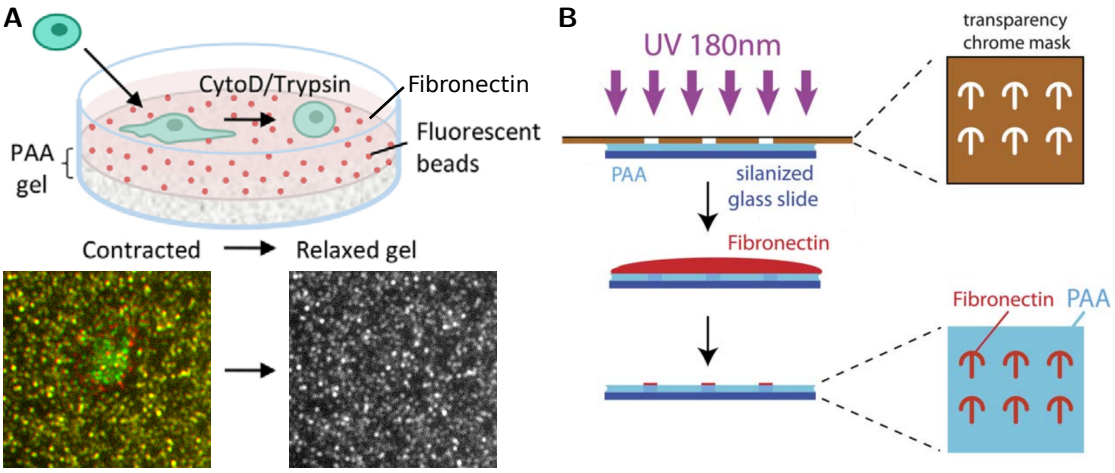

Figure 1.6: Two-dimensional traction force microscopy and fabrication of adhesive micropatterns. **(A)** Principles of two-dimensional traction force microscopy. Cells attach to and deform an elastic substrate. The cellular traction force can be reconstructed from the deformation of the substrate. For more details, see main text. **(B)** Micropatterning methods allow to design multiples of arbitrary miniaturized fibronectin patterns to study cellular behavior on normalized extracellular conditions. Figures adapted from: **A**, *Auernheimer et al.* [2015], bead images by courtesy of Jana Hanke, University of Göttingen; **B**, *Tseng et al.* [2011].

solved by discretizing the integral via Delaunay triangulation and interpolating the stress field based on the finite set of nodes, referring to their method as Boundary element method (BEM).
However, the original Green's function based approach has at least two drawbacks, which can be both ascribed to the long-ranged nature of elasticity theory. First, the matrix $\mathbf{G}$ is dense, such that its inversion is time-consuming and strongly depends on mathematical approximations if requiring a high-resolution estimation of traction stresses. Second, since elastic interactions are long-ranged, any traction vector can significantly contribute to the displacement field at any position, even if both are infinitely far away from each other. This becomes crucial in the presence of noise, which is ubiquitous in the acquisition of the bead displacements. Typical noise sources are uncertainties in the process of image acquisition, an irregular gel stiffness or gel swelling due to exposure to light.
To counteract the first issue, *Butler et al.* [2002] solved Equation 1.1 in Fourier space, where the real-space integral turns into a product of matrices and, with this, drastically reduces the typical computation time. To distinguish their method from the original calculation, they termed their method Fourier Transform Traction Cytometry (FTTC). The second issue was resolved by *Schwarz et al.* [2002], who showed that only by using a regularization scheme a reliable estimate of the traction stresses from noise-affected bead displacements can be achieved. *Sabass et al.* [2008] finally demonstrated that the conventionally-used Tikhonov regularization approach yields comparable results for the both BEM and FTTC.

To the present and in contempt of all recent advances in the field, the approach described so far is the standard TFM technique and will be used to quantify cellular forces throughout this manuscript. We will further provide the mathematical details and evaluate regularized FTTC in Chapter 2. In the remainder of this section, we will discuss recent extensions and improvements of TFM.
To account for the finite thickness of the substrate, *Merkel et al.* [2007] calculated a correction formula for the Boussinesq solution. *Sabass et al.* [2008] further introduced two differently colored types of fluorescing beads to increase the resolution of the displacement measurement. *Trepat et al.* [2009] showed that TFM can also be applied to calculate traction forces of collectively migrating cells. By treating the cell layers as a thin homogeneous elastic sheet, they used a finite element approach to estimate internal stresses withing the cell layer, denoting their method monolayer stress microscopy (see Chapter 6 for more details). *Tseng et al.* [2011] used deep UV printing to microfabricate fibronectin coatings of any shape, allowing to introduce normalized conditions to study average contractile behavior of cells (see Figure 1.6B). Chapters 3 and 4 will present experimental and theoretical findings on cells adhering to these micropatterns.
In the more recent time, *Han et al.* [2015] and *Brask et al.* [2015] combined BEM with sparse regularization instead of the commonly-used Tikhonov regularization approach, showing that the prior assumption of a sparse traction field expressing only at the discrete focal adhesion sites yields a more precise estimation of traction forces. We will pick up on regularization protocols in Chapter 2 of this manuscript.
Soiné et al. [2015] coupled an extensive image processing algorithm and a computer simulation to support the information about the bead displacements. With this, they not only managed to significantly improve the precision of traction stress quantification and location in a regularization-less manner, but also but also could infer internal stresses along subcellular cytoskeletal components. The idea of *Soiné et al.* [2015] will be further thematized in Chapter 8.
Also the experimental technique itself undergoes a permanent improvement. For example, *Colin-York et al.* [2016] managed to increase the spatial resolution and accuracy of TFM by using Stimulated-Emission-Depletion (STED) fluorescence microscopy for the acquisition of the registration of bead positions. *Bergert et al.* [2016] applied the technique of electrohydrodynamic nanodrip-printing of quantum dots to print confocal arrays of bead-like features. This allows to obviate the need of a cell-free reference image to quantify the displacements induced by the cell and facilitates a live calculation of traction stresses and direct correlation of forces with biochemical signals without detaching the cell.
For more detailed reviews and guidelines for TFM, the reader is referred to *Style et al.* [2014], *Plotnikov et al.* [2014] and *Schwarz and Soiné* [2015].

2.5-Dimensional Traction Force Microscopy As Figure 1.5A sketchily illustrates, cells indeed not only contract parallel to the surface of the elastic gel but also generate vertical displacements, which usually are about an order of magnitude lower than the planar forces. In the typical situation, a cell raises the gel underneath its boundary, where most of the focal adhesion sites are located, and compresses the substrate underneath

its nucleus. This is similar to the behavior of a fluid droplet on top of a soft substrate, the dynamics of which are determined by an interplay of surface tension and capillary pressure. However, the force-generating mechanisms in cells are different.
To account for z-displacements generated by cellular contraction, *del Álamo et al.* [2013] extended the Green's function-based approach of *Butler et al.* [2002] and formulated the three-dimensional Green's function for the case of a flat substrate filling the semi-infinite half space. Even years before, *Maskarinec et al.* [2009] introduced an alternative approach to take vertical displacements into consideration without requiring the knowledge of the Green's function. Once they determined the bead displacements, instead of inverting Equation 1.1, they calculated the strain tensor $\epsilon = \nabla\mathbf{u}+\nabla\mathbf{u}^T/2$ and used the constitutive relation of the gel to deduce the stress exerted by the cell. Since there is not need for matrix inversion, this method is denoted as the direct approach. In particular, the direct approach allows to use arbitrary constitutive material laws, e.g. viscoelastic or non-linear [*Toyjanova et al.*, 2014a, b]. Another strategy, which does not require the knowledge of the Green's function, is the application of the finite element (FE) method to infer traction stresses based on the measured displacement field. For example, *Soiné et al.* [2016] used an FE simulation to compute the traction forces of cells adhering to substrates with a non-planar topology.

Three-Dimensional Traction Force Microscopy The techniques presented so far allow to give precise information on the traction forces adherent cells exert locally via their focal adhesions and the total contractile efficacy of the cell. However, as e.g. Figure 1.4A shows, cells are usually moving and adhering in three-dimensional (3D) extracellular matrices. Thus, to determine the forces and their distribution across the cellular surface in *in vivo* situations, 3DTFM methods are being developed (see Figure 1.5B). For all 3D force quantification measurements, one has however to take into account that, in 3D confinements, cellular forces do not only arise due to contraction of the cytoskeleton, but also due to pushing forces exerted by the polymerization of actin against the lamellipodium, aiming at remodeling the extracellular environment.
Two techniques became prominent in the recent years. As in the related two-dimensional model, *Legant et al.* [2010] used a 3D hydrogel containing fluorescent beads surrounding an enclosed cell. By means of volume rendering, a finite element representation of the cell volume was generated and allowed to reconstruct the local discretized Green's function. A comparison of the predicted hydrogel displacements in the simulated volume and the experimentally acquired bead displacements was then used to determine the traction forces exerted by the cell. *Steinwachs et al.* [2016] determined traction stresses from material displacements in non-linear 3D collagen networks, which were designed to mimic the physiological conditions of the ECM. By assuming an isotropic and homogeneous distribution of polymers in the network and employing an averaging scheme, they obtained a macroscopic constitutive law for the material the cells were embedded in. This was followed by a FE representation of the polymer network and a conjugate gradient (CG) algorithm intending to find the contractile forces from minimizing the distance of simulated and measured network displacements.

Micropillar Arrays *Tan et al.* [2003] introduced an alternative method in which the independent inclination of elastomeric posts, arranged in regular microfabricated arrays, is used to quantify cellular and subcellular distribution of traction stresses (see Figure 1.5C). The width and height of the posts determines the substrate stiffness. Compared to TFM, this method has the advantage that no information about the reference state is required and the computation is quite straightforward. On the contrary, the method only allows to compute stresses at discrete sites and the range of possible substrate stiffnesses appears to be very limited [*Roca-Cusachs et al.*, 2017].

Molecular Force Sensors *Grashoff et al.* [2010] pioneered in designing and calibrating a molecular biosensor which allows to quantify forces experienced by specific proteins of the FA (see Figure 1.5D). The biosensor is composed of two fluorophores connected by an elastic linker and can be non-covalently integrated between head and tail domain of a protein. If the sensor experiences an external force, the elastic linker is extended, which leads to a decrease of the FRET efficiency, i.e. the energy transfer between the fluorophores. *Grashoff et al.* [2010] applied their method to the particular case of vinculin, whose recruitment to FAs is known to be force-dependent (see Figure 1.4B). The method allows to precisely determine subcellular forces in the range of single piconewtons. A significant drawback of the method is however the missing information about the force directions.

1.2.2 Single-Scale Force Quantification Methods

Compared to the previous section, single-scale force quantification methods usually allow to measure cellular forces only on a single spatial scale with one single measurement. Still, most of these methods provide access either to microscopic scales or cellular dynamics which are not approachable with the methods described so far. In the following, we will give a brief overview on single-scale methods.

Magnetic Tweezers Magnetic tweezers are one of the oldest methods to measure microscopic forces on cellular and molecular scales and goes back to the work of *Crick and Hughes* [1950]. Figure 1.7A sketches the principle of magnetic tweezers. A usually paramagnetic microbead is attached to a molecule of interest. The sample is then manipulated in an external magnetic field. The microbead, whose induced magnetic moment is proportional to the magnitude of the external field, experiences a force along the gradient of the magnetic field. This force can be controlled by either moving the external field vertically or rotating the external field. The force on the microbead as a function of magnet distance can then be calibrated from the transverse fluctuations through the equipartition relation and used in single-molecule force spectroscopy [*Neuman and Nagy*, 2008].

Optical Tweezers The functionality of an optical tweezer is similar to those of a magnetic tweezer and goes back to the pioneering work of *Ashkin et al.* [1986], who observed that dielectric particles experience a restoring force if displaced from the focal point of a

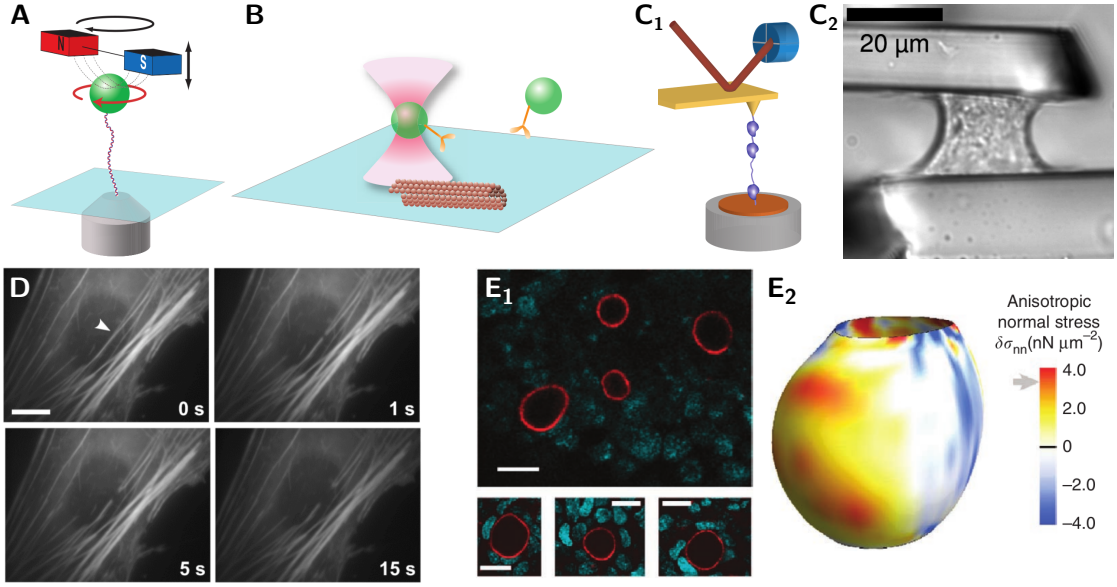

Figure 1.7: Classical and modern single-scale force quantification methods in mechanobiology. **(A)** Magnetic tweezers. **(B)** Optical tweezers. **(C)** Cantilevers. **(D)** Laser ablation. **(E)** Microdroplets. Scale bars are: **D**, 10 μm; **E**, 20 μm. Figures adapted from: **A-C$_1$**, *Neuman and Nagy* [2008]; **C$_2$**, *Mitrossilis et al.* [2009]; **D**, *Kumar et al.* [2006]; **E**, *Campàs et al.* [2014].

focused laser beam (see Figure 1.7B). The attracting electric field gradient generated by the laser exerts a force on the particle which is linear for small displacements, such that Hooke's law holds. The spring constant can be calibrated e.g. from fluid drag forces or thermal fluctuations experienced by the particle. For instance, *Finer et al.* [1994] used the method to measure a force of $3-4\,\mathrm{pN}$ and stepsize of 11 nm of single myosin motors when attached to actin filaments.

Cantilevers Cantilever methods exist on multiple spatial scales, as illustrated in Figure 1.7C. On the microscopic scale, *Marti et al.* [1988] showed that a standard atomic force microscope (AFM) can be used to measure forces exerted by single biomolecules. The molecule of interest is attached to the cantilever tip of the AFM and a movable platform. By increasing the distance between the platform and the cantilever tip, the force exerted on the molecule can be extracted from the deflection of the cantilever tip. *Mitrossilis et al.* [2009] developed a cantilever technique which not only allows to measure the overall contractile forces exerted by cells, but also the speed of shortening of isolated cells. In their setup, they use a rigid and a flexible microplate to which the cell attaches via its FAs. The stiffness of the environment is defined by the spring constant of the flexible microplate. By measuring the displacement of the flexible microplate, one can directly calculate the force via Hooke's law and the cell shortening velocity from the rate of force increase.

Laser Ablation So far, we presented methods which allow to deduce absolute force values from calibrated physical systems. Instead of measuring the force directly, *Kumar et al.* [2006] introduced a method which combines a laser nanoscissor and fluorescence photobleaching to cut and visualize the retraction dynamics of single stress fibers (see Figure 1.7D). By coupling an active viscoelastic model to the retraction dynamics, it is possible to infer the involved viscoelastic properties and stresses exerted by single stress fibers, as e.g. shown by *Colombelli et al.* [2009].

Microdroplets *Campàs et al.* [2014] developed a method which allows to quantify internal cell-generated mechanical stresses *in vivo*. They embed fluorescent typically cell-sized oil microdroplets, which are coated with ligands for integrins and cadherins, into cell layers. The deformations of single droplets by the cells are then visualized using fluorescence microscopy and image analysis, which allows to determine local stresses in the cell layer (see Figure 1.7E). By using magnetically responsive microdroplets, the droplets can even be used to generate forces within the cell layer which are regulated by an external magnetic field [*Serwane et al.*, 2017]. However, due to the incompressibility of the oil droplets, the method only allows to quantify and exert anisotropic stresses, which is a drawback of the method.

1.3 Models of Cellular Contractility

In this section, we will introduce physical models commonly used to mathematically capture the dynamics and effects of cellular contractility. In particular, we are looking for a convenient model to describe the traction forces exerted by adhering cells, which comprise an inhomogeneous distribution of actin and myosin, on a flat elastic substrate. This is why the model should allow for both the characterization of the internal structure and elastic coupling of the cells to the substrate. The model should further facilitate to relate local and global mechanical properties of the actin CSK in a simple mathematical framework.
In the following, we will classify mathematical models of cellular contractility into two groups: Bulk-based and interface-based models. We will, in particular, argue that the continuum modeling approach is the most suitable approach covering all of these demands, which is why we will use it throughout this manuscript.

1.3.1 Bulk-Based Models

Bulk-based models aim at describing cellular contractility based on internal mechanical properties and the structure of the cellular actin CSK. Traction stresses are then calculated from the mechanical coupling of the actin bulk to its environment. We will now describe the two most prominent approaches in this field: Continuum and network models.

Continuum Model The idea to describe cellular contractility by means of a continuum model is descended from the study of *Nelson et al.* [2005], who applied the model to

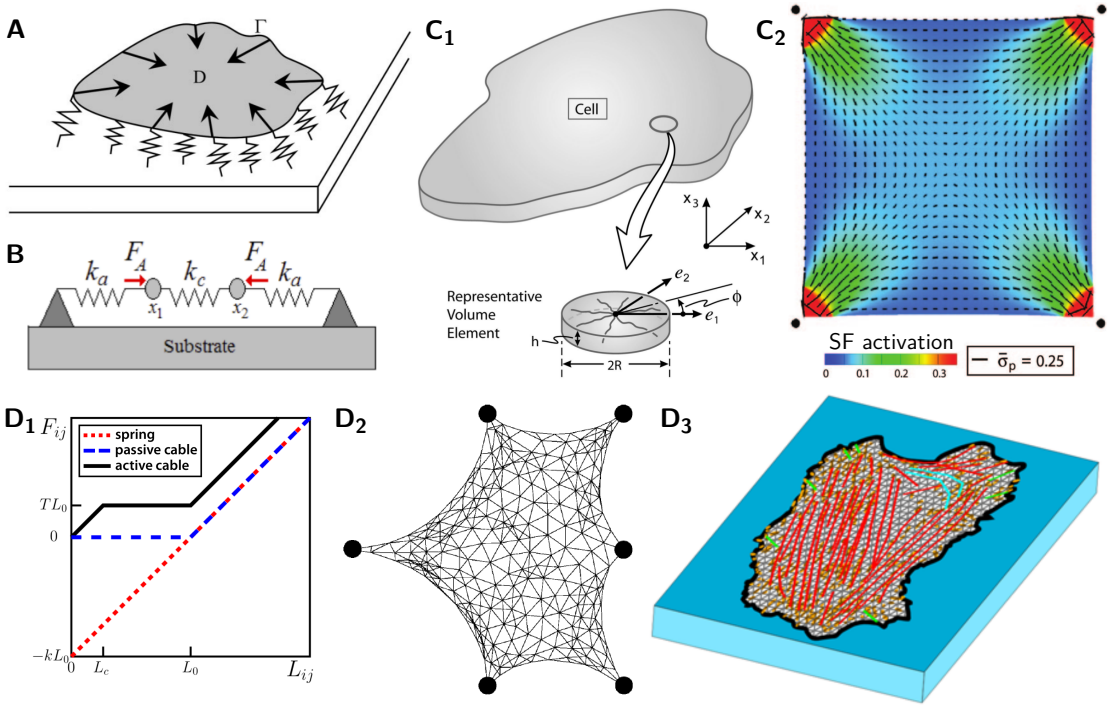

Figure 1.8: Bulk-based models to describe and predict cellular contractility. **(A)** Thermoelastic continuum model with discrete and **(B)** continuum substrate representation. **(C)** Multiscale continuum model with biochemical stress fiber generating mechanism. **(D)** Discrete cable networks. Figures adapted from: **A**, *Edwards and Schwarz* [2011]; **B**, *Banerjee and Marchetti* [2012]; **C**, *Deshpande et al.* [2006]; $\mathbf{E_1}$, *Torres et al.* [2012]; $\mathbf{E_2}$, *Bischofs et al.* [2008]; $\mathbf{E_3}$, *Soiné et al.* [2015].

explain mechanical stresses during cellular growth. In their model, the cell is represented by an elastic continuum of stiffness tensor C_{ijkl} and its contractility is introduced as a thermal stress tensor $\sigma_{ij}^{\mathrm{th}}$ to the elastic bulk, yielding the constitutive relation

$$\sigma_{ij} = C_{ijkl}\epsilon_{kl} + \sigma_{ij}^{\mathrm{th}}\,, \tag{1.2}$$

with stress and strain tensors σ_{ij} and ϵ_{ij}, respectively. The deformation of the cell is then described by the force balance equation

$$\partial_j \sigma_{ij} = f_i\,, \tag{1.3}$$

where f_i is the sum of all forces acting on the cell. Depending on the complexity of the external force and the anisotropy of the stiffness and thermal stresses, the cell forces can be either computed analytically or via a finite element simulation.
Deshpande et al. [2006, 2007] coupled a biochemical kinetic equation, describing stress fiber (SF) generation based on external mechanical signals, to the continuum model.

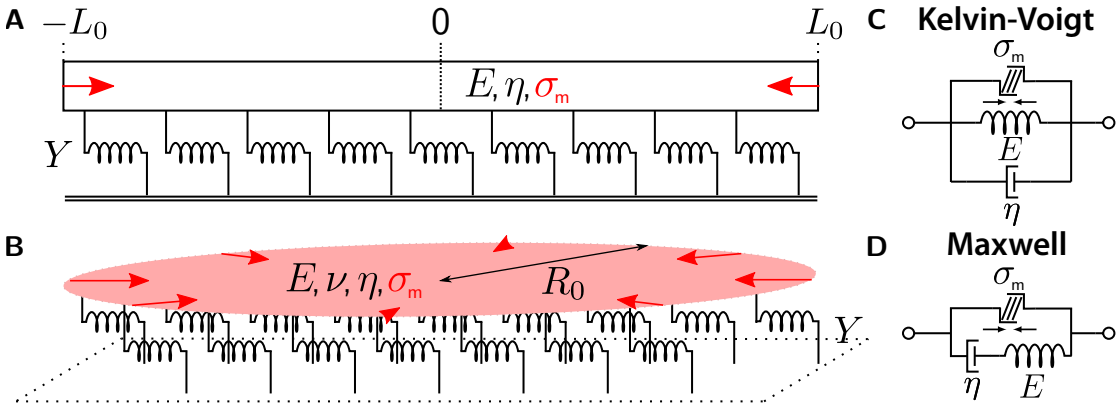

Figure 1.9: Thermo-viscoelastic continuum models used to model the actin cytoskeleton and the cell-matrix interaction in the course of this manuscript: **(A)** One-dimensional contractile bar of length $2L_0$ and **(B)** two-dimensional contractile disc of radius R_0 with elastic modulus E, Poisson's ratio ν, viscous modulus η, contraction stress σ_m and coupling spring stiffness density Y representing the cell-matrix interaction. In both cases, the foundation springs can only move horizontally. **(C-D)** Rheological models of the actin cytoskeleton: Kelvin-Voigt model **(C)** with a parallel arrangement of springs and dashpots, and Maxwell model **(D)** with a serial arrangement of both elements. In each case, a parallel contractile stress σ_m represents the contraction due to the myosin motors.

They captured the effect of stiffness and stress anisotropy due to SFs by an orientation-dependent order parameter field and averaged over orientations to compute the equivalent macroscopic properties in the continuum model (see Figure 1.8C).
Edwards and Schwarz [2011] used the continuum modeling approach to describe the localization of traction forces in adhering cells. They showed that the experimentally observed localization of traction forces at the periphery of single cells and cell layers can be reduced to the elastic problem of a contractile elastic layer of finite size coupled to an elastic foundation (see Figure 1.8A). In practice, they found that the external restoring force

$$f_i = Y u_i \,, \tag{1.4}$$

with spring stiffness density Y and displacement u_i, is sufficient to qualitatively describe the force distribution in adherent cells. Here, $Y = kN$ is a simplified representation combining the stiffness of focal adhesions and the substrate stiffness in the form of springs of stiffness k and spring density N. The parameter k and N are, in general, chosen to be constant, but can also be extended by a position dependence. The traction forces T_i exerted by the cell can then simply be read out from the displacement of these coupling springs via

$$T_i = Y u_i \,. \tag{1.5}$$

Edwards and Schwarz [2011] investigated both the one-dimensional case of an elastic bar and the two-dimensional case of an elastic disc, as illustrated in Figures 1.9A and B,

respectively. They analytically showed that the length scale l_p of force penetration in the medium is determined by both cellular and substrate stiffness. *Banerjee and Marchetti* [2012] showed how the theory can be extended to continuum substrates, as depicted in Figure 1.8B, by using a Green's function approach and established a formula to estimate l_p and, with this, Y from experimental parameters.
Mertz et al. [2012, 2013] used the model to explain the characteristic scaling of traction forces with the size of cell colonies and to capture the cross talk between the cells via adherens junctions. *Oakes et al.* [2014] further extended the model equations by a line tension to account for the fact that cellular traction forces often correlate with the local geometry of the cell contour.
In the context of this manuscript, we will use the model of *Edwards and Schwarz* [2011] with both elastic and viscoelastic constitutive laws to describe cellular contractility. Standard choices for viscoelastic models are the Kelvin-Voigt model and the Maxwell model (see Figures 1.9C and D, respectively).
A Kelvin-Voigt model connects springs and dashpots in parallel, such that the dashpots act as viscous dampers in the restoring process of the springs and any deformation of the material is reversible. For example, *Besser et al.* [2011] used the Kelvin-Voigt model to describe the retraction dynamics of laser-ablated stress fibers.
A Maxwell model connects springs and dashpots in series. Here, both springs and dashpots move independently, such that the deformation becomes partly irreversible due to the irrestorable flow of the dashpot. *Saha et al.* [2016], for instance, use a Maxwell model to deduce effective material properties of the actin cortex from laser ablation experiments.
Taken together, the continuum approach is a very versatile method. It can be applied and related on multiple spatial scales. Further, it allows to incorporate inhomogeneous and anisotropic cellular properties and establish a coupling of the cell to its environment. On the downside, due to the repelling elastic forces, the boundary of a continuum bulk does not adopt an invaginated circular shape as expected from experiments with cells attached to adhesive islands (compare invaginations in Figure 1.8C and D). However, an extension of the standard FEM approach by a separated modeling of the cell bulk and surface allows to reproduce the experimentally observed shapes [*Vernerey and Farsad*, 2011].

Active Cable Network Motivated by the experimental findings by *Gittes et al.* [1993] and *Kojima et al.* [1994], revealing that actin filaments behave like springs upon extension, but cannot support compressive loads without buckling, depolymerizing or sliding, *Coughlin and Stamenović* [2003] introduced a cable network to describe the deformability of the actin CSK of adherent cells. As highlighted in Figure 1.8D$_1$, a cable does not exhibit an elastic counterforce upon contraction, as springs do.
Bischofs et al. [2008] and *Torres et al.* [2012] demonstrated that, by applying a constant tension at each network link, yielding the so-called active cable network, one can reproduce the circular arc shape of the cellular outline as observed in cells adhering to small adhesive islands (see Figure 1.8D$_2$). This finding was further confirmed by *Brand et al.* [2017] for cells adhering to microposts in a three-dimensional scaffold.

One advantage of the active cable network model, or network models in general, is the possibility to vary cellular properties locally or introduce discrete elements such as stress fibers (SFs). This was e.g. exploited by *Soiné et al.* [2015], who used the model to support the reconstruction of traction forces by representing the architecture of the actual actin CSK via a cable network with embedded contractile SF links, which were attached to a three-dimensional elastic substrate at their ends (see Figure 1.8D$_3$). By comparing experimental and simulated displacements of the substrate, their method not only allowed to reconstruct cellular traction forces with a high precision but also to infer the contractile properties of single SFs in the network.
In the recent time, *Kassianidou et al.* [2017] used the model to reveal that the tension borne by single SFs depend on the SF geometry and their embedding into the actin CSK. *Oakes et al.* [2017] further extended the cable links to viscoelastic cables and established link creation and removal rules to account for the (de-)polymerization of actin to show, based on the optogenetic regulation of the CSK, that SF contractility dominates the contractility of a potential background actin network.
One drawback of active cable networks is, however, the huge and long-lasting computational effort per simulation, since each link has to be treated separately. Another disadvantage arises from the large parameter space and the inaccessible mathematical framework to parameterize the mechanical properties of single links from global properties of the cell and vice versa.

1.3.2 Interface-Based Models

Interface-based models aim at describing cellular contractility based on the dynamics of the cellular interface. Traction stresses are, in general, inferred from the shape of the cellular envelope. We will now describe the most prominent approaches in this field of models: Contour models, Cellular Potts models, phase-field and vertex models.

Contour Model A reasonable idea is to calculate the traction stress of a cell from the shape of its contour. This was first motivated by *Zand and Albrecht-Buehler* [1989] who found that those edges of spread fibroblasts which were spanning non-adhesive area were supported by single stress fibers, which established a circular arc shape of the cellular outline. This observation was confirmed by *Bar-Ziv et al.* [1999], who further showed that even after a controlled degradation of the actin CSK the edges of the cellular outline can be described by invaginated circles, with decreasing arc radius R for increasing degradation. The authors suggested that the shape of the cellular contour can be a consequence of the counterplay of a surface tension σ and a line tension λ, which determine the arc radius via the Laplace law $R = \lambda/\sigma$, yielding the so-called simple tension model (STM).
Experiments on cells attached to adhesive islands, however, showed that the arc radius reveals a further dependence on the distance d of the adhesion points, as Figure 1.10A illustrates [*Bischofs et al.*, 2008]. This observation was used to effectively extend the STM by an elastically modified line tension $\lambda(d)$. They obtained an analytical expression for the radius $R(d)$ which could be used to reproduce the experimental results, resulting in the tension-elasticity model (TEM). *Bischofs et al.* [2009] finally demonstrated how

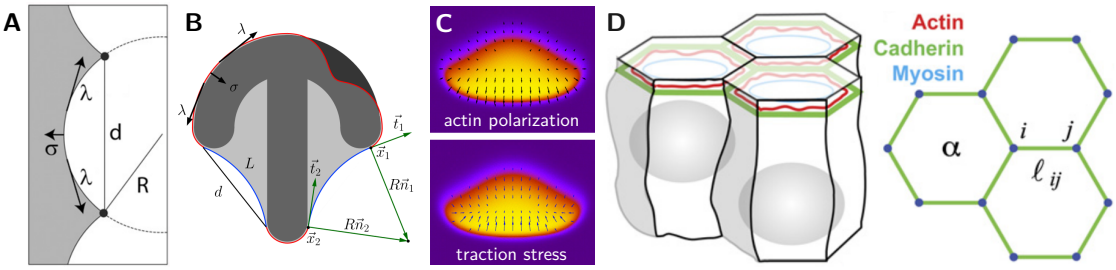

Figure 1.10: Interface-based models to describe and infer cellular contractility. **(A)** Contour model. **(B)** Cellular Potts model. **(C)** Phase field model. **(D)** Vertex model. Figures adapted from: **A**, *Bischofs et al.* [2008]; **B**, *Albert and Schwarz* [2014]; **C**, *Ziebert et al.* [2011]; **D**, *Farhadifar et al.* [2007].

the TEM can be used to calculate the distribution of traction forces exerted by the cell. However, since the model does not incorporate the internal structure of the cellular actin CSK, it is only applicable to the special cases stated above and will not be further considered.

Cellular Potts Model Like a contour model, the Cellular Potts model (CPM) describes cellular traction forces via geometrical tension, inferred from the shape of the cellular outline (see Figure 1.10B and *Albert and Schwarz* [2014]). The shape is, however, computed dynamically from a probabilistic simulation. The cell and its environment are represented by occupied and free lattice sites, respectively, while the cell shape is propagated by means of a probabilistic algorithm which randomly inverts lattice sites based on a Hamiltonian, similar to the Ising model. The Hamiltonian is essentially composed of two contributions: one that favours tension and one that favours adhesion. Thus, the overall spreading and migration process of a cell is determined by a balance of both contributions.
In the scope of cell mechanics, the approach was e.g. used by *Marée et al.* [2006, 2012] to model the polarization and movement of fish keratocytes. *Käfer et al.* [2007] used the CPM to explain cell packing of Drosophila cells and *Vianay et al.* [2010] adapted the model to reproduce shapes of cells spreading on a protein lattice. In the recent years, *Albert and Schwarz* [2014, 2016] showed that the experimentally observed shape of both cells and ensembles of cells on adhesive micropatterns could be well described by the dynamics predicted by the CPM. The authors also used the model to qualitatively reconstruct cellular traction forces from the cell shapes.
However, by design, the CPM does neither allow for the modeling of the internal architecture of the actin CSK, which apparently regulates cell spreading, nor an efficient way to implement cellular mechanosensing exists (see e.g. [*van Oers et al.*, 2014]).

Phase Field Model Like the CPM, the Phase Field model (PFM) is designed to describe the motion of a closed interface via a minimal set of equations. *Shao et al.* [2010] adapted the PFM to predict the morphodynamics of moving fish keratocytes. In its basic form, the cell interface is described by a phase field $\rho(x, y, t)$, with $\rho = 1$ and $\rho = 0$ representing

the inside and outside of the cell, respectively, with a smooth variation in between. The propagation of the phase field is then determined by means of an overdamped equation of motion.
Ziebert et al. [2011] coupled the phase field dynamics to a vector field **p**, which describes the actin polarization and, with this, not only allows to reproduce the motion and shape of keratocytes, but also to qualitatively predict the traction forces exerted by the moving keratocytes (see Figure 1.10C). Here, the traction forces are calculated from the sum of the actin polymerization force and the viscous drag force, taking into account that the cell is an isolated system. *Ziebert and Aranson* [2013] further extended the model to account for adhesion growth and mechanosensing, while *Löber et al.* [2014] could improve the model to locally resolve traction forces in the process of durotaxis.
The model is, however, primarily designed to describe the shape dynamics of moving cells which are driven by dynamically changing force fields and is not suited to reproduce the static situation of an adherent cell. It also has no representation for the material properties of the cell, such as its elasticity or viscosity. Further, even in the simplest setting, the dynamics of the PFM are highly nonlinear which makes it difficult to extract tangible mechanical properties of the cell.

Vertex Model In the scope of cell mechanics, vertex models (VMs) are primarily used to describe cell packing in epithelia [*Farhadifar et al.*, 2007]. For example, *Hufnagel et al.* [2007] used a VM to investigate the size determination process during tissue growth.
The epithelium is described by a network of polygonal cells whose configuration is defined by the positions of the vertices of the polygons (see Figure 1.10D). For each vertex, an energy function is defined, which depends on geometrical quantities area and perimeter of adjacent polygons and the length of adjacent links. In general, the energy function can be arbitrarily extended. The energy function is then minimized to satisfy force balance at each vertex. The internal forces in the network are then inferred from the contours of the polygons w.r.t. to their resting configuration. The VM is, however, not suited as a model for both single and adherent cells.

1.4 Outline

In this manuscript, we combine traction force microscopy, finite element simulations and multiscale modeling to quantify cellular contractility and interrelate contractility with the internal organization of the actin cytoskeleton. The manuscript is divided into three parts.
Part I covers the algorithms used throughout this thesis to reconstruct cellular traction stress from substrate deformations. In **Chapter 2**, we introduce the software framework developed in the course of this work to enable a reliable, time- and resource-efficient and automatized estimation of cellular traction forces by means of regularized Fourier Transform Traction Cytometry (FTTC). We thereafter continue with an analytical investigation of regularization in FTTC, highlighting its indispensability in the process of traction force reconstruction. The chapter is completed with an extensive comparison

of well-established parameter estimation and regularization strategies, revealing the superiority of the commonly used Tikhonov regularization in the particular case of FTTC.
Part II of this manuscript connects traction force reconstruction with computational modeling of the force-generating cellular cytoskeleton on multiple spatial scales. In **Chapter 3**, a thermo-viscoelastic continuum model with viscoelastic coupling is introduced to capture the dynamics of force generation and cytoskeletal flows resulting from the spatiotemporal regulation of the RhoA signaling pathway by means of an optogenetic probe in mouse embryo fibroblasts. The model allows to explain the elastic-like relaxation of stress fibers (SFs) after short photoactivation periods and to find the characteristic relaxation time of a SF for the transition from solid-like to fluid-like behavior. We will moreover use the model to identify zyxin as a key regulator of the elasticity of SFs. The model is finally extended to two dimensions to establish a physical correspondence between the continuum model and the discrete viscoelastic cable network presented by *Brand* [2017].
In **Chapter 4**, we extend the continuum model by an anisotropic contractile stress and inhomogeneous coupling to investigate the influence of the structure of the adhesive area on the contractility of fibroblast cells. We verify by means of finite element simulations that the polarity of the actin cytoskeleton, which is indeed determined by the shape of the adhesive area, regulates the magnitude and dynamics of the cellular contractile energy as well as the traction pattern, even if the cells adopt the same spread area and contour. The modeling approach further allows to specify the effect of an increasing duration of photoactivation and of an increasing spread area on the overall efficiency and dynamics of the cellular force production.
Thereafter, in **Chapter 5**, we reconstruct the dynamics of force generation in human blood platelets spreading onto elastic substrates of variable stiffness, which yields characteristic contractile patterns of individual platelets. We can explain the force anisotropy of platelets by means of simulated patterns of randomly positioned traction spots. The specific correlation between the maximum force level a platelet reaches and its spread area can be well-described by our continuum model, which then allows both to estimate the typical internal stress of platelets and to explain why the mechanosensitivity of platelets only appears for a much softer substrate stiffness regime than those of fibroblasts.
In **Chapter 6**, we demonstrate that our continuum model is also applicable to examine the early-stage dynamics of force generation in a collectively migrating layer of Madin-Darby Canine Kidney (MDCK) cells. In particular, we first show by means of traction force reconstruction that the selective emergence of a leader cell at the margin of the layer depends on the dynamics of its follower cells. We then map our model to the cell layer and find that the origin and maintenance of leader cells as well as characteristic length scales between neighboring leader cells can be explained by the force transduction in elastic sheets with elastic substrate coupling. We further reduce our model to one dimension, which allows for an analytical treatment of the biological system.
Part III of this manuscript finally aims at establishing a mathematical relation between the microscopic composition of the actin cytoskeleton and the macroscopic mechanical properties of a cell. For this purpose, **Chapter 7** starts with an adaptation of the so-called asymptotic homogenization technique to the one-dimensional continuum model

presented so far. This allows us to analytically derive formulae to connect local and global mechanical properties of a viscoelastic contractile bar with an inhomogeneous distribution of stiffness, viscosity and contractile stress. For the particular example of a stress fiber, we then use the formulae to relate micro- and macroscopic mechanical properties known from literature, revealing that a stress fiber locally exhibits properties which are usually attributed to a mechanical metamaterial. We conclude the chapter by presenting mechanisms which are likely to contribute to this uncommon mechanical behavior.

Chapter 8 finally connects the three parts of this manuscript. Here, we adapt the asymptotic homogenization technique to our two-dimensional model in order to infer the internal and traction stress pattern of a cell from its actin polarity, which itself is determined by means of quantitative image analysis. We optimize the resulting algorithm based on existing experimental data and use the algorithm to predict cellular traction stresses in novel environments.

Part I

From Substrate Deformations to Forces - Quantification of Cellular Forces

2 Regularization for Fourier-Based Traction Force Microscopy

Traction force microscopy (TFM), as it is used nowadays, has been introduced in the pioneering work by *Dembo and Wang* [1999], who built up on the finding by *Harris et al.* [1980] that biological cells, once seeded on an elastomeric silicon rubber substrate, create wrinkles due to the, mainly planar, contractile shear stresses they exert on the substrate. In order reconstruct these contractile stresses, *Dembo and Wang* [1999] blended sub-micrometer-sized fluorescent beads into an elastic polyacrylamide substrate of known Young's modulus and Poisson's ratio and quantified the displacement of these beads, once the cell adhered to the substrate.

By choosing the size of the substrate by orders of magnitude larger than the cell size, *Dembo and Wang* [1999] made the plausible assumption that the substrate can be treated as a semi-infinite elastic half-space, such that one can directly write down the Fredholm integral-type relation between the effected bead displacements and the stresses causing these. *Butler et al.* [2002] further transformed this Green's function based approach to Fourier space, allowing a considerably faster computation of traction stresses by exploiting the convolution theorem.

In practice, the acquisition of displacements from the movement of single beads is, however, subject to noise, be it due to limitations in the optical resolution of the microscope or the heterogeneity of the substrate stiffness [*Schwarz and Soiné*, 2015]. Since further, the Green's function of a two-dimensional elastic problem is of long-ranged nature, the inverse traction reconstruction problem becomes ill-posed, because any displacement vector can be the result of any stress contribution, even it both are far away from each other. In this situation, regularization is required to hamper an overfitting of the noise-affected displacement field [*Schwarz et al.*, 2002].

In this context, a typical choice is 0^{th}-order Tikhonov regularization, which penalizes a too large total traction force and allows to calculate the solution vector analytically [*Phillips*, 1962; *Tikhonov*, 1963]. *Sabass et al.* [2008] showed that Tikhonov regularization performs comparably well in the case of both real-space and Fourier-based TFM. *Han et al.* [2015] and *Brask et al.* [2015] further used sparse regularization in real-space TFM to exploit the additional information that cells exert traction stresses only at discrete sites.

In order to obtain a reasonable estimate of the traction field, the heuristic data-driven methods *L-curve* and *Generalized Cross-Validation* became most popular, since they do not require any prior knowledge about the solution vector [*Golub et al.*, 1979; *Hansen*, 1992]. However, although two-dimensional Fourier-based TFM is a widely used technique to quantify cellular forces, current software packages, such as those used in *Han et al.*

[2015] or *Martiel et al.* [2015], are still incomplete when it comes to the automatized estimation of the regularized traction field.
In this chapter, we introduce and optimize the existing FTTC algorithm, which will be used as a basis for the following chapters to establish the necessary connection between cellular stresses and modeling. The optimization procedure will allow to develop a software tool with automatized regularization for Fourier-based TFM.
In particular, we start with a description of the full algorithm to calculate traction stresses from reference and displaced bead images in two dimensions (see Section 2.1). Thereafter, in Section 2.2, we demonstrate the importance of regularization in TFM by means of a theoretical investigation, supported by experimental analysis of artificial data sets. In Section 2.3, we perform a quantitative comparison of standard data-driven Tikhonov-regularization methods and bring up their advantages and disadvantages with respect to an incorporation into an automatized scheme. Finally, in Section 2.4, we go a step further and quantify the performance of sparse and anti-sparse regularizers as compared to Tikhonov regularization, showing that in the ideal case of a displacement field subject only to white noise, a sparse regularization method is able to outperform Tikhonov regularization.

2.1 Software Framework

We start with a description of the software pipeline used to calculate traction stresses from raw bead images. Figure 2.1 illustrates the coarse schematic of the workflow. The software has two entries for input data, which is left to the user's decision: Either one starts with, at least two, 8-bit bead images and computes the displacements first before dealing with the calculation of traction stresses, or, one starts immediately with an existing file containing positions and displacements which has been exported from other software packages.
As colors in Figure 2.1 indicate, the software pipeline can be splitted into two consecutive processes: The calculation of a displacement field from a reference and one or more deformed bead images, which will be discussed in Subsection 2.1.1 and the calculation of traction stress fields from displacement fields, which will be in the focus in Subsection 2.1.2. In Subsection 2.1.3, we will conclude with listing quantities which will later be used to quantify the contractile behavior of cells.
The software is written in the Python Programming Language [*Van Rossum et al.*, 2007]. Computation and visualization are conducted with the scientific packages NumPy [*Walt et al.*, 2011], SciPy [*Jones et al.*, 2014], Matplotlib [*Hunter*, 2007] and PyQt [*Summerfield*, 2007].

2.1.1 Calculation of Displacements from Bead Images

In the first step of feature acquisition and tracking, we have to consider two different cases: For the situation of a large bead density, in particular, if the cell size is much larger than the typical distance between two beads, it makes sense to assume that neighboring beads move uniformly and thus one can average over the motion of several beads without

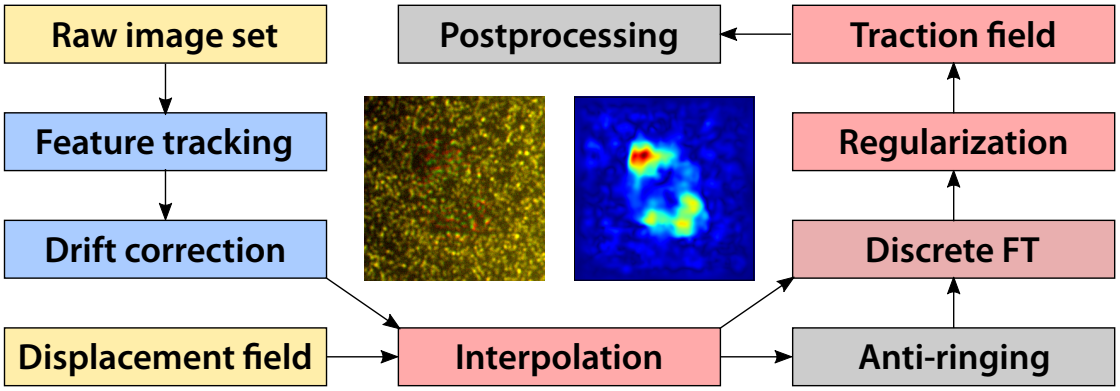

Figure 2.1: Schematic of the workflow of the TFM software developed and used in the course of this thesis. *Yellow* boxes represent the input data, *blue* boxes denote steps of the algorithm to calculate a displacement field from bead images, while *red* boxes denote steps to calculate traction stresses from an arbitrary displacement field. *Grey* boxes refer to optional steps. The enclosed images show exemplary bead images with color-coded displacements (*left*) and the corresponding traction stress field (*right*). Enclosed bead image by courtesy of Jana Hanke, University of Göttingen.

losing spatial information. In this case, we will use Particle image velocimetry (PIV), which has a long tradition in the subject of hydrodynamics [*Chu et al.*, 1985; *Willert and Gharib*, 1991; *Raffel et al.*, 1998; *Adrian and Westerweel*, 2011] and which has already been applied as feature tracking technique in TFM (see e.g. *Style et al.* [2014]).
In the case of a low bead density, neighboring beads cannot be considered as moving uniformly any more and one has to track each bead individually. Here, two state-of-the-art choices are Particle tracking velocimetry and Optical flow. Of these, particle tracking velocimetry is the common method applied in the case of a low bead density and, further, is the standard option in three-dimensional feature acquisition (see e.g. *Schwarz and Soiné* [2015]). We will, however, only consider the optical flow algorithm for at least two reasons [*Fortun et al.*, 2015]. First, particle tracking algorithms usually require a large number of input parameters, making the bead tracking setup error-prone and non-generalizable. Second, the computational cost of the optical flow algorithm is up to orders of magnitude lower than those of a typical particle tracking algorithm [*Holenstein et al.*, 2017].

Particle image velocimetry (PIV) In the general setting of the PIV algorithm, we start with partitioning both the relaxed bead image and the deformed bead image into patches R and D of window size w_R and w_D, respectively. According to the thumb rule designed by *Westerweel* [1997], the patch size ideally should be chosen equal or larger than four times a typical displacement of the features. *Scarano and Riethmuller* [1999] use an iterative multi-grid approach, allowing to start at a coarse scale and refining the precision of the measurement with each iteration. Also, w_D can be, in general, chosen to be larger than w_R to account for features leaving the patch between the two images. The total number of patches is determined by the allowed overlap of neighboring patches, whereas

an overlap of 50 % appears to be ideal in terms of under- and oversampling of information [*Hinsch*, 2002; *Stamhuis*, 2006].
After partitioning the image, we compute the discretized cross-correlation function $C(r,s)$ of corresponding mean-normalized patches

$$C(r,s) = \frac{1}{w_R^2} \cdot \sum_{i=1}^{w_R} \sum_{j=1}^{w_R} \left[R(i,j) - \bar{R}\right] \left[D(i+r, j+s) - \bar{D}\right] , \tag{2.1}$$

with discrete indices r and s. The cross-correlation function can be efficiently computed by means of fast Fourier transforms, as described by *Willert and Gharib* [1991], but then one has to choose $w_R = w_D$. The distance of the peak $C(r_{\max}, s_{\max})$ from the center of the patch corresponds to the average feature displacement within the image patch, but has integer indices. In order to gain a subpixel accuracy, we fit a Gaussian curve to the discrete pixel values surrounding the peak [*Lourenco and Krothapalli*, 1995]:

$$u_x = r_{\max} + \frac{\ln C(r_{\max}-1, s_{\max}) - \ln C(r_{\max}+1, s_{\max})}{2\ln C(r_{\max}-1, s_{\max}) - 4\ln C(r_{\max}, s_{\max}) + 2\ln C(r_{\max}+1, s_{\max})} , \tag{2.2}$$

and in an equivalent manner for u_y.
Typically, the algorithm described so far produces spurious vectors, e.g. in regions with a low intensity difference between bead signal and background or along the boundaries of the image. We use two consecutive registration techniques to uncover these vectors. First, we introduce a threshold for the minimal signal-to-noise ratio in the correlation function. If the ratio between the highest and second highest peak is lower than this threshold, the displacement vector is removed [*Adrian and Westerweel*, 2011]. Second, we apply the so-called normalized median test, introduced by *Westerweel and Scarano* [2005]. Here, we compute the residual $r_i = |\mathbf{u}_i - \mathbf{u}_m|$ for the eight displacement vectors $\mathbf{u}_i$ surrounding the displacement $\mathbf{u}_0$ with $\mathbf{u}_m = \text{median}(\{\mathbf{u}_i \,|i = 1, ..., 8\})$. We can then quantify the deviation of $\mathbf{u}_0$ from the neighboring displacement via the normalized residual $r_0 = |\mathbf{u}_0 - \mathbf{u}_m| / r_m$ with $r_m = \text{median}(\{r_i \,|i = 1, ..., 8\})$. By introducing a maximal normalized residual threshold r_{th}, we can drop out all vectors, for which $r_0 > r_{\text{th}}$. The discarded vectors are finally replaced by the median of their surrounding vectors.
With this procedure, we end up with continuous coordinates $\mathbf{x} = (x, y)$, representing the centers of the patches, and the corresponding displacement vectors $\mathbf{u} = (u_x, u_y)$. We will apply the PIV algorithm in Chapters 3, 4 and 6. In particular, we will use the software *OpenPIV* to conduct the calculations described above [*Taylor et al.*, 2010].

Kanade-Lucas-Tomasi (KLT) optical flow algorithm In the KLT algorithm, we start with a *Shi-Tomasi* corner tracking algorithm to register the relevant features of the image, i.e. the beads. For each pixel of the image I, a surrounding patch of block size (b_x, b_y) is defined. Then, the patch is shifted by (x, y) and the sum of squared differences (SSD)

between the shifted and original patch is calculated:

$$\mathrm{SSD}(x,y) = \sum_{i=1}^{b_x}\sum_{j=1}^{b_y} \left(I\left(i+x, j+y\right) - I\left(i,j\right)\right)^2 . \tag{2.3}$$

By using the Taylor expansion

$$I\left(i+x, j+y\right) \approx I\left(i,j\right) + I_x\left(i,j\right)x + I_y\left(i,j\right)y\,, \tag{2.4}$$

we can rewrite Equation 2.3 as

$$\mathrm{SSD}(x,y) = \begin{pmatrix} x & y \end{pmatrix} \mathbf{A} \begin{pmatrix} x \\ y \end{pmatrix} , \tag{2.5}$$

with A being the structure tensor

$$\mathbf{A} = \sum_i \sum_j \begin{pmatrix} I_x^2 & I_x I_y \\ I_x I_y & I_y^2 \end{pmatrix} . \tag{2.6}$$

In our case, a feature is characterized by a large variation of SSD in all directions (x, y). Consequently, at a feature point, A will have large eigenvalues (λ_1, λ_2). The Shi-Tomasi corner detector computes $R = \min(\lambda_1, \lambda_2)$ and takes those N points with largest R as relevant features of the image [*Shi et al.*, 1994]. We furthermore specify the minimal feature distance $D_{\min}$, such that, in the case of large beads, one bead will not be classified as two or more features. Moreover, a quality level q is prescribed which ensures that those features with $R < q \cdot R_{\max}$ are rejected. The result of this corner tracking algorithm is a discrete set of bead positions.
Having determined the feature positions in the reference frame, we continue with the measurement of their displacements. For this, we use the pyramidal Kanade-Lucas-Tomasi (KLT) optical flow algorithm, which is based on two crucial assumptions [*Lucas et al.*, 1981; *Bouguet*, 2001]. First, we assume that pixel intensities $I(x, y, t)$ at position (x, y) and time t stay approximately constant between two consecutive frames:

$$I(x,y,t) = I(x+\Delta x, y+\Delta y, t+\Delta t) \approx I(x,y,t) + I_x\Delta x + I_y\Delta y + I_t\Delta t\,. \tag{2.7}$$

Dividing by Δt leads to the so-called *optical flow equation*

$$I_x v_x + I_y v_y + I_t = 0\,, \tag{2.8}$$

with unknowns (v_x, v_y). This equation is underdetermined, such that we need a second assumption. The general idea of the Kanade-Lucas algorithm is that, similar to PIV, neighboring pixels, determined by the window size w, have a similar motion. This yields the overdetermined equation

$$\mathbf{S} \begin{pmatrix} v_x \\ v_y \end{pmatrix} = \mathbf{t}\,, \tag{2.9}$$

where $\mathbf{S}$ is a $(w^2 \times 2)$-matrix with rows (I_x, I_y) at the corresponding window positions and $\mathbf{t}$ a vector of length w^2 and elements $-I_t$. Multiplying Equation 2.9 with $\mathbf{S}^T$ and inversion finally leads to the least squares problem

$$\begin{pmatrix} v_x \\ v_y \end{pmatrix} = \left(\mathbf{S}^T\mathbf{S}\right)^{-1}\mathbf{S}^T\mathbf{t}\,, \tag{2.10}$$

which can be solved exactly. The displacements are then simply calculated via $\mathbf{u} = \mathbf{v}\Delta t$. If the bead displacements are large, we have to sum up the displacements from the comparison of two succeeding bead images (i.e. *Lagrangian* method). In this case, the linear approximation in Equation 2.7 leads to an additive imprecision in the computed bead displacements. We can, however, resolve this issue to a large extent by defining

$$\mathbf{u}(t, t+\Delta t) := \frac{1}{2}\left(\mathbf{u}(t, t+\Delta t) - \mathbf{u}(t+\Delta t, t)\right)\,. \tag{2.11}$$

In the case of the *pyramidal* Kanade-Lucas-Tomasi (KLT) optical flow algorithm, the described algorithm is performed $P_{\max}$ times iteratively for shrinking window sizes, starting from $P_{\max} \cdot w$ [*Bouguet*, 2001]. Calculated displacements in one iteration are then used as bias for the succeeding iterations. The output of the algorithm finally is a discrete irregular displacement field for the set of calculated bead positions.
We will apply the KLT algorithm in Chapter 5. In particular, we will use the software *OpenCV* to conduct the calculations described above [*Bradski*, 2000; *Pulli et al.*, 2012].

After the feature and displacement acquisition steps described above, we proceed with a drift correction of the calculated displacements, common to both methods. For this, we calculate the mean displacement $\bar{\mathbf{u}}_{\text{drift}}$ in a region far from the cell where we assume that displacements due to the traction of the cell should have vanished. The final displacement field is the difference $\mathbf{u} \to \mathbf{u} - \bar{\mathbf{u}}_{\text{drift}}$.

2.1.2 Calculation of Traction Stresses from Displacements

Since Fourier-based methods in general require a regular computation grid, we start with a cubic spline inter- and extrapolation of the irregular displacement field to a regular grid of desired mesh size. In particular, we use the quickhull algorithm, introduced by *Barber et al.* [1996], to triangulate the input displacement field and a Clough-Tocher scheme to generate a piecewise cubic interpolating Bezier polynomial to each triangle [*Clough and Tocher*, 1965]. For extrapolation, we further apply a smooth cubic bivariate spline algorithm. Both, inter- and extrapolation algorithms, are incorporated in the Python package SciPy [*Jones et al.*, 2014].
Fourier-based calculations over finite domains always impose periodic boundary conditions and therefore are always subject to so-called *ringing* artifacts along the boundary of the image. This is especially the case if bead displacements do not vanish in the vicinity of the boundary, as e.g. in the case of collectively migrating cells. If these artifacts overly affect the displacement field, we use one of the two following methods to counteract these. One option is a so-called Tukey filter, which, for a one-dimensional sequence of N samples,

weights each sample n by the function [*Tukey*, 1967]

$$w(n) = \begin{cases} \frac{1}{2}\left[1+\cos\left(\pi\left(\frac{2n}{\alpha(N-1)}\right)\right)\right], & \text{if } 0 \le n \le \frac{\alpha(N-1)}{2} \\ 1, & \text{if } \frac{\alpha(N-1)}{2} \le n \le (N-1)\cdot\left(1-\frac{\alpha}{2}\right) \\ \frac{1}{2}\left[1+\cos\left(\pi\left(\frac{2n}{\alpha\left(N-\frac{2}{\alpha}+1\right)}\right)\right)\right], & \text{if } (N-1)\cdot\left(1-\frac{\alpha}{2}\right) \le n \le N-1 \end{cases}, \tag{2.12}$$

with the parameter $0 \le \alpha \le 1$, where $\alpha = 0$ is the full rectangular window and $\alpha = 1$ is a Hann window [*Harris*, 1978]. Setting $\alpha > 0$ will always enforce a smooth decay of the displacement field towards the boundary.
The second option to counteract ringing artifacts is via padding [*Style et al.*, 2014]. Here, we mirror the displacement field along its edges, yielding a new image of size $3N$. We introduce another factor $0 \le \beta \le 1$, which determines the final size to which the image is duplicated, with $\beta = 0$ giving the original image and $\beta = 1$ the full image with its mirror images.
The resulting regular drift-free displacement field is then Fourier-transformed and converted to traction stresses using regularized FTTC [*Sabass et al.*, 2008]. In particular, we use the numerical scheme explained in detail in *Plotnikov et al.* [2014]. Briefly worded, in FTTC, traction stresses $\mathbf{t}$ are reconstructed from substrate displacements $\mathbf{u}$ in Fourier space [*Butler et al.*, 2002]. In real space, these quantities are related via a Green's function $\mathbf{G}(\mathbf{x})$ as

$$u_i(\mathbf{x}) = \int \sum_{j=1}^{2} G_{ij}\left(\mathbf{x}-\mathbf{x}'\right) t_j\left(\mathbf{x}'\right) \mathrm{d}\mathbf{x}', \tag{2.13}$$

with

$$\mathbf{G}(\mathbf{x}) = \frac{1+\nu}{\pi E r^3}\begin{pmatrix} (1-\nu)r^2+\nu x^2 & \nu xy \\ \nu xy & (1-\nu)r^2+\nu y^2 \end{pmatrix}, \tag{2.14}$$

using substrate stiffness E, Poisson's ratio ν and $r^2 = x^2 + y^2$ [*Dembo and Wang*, 1999]. In Fourier space, the integral turns into a product

$$\hat{u}_i(\mathbf{k}) = \sum_{j=1}^{2} \hat{G}_{ij}(\mathbf{k})\,\hat{t}_j(\mathbf{k}), \tag{2.15}$$

now with the Fourier-transformed Green's function

$$\hat{\mathbf{G}}(\mathbf{k}) = \frac{2(1+\nu)}{E k^3}\begin{pmatrix} (1-\nu)k^2+\nu k_y^2 & -\nu k_x k_y \\ -\nu k_x k_y & (1-\nu)k^2+\nu k_x^2 \end{pmatrix}, \tag{2.16}$$

using $k^2 = k_x^2 + k_y^2$.
The inverse problem of calculating of stresses (i.e. causes) from displacements (i.e. effects) under existence of noise is known to be *ill-posed*, since, due to the long-ranged (i.e. $1/r$) nature of elasticity theory, any traction spot can contribute to a displacement, even if it is far away. Noise is omnipresent in the measured displacement field, be it because of

limitations in the resolution of the microscopy images or the inhomogeneous properties of the elastic substrate [*Schwarz and Soiné*, 2015]. In general, we do not know neither the amplitude nor the color of the noise in the displacement data, since signal and noise are usually inseparably intermixed. We therefore prefer a regularization approach, as applied by *Schwarz et al.* [2002], over a filtering approach, as used e.g. by *Butler et al.* [2002] or *Huang et al.* [2009].
In particular, we use a 0^{th}-order Tikhonov regularization [*Phillips*, 1962; *Tikhonov*, 1963], which was shown to yield robust results for both TFM in real space as well as in Fourier space [*Sabass et al.*, 2008]. If writing Equation 2.15 as a linear matrix equation

$$\hat{\mathbf{u}} = \hat{\mathbf{G}}\hat{\mathbf{t}}\,, \tag{2.17}$$

we can define the 0^{th}-order Tikhonov problem as the minimization problem

$$\min_{\hat{\mathbf{t}}} \|\hat{\mathbf{G}}\hat{\mathbf{t}} - \hat{\mathbf{u}}\|_2^2 + \lambda^2 \|\hat{\mathbf{t}}\|_2^2\,, \tag{2.18}$$

with regularization parameter λ, which determines the trade-off between overfitting and oversmoothing the data. The first summand of Equation 2.18 is called *regressor*, while the second summand is the *regularizer*. In general, any operator $\mathbf{L}$ can be applied to $\hat{\mathbf{t}}$ in the regularizer, but it turned out that $\mathbf{L} = \mathbb{1}$ yields best results [*Sabass et al.*, 2008].
Tikhonov regularization is particularly practical for computational reasons. We can find an explicit formulation of the Tikhonov-regularized solution by expanding Equation 2.18 and zeroing the gradient of the term with respect to $\hat{\mathbf{t}}$, which yields

$$\hat{\mathbf{t}} = \left(\hat{\mathbf{G}}^T\hat{\mathbf{G}} + \lambda^2\mathbb{1}\right)^{-1}\hat{\mathbf{G}}^T\hat{\mathbf{u}} := \hat{\mathbf{G}}_\lambda^{\#}\hat{\mathbf{u}}\,, \tag{2.19}$$

with the so-called *regularized inverse* $\hat{\mathbf{G}}_\lambda^{\#}$ [*Hansen*, 1992]. The last equation allows to get a clearer understanding of the role of the regularization parameter. A too small λ will lead to the non-regularized estimate $\hat{\mathbf{t}} = \hat{\mathbf{G}}^{-1}\hat{\mathbf{u}}$, which will act as a high-pass filter on $\hat{\mathbf{u}}$ due to the $1/k$-dependence of $\hat{\mathbf{G}}$, as illustrated in Figure 2.2E for an artificial stress field. On the other hand, a too large λ will overrule the high frequency components of $\hat{\mathbf{G}}$, yielding the estimate $\hat{\mathbf{t}} = 1/\lambda^2\hat{\mathbf{G}}^T\hat{\mathbf{u}}$, which will act as a low-pass filter on $\hat{\mathbf{u}}$. Figure 2.2F shows the resulting estimated stress field for a too large λ, as compared to an ideal Tikhonov estimate in Figure 2.2C.
To estimate the regularization parameter λ, we use Generalized Cross-Validation (GCV), which was introduced by *Golub et al.* [1979] and allows to find a λ close to the ideal case (see Figure 2.2D as compared to 2.2C). We will discuss and investigate estimators for Tikhonov regularization further in Section 2.3 and thereafter attend to alternative norms for the regularizer in Section 2.4.

2.1.3 Postprocessing of Traction Stresses

Once the traction stresses $\mathbf{t}$ have been calculated, we can introduce the following quantities to coarsely characterize the contractile strength and features of the traction pattern of a

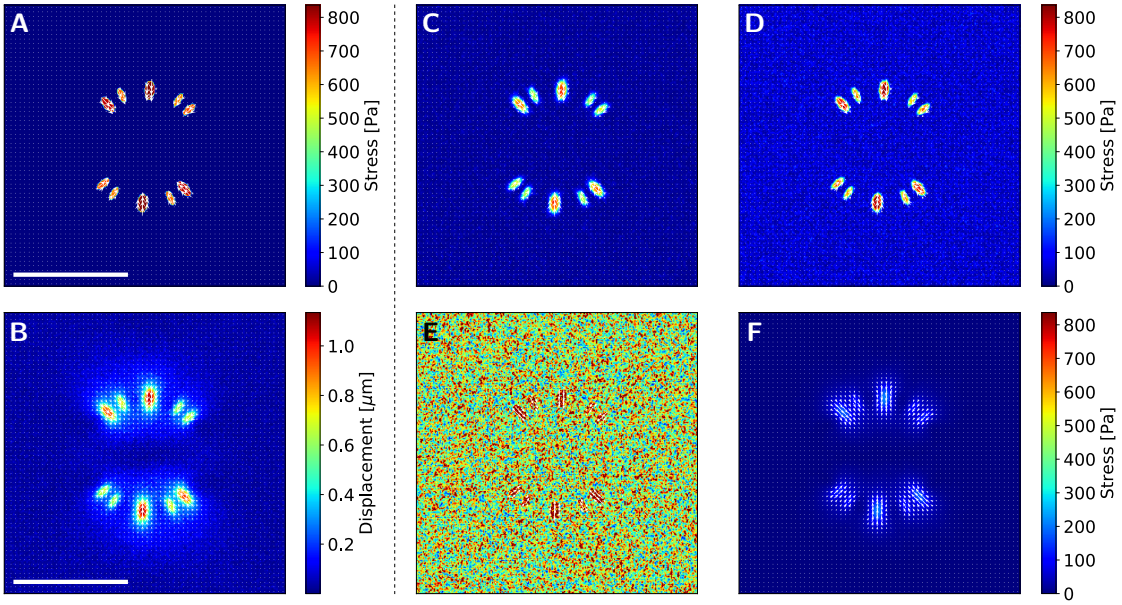

Figure 2.2: 0th-order Tikhonov regularization applied to an exemplar stress field. **(A)** Original stress field. Simulation parameters are: $E_S = 10\,\text{kPa}$, $\nu_S = 0.5\,\text{kPa}$ and 0.1 microns per pixel. **(B)** Calculated displacement field with additional white noise with maximal amplitude equaling $1/30$ of the maximal displacement. **(C)** Reconstructed stress field with minimal Euclidean distance from the original stress field. The regularization parameter equals $\lambda = 4 \times 10^{-4}$. **(D)** Reconstructed stress field using GCV. The regularization parameter equals $\lambda = 2 \times 10^{-4}$. **(E)** Reconstructed stress field without regularization ($\lambda = 0$). **(F)** Reconstructed stress field with a too large regularization parameter. Here, the regularization parameter equals $\lambda = 2 \times 10^{-3}$.

cell.

Strain energy The strain energy is the energy that the cell invests to deform the substrate and is defined by [*Butler et al.*, 2002]

$$U = \frac{1}{2} \int_A \mathbf{t}\,(\mathbf{x})\,\mathbf{u}\,(\mathbf{x})\;\mathrm{d}x\mathrm{d}y\,, \tag{2.20}$$

where A is the cell area.

Total force The total force of the cell is a similar measure as compared to the energy, yielding

$$F = \int_A |\mathbf{t}\,(\mathbf{x})\,|\,\mathrm{d}x\mathrm{d}y\,, \tag{2.21}$$

with the cell area A. Here, the direction of stresses as compared to the displacement does not enter the equation.

Dipole moments We define the dipole matrix $\mathbf{M}$ of the cell by means of [*Butler et al.*, 2002]

$$M_{ij} = \int_A x_i t_j \, \mathrm{d}x\mathrm{d}y \,. \tag{2.22}$$

Since the net force vanishes for isolated adherent cells, the matrix $\mathbf{M}$ is symmetric and thus can be diagonalized. The resulting eigenvalue of $\mathbf{M}$ with largest (lowest) absolute magnitude is then called *major* (*minor*) *dipole moment*. The corresponding eigenvectors are called *major* and *minor dipole axis*.

Quadrupole moments We further define the quadrupole tensor $\mathbf{Q}$ via

$$Q_{ijk} = \int_A x_i x_j t_k \, \mathrm{d}x\mathrm{d}y \,, \tag{2.23}$$

where x_i are coordinates with respect to the major dipole axis [*Tanimoto and Sano*, 2014]. We can interpret $x_i x_j$ as weighting factors for the traction stress t_k. E.g. a stress vector located on the x-axis, except for $x = 0$, and pointing in the positive direction of the minor dipole axis will positively contribute to the the quadrupole moment Q_{112}, while it will not contribute to the moment Q_{222} at all.

2.2 On the Need for Regularization in Fourier-Based TFM

Before delving deeper into the investigation of estimation methods in the context of Tikhonov regularization and the analysis of regularization schemes beyond Tikhonov methods, we will use a theoretical calculation to highlight the ill-posedness of the problem of calculating stresses from displacements in FTTC and, thus, the importance of regularization. We will start with a formal definition of ill-posedness in Section 2.2.1 and then apply the definition to the FTTC problem in Section 2.2.2.

2.2.1 Definition of Ill-Posedness

In general, a problem is called *well-posed* if

1. a solution exists (*existence*).
2. the solution is unique (*uniqueness*).
3. the solution's behavior continuously changes with initial conditions (*stability*).

If any of the three points is not fulfilled, the problem is *ill-posed*. Regarding the well-posedness of the inverse problem of calculating stresses from displacements in FTTC,

we know that due to the long-ranged nature of elasticity theory, any traction spot can contribute to a displacement, even if it is far away. This already indicates why our problem might be ill-posed.
We can also define the terms *well-posedness* and *well-conditionedness* more formally and apply these definitions to FTTC. According to *Hohmann and Deuflhard* [2003], we call a problem (f, x) *well-posed*, if an *absolute norm-wise condition number* κ_{abs} exists, such that

$$|\tilde{x} - x| \leq \kappa_{\text{abs}} \cdot |f(\tilde{x}) - f(x)|, \text{ for } \tilde{x} \to x\,. \tag{2.24}$$

It is called *ill-posed*, if κ_{abs} does not exist, i.e. $\kappa_{\text{abs}} = \infty$.
Analogously, the *relative norm-wise condition number* of a problem (f, x) is the smallest number κ_{rel}, such that

$$\frac{|\tilde{x} - x|}{|x|} \leq \kappa_{\text{rel}} \cdot \frac{|f(\tilde{x}) - f(x)|}{|f(x)|}, \text{ for } \tilde{x} \to x\,. \tag{2.25}$$

A problem (f, x) is said to be *well-conditioned* if its condition number is small and *ill-conditioned* if it is large. Naturally, the meaning of "small" and "large" has to be considered separately for each problem.
In general, there is no clear connection between the two definitions. A well-posed problem can also be ill-conditioned, while an ill-posed has to be ill-conditioned. For the reverse correlation, we know the following relation, e.g. from *Hitz et al.* [2012]: If a problem is ill-conditioned and $\kappa_{\text{rel}} = \infty$, then also $\kappa_{\text{abs}} = \infty$ which means that it is also ill-posed.

2.2.2 Application to the Inverse Problem in FTTC

We can apply the foregoing definitions to any linear system $Ax = b$ and calculate the relative condition number for the particular case. Let x be a solution to $Ax = b$, and $\tilde{x} = x + \Delta x$ a solution to $A\tilde{x} = b + \Delta b$. Then, we have, on the one hand,

$$A\Delta x = \Delta b \iff \Delta x = A^{-1}\Delta b \iff \|\Delta x\| = \|A^{-1}\Delta b\| \leq \|A^{-1}\|\|\Delta b\|\,, \tag{2.26}$$

and, on the other hand,

$$Ax = b \iff \|Ax\| = \|b\| \leq \|A\|\|x\| \iff \frac{\|A\|}{\|b\|} \geq \frac{1}{\|x\|}\,, \tag{2.27}$$

which together yield the inequality

$$\frac{\|\Delta x\|}{\|x\|} \leq \|A\|\|A^{-1}\|\frac{\|\Delta b\|}{\|b\|}\,. \tag{2.28}$$

From the last expression, we can finally extract the relative condition number

$$\kappa_{\text{rel}} = \|A\|\|A^{-1}\| \geq \|AA^{-1}\| = 1\,. \tag{2.29}$$

In FTTC, we have to solve the set of linear equations $\hat{\mathbf{G}}\hat{\mathbf{t}} = \hat{\mathbf{u}}$ for $\hat{\mathbf{t}}$. Here, $\hat{\mathbf{G}}$ is the Fourier-transformed Green's function, $\hat{\mathbf{t}}$ and $\hat{\mathbf{u}}$ are the Fourier transforms of the traction stresses $\mathbf{t}$ and the displacements $\mathbf{u}$, respectively. It has to be noted here, that, because the Fourier transform is norm preserving (Theorem of Plancherel), it does not matter if we deal with the problem in real or in Fourier space.
If the two-dimensional stress or displacement field consists of N discrete points, then $\hat{\mathbf{t}}$ and $\hat{\mathbf{u}}$ are column vectors of length $2N$:

$$\hat{\mathbf{t}} = \begin{pmatrix} \hat{\mathbf{t}}_{x,1} \\ \hat{\mathbf{t}}_{y,1} \\ \vdots \\ \hat{\mathbf{t}}_{x,N} \\ \hat{\mathbf{t}}_{y,N} \end{pmatrix}, \ \hat{\mathbf{u}} = \begin{pmatrix} \hat{\mathbf{u}}_{x,1} \\ \hat{\mathbf{u}}_{y,1} \\ \vdots \\ \hat{\mathbf{u}}_{x,N} \\ \hat{\mathbf{u}}_{y,N} \end{pmatrix}, \tag{2.30}$$

The Fourier transform of the Green's function, i.e. $\hat{\mathbf{G}}$, is the symmetric $2N \times 2N$ matrix with the (2×2)-blocks

$$\hat{\mathbf{G}}_{\text{block}}\left(k_x = \alpha, k_y = \beta\right) = \frac{V}{\left(\alpha^2 + \beta^2\right)^{\frac{3}{2}}} \cdot \begin{pmatrix} \alpha^2 + \beta^2 - \nu\alpha^2 & -\nu\alpha\beta \\ -\nu\alpha\beta & \alpha^2 + \beta^2 - \nu\beta^2 \end{pmatrix} \tag{2.31}$$

on its diagonal and with the constant

$$V = \frac{2\left(1 + \nu\right)}{E}, \tag{2.32}$$

where E is the Young's modulus of the substrate and ν is the Poisson's ratio. The discrete wave vectors k_x and k_y are samples from the arrays

$$\tilde{k}_x = \frac{2\pi}{i_{\max}\mu} \cdot \left[-\tfrac{i_{\max}}{2} \quad \dots \quad \tfrac{i_{\max}}{2} - 1\right], \tag{2.33}$$

$$\tilde{k}_y = \frac{2\pi}{j_{\max}\mu} \cdot \left[-\tfrac{j_{\max}}{2} \quad \dots \quad \tfrac{j_{\max}}{2} - 1\right], \tag{2.34}$$

with the dimensions of the displacement field defined by $(i_{\max} \times j_{\max})$ and the mesh size of the discrete grid denoted by μ in pixels. The arrays themselves contain integer numbers separated by 1.
The eigenvalues of $\hat{\mathbf{G}}$ are then the combination of the eigenvalues of each of these blocks:

$$\text{eig}\left(\hat{\mathbf{G}}_{\text{block}}\right) = V \cdot \left\{ \frac{1}{\sqrt{\alpha^2 + \beta^2}}, \frac{1 - \nu}{\sqrt{\alpha^2 + \beta^2}} \right\}. \tag{2.35}$$

In practice, we avoid the divergence at $(k_x = 0, k_y = 0)$ by filling in $\hat{\mathbf{G}}\left(k_x = 0, k_y = 0\right) = 0$, and, with this, assuming that the net force vanishes which is a plausible assumption for an isolated adhering cell. Therefore, we can ignore the case $(\alpha = 0, \beta = 0)$ (which would result in the two largest eigenvalues being ∞) and go for the smallest and third-largest

eigenvalue of $\hat{\mathbf{G}}$. Assuming a square grid, i.e. $i_{\max} = j_{\max}$, we find by using Equation 2.33 that the largest absolute wave number is

$$k_{\max} = k\left(\alpha = -\frac{\pi}{\mu}, \beta = -\frac{\pi}{\mu}\right) = \sqrt{\left(\frac{\pi}{\mu}\right)^2 + \left(\frac{\pi}{\mu}\right)^2} = \frac{\sqrt{2}\pi}{\mu}\,, \tag{2.36}$$

while the smallest absolute wave number is

$$k_{\min} = k\left(\alpha = \frac{2\pi}{i_{\max}\mu}, \beta = 0\right) = \frac{2\pi}{i_{\max}\mu}\,. \tag{2.37}$$

It follows that the largest (absolute) eigenvalue of $\hat{\mathbf{G}}$ is

$$|\lambda_{\max}| = \frac{1}{k_{\min}} = \frac{\mu i_{\max}}{2\pi}\,, \tag{2.38}$$

and the smallest (absolute) eigenvalue of $\hat{\mathbf{G}}$ is

$$|\lambda_{\min}| = \frac{1-\nu}{k_{\max}} = \frac{(1-\nu)\,\mu}{\sqrt{2}\pi}\,, \tag{2.39}$$

such that the resulting condition number for the normal matrix $\hat{\mathbf{G}}$ is

$$\kappa_{\text{rel}} = \frac{|\lambda_{\max}|}{|\lambda_{\min}|} = \frac{\sqrt{2}}{2\,(1-\nu)} i_{\max} \approx i_{\max}\,. \tag{2.40}$$

This result is intuitive: If $i_{\max}$ is small, i.e. close to 1, the resolution is so low that the displacement data cannot be overfitted and the problem becomes well-posed. Since $i_{\max}$ is always distinctly larger than 1 in our case, ideally ∞, the condition number also goes to ∞, which again speaks for an *ill-posed* problem. The fact, that κ depends on $i_{\max}$ in exactly this way, is a consequence of the long-ranged nature in elasticity theory.
We can verify this statement by using the artificial stress field from Figure 2.2. The original stress field consists of elliptical stress spots of maximal stress 1 kPa. After calculating the corresponding displacement field, we add white noise with magnitude 15 % of the maximal displacement. As Figure 2.3 illustrates, we start from the original size $i_{\max} = 250\,\text{pix}$ and decrease the size by a factor 2 if going from Panel A to D, while leaving the pattern itself untouched. The panels show the non-regularized reconstructed traction stress fields. Qualitatively, we find that the signal-to-noise ratio increases if we reduce the image size, at the expense of resolution.
Figure 2.3E quantifies this effect via the resulting image distance between the original and reconstructed stress field as a function of the regularization parameter. We find that the statement $\kappa \approx i_{\max}$ is represented in two aspects. First, with decreasing image size, the ideal regularization parameter decreases in the direction of the non-regularized case $\lambda = 0$. Second, the absolute difference between the minimal Euclidean distance and the Euclidean distance in the non-regularized case decreases, indicating that with a very small image size the regularization becomes redundant.

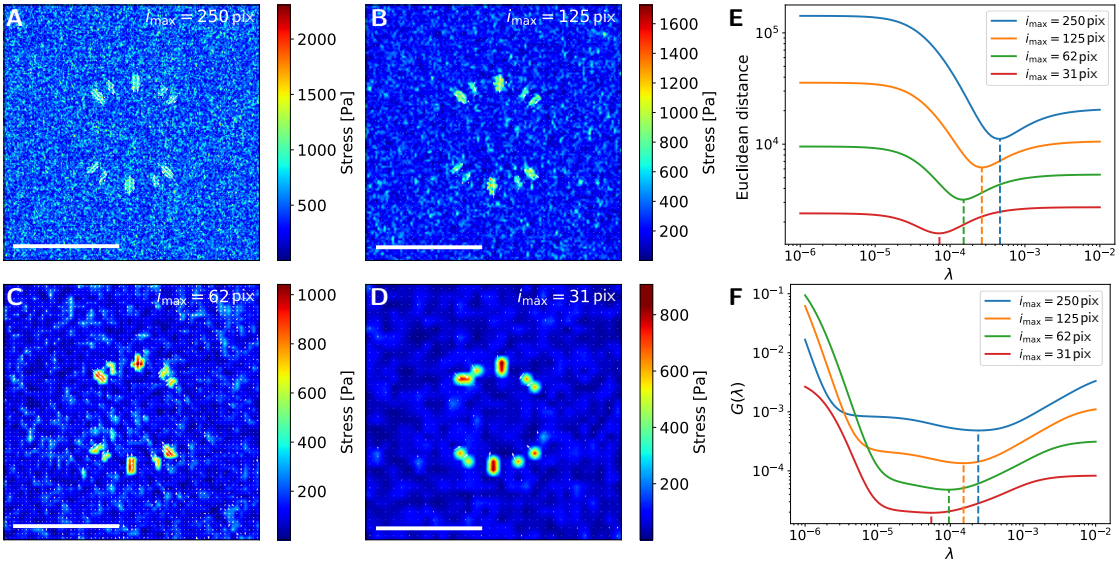

Figure 2.3: With decreasing image size $i_{\max}$, the non-regularized reconstructed stress field approaches the original one in terms of stress magnitudes at the expense of resolution. Panels **A-D** show the non-regularized reconstructed stress field for $i_{\max} = 250\,\text{pix}$ **(A)**, for $i_{\max} = 125\,\text{pix}$ **(B)**, for $i_{\max} = 62\,\text{pix}$ **(C)** and for $i_{\max} = 31\,\text{pix}$ **(D)**. **(E)** Euclidean distance between the regularized reconstructed stress field and the original stress field as a function of λ and $i_{\max}$. Dashed lines indicate the minima of the curves. **(F)** GCV function $G(\lambda)$ as a function of $i_{\max}$. Dashed lines indicate the minima of the curves.

2.3 Investigation of Tikhonov-Based Methods for Fourier-Based TFM

As presented by *Bauer and Lukas* [2011], the choice methods for the regularization parameter can be classified into three different categories:

- *A priori methods*, which require information about the noise involved in the problem and the smoothness of the target vector $\hat{\mathbf{t}}$.
- *A posteriori methods*, which require information about the noise involved in the problem.
- *Data-driven methods* do not require any prior knowledge.

Since the information about the smoothness of the target vector is not known in our case, we will skip a priori methods. Also, the magnitude and structure of the noise is not measurable, since signal and noise are usually inseparably intermixed, due to the long-ranged nature of elasticity theory. We will therefore prefer data-driven methods in the following, but, nevertheless, also analyze the performance of an a-posteriori method. We will start with the description of Tikhonov-based parameter choice methods in Section 2.3.1 and, thereafter in Section 2.3.2, benchmark the methods against each other

based on synthetic stress fields. In particular, we will focus on the applicability of the investigated methods in an automated regularization algorithm.

2.3.1 Standard Tikhonov-Based Parameter Choice Methods

In the following, we will briefly introduce the data-driven choice methods *L-curve* and *Generalized Cross-Validation* as well as an a-posteriori method based on the *Normalized Cumulative Periodogram* for estimating the regularization parameter λ. In all three cases, we use the algorithms implemented by *Hansen* [1994] to compute the estimate.

L-curve method The L-curve method was developed by *Hansen* [1992, 1999] and allows to estimate the regularization parameter by means of a graphical procedure. *Hansen* [1992] used the fact that, when plotting the two norms from Equation 2.18 against each other in a log-log-plot for different values of λ, one ideally obtains an L-shaped curve, whose corner denotes a good trade-off between over- and undersampling.
More precisely, we define $\eta(\lambda) = \|\hat{\mathbf{t}}_\lambda\|_2$ and $\rho(\lambda) = \|\hat{\mathbf{G}}\hat{\mathbf{t}}_\lambda - \hat{\mathbf{u}}\|_2$, and their logarithms $\tilde{\eta} = \log\eta$ and $\tilde{\rho} = \log\rho$. Then, the L-curve is the plot of $\tilde{\eta}(\lambda)$ versus $\tilde{\rho}(\lambda)$. We can then compute the corner by calculating the curvature $\kappa(\lambda)$, yielding

$$\kappa = 2\frac{\tilde{\rho}'\tilde{\eta}'' - \tilde{\rho}''\tilde{\eta}'}{\left[(\tilde{\rho}')^2 + (\tilde{\eta}')^2\right]^{\frac{3}{2}}}, \tag{2.41}$$

with apostrophes denoting derivatives with respect to λ. *Hansen* [1992] introduces a SVD-based scheme to compute the curvature κ without using numerical differentiation.

Generalized Cross-Validation (GCV) The natural way to quantify the goodness of the estimate $\hat{\mathbf{t}}_\lambda$ is to test its prediction capability. This is the basic strategy of ordinary leave-one-out cross-validation or Allen's PRESS [*Allen*, 1974; *Stone*, 1974; *Geisser*, 1975]. Here, one first computes the $\hat{\mathbf{t}}_\lambda^{(i)}$ with the i^{th} row of $\hat{\mathbf{u}}$ omitted, and then uses $\hat{\mathbf{t}}_\lambda^{(i)}$ to predict the row $\hat{\mathbf{u}}^i$, yielding the minimization of the function

$$\sum_i^N \frac{1}{N}\left(\left(\hat{\mathbf{G}}\hat{\mathbf{t}}_\lambda^{(i)}\right)^i - \hat{\mathbf{u}}^i\right)^2. \tag{2.42}$$

This procedure, however, entails at least two disadvantages in our case. First, the typical image size is in the order of (1000×1000) pix, such that $\hat{\mathbf{G}}$ becomes a matrix of 2×10^6 pix, yielding a long computational effort. Second, the matrix $\hat{\mathbf{G}}$ is sparse, containing non-zero values only along its diagonal and both first minor diagonals, making the rows uncorrelated.
To counteract this case, *Golub et al.* [1979] derived a parameter choice method which is fast, independent of any permutation and close to ideal for diagonal matrices, referred to as Generalized Cross-Validation (GCV). In GCV, the best estimation for λ minimizes

the function

$$G(\lambda) = \frac{\|\hat{\mathbf{G}}\hat{\mathbf{t}}_\lambda - \hat{\mathbf{u}}\|_2^2}{\mathrm{tr}\left(\mathbb{1} - \hat{\mathbf{G}}\hat{\mathbf{G}}_\lambda^{\#}\right)^2}\,. \tag{2.43}$$

The function always has a minimum for a finite non-zero value of λ. A decrease of λ leads to a decrease of both nominator and denominator and vice versa. The function $G(\lambda)$ is easy to compute in our case because the Singular value decomposition (SVD) of $\hat{\mathbf{G}}$ is known [*Hansen*, 1994]. Figure 2.3F shows exemplary courses of $G(\lambda)$ for the investigated artificial stress fields. One finds that the regularization parameters estimated by means of GCV lie close to the ideal values.

Normalized Cumulative Periodogram (NCP) method In general, a large regularization parameter λ smooths out both the noise and the high-frequency components of the signal we want to extract. On the other hand, a low λ leads to a regularization result which is dominated by noise via the residual vector $\mathbf{e}_\lambda = \hat{\mathbf{G}}\hat{\mathbf{t}}_\lambda - \hat{\mathbf{u}}$. *Hansen et al.* [2006] introduced a method which selects λ in such a way that the residual vector switches its behavior from "signal" to "noise" by evaluating the Normalized Cumulative Periodogram of $\mathbf{e}_\lambda$. Briefly worded, we first compute the power spectrum of $\mathbf{e}_\lambda$ via $(p_\lambda)_k = |\mathcal{F}(\mathbf{e}_\lambda)|_k^2$ with index k and the Fourier transformation indicated by $\mathcal{F}(\cdot)$. The NCP of $\mathbf{e}_\lambda$ is then given by the vector $c(\mathbf{e}_\lambda) \in \mathbb{R}^{q-1}$ with

$$c(\mathbf{e}_\lambda) = \frac{\|(p_\lambda)_{2:k+1}\|_1}{\|(p_\lambda)_{2:q}\|_1}\,, \tag{2.44}$$

with $q = \lfloor N/2 \rfloor + 1$, $k = 1, ..., q-1$ and N being the dimension of $\hat{\mathbf{u}}$. For white noise, the expected power spectrum is independent of the frequency, and thus the expected NCP is a straight line from $(0,0)$ to $(q,1)$. We therefore choose those λ for which the distance between the NCP and this straight line is a minimum. It has to be noted that, as compared to the previous two methods, this procedure assumes that only white noise is present in $\hat{\mathbf{u}}$.

2.3.2 Tikhonov-Based Methods Applied to FTTC

We continue, in the following, with the presentation of the algorithm to generate synthetic images first. Thereafter, we will introduce the quality measure we use to compare the presented parameter choice methods. In the last paragraph, we will finally evaluate the presented algorithms with respect to the synthetic traction stress images.

Generation of traction patterns As an idealization of a typical stress pattern generated by a single cell with zero net force, traction stress fields of image size $i_{\max}$ are generated with elliptically shaped spots of constant stress lying on a symmetric ring of radius R, as depicted in Figure 2.2A. We introduce 2×5 traction spots in total, whose exact position is constrained to the angular range $[40°, 140°]$ and subject to angular noise. The mean ellipse axes depend on the image size to be able to analyze the effect of spatial extent

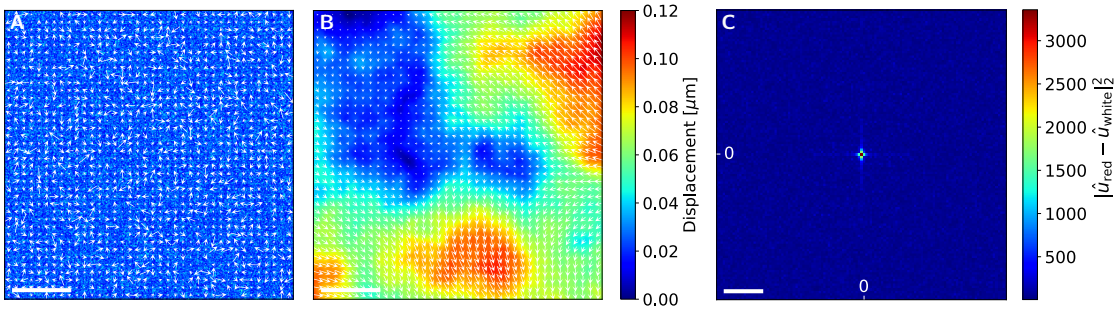

Figure 2.4: Exemplar noise patterns of different "color". **(A)** White noise. **(B)** Red or *Brownian* noise. **(C)** Euclidean distance between white and red noise for the same displacement field, shown in Fourier space. Scale bars are 20 μm in **A** and **B**, 1 μm^{-1} in **C**.

and variation of noise on the regularization ability. We use two different spot sizes, either with mean ellipse axes $(a_{\text{small}}, b_{\text{small}})$ or $(a_{\text{large}}, b_{\text{large}})$. The stress magnitude in a spot depends on the spot size, as one would expect for FAs. Table A.1 lists the numerical values as well as parameter dependencies we used in the simulations.
Unlike previous analyses e.g. by *Sabass et al.* [2008]; *Han et al.* [2015]; *Brask et al.* [2015], we do not only consider white noise as a model for image acquisition problems, which we add to the reconstructed displacement field, but also correlated *red* (or *Brownian*) noise modeling smooth inhomogeneities in the substrate stiffness. In the case of red noise, the power spectrum depends on the frequency as $p \sim 1/\omega^2$ [*Barnes and Allan*, 1966]. We use the algorithm introduced by *Lennon* [2000] to generate red noise. For both types of noise, we choose a standard deviation equaling $5 - 15\,\%$ of the maximal absolute displacement $u_{\max}$, which are typical noise magnitudes in real measured displacement fields.
Figure 2.4 shows a void displacement field with exemplar patterns of white noise, in Panel A, and red noise, in Panel B, highlighting the spatial correlation of red noise as compared to white noise. Figure 2.4C shows the image distance of both noise fields in Fourier space. The large peak at $(k_x = 0, k_y = 0)$ indicates that for red noise the low frequency components dominate.

Evaluation methods We will compute the optimal regularization parameter λ_{ED} by finding the minimum of the Euclidean distance (ED) between the original and reconstructed traction image, since this distance measure fairly considers both traction stresses within the spot regions and misclassified traction stresses outside this regions. Alternatively, we can compute λ_{EDS} from the minimum of the Euclidean distance when only considering the traction spots, but this choice does not penalize the traction stress surrounding the actual stress signal due to the influence of noise. We further omit conclusions based on the measurement of the deviation of the traction magnitude (DMS), as was presented by *Sabass et al.* [2008]. This is for the intuitive reason that DMS only compares the norms of the full traction spots of the original and reconstructed traction field. However, it does not penalize the variation of the stress signal. E.g. an unregularized traction spot

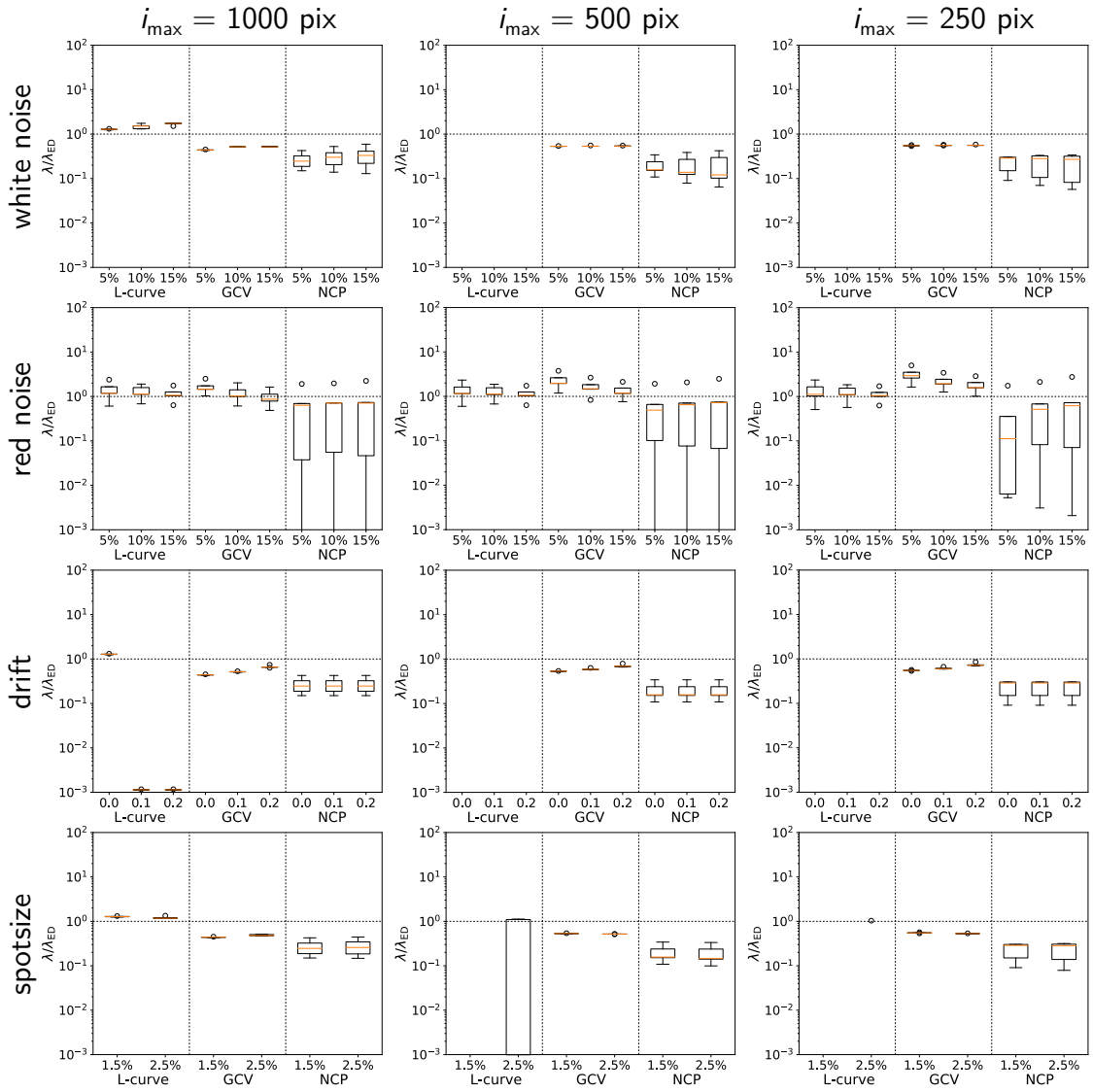

Figure 2.5: Comparison of Tikhonov-based regularization protocols as a function of displacement field size $i_{\max}$, noise color and magnitude, average displacement drift and average spot size. The field size is given in pixels, the noise magnitude in percent of maximal displacement, drift is given in pixels and spot size denotes the average size of the long axis of the elliptical force spot as percentile of the field size. The quality measure denotes the ratio of the regularization parameter λ using the respective algorithm and the ideal regularization parameter λ_{ED} based on the Euclidean distance between total original and reconstructed stress field. *Yellow lines* denote the median values, *boxes* are the midspread, while *whiskers* contain 99.3 % of the data. *Circles* denote outliers. Missing boxes have a median $\lambda/\lambda_{\mathrm{ED}} < 10^{-3}$.

comprising a binary stress field of varying stresses of 1000 Pa and 0 Pa will yield the same DMS value as compared to a constant stress spot of 500 Pa.

Simulation results We generate 5 random synthetic stress fields per data point as previously described and calculate the corresponding displacement fields. We then compare the performance of the described parameter choice methods for three different image sizes and based on four criteria: level of white noise, level of red noise, drift level or average traction spot size. The performance of the Tikhonov-based methods is measured via the deviation of the calculated regularization parameter λ from the ideal parameter λ_{ED}.
Figure 2.5 shows the resulting performance of the three introduced parameter choice methods. We find that GCV entails the overall best and most robust performance with respect to all modifications. With increasing noise or drift level, the GCV result even approaches the ideal regularization result.
The a-posteriori method using NCP also reveals a good regularization ability, but is always worse than GCV and deviates by about an order of magnitude in terms of λ from the ideal result. As expected, the method does not yield satisfactory results when confronted with correlated noise. In this case, the regularization performance shows a huge variation in terms of λ.
The L-curve method exhibits a inadequate regularization performance. For the largest image size and a vanishing drift, it yields best results. However, for a decreasing image size, the method abruptly ceases functioning except for the situation with a pure red noise background. We further find that for a large traction spot size, the L-curve method still works in some situations, indicating that the regularization capability of the L-curve depends on the spatial range of the traction spot compared to those the noise variations. Apparently, for decreasing $i_{\max}$, the problem becomes more and more well-posed, which is expressed in the lacking estimation ability of the L-curve. However, we find in Figure 2.3 that even for $i_{\max} \approx 100$ a regularization is required to attenuate the impact of noise. This is not feasible by means of the L-curve, as Figure 2.5 clarifies.
To figure out the reason for the unreliable estimation by means of the L-curve method, we delve into analyzing the curvature κ of the L-curve for the different cases presented above. Figure 2.6A shows a representative curvature for the case of white noise and a decreasing image size. Surprisingly, we find that for small λ, the curvature always increases to a much larger value than for the maximum of interest at about $\lambda = 4 \times 10^{-3}$. The resulting courses of the curvature suggest, that even for $i_{\max} = 1000$, we will have $\kappa \to \infty$ if $\lambda \to 0$, if increasing the parameter range of the curve. Further, we find that the maximum of interest, which is located between $\lambda = 10^{-3}$ and $\lambda = 10^{-2}$, decreases with decreasing image size and finally vanishes.
In the case of pure red noise, as shown in Figure 2.6B, the curvature seems to be unaffected by the image size, as one would expect from an ideal parameter choice method. A drift in the displacement field has a similar effect on the regularization capability of the L-curve method as a decreasing image size with white background noise (see Figure 2.6C). Here, the peak of interest at about $\lambda = 4 \times 10^{-3}$ shrinks and the curvature comprises an

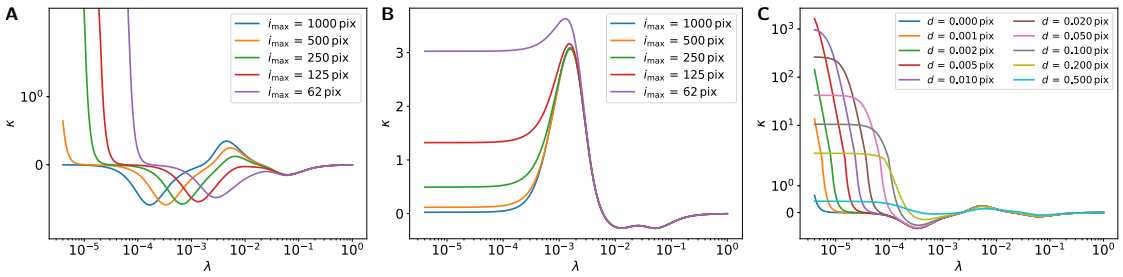

Figure 2.6: The L-curve is unsuited to robustly determine the regularization parameter λ in general. The figure shows the curvature κ of the L-curve as a function of the regularization parameter and the size of the synthetic displacement field $i_{\max}$, which subject to white noise **(A)**, red noise **(B)** or drift d **(C)**.

undesired peak for lower values of λ. This second peak decreases for increasing drift, which leads to the paradox situation that for a very large drift of about 1 pix and larger, the measured maximum of the curvature is close to the ideal regularization parameter.
Figure A.1 finally shows, for reasons of comparison, the regularization performance of the parameter choice methods with respect to the ideal regularization parameter λ_{EDS}, which only considers the reconstruction of the stress spots themselves. In general, we find similar results as in Figure 2.5, but the estimated parameters are moved by about a half order of magnitude to larger λ, indicating that regularization tends to underestimate stresses in the spot regions at the expense of preventing a overestimation of stresses apart from the traction spots.
Overall, these results reveal that the L-curve is unsuitable to serve as a Tikhonov-based method in an automatized regularization algorithm. The GCV method shows the most reliable results and will be used in the remainder of this thesis to reconstruct traction forces.

2.4 Investigation of Regularizers for Fourier-Based TFM

Tikhonov regularization is only one particular choice in the context of mathematical techniques to solve inverse problems. The advantage with respect to other regularization methods is the fact that we can calculate an explicit formula for $\hat{\mathbf{t}}_\lambda$, which allows a fast computation of the regularized solution. *Golub et al.* [1999] provides an alternative formulation of Tikhonov regularization by rewriting the minimization problem as

$$\min_{\hat{\mathbf{t}}} \|\hat{\mathbf{G}}\hat{\mathbf{t}} - \hat{\mathbf{u}}\|_2^2 \,, \tag{2.45}$$

subject to

$$\|\hat{\mathbf{t}}\|_2^2 = \sqrt{\hat{t}_1^2 + \ldots + \hat{t}_N^2} \leq \delta \,, \tag{2.46}$$

where δ is some monotonic function of λ.
We can interpret this formulation by means of the two-dimensional minimization problem

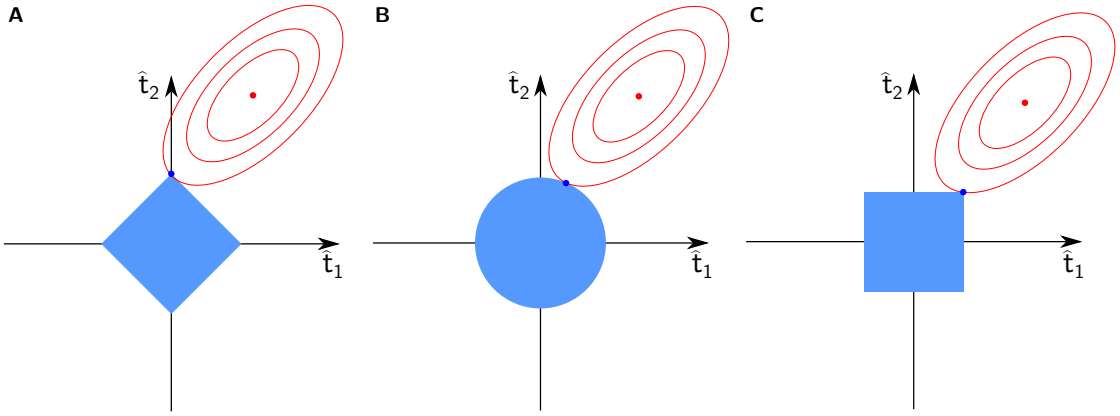

Figure 2.7: Schematic view of the minimization of the objective function during regularization for regularizers of different norm in a two-dimensional feature space. *Red lines* show isolines of the regressor with its minimum indicated by the *red dot*. The *light blue* area indicates the L_p-norm ball which constrains the position of the overall minimum of the sum of regressor and regularizer to its interior. **(A)** For L_1-Regularization, the overall minimum of the objective function will lie at the corner of the square and, with this, force a sparse solution. **(B)** For L_2-Regularization, the overall minimum of the objective function will lie at the circle line, giving each feature vector the same weight. **(C)** For L_∞-Regularization, the overall minimum of the objective function will lie at the corner of the square and, with this, force a spread solution. Image adapted from *Tibshirani* [1996].

sketched in Figure 2.7B. Here, the solution of the least-squares problem 2.45 is illustrated as the red dot which is surrounded by ellipses representing isolines with respect to the residual vector. Imposing the constraint 2.46 means that the solution of the least-squares problem is orthogonally projected onto the unit hyperball of radius δ.
A ball has the feature that it does not give preference to particular solutions as long as the norm constraint is fulfilled. However, we can also impose other norms for the regularizer, which allow to determine a favored solution. In Section 2.4.1, we will introduce different norms used in the minimization problem and discuss their effect on the solution. Thereafter, in Section 2.4.2, we will apply the regularization algorithms to the problem of Fourier-based force reconstruction.

2.4.1 Definition and Implementation of Regularizers

In the following, we will introduce sparse and anti-sparse regularizers and briefly introduce the algorithms to impose these. We will first start with L^1-regularization, which has already been introduced in the context of real-space TFM by *Han et al.* [2015] or *Brask et al.* [2015] and is also commonly known as *sparse* regularization, *compressed sensing* or *Lasso regression*. Thereafter, we will introduce *Elastic net* regularization, which is a combination of L^1- and Tikhonov-regularization. Finally, we will turn to anti-sparse or L^∞-regularization.

Sparse or L^1-Regularization In sparse regularization, we solve the following minimization problem [*Tibshirani*, 1996]:

$$\min_{\hat{\mathbf{t}}} \|\hat{\mathbf{G}}\hat{\mathbf{t}} - \hat{\mathbf{u}}\|_2^2 \,, \tag{2.47}$$

subject to

$$\|\hat{\mathbf{t}}\|_1 = \left|\hat{t}_1 + ... + \hat{t}_N\right| \leq \delta \,. \tag{2.48}$$

Figure 2.7A illustrates the implication of using the L^1-norm instead of the L^2-norm in the regularizer for a two-dimensional problem. The hyperball, in this case, is the number of points for which the constraint $\left|\hat{t}_1 + \hat{t}_2\right| \leq \delta$ is satisfied, i.e. the constraint region is a square whose corners are lying on the axes. During minimization, the corners of the constraint region are preferred, because these are in general the first points which are hit by the isolines of the norm of the residual vector when projecting the solution of the least-squares problem. Since the corners are exactly those point, at which only one component of the solution vector $\hat{\mathbf{t}}_\lambda$ is non-zero, L^1-regularization usually leads to a sparse solution.
One disadvantage of this method as compared with Tikhonov-regularization is the computational effort to compute the solution vector. In this case, we cannot compute an explicit formulation for the solution vector and have to use a numerical scheme, because the objective function is not differentiable at any $\hat{t}_i = 0$. In particular, we use an IRLS-algorithm, which was developed by *Scales et al.* [1988] and already applied to the problem of sparsity-inducing force reconstruction in real-space by *Han et al.* [2015]. Briefly worded, we solve the equation

$$\left(2\hat{\mathbf{G}}^T\hat{\mathbf{G}} + \lambda\mathbf{W}^n\right)\hat{\mathbf{t}}^n = 2\hat{\mathbf{G}}^T\hat{\mathbf{u}} \,, \tag{2.49}$$

with the diagonal matrix $W_{ii}^n = {}^1/_{|\hat{t}_i^n|}$ and the initial matrix $W_{ii}^0 = \mathbb{1}$. The equation is recalculated until $\hat{\mathbf{t}}^n$ fulfills the following criterion:

$$\frac{\left\|\hat{\mathbf{t}}^n - \hat{\mathbf{t}}^{n-1}\right\|_2}{1 + \left\|\hat{\mathbf{t}}^{n-1}\right\|_2} < \epsilon \,, \tag{2.50}$$

with $\epsilon > 0$. To circumvent a non-differentiable situation, we introduce another threshold value ξ, such that $W_{ii} = {}^1/_\xi$ for $|\hat{t}_i| \leq \xi$. Table A.1 lists the threshold values and the maximum number of iterations used in the following subsection.

Elastic Net Regularization Elastic net regularization was introduced by *Zou and Hastie* [2005] and yields a combination of sparse and Tikhonov regularization. Here, one solves the following minimization problem:

$$\min_{\hat{\mathbf{t}}} \|\hat{\mathbf{G}}\hat{\mathbf{t}} - \hat{\mathbf{u}}\|_2^2 + \lambda\left(\alpha\|\hat{\mathbf{t}}\|_1 + (1-\alpha)\|\hat{\mathbf{t}}\|_2^2\right) \,, \tag{2.51}$$

with a second parameter $0 \leq \alpha \leq 1$ which determines the weighting of the L^1- versus the L^2-norm and, with this, predefines the sparsity of the solution. For $\alpha = 0$, we obtain

the Tikhonov problem, while $\alpha = 1$ yields sparse regularization. Equation 2.51 thus formulates a whole family of minimization problems.
In the following, we will restrict ourselves to the problems $\alpha = 0.9$, $\alpha = 0.99$ and $\alpha = 0.999$. We will use the IRLS-based algorithm described in the previous paragraph to determine the solution vector $\hat{\mathbf{t}}_\lambda$.

Anti-sparse or L^∞-Regularization Anti-sparse, or *spread*, regularization tries to distribute the information uniformly in the solution vector $\hat{\mathbf{t}}_\lambda$, by solving the minimization problem [*Fuchs*, 2011]:

$$\min_{\hat{\mathbf{t}}} \|\hat{\mathbf{G}}\hat{\mathbf{t}} - \hat{\mathbf{u}}\|_2^2 \,, \tag{2.52}$$

subject to

$$\|\hat{\mathbf{t}}\|_\infty = \max_{i\in\{1,\dots,N\}} |\hat{t}_i| \leq \delta \,. \tag{2.53}$$

As Figure 2.7C demonstrates, for the particular example of a two-dimensional minimization problem, imposing the L^∞-norm leads to a square-shaped constraint region, whose edges are parallel to the axes. Thus, the problem prefers solutions with maximal distance from the center. In particular, the problem of Fourier-based force reconstruction might benefit from a spread representation in Fourier space because a spread signal in Fourier space yields a sparse signal in real space and vice versa.
Jégou et al. [2011] provide an efficient algorithm to solve the anti-sparse problem, which we will use in the following. Since $\|\hat{\mathbf{t}}\|_\infty$ is not differentiable at all, standard IRLS-methods as before cannot be used and one has to work with sub-gradients and sub-differential sets. They define the gradient $\partial\|\hat{\mathbf{t}}\|_\infty$ via:

$$\partial\|\hat{\mathbf{t}}\|_\infty = \left\{\mathbf{v} \in \mathbb{R}^N : \|\mathbf{v}\| \leq 1\right\} \,, \tag{2.54}$$

for $\hat{\mathbf{t}} = \mathbf{0}$ and

$$\partial\|\hat{\mathbf{t}}\|_\infty = \left\{\mathbf{v} \in \mathbb{R}^N : \|\mathbf{v}\| = 1,\, v_i\hat{t}_i \geq 0 \text{ if } |\hat{t}_i| = \|\hat{\mathbf{t}}\|_\infty,\, v_i = 0 \text{ else}\right\} \,, \tag{2.55}$$

for $\hat{\mathbf{t}} \neq \mathbf{0}$. Then, the vector $\hat{\mathbf{t}}_\lambda$ is a solution of the problem iff there exists some $\mathbf{v} \in \partial\|\hat{\mathbf{t}}\|_\infty$ such that

$$\hat{\mathbf{G}}^T\left(\hat{\mathbf{G}}\hat{\mathbf{t}}_\lambda - \hat{\mathbf{u}}\right) + \lambda\mathbf{v} = 0 \tag{2.56}$$

is fulfilled.

2.4.2 Sparse and Anti-Sparse Regularizers Applied to FTTC

In the following, we apply the sparsity and anti-sparsity-inducing regularization algorithms introduced in the previous section to the problem of reconstructing the synthetic traction stress fields introduced in Section 2.3.2. In particular, we use two different image sizes $i_{\max} = 500\,\text{pix}$ and $i_{\max} = 125\,\text{pix}$ and compare the performance of the described algorithms based on three criteria: level of white noise, level of red noise or average traction spot size. We use the minimally achievable Euclidean distance $|\hat{\mathbf{t}}_{\text{orig}} - \hat{\mathbf{t}}_{\text{rec}}|$ between the

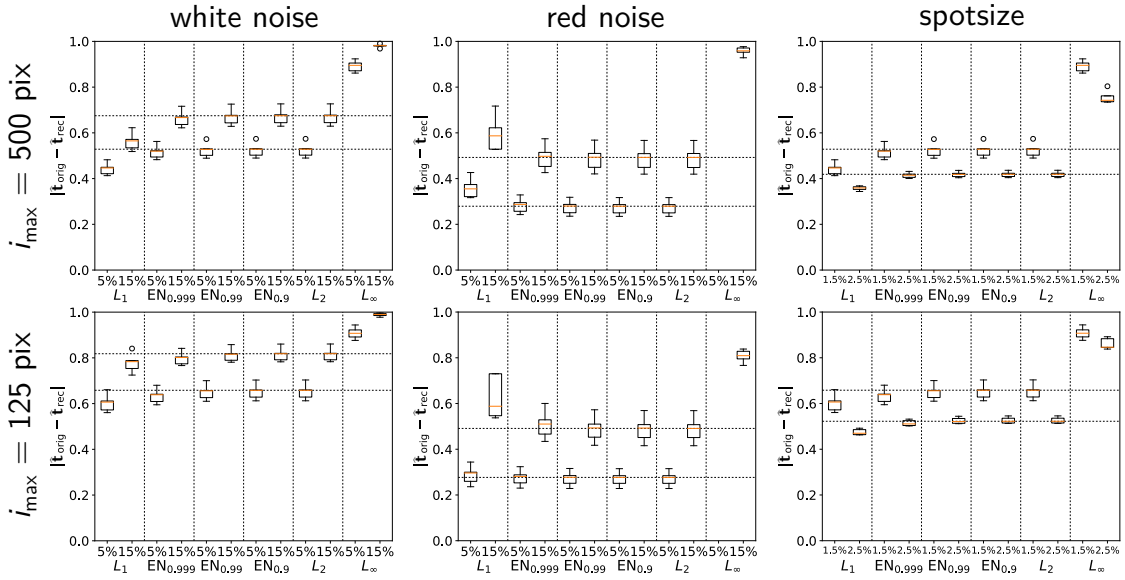

Figure 2.8: Performance comparison of different regularizers as a function of displacement field size $i_{\max}$, noise color and magnitude, and average spot size in terms if the Euclidean distance between the total original and reconstructed stress fields. The field size is given in pixels, the noise magnitude in percent of maximal displacement and spot size denotes the average size of the long axis of the elliptical force spot as percentile of the field size. *Boxes* have same meaning as in Figure 2.5.

original and reconstructed stress field to reveal the capabilities of the presented methods independent of any parameter choice methods.

Simulation results Figure 2.8 show the regularization capability when imposing different norms on the regularizer. Surprisingly, we find that in the ideal case of a displacement field which is only subject to white noise, the sparse regularization yields best performance, with a maximally achievable increase in regularization efficacy of up to 30 % as compared to Tikhonov or L^2-regularization. The situation is, however, different for the case of red noise, for which we obtain the best results if using L^2-regularization. We further find a smooth transition of the regularization performance when going from L^1 to L^2 by means of Elastic net (EN_α) regularization.
The anti-sparse norm always performs worse than both L^1 to L^2. In this case, the distance $|\hat{\mathbf{t}}_{\mathrm{orig}} - \hat{\mathbf{t}}_{\mathrm{rec}}|$ is always close to 1, which means that a reconstructed stress field full of zeros would yield the same result. We also find that, as expected, the reconstruction efficacy decreases with increasing noise magnitude for both types of noise. On the other hand, the performance improves if the traction spot size increases, i.e. if the spatial scale of the signal increases with respect to the scale of the noise variations.
Overall, we note that with L^1-regularization we are theoretically able to improve the the regularization result, while L^∞-regularization always performs worse. We can explain this

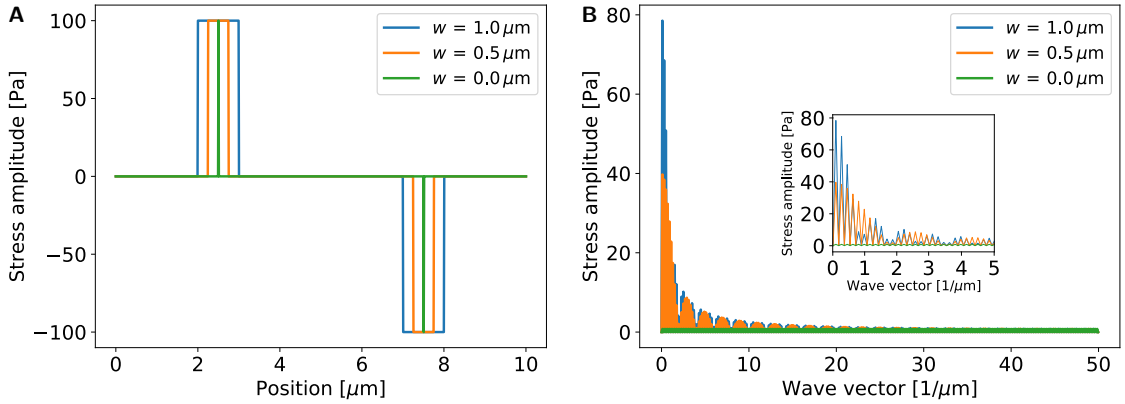

Figure 2.9: Illustration showing one-dimensional stress fields **(A)** and their Fourier transforms **(B)**. Sparse stress spots in real space are spread distributions in Fourier space and vice versa. With increasing width of the stress spot in real space, the sparseness of the stress signal in Fourier space increases.

finding by means of a one-dimensional example in which the traction spots are represented as Heaviside functions of different widths.
Figure 2.9A shows one-dimensional spots of different size in real space and Figure 2.9B their representation in Fourier space. We find that, with increasing spot size, the sparsity of the signal in Fourier space increases. Only for the δ-peak in real space, we get a spread function in Fourier space. Since we deal with large traction spots as compared to the pixel size in our two-dimensional traction stress fields, we are rather imposing a sparse than a spread representation in Fourier space, which explains the regularization capability of L^1-regularization as compared to L^∞-regularization.
Figure A.2 qualitatively shows the performance of different regularization norms when applied to the reconstruction problem of an exemplar synthetic stress field. In the case of white noise, the L^1-norm-based estimation is best since it yields the best estimate of the stress within the spot regions. However, the background displays an undesirable effect of sparse regularization in Fourier space: A high-frequent component $\hat{\mathbf{t}}_\lambda$ generates a noticeable background pattern in the periphery of the force spots, if comparing the reconstruction results with those achieved by means of Tikhonov regularization. The latter underestimates the traction spots themselves, but provides a smooth background. L^∞-regularization does not fully manage to find a signal with a spread representation in Fourier space. We can, however, guess from the reconstructed traction pattern where the actual traction spots are situated.
In the case of red noise, L^1-regularization performs worse than L^2-regularization due to ringing artifacts, while the L^2-regularized estimate remains comparatively unperturbed. L^∞-regularization does not work at all in the case of red noise, since the displacement field does not contain any component with a flat power spectrum in Fourier space.

2.5 Conclusion

In this chapter, we introduced the TFM algorithm which will be used throughout this manuscript to calculate traction stress from bead images. The resulting software pipeline was further incorporated into an easy-to-use graphical interface based software tool which can be applied to a wide range of traction stress reconstruction problems.
In particular, we investigated the importance and the effect of regularization in the problem of Fourier-based TFM. By means of a theoretical calculation, we showed and simulatively verified that regularization becomes the more important for images the larger the image information is, which is due to the long-ranged nature of elasticity theory.
We then designed synthetic stress fields, aiming at mimicking experimental traction stress fields, to analyze the capabilities of existing Tikhonov-based regularization methods. In particular, we investigated the regularization performance on both uncorrelated and correlated background noise, since both types of noise are existent in experimentally acquired displacement fields. Here, we found that GCV is the most robust estimator in the context of FTTC, while, compared to this, the usually applied L-curve method only performs robustly if correlated noise or a large drift is present in the displacement field.
We finally investigated the maximum achievable regularization performance with respect to the regularization norm. Here, we found that, when regarding the ideal white noise case, a sparse regularizer can considerably improve the regularization results, even although the signal is sparse in real space and the regularization is accomplished in Fourier space. If, however, imposing correlated noise in the displacement field, Tikhonov regularization is the best choice. An anti-sparse regularizer was found to perform worse than both sparse and Tikhonov regularizer for all investigated patterns. This can be explained by the finite extension of the signal in real space and, with this, a representation in Fourier space which is far from anti-sparse.
The application of a sparse regularizer would require both a drastic increase in computation time and a robust data-driven regularization method, which is however not investigated for the special case of FTTC so far. We will therefore stick with the Tikhonov-based GCV estimator to compute the traction stresses in the following chapters.

Part II

From Forces to Macroscopic Models - Continuum Modeling of Cellular Contractility

3 Viscoelastic Specification of Stress Fiber Dynamics

Biological cells are known to exhibit viscoelastic material properties, which are mainly determined by the composition of the actin cytoskeleton (CSK). On the one hand, cells respond elastically to fast mechanical stimuli in order to withstand irreversible changes of their mechanical state, which manifests an inherent memory in the cytoskeletal architecture. In this sense, cells can be seen as elastic solids. On the other hand, cells must allow for cytoskeletal flow and remodeling on the long run, making them appear like viscous fluids.
The exact contribution of elastic, i.e. spring-like, viscous, i.e. dashpot-like, as well as actively contractile components in general is rich in variety and strongly depends on both the applied experimental tools and protocols supporting the material models, on the one hand, and the local architecture of the actin CSK which is probed in the experiment, on the other hand. For example, the studies of *Colombelli et al.* [2009] and *Besser et al.* [2011] reveal by means of laser ablation experiments that the short-term dynamics of stress fibers (SFs) can be described by a Kelvin-Voigt model, i.e. a parallel arrangement of springs and dashpots as depicted in 1.9C. At the same time, laser ablation experiments performed by *Saha et al.* [2016] as well as microrheological cantilever measurements by *Étienne et al.* [2015] reflect the fluid-like dynamics of the CSK. In this case, a Maxwell model, i.e. a serial arrangement of springs and dashpots, as illustrated in 1.9D, is appropriate to explain the cortical dynamics.
Another recently developed promising approach to analyze the material properties of the CSK is optogenetics [*Strickland et al.*, 2012; *Weitzman and Hahn*, 2014; *Karunarathne et al.*, 2015]. Optogenetic regulation has already been used before e.g. to control the motility of living cells [*Wu et al.*, 2009]. Optogenetic regulation has several advantages to previously used tools. Compared with approved methods, such as microrheological experiments or chemical treatments, it allows for both a local and temporary regulation of the CSK. Their reversibility makes optogenetics furthermore preferable to laser ablation [*Valon et al.*, 2017].
Regarding the optogenetic regulation of cellular forces, the following two recent optogenetic tools became prominent: A Light-Oxygen-Voltage (LOV)-domain-based optogenetic probe developed by *Wagner and Glotzer* [2016], on the one hand, and a cryptochrome-based optogenetic probe introduced by *Valon et al.* [2017], on the other hand. Both methods have in common that they rely on the control the subcellular activation of the small GTPase RhoA, which, in its active state, is known to regulate the polymerization of actin and the activity of myosin II [*Ridley and Hall*, 1992; *Chrzanowska-Wodnicka and Burridge*, 1996]. The former method will be exploited in this chapter in order to specify

the viscoelastic properties of SFs, while latter method will be used in Chapter 4.
In this chapter, we will introduce a viscoelastic continuum model which captures the time course of the contractile energy as well as the SF dynamics upon LOV-domain-based optogenetic spatiotemporal regulation of RhoA in fibroblast cells. In particular, the model allows to determine the viscoelastic relaxation time of SFs which can be seen as transition between time regimes in which the CSK response elastic or viscous. The model moreover allows to unveil that the elasticity of SFs is mainly maintained by the protein zyxin, which is known to function as repair protein in SFs [*Smith et al.*, 2010]. We will finally use the model as a basis to parameterize a discrete viscoelastic cable network introduced by *Brand* [2017], allowing a specification of discrete structures of the cytoskeleton, such as SFs or the actin cortex.
The results presented in the following originate from a collaborative work together with Patrick Oakes, Elizabeth Wagner, Margaret Gardel and Michael Glotzer from the University of Chicago, who performed all experiments, and Marco Linke and Christoph Brand from the group of Ulrich Schwarz, who contributed to the image analysis and modeling work, respectively. The results are documented in detail in *Oakes et al.* [2017].

3.1 Optogenetic Setup and Activation Protocol

The actin CSK of adhering NIH 3T3 fibroblasts was optogenetically regulated following the optogenetic setup introduced by *Wagner and Glotzer* [2016]. Figure 3.1A illustrates the optogenetic probe, which consists of two different types of proteins: LOVpep proteins are anchored to the plasma membrane and photorecruitable GEFs (prGEF), each consisting of a $(PDZ)_2$-mCherry-LARG(DH) protein construct, are distributed throughout the cytosol. Upon local illumination by a 405 nm laser, the LOVpep molecule undergoes a conformational change and, with this, allows the recruitment of the prGEF to the plasma membrane.
Figure 3.1B demonstrates an increased concentration of prGEF in the activation region during illumination of blue light. Removal of the blue light leads to a refolding of the LOVpep molecule and stops further recruitment of prGEF. At the plasma membrane, prGEF phosphorylates the inactive RhoA-GDP molecules which are predominantly located close to the plasma membrane. As illustrated in Figure 1.3E, activation of RhoA stimulates the polymerization of actin via the effector Dia and the activation of myosin II via phosphorylation of the Rho-associated protein kinase (ROCK).
Figure 3.1C and 3.1D show the intensity of the fluorescently labelled actin and activity of the myosin light chain (MLC), respectively. Local activation of RhoA yields both an increased actin polymerization and myosin activity in the activation region. Upon removal of the activating light, the heightened actin concentration and myosin activity disperse throughout the cell.
In a typical experiment, cells are imaged for 45 min. During the first 15 min, cells remain untouched to figure out the steady state of the system. In the following 15 min time slot, cells are locally illuminated every 20 s for 960 ms with laser light of power $< 1\,\mu\mathrm{Js}^{-1}$. In the final 15 min, the cells again remain untouched and the recovery of the CSK is imaged.

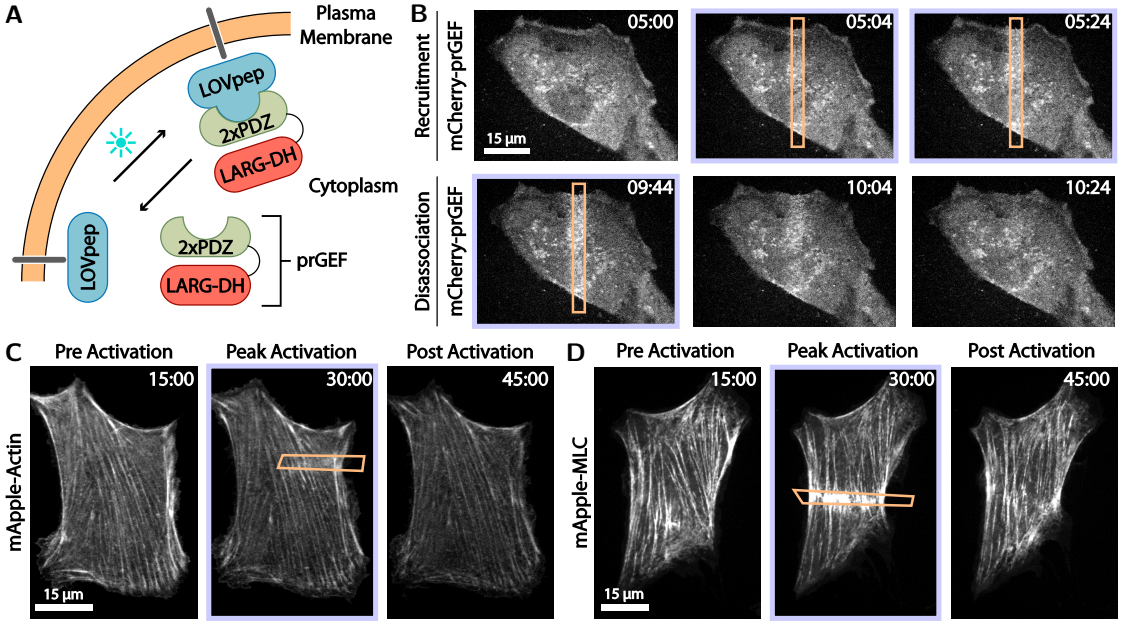

Figure 3.1: Optogenetic control of RhoA and its downstream effectors. **(A)** LOVpep molecules are anchored to the plasma membrane and photorecruitable GEFs (prGEFs) are distributed throughout the cytosol. Upon stimulation with blue light, a LOVpep molecule undergoes a conformational change, allowing the recruitment of the prGEF to the plasma membrane, where it can activate RhoA. Removal of the activating light leads to a refolding of the LOVpep molecule and stops further recruitment of prGEF. **(B)** Images of a cell expressing prGEF. A localized activating light (*orange* box) triggers a rapid accumulation of prGEF in the activation region. After removing the activating light, the accumulated prGEF disperses back into the cytosol. **(C)** and **(D)** show the intensity of the fluorescently labelled actin and activity of the MLC, respectively. Local activation of RhoA yields both an increased actin polymerization and myosin activity in the activation region (*orange* box). Upon removal of the activating light, the heightened actin concentration and myosin activity disperse throughout the cell. Time is min:sec. Scale bars are 15 μm. Image adapted from *Oakes et al.* [2017].

The time scales of prGEF regulation, on the one hand, and the regulation of its effectors actin and myosin, on the other hand, differ by about one order of magnitude, as Figure 3.2 demonstrates. Here, the temporal evolution of the average fluorescence intensity in the local recruitment region is illustrated. While the intensity of prGEF increases and decreases within tens of seconds, actin and myosin are both regulated on a time scale of hundreds of seconds.

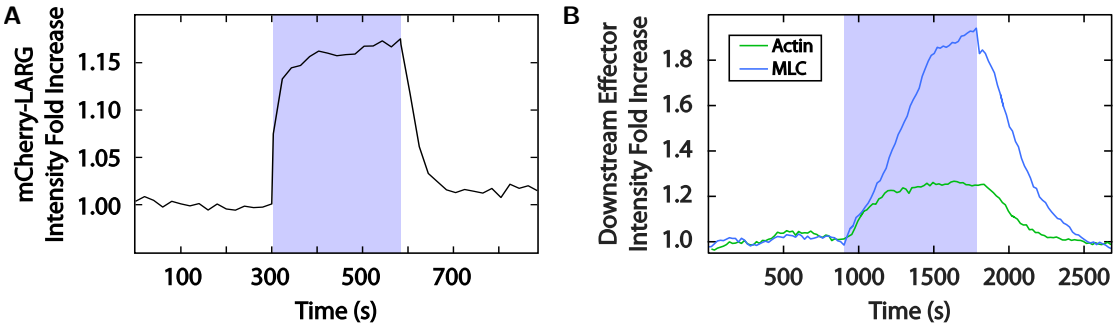

Figure 3.2: Activation of RhoA induces an increase of actin polymerization and myosin activity on the timescale of minutes. While blue light activation (*blue* rectangle) yields a instantaneous increase (or decrease) in the prGEF intensity **(A)**, its downstream effectors actin and MLC increase (or decrease) on the slower timescale of minutes **(B)**. Image adapted from *Oakes et al.* [2017].

3.2 Quantification of Traction Stresses Induced by Optogenetics

In the following, we determine the effect of local RhoA activation on the overall contractility of the cell. For this, cells were plated on circular shaped fibronectin patterns on top of a PAA gel of Young's modulus 25.8 kPa and Poisson's ratio 0.5 and contractile stresses of the cells were quantified by means of FTTC, as describe in Chapter 2. Figure 3.3A illustrates exemplar traction stresses an activated cell exerts on the PAA gel.
We find that local RhoA activation elicits a global increase of traction stresses which are transmitted via SFs to the periphery of the cell. After removal of the activation light, the cell reverses to the contractile state it adopted before the activation. This is illustrated in Figure 3.3B, which shows the strain energy and total force exerted by the cell as a function of time. The strain energy shows a repeating temporal pattern during each activation period: a fast rise on the time scale of single minutes, passing into a slower growth and a fast decay after removal of the activating light, again on a time scale of minutes.
In each activation period in Figure 3.3, the area of the activation region is increased from $30\,\mu m^2$ by a factor of 3 during the second activation and another factor of 2 during the third activation. With increasing size of the activation region, the strain energy as well as the total traction force increase proportional to the activation area. This can be explained by the fact that the activation region is increased perpendicular to the dominant direction of SFs, which is implied from the traction images, and the activation of an increasing number of SFs in parallel is assumed to lead to an increasing force.
Figures 3.3C and 3.3D show the dipole and quadrupole moments of the cell during local RhoA activation. Throughout the experiment, the cell reveals a preferred orientation into the direction of SFs, indicated by thick white lines in Figure 3.3A. In contrast, no dominant quadrupole moment can be detected. The persistence of the quadrupole moment suggests that the cytoskeleton does no change its preferred direction of action

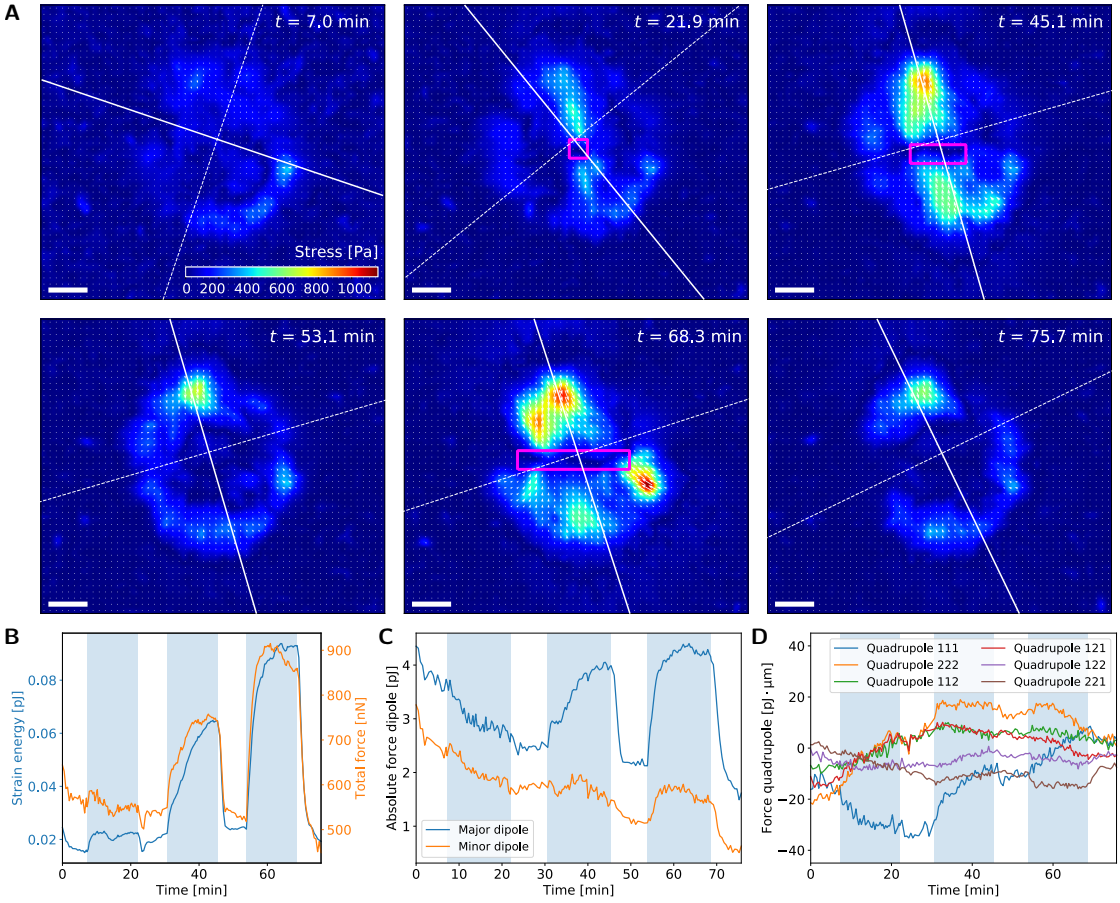

Figure 3.3: Local activation of RhoA leads to globally increased traction stresses. The increase of overall traction stresses correlates with the size of the activation region. **(A)** Exemplary time sequence of traction stresses during local RhoA activation and relaxation. The activation region is shown as *pink* box. Force dipole axes are depicted as *white lines*, of which *full lines* represent the dominant dipole axis. Scale bars are 10 μm. **(B)** Temporal evolution of the cellular strain energy and total force. Activation periods are depicted as *blue* rectangles. **(C)** Temporal evolution of the major and minor force dipole moments of the cell. **(D)** Temporal evolution of the cellular force quadrupole moments w.r.t. the major dipole axis.

during the experiment.
Interestingly, the activation regions themselves remain stress-free which can be explained by the fact that motors which are activated over-than-average within the activation region pull into random directions along newly-polymerized actin filaments and, with this, add up to a zero net force. Motors outside the activation region however remain ordered and pull along the SFs.
Another possible explanation is the lack of FAs in the central region of the cell. On the one hand, fibroblasts tend to place most of their FAs at the periphery. On the other

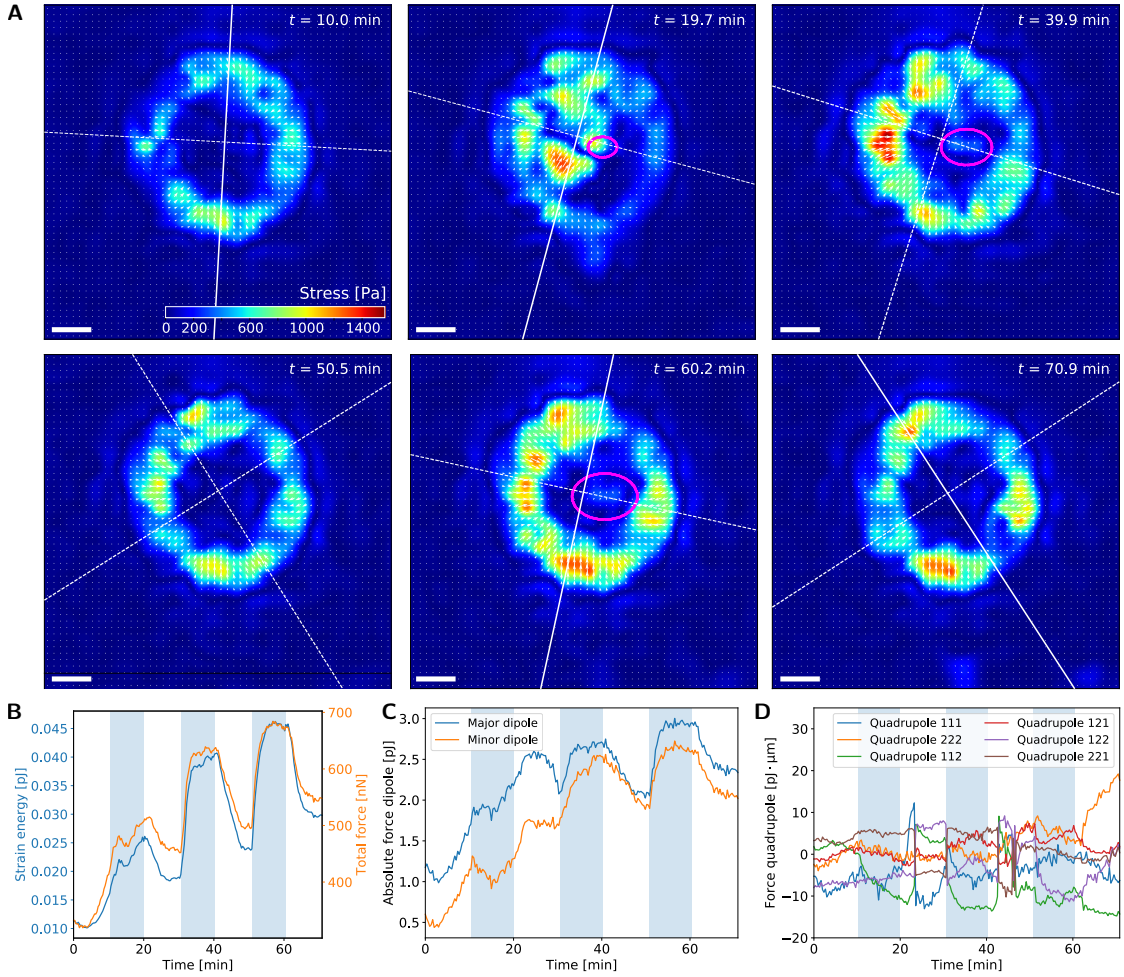

Figure 3.4: As in Figure 3.3, local activation of RhoA leads to globally increased traction stresses. Here, the cell exhibits an increasing background contraction even without external activation, leading to a steady increase of the strain energy baseline. In contrast to Figure 3.3, Quadrupole Q_{112} is the dominating quadrupole moment. **(A)** Exemplary time sequence of traction stresses during local RhoA activation and relaxation. The activation region is shown as *pink* box. Force dipole axes are depicted as *white lines*, of which *full lines* represent the dominant dipole axis. Scale bars are 10 μm. **(B)** Temporal evolution of the cellular strain energy and total force. Activation periods are depicted as *blue* rectangles. **(C)** Temporal evolution of the major and minor force dipole moments of the cell. **(D)** Temporal evolution of the cellular force quadrupole moments w.r.t. the major dipole axis.

hand, the local RhoA activation and the subsequent over-than-average activity of myosin II in the activation region, as indicated in Figure 3.2, could force the cell to rip off the substrate below the activation region.
Figure 3.4A shows a second cell which supports the second of these arguments. Here, we

can register a non-zero stress within the activation region during first activation period, which vanishes in the remaining periods.
In contrast to the first cell, the second cell shows a more isotropic stress field with permanently changing major dipole axis. This is also indicated by Figures 3.4C and 3.4D: The ratio of major and minor dipole is close to one and the evolution of quadrupoles shows a spiky pattern, implying a frequent change of dipole axes.
As Figure 3.4B demonstrates, an increase of the activation region does not only increase the strain energy and total force, but also the baseline of both quantities. At the same time, the relative strain energy or force gain upon photoactivation with respect to the preceding baseline level remains constant, irrespective of the size of the activation region. This can be interpreted in two ways: On the one hand, here, in contrast to the first cell, the activation region increases in both directions, such that illuminating a larger activation area does not imply hitting a larger amount of SFs. On the other hand, the local RhoA activation might lead to a reshuffling of the total CSK resulting in a modified tensional state.

3.3 Quantification of Viscoelastic Flows Induced by Optogenetics

As Figure 3.1 suggests, the local activation of RhoA not only triggers a heightening of the actin concentration and the myosin activity inside the activation region, but also affects the dynamics of the actin CSK outside the region. To uncover these dynamics, we used live cell imaging and an optical flow algorithm to determine spatiotemporally averaged flows of the CSK, which is described in detail in *Linke* [2017].
Figure 3.5 quantifies the global restructuring of the CSK during local activation of RhoA. In Figure 3.5A, the myosin activity of a cell attached to a glass substrate is shown before, during and after two separate periods of local RhoA activation. As before, during local RhoA activation, the myosin activity predominantly accumulates inside the activation region. Furthermore, we find that mainly SFs are affected by the optogenetic activation: Existing SFs lines rather thicken than new SFs are created.
Figure 3.5B allows a quantification of the dynamic shift of myosin activity during the sequential local activations of RhoA. Here, the fluorescent myosin signal along the green line in Figure 3.5A, i.e. along a single SF, is plotted as a function of time in a kymograph. Two effects become obvious during and after both activation periods: First, during local RhoA activation, myosin flows into the activation region while preserving its periodic arrangement along the fiber. Second, after the activating light is removed, we observe a weaker elastic-like outflow of myosin from the former activation region.
As Figures 3.5C and 3.5D show, an equivalent elastic-like behavior can be observed if imaging the dynamics of α-actinin molecules along the stress fiber, suggesting that the SF as a whole, and not only single constituents, contracts and recoils during and after activation, respectively. Interestingly, for some SFs we observe that single lines in the kymograph split into two separate lines, as indicated by the blue arrow. This reflects the incorporation of new sarcomeres into the existing SF.

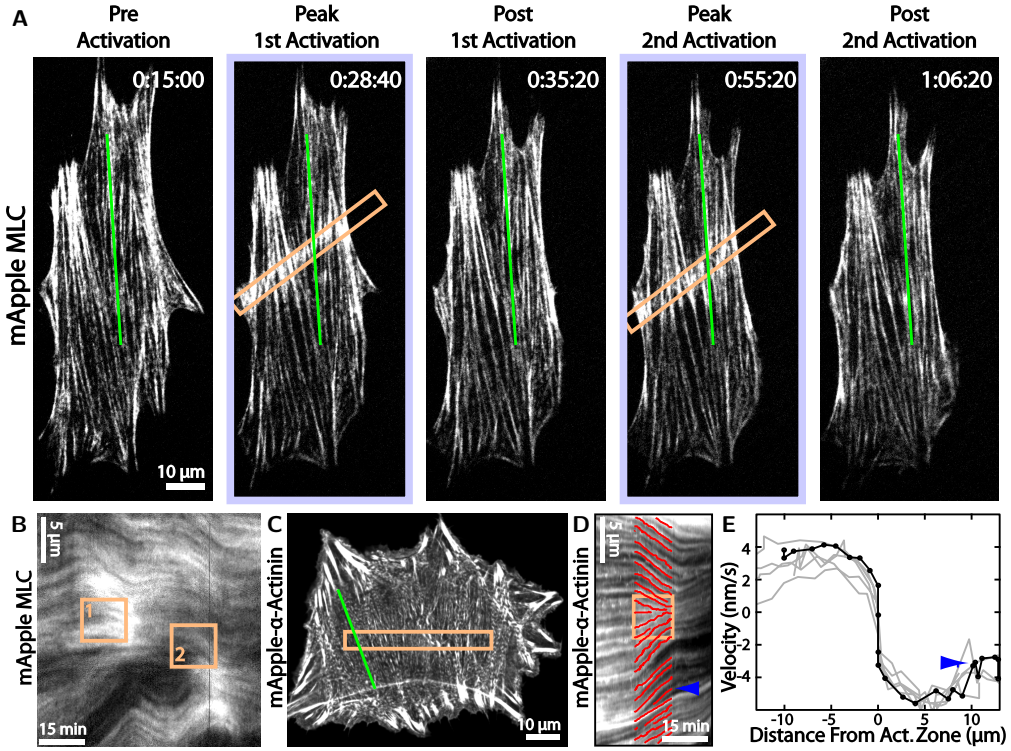

Figure 3.5: Local RhoA activation initiates a contractile flow along stress fibers towards the region of activation. After removing the activating light, stress fibers relax elastically. **(A)** Image showing the MLC activity of a cell before, during and after two separate periods of local RhoA activation. Stress fibers are the predominant cytoskeletal elements which are affected by the activation. Time is hr:min:sec. **(B)** Kymograph along the *green* line in Panel **A** showing the inflow of myosin along a stress fiber into the activation region during RhoA activation and outflow of myosin when the activation stops. After relaxation, the flow reverses direction. In general, the reversal flow is weaker than the inflow. **(C)** and **(D)** illustrate the equivalent behavior of regions of heightened α-actinin during RhoA activation, whereas Panel **D** shows the kymograph along the *green* line in Panel **C**. **(E)** Flow velocity of the stress fibers as a function of the distance from the activation zone. Adjacent sarcomeres move at approximately the same velocity. The *blue* arrowhead indicates that new sarcomeres are incorporated during activation. Image adapted from *Oakes et al.* [2017].

Figure 3.5E depicts the measured flow velocity as a function of the distance from the center of the activation region during local RhoA activation. With increasing distance, the magnitude of the velocity increases in a sigmoid-like shape, reaching a maximum velocity of approximately $4\,^{nm}/_{s}$ at the boundary of the activation region. Outside the activation region, adjacent sarcomeres move at approximately the same velocity, suggesting a steady afterflow of sarcomeres from the FA sites.
A crucial role in the regulation of SF mechanics is attributed to the mechanosensitive

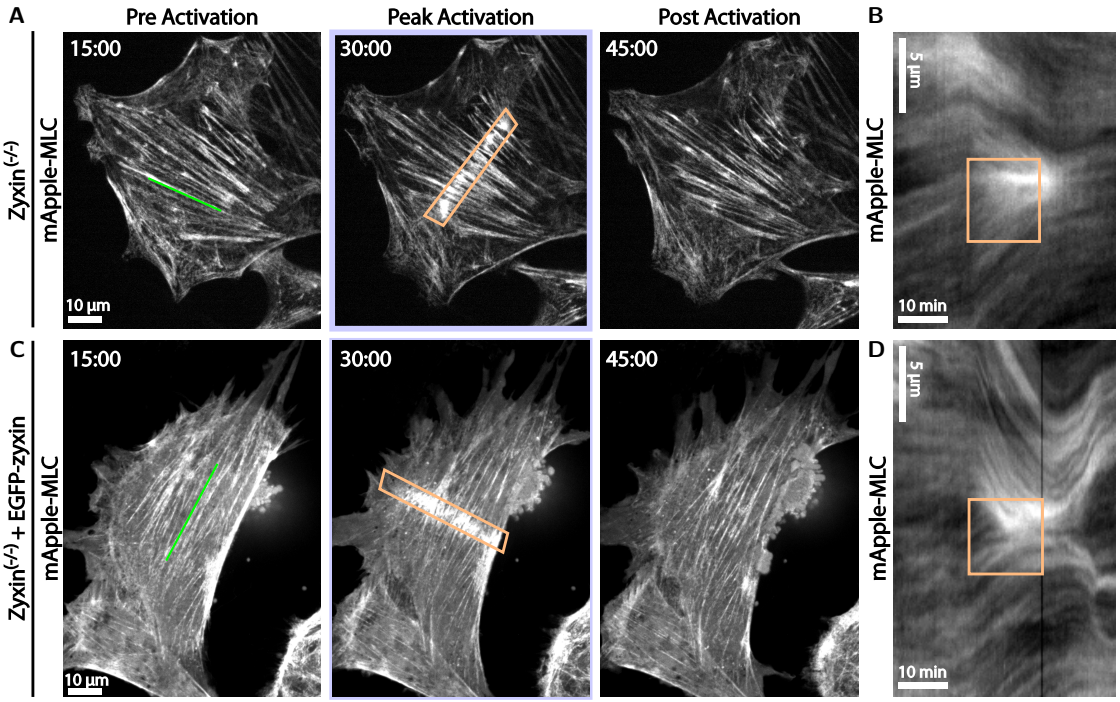

Figure 3.6: Zyxin accomplishes the elastic-like behavior of SFs. **(A)** and **(B)** show an image of a zyxin-depleted cell expressing MLC and the kymograph along the stress fiber marked by the *green* line in Panel **A**, respectively. Depletion of zyxin eliminates the elastic relaxation upon removal of the activating light. **(C-D)** Reactivation of zyxin recovers the elastic property of stress fibers. Time is min:sec. Image adapted from *Oakes et al.* [2017].

protein zyxin, which is known to dynamically localize to sites of strain along SFs and at FAs, and thus, comes into question when seeking for the molecular origin of the measured elastic-like relaxation of the SF [*Yoshigi et al.*, 2005; *Smith et al.*, 2010]. We conducted experiments on fibroblast cells in which zyxin was depleted ($Zyxin^{-/-}$- or zyxin-null-cells) and on zyxin-depleted cells in which zyxin was recovered again by expression of EGFP-zyxin ($Zyxin^{-/-}$+EGFP-zyxin- of zyxin-rescue-cells).

Figure 3.6 shows the effect of the absence and subsequent recovery of zyxin on the dynamics of SFs during the local activation of RhoA. $Zyxin^{-/-}$-cells, as illustrated in Panels 3.6A, still reveal a heightened myosin activity along SFs inside the activation region. As Panel 3.6B demonstrates, myosin flows into the activation region during activation, as observed for wild type cells. However, after the activation stops, the elastic-like outflow is much weaker or even vanished. After recovery of zyxin, the reversal flow property returns again, as shown in Panel 3.6D, suggesting than zyxin is required for maintaining the elasticity of SFs.

3.4 Simulation of Traction Stresses and Viscoelastic Flows

To get to the bottom of the underlying mechanical principles, we build a physical model that captures the introduced physical response. More precisely, we are looking for a continuum model consistent with the following requirements:

- The model should allow material flow to occur, at least on the time scale of tens of minutes, on which the stress fibers flow (see e.g. Figure 3.5B).
- It also should allow for an elastic component because forces are transmitted quickly over large distances and SFs relax elastic-like (see e.g. Figures 3.3 and 3.5B, respectively).
- Flow should be driven by gradients in myosin II activity generated by local RhoA-activation (see e.g. Figure 3.1E).

The simplest model fulfilling these requirements is an *active Maxwell model*, which consists of a serial arrangement of springs and dashpots in parallel to additional active stress elements, which generate a time-dependent contractile stress σ_{m} (see *red* rectangle in Figure 3.7 A). An active Maxwell model is also used in the theory of active gels, which has been applied to a wide range of flow phenomena in cells and tissue (see e.g. *Prost et al.* [2015] for a review).
We exclude other models for the following reasons. A solid model, e.g. a purely elastic or a Kelvin-Voigt one, has the property to relax to its initial configuration once all stresses vanish. This disagrees with the flow data in Figure 3.5, which shows that the backflow after relaxation is significantly lower than the inflow during activation. Thus, the initial configuration is not reached anymore. We conclude that the system must have a viscous component, so that it can lose memory.
We also exclude a purely viscous model, in which both the inflow during RhoA activation and the outflow during relaxation are driven by myosin II activity. Here, the backflow after relaxation could be explained by the fact that the myosin motors outside the activation region work under stalling conditions and produce a larger effective stress during relaxation than the motors inside the activation region. However, we note that zyxin is not known to alter the myosin-II motor activity. Otherwise we would expect a significant change of the inflow dynamics already during RhoA activation if zyxin is absent, which is not observed. Further, this option would lead to a backflow during relaxation even in the absence of zyxin, which is also not observed (compare Figure 3.6B). We conclude that an elastic component is needed to explain the strong backflow.
The only suitable two-element spring-dashpot model which incorporates both an elastic and a viscous behavior is the active Maxwell model used here. In the following, we will first describe the constitutive relation of the model. We then derive the equations of motion and the finite element formulation in one dimension. We will stay in one dimension since both the traction stress patterns (see Figure 3.3) as well as the live cell imaging of actin and myosin (see e.g. Figure 3.1) suggest a dominant orientation of stresses and cytoskeletal flows for the most cells, with many SFs arranged in parallel. Thus, we will

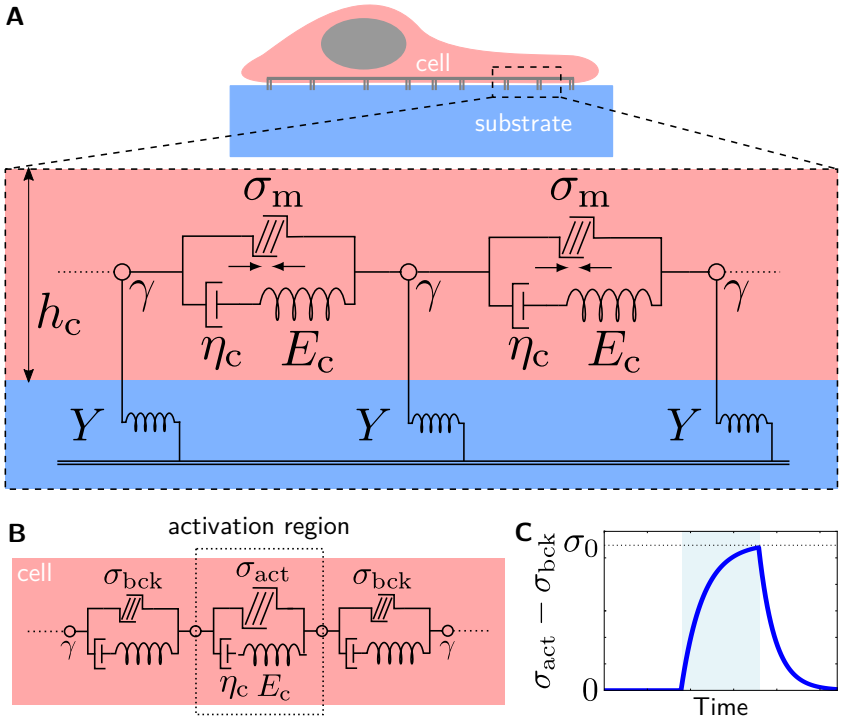

Figure 3.7: An active Maxwell model is used to reproduce the dynamics of the actin CSK during local activation of RhoA. **(A)** Effective one-dimensional representation of a cell adhering to an elastic substrate: The cell is represented by a myosin-II-motor driven viscoelastic bar which is viscoelastically connected to its environment. In the non-activated case, each motor is assumed to exert the same contractile stress. For an explanation of the involved parameters, the reader is referred to the main text. **(B)** During activation, motors within the activation region pull stronger. Effectively, only the stress difference at the boundary enters the governing equations of the model. **(C)** Typical stress profile during activation of RhoA. We assume an exponential plateauing of the active stress with activation and relaxation time constants τ_act and τ_rel.

consider a cell as a two-dimensional viscoelastic stripe of length $2L_\mathrm{c}$ in x-direction which contracts only along x-direction and has a vanishing strain $\epsilon_{yy} = 0$ in y-direction, similar to the elastic model presented by *Edwards and Schwarz* [2011].

3.4.1 One-Dimensional Active Maxwell Model

On a coarse-grained level, cells and tissue obey the fundamental equations of viscoelasticity [*Tlili et al.*, 2015]:

- Momentum conservation: $\rho \mathbf{a}(\mathbf{x}, t) = \nabla \cdot \boldsymbol{\sigma}(\mathbf{x}, t) + \mathbf{f}(\mathbf{x}, t) \approx 0$ for tissue
- Angular momentum conservation: $\sigma_{ij} = \sigma_{ji}$
- Constitutive relation: $\sigma_{ij}(\epsilon_{ij}, \dot{\epsilon}_{ij}, ...)$

Here, ρ is the mass density, $\mathbf{a}(\mathbf{x},t)$ the acceleration vector, $\boldsymbol{\sigma}(\mathbf{x},t)$ the stress tensor, $\mathbf{f}(\mathbf{x},t)$ represents external forces and $\boldsymbol{\epsilon}(\mathbf{x},t)$ the linear strain tensor

$$\epsilon_{ij} = \frac{1}{2}\left(\frac{\partial u_i}{\partial x_j} + \frac{\partial u_j}{\partial x_i}\right), \tag{3.1}$$

with u_i being the components of the displacement vector. In the following, we will rename the xx-components of the stress and strain tensors to σ and ϵ, respectively, since we are effectively staying in one dimension.
Figure 3.7 illustrates the active Maxwell model and its coupling to the extracellular environment. We can use the dissipation function formalism derived by [*Tlili et al.*, 2015] to calculate the constitutive equation of the underlying model of the actin CSK, as depicted in Figure 1.9D. Starting from the generalized description of the material, we can write down the energy function $\mathcal{E} = \mathcal{E}(\epsilon, \epsilon_1, ..., \epsilon_m)$ and dissipation function $\mathcal{D} = \mathcal{D}(\dot{\epsilon}, \dot{\epsilon}_1, ..., \dot{\epsilon}_m)$ of the system:

$$\mathcal{E}(\epsilon, \epsilon_\eta) = \frac{1}{2}\frac{E_\mathrm{c} h_\mathrm{c}}{1-\nu_\mathrm{c}^2}(\epsilon - \epsilon_\eta)^2, \tag{3.2}$$

$$\mathcal{D}(\dot{\epsilon}, \dot{\epsilon}_\eta) = \frac{1}{2}\frac{\eta_\mathrm{c} h_\mathrm{c}}{1-\nu_\mathrm{c}^2}\dot{\epsilon}_\eta^2 + \sigma_\mathrm{m} h_\mathrm{c}\dot{\epsilon}, \tag{3.3}$$

with ϵ_η being the internal strain of the dashpot, and E_c, η_c and σ_m the Young's modulus, the viscosity and the motor stress of the cell, respectively. The parameter ν_c denotes the Poisson's ratio of the cell. The height h_c of the cell is further assumed to be $h_\mathrm{c} \ll L_\mathrm{c}$. Thus, displacements in z-direction can be neglected and the resulting two-dimensional moduli are $m^{2\mathrm{D}} = m^{3\mathrm{D}} h_\mathrm{c}$, when performing spacial averaging along the height of the stripe (see e.g. *Novozhilov* [1961]). Using the rules

$$h_\mathrm{c}\sigma = \frac{\partial \mathcal{D}}{\partial \dot{\epsilon}} + \frac{\partial \mathcal{E}}{\partial \epsilon}, \tag{3.4}$$

$$0 = \frac{\partial \mathcal{D}}{\partial \dot{\epsilon}_\eta} + \frac{\partial \mathcal{E}}{\partial \epsilon_\eta}, \tag{3.5}$$

derived by *Tlili et al.* [2015], we arrive at the relations

$$\sigma = \sigma_\mathrm{m} + \frac{E_\mathrm{c}}{1-\nu_\mathrm{c}^2}(\epsilon - \epsilon_\eta), \tag{3.6}$$

$$0 = -\frac{E_\mathrm{c}}{1-\nu_\mathrm{c}^2}(\epsilon - \epsilon_\eta) + \frac{\eta_\mathrm{c}}{1-\nu_\mathrm{c}^2}\dot{\epsilon}_\eta. \tag{3.7}$$

Elimination of the internal variable ϵ_η yields the constitutive relation of the active Maxwell model

$$\frac{\sigma - \sigma_\mathrm{m}}{\tau_\mathrm{c}} + (\dot{\sigma} - \dot{\sigma}_\mathrm{m}) = \frac{E_\mathrm{c}}{1-\nu_\mathrm{c}^2}\dot{\epsilon}, \tag{3.8}$$

with the relaxation time constant $\tau_\mathrm{c} = \eta_\mathrm{c}/E_\mathrm{c}$.

During the experiments, the cytoskeleton experiences a Stokes' law friction γ with the surrounding cytoplasm. Cells on elastic substrates are, in addition, elastically coupled to their environment, which is represented by springs of stiffness density Y arranged in series with the Stokes' elements (see *blue* rectangle in Figure 3.7 A). This yields the two dependent force balance equations

$$\begin{aligned} h_\mathrm{c}\frac{\partial\sigma}{\partial x}(x,t) &= \gamma v_\gamma(x,t)\ , \\ h_\mathrm{c}\frac{\partial\sigma}{\partial x}(x,t) &= Y u_Y(x,t)\ . \end{aligned} \tag{3.9}$$

Here, $u_Y(x,t)$ and $v_\gamma(x,t) = \dot{u}_\gamma(x,t)$ are the displacement of the coupling springs and velocity of the coupling Stokes' elements, respectively. We denote $u = u_Y + u_\gamma$ as the total displacement. Note that the two terms on the right would add up for a model with parallel elements. Here, however, we have serial elements and therefore two equations involving the same force (which in turn is the derivative of the stress).
In the following step, we will derive the PDE which governs the evolution of the tissue by combining the constitutive relation 3.8 and the momentum conservation 3.9. We first calculate the derivative of Equation 3.8 with respect to space x and the derivative of the momentum conservation (see Equation 3.9) with respect to time t to obtain

$$\frac{\partial}{\partial x}(\sigma + \tau_\mathrm{c}\dot{\sigma}) - \frac{\partial}{\partial x}(\sigma_\mathrm{m} + \tau_\mathrm{c}\dot{\sigma}_\mathrm{m}) = \frac{\eta_\mathrm{c}}{1-\nu_\mathrm{c}^2}\frac{\partial^2\dot{u}}{\partial x^2} \tag{3.10}$$

and

$$\begin{aligned} h_\mathrm{c}\frac{\partial^2\sigma}{\partial x\partial t} &= \gamma\frac{\partial^2 u_\gamma}{\partial t^2}\ , \\ h_\mathrm{c}\frac{\partial^2\sigma}{\partial x\partial t} &= Y\frac{\partial u_Y}{\partial t}\ . \end{aligned} \tag{3.11}$$

Regarding the distribution of stresses σ_m along the viscoelastic bar, we make the simple assumption, that σ_m stays constant along the bar. Thus, the derivative $\partial\sigma_\mathrm{m}/\partial x$ vanishes along the whole bar. The only position at which $\partial\sigma_\mathrm{m}/\partial x$ does not vanish is the boundary between activation and non-activation region during RhoA activation as well as the cell boundary (see Figure 3.7 B). Therefore, $\partial\sigma_\mathrm{m}/\partial x$ can be skipped in Equation 3.10 and later introduced as a Neumann boundary condition (see Equation 3.21). In has to be noted here, that the resulting PDE 3.10 would also hold for a a linear relation between the motor stress σ_m and the active strain rate $\dot{\epsilon}$, which is a plausible linearized approximation of the concave force-velocity relation measured by *Hill* [1939], yielding rather similar qualitative results, but allowing a much simpler mathematical treatment [*Besser et al.*, 2011].

We can now insert Equations 3.9 and 3.11 into 3.10 with the aim to eliminate $\partial\sigma/\partial x$ and $\partial^2\sigma/\partial x\partial t$, which yields the evolution equation

$$\begin{aligned}\frac{\eta_\mathrm{c} h_\mathrm{c}}{1-\nu_\mathrm{c}^2}\frac{\partial^3 u}{\partial t\partial x^2} &= \tau_\mathrm{c}\gamma\frac{\partial^2 u_\gamma}{\partial t^2} + \gamma\frac{\partial u_\gamma}{\partial t}\,,\\ \frac{\eta_\mathrm{c} h_\mathrm{c}}{1-\nu_\mathrm{c}^2}\frac{\partial^3 u}{\partial t\partial x^2} &= \tau_\mathrm{c} Y\frac{\partial u_Y}{\partial t} + Y u_Y\,,\end{aligned} \tag{3.12}$$

or, in a rescaled version,

$$\tau_\mathrm{c}\frac{\partial^3 u}{\partial t\partial x^2} = \tau_\mathrm{c}\tilde{\gamma}\frac{\partial^2 u_\gamma}{\partial t^2} + \tilde{\gamma}\frac{\partial u_\gamma}{\partial t}\,, \tag{3.13}$$

$$\tau_\mathrm{c}\frac{\partial^3 u}{\partial t\partial x^2} = \frac{\tau_\mathrm{c}}{l_\mathrm{p}^2}\frac{\partial u_Y}{\partial t} + \frac{u_Y}{l_\mathrm{p}^2}\,, \tag{3.14}$$

with the *force localization* or *penetration length* [*Edwards and Schwarz*, 2011; *Banerjee and Marchetti*, 2012]

$$l_\mathrm{p} = \sqrt{\frac{h_\mathrm{c} E_\mathrm{c}}{Y\left(1-\nu_\mathrm{c}^2\right)}}\,, \tag{3.15}$$

and

$$\tilde{\gamma} = \frac{\gamma\left(1-\nu_\mathrm{c}^2\right)}{E_\mathrm{c}}\,. \tag{3.16}$$

At the beginning of the simulation, we assume that the displacement and the strain in the cell is zero, which leads to the initial conditions

$$u(x, t=0) = 0 \tag{3.17}$$

$$\frac{\partial u(x, t=0)}{\partial x} = 0\,. \tag{3.18}$$

For all simulations of the cell both on the elastic substrate and on glass, we assume free boundaries, i.e.

$$\sigma(x = \pm L_\mathrm{c}, t) = 0\,, \tag{3.19}$$

yielding

$$\frac{E_\mathrm{c}}{1-\nu_\mathrm{c}^2}\dot{\epsilon}(x = \pm L_\mathrm{c}, t) = -\dot{\sigma}_\mathrm{bck} - \frac{\sigma_\mathrm{bck}}{\tau_\mathrm{c}}\,, \tag{3.20}$$

with σ_bck being the contractile background stress in the cell which is present without external activation of RhoA. In our simulations, we assume a constant contractile background stress, thus $\dot{\sigma}_\mathrm{bck} = 0$. Fixed boundaries would give rise to an increase of the slope of the paths of the kymographs towards the activation region during RhoA activation, which is not observed (compare Figure 3.5D). From the biological perspective, by using free boundaries, we assume a formation of new SF material at the FAs during RhoA activation (see e.g. *Oakes et al.* [2012]).

We further model the cellular contraction due to RhoA activation as a constant interior boundary stress which is applied at a distance $l_0 < L$ from the center of the layer in the Eulerian frame, because the activation area does not change in size as the material is contracting. Since we wrote down our equations in the material frame, i.e. the Lagrangian frame, so far, we will change the spacial coordinates to capital letters in the following equation, symbolizing that the Neumann boundary condition stays fixed in the Eulerian frame. The final boundary condition yields

$$\frac{E_\mathrm{c}}{1-\nu_\mathrm{c}^2}\dot{\epsilon}(X=\pm l_0,t) = -\dot{\sigma}_\mathrm{act} - \frac{\sigma_\mathrm{act}}{\tau_\mathrm{c}}\,. \tag{3.21}$$

The stress profile during local activation of RhoA follows an exponentially saturating function, as illustrated in Figure 3.7C. This reflects the average intensity profiles of actin and myosin in Figure 3.2. Upon activation, the profile denotes

$$\sigma_\mathrm{act}(t) = \sigma_\mathrm{bck} + \begin{cases} \sigma_0\left(1-\exp\left(-\frac{t-t_0}{\tau_\mathrm{act}}\right)\right) & \text{for } t_0 \le t \le t_\mathrm{act} \\ \sigma_0\left(1-\exp\left(-\frac{t_\mathrm{act}-t_0}{\tau_\mathrm{act}}\right)\right)\exp\left(-\frac{t-(t_0+t_\mathrm{act})}{\tau_\mathrm{rel}}\right) & \text{else} \end{cases}, \tag{3.22}$$

with activation and relaxation time constants τ_act and τ_rel, photoactivation time t_0 and photoactivation duration t_act. The parameter σ_0 denotes the maximum photoactivation stress the cell reaches.

3.4.2 Numerical Implementation of the One-Dimensional Active Maxwell Model

We use a Finite Element (FE) approach with a backward difference scheme to compute the displacements $u(x,t)$ in Equations 3.13 and 3.14. For this, we discretize the time $t = m\Delta t$ and space $x = i\Delta x$ with $m \in \{0,...,T/\Delta t\}$ and $i \in \{-I+1,...,I-1\}$. With the Finite Difference (FD) approximation, we have

$$\begin{aligned} u(x,t) &= u_i^m\,, \\ \frac{\partial u}{\partial t} &= \frac{u_i^m - u_i^{m-1}}{\Delta t}\,. \\ \frac{\partial^2 u}{\partial t^2} &= \frac{u_i^m + u_i^{m-2} - 2u_i^{m-1}}{(\Delta t)^2}\,. \end{aligned} \tag{3.23}$$

The weak formulation of Equations 3.13 and 3.14 amounts to

$$\tau_\mathrm{c}\int_\Omega \frac{\partial^3 u}{\partial t \partial x^2}\,v\,\mathrm{d}x = \tau_\mathrm{c}\tilde{\gamma}\int_\Omega \frac{\partial^2 u_\gamma}{\partial t^2}\,v\,\mathrm{d}x + \tilde{\gamma}\int_\Omega \frac{\partial u_\gamma}{\partial t}\,v\,\mathrm{d}x\,, \tag{3.24}$$

$$\tau_\mathrm{c}\int_\Omega \frac{\partial^3 u}{\partial t \partial x^2}\,v\,\mathrm{d}x = \frac{\tau_\mathrm{c}}{l_\mathrm{p}^2}\int_\Omega \frac{\partial u_Y}{\partial t}\,v\,\mathrm{d}x + \frac{1}{l_\mathrm{p}^2}\int_\Omega u_Y\,v\,\mathrm{d}x\,, \tag{3.25}$$

with region Ω and test function v. We can partially integrate the term on the LHS which results in

$$\tau_\mathrm{c} \int_\Omega \frac{\partial^3 u}{\partial t \partial x^2}\, v \,\mathrm{d}x = \left[\tau_\mathrm{c} \frac{\partial^2 u}{\partial t \partial x}\, v\right]_{\partial\Omega} - \tau_\mathrm{c} \int_\Omega \frac{\partial^2 u}{\partial t \partial x}\, \frac{\partial v}{\partial x}\,\mathrm{d}x\,. \tag{3.26}$$

Then, the discretized version of Equations 3.24 and 3.25 is

$$\begin{aligned}\left[\tau_\mathrm{c} \frac{\partial^2 u_i^m}{\partial t \partial x}\, v\right]_{\partial\Omega} - \frac{\tau_\mathrm{c}}{\Delta t} \int_\Omega \left(\frac{\partial u_i^m}{\partial x} - \frac{\partial u_i^{m-1}}{\partial x}\right) \frac{\partial v}{\partial x}\,\mathrm{d}x = \\ \tau_\mathrm{c}\tilde{\gamma} \int_\Omega \frac{u_{\gamma,i}^m + u_{\gamma,i}^{m-2} - 2u_{\gamma,i}^{m-1}}{(\Delta t)^2}\, v \,\mathrm{d}x + \tilde{\gamma} \int_\Omega \frac{u_{\gamma,i}^m - u_{\gamma,i}^{m-1}}{\Delta t}\, v \,\mathrm{d}x\,,\end{aligned} \tag{3.27}$$

and

$$\begin{aligned}\left[\tau_\mathrm{c} \frac{\partial^2 u_i^m}{\partial t \partial x}\, v\right]_{\partial\Omega} - \frac{\tau_\mathrm{c}}{\Delta t} \int_\Omega \left(\frac{\partial u_i^m}{\partial x} - \frac{\partial u_i^{m-1}}{\partial x}\right) \frac{\partial v}{\partial x}\,\mathrm{d}x = \\ \frac{\tau_\mathrm{c}}{l_\mathrm{p}^2} \int_\Omega \frac{u_{Y,i}^m - u_{Y,i}^{m-1}}{\Delta t}\, v \,\mathrm{d}x + \frac{1}{l_\mathrm{p}^2} \int_\Omega u_{Y,i}^m\, v \,\mathrm{d}x\,,\end{aligned} \tag{3.28}$$

respectively. The initial and boundary conditions from Equations 3.17–3.21 are implemented as

$$\begin{aligned} u_i^0 &= 0 \\ \frac{u_i^0 - u_i^{-1}}{\Delta t} &= 0 \\ u_{\pm(I-1)}^m &= 0 \\ \frac{E_\mathrm{c}}{1-\nu_\mathrm{c}^2}\left(\frac{\partial u_{\pm(I-1)}^m}{\partial x} - \frac{\partial u_{\pm(I-1)}^{m-1}}{\partial x}\right) &= -\frac{\sigma_\mathrm{bck}^m}{\tau_\mathrm{c}} \\ \frac{E_\mathrm{c}}{1-\nu_\mathrm{c}^2}\left(\frac{\partial u_{\pm(j+1)}^m}{\partial x} - \frac{\partial u_{\pm(j+1)}^{m-1}}{\partial x}\right) &= -\frac{1}{\Delta t}\left(\sigma_\mathrm{act}^{m+1} - \left(1 - \frac{\Delta t}{\tau_\mathrm{c}}\right)\sigma_\mathrm{act}^m\right)\,, \end{aligned} \tag{3.29}$$

applying an active stress σ_act at position $i = \pm j$ at some time step $m = m_0$. Since the position at which σ_act is applied is staying fixed in the Eulerian frame, we are moving the Neumann boundary to those position in the mesh, for which the sum of the position x in the Lagrangian frame and displacement u equals $\pm l_0$. We evaluate this sum at each time step of the simulation. The equations are calculated with the FE solver FEniCS [*Alnæs et al.*, 2015].

3.4.3 Parameterization of the One-Dimensional Active Maxwell Model

Equations 3.13, 3.14, 3.20 and 3.22 contain the following free parameters: elastic modulus E_c, viscous modulus η_c, friction coefficient γ, maximal active stress σ_0, global (background) stress σ_bck, the stress activation and relaxation time constants τ_act and τ_rel and the

penetration length l_p. The penetration length is calculated from an interpolation formula derived by *Banerjee and Marchetti* [2012]:

$$l_\mathrm{p} = \sqrt{\frac{E_\mathrm{c} h_\mathrm{c} L_\mathrm{c} l_\mathrm{sarc}}{k_\mathrm{a}} + \frac{E_\mathrm{c} h_\mathrm{c} h_\mathrm{eff}}{\pi E_\mathrm{s}}} \tag{3.30}$$

and

$$h_\mathrm{eff}^{-1} = \frac{1}{h_\mathrm{s} 2\pi\,(1+\nu_\mathrm{s})} + \frac{1}{L_\mathrm{c}} \tag{3.31}$$

with parameters taken from Table A.2. The remaining parameters are obtained by the conjugate-gradient based iterative parameter optimization method of *Nelder and Mead* [1965].

We aim at explaining two different experiments by means of the introduced one-dimensional active Maxwell model. First, we reproduce the evolution of the strain energy U_s (compare Figure 3.3B), which the cell invest to deform the elastic substrate during photoactivation. This is done by summing over the displacements u_Y of the coupling springs via [*Oakes et al.*, 2014]

$$\begin{aligned} U_\mathrm{s} &= \frac{1}{2}\int_A \mathbf{T}\mathbf{u}_{Y,\mathrm{s}}\,\mathrm{d}A = \frac{Y^2}{2Y_\mathrm{s}}\int_A \mathbf{u}_Y^2\,\mathrm{d}A = \frac{Y^2}{2Y_\mathrm{s}}\int_{-L_{\mathrm{c},y}}^{L_{\mathrm{c},y}}\int_{-L_{\mathrm{c},x}}^{L_{\mathrm{c},x}} u_{Y,x}^2\,\mathrm{d}x\mathrm{d}y \\ &\approx \frac{2Y^2 L_{\mathrm{c},y}}{2Y_\mathrm{s}}\int_0^{L_{\mathrm{c},x}} u_{Y,x}^2\,\mathrm{d}x \equiv \alpha\int_0^{L_{\mathrm{c},x}} u_{Y,x}^2\,\mathrm{d}x \end{aligned} \tag{3.32}$$

with the cell width $2L_\mathrm{c}$, the two-dimensional traction field of the cell $\mathbf{T} = Y\mathbf{u}_Y = Y_\mathrm{s}\mathbf{u}_{Y,\mathrm{s}}$, the substrate displacement $\mathbf{u}_{Y,\mathrm{s}}$ and the contribution of the substrate stiffness to the spring stiffness density $Y_\mathrm{s} = {}^{\pi E_\mathrm{s}}/_{h_\mathrm{eff}}$. The latter is estimated by the second addend in Equation 3.30. With the parameter value listed in Table A.2, we get $Y_\mathrm{s} = 2.0 \times 10^8\,\mathrm{N/m^3}$. The parameter α is used as a further free parameter in the optimization algorithm. Thus, we only have to consider the computation of u_Y from Equation 3.14 to be able to calculate the strain energy. In Equation 3.32, we assume that the y-dimension remains unaffected by a contraction in x-direction. It has to be noted here that the comparison of an absolute one-dimensional energy with the experimental two-dimensional energy is ill-defined and the above approximate formulation is only suited to find the correct length and time scales of the biological system. For a description of absolute energy values, a two-dimensional model is more appropriate and will be considered in Chapter 4.

Second, we are interested in describing the kymograph dynamics which emerge from the dynamics of the sarcomeres during local RhoA activation (compare e.g. Figure 3.5). In this case, cells are adhering to a glass substrate, so that we can approximately assume $u_Y = 0$, leaving $u = u_\gamma$. Therefore, in this second case, we are only interested in solving Equation 3.13.

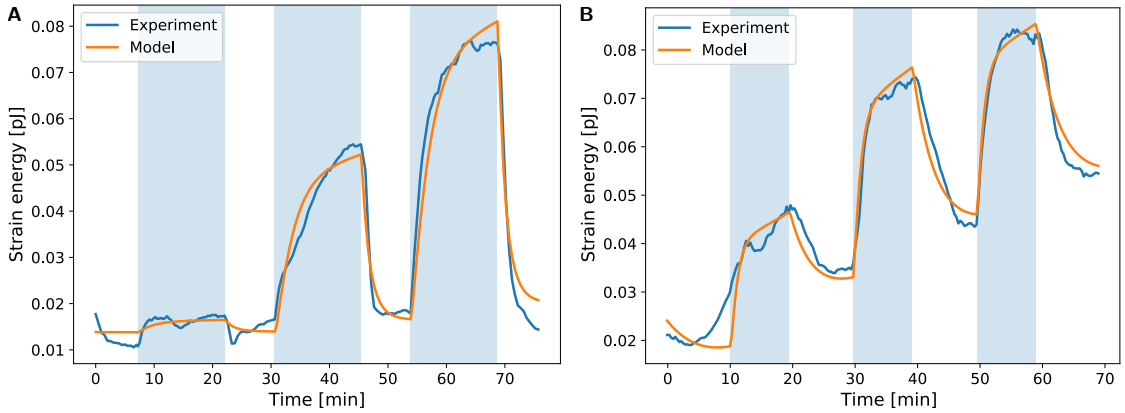

Figure 3.8: Viscoelastic model captures the temporal evolution of the strain energy. **(A)** and **(B)** show the strain energy curves and their corresponding model fits for the exemplar cells from Figure 3.3 and 3.4, respectively.

3.4.4 Simulation Results

We applied the numerical scheme and fitting procedure presented so far to derive numerical values to characterize the experimental results. Figure 3.8 as well as Table A.2 show the model fit to the time course of the strain energy curves presented in Figures 3.3 and 3.4. Qualitatively, the energy curves of the model fits well to the experimental data. The parameter values yield a Maxwell relaxation time constant $\tau_c \approx 42.79\,\text{min}$ for *cell 1* presented in Figure 3.3 and $\tau_c \approx 9.22\,\text{min}$ for *cell 2* presented in Figure 3.4, Similar material relaxation times for cells were acquired in a recent study by *Étienne et al.* [2015] by means of cantilever measurements.
Interestingly, the relaxation time constants of the two cells differ by almost one order of magnitude. This can be explained by the lower viscosity of the cell 2, as we can already guess from the constantly increasing baseline of the contractile energy in Figure 3.4B. The comparably low viscosity might be a consequence of the rather isotropic arrangement of the CSK of cell 2, suggesting an increased restructuring activity as compared to cell 1.
We further mapped the dynamics of our model to the kymographs entailing the myosin activity along a SF during local RhoA activation, similar to those presented in Figure 3.5B. In order to realize a reasonable comparison with the model, we hand-marked about 10 bright paths per kymograph, each path consisting of 13 points along the time axis. These points served as reference values for the SF dynamics and were used to constrain the model parameters. For each cell type, i.e. wild-type, zyxin-null and zyxin-rescue cells, we investigated up to 5 kymographs of at least 2 different cells per type (see Figure 3.9).
Figure 3.9 illustrates the model fits to four representative kymographs per cell type. We can see a qualitatively excellent agreement between model and experiment. It has to be noted that the background stress σ_{bck} does not account for asymmetric flows of the SF with respect to the center of the activation region, which would otherwise lead to numerical instabilities due to an asymmetric mesh subject to free boundaries.
Furthermore, Figure 3.10 and Table A.3 reveal the parameter values we can deduce from

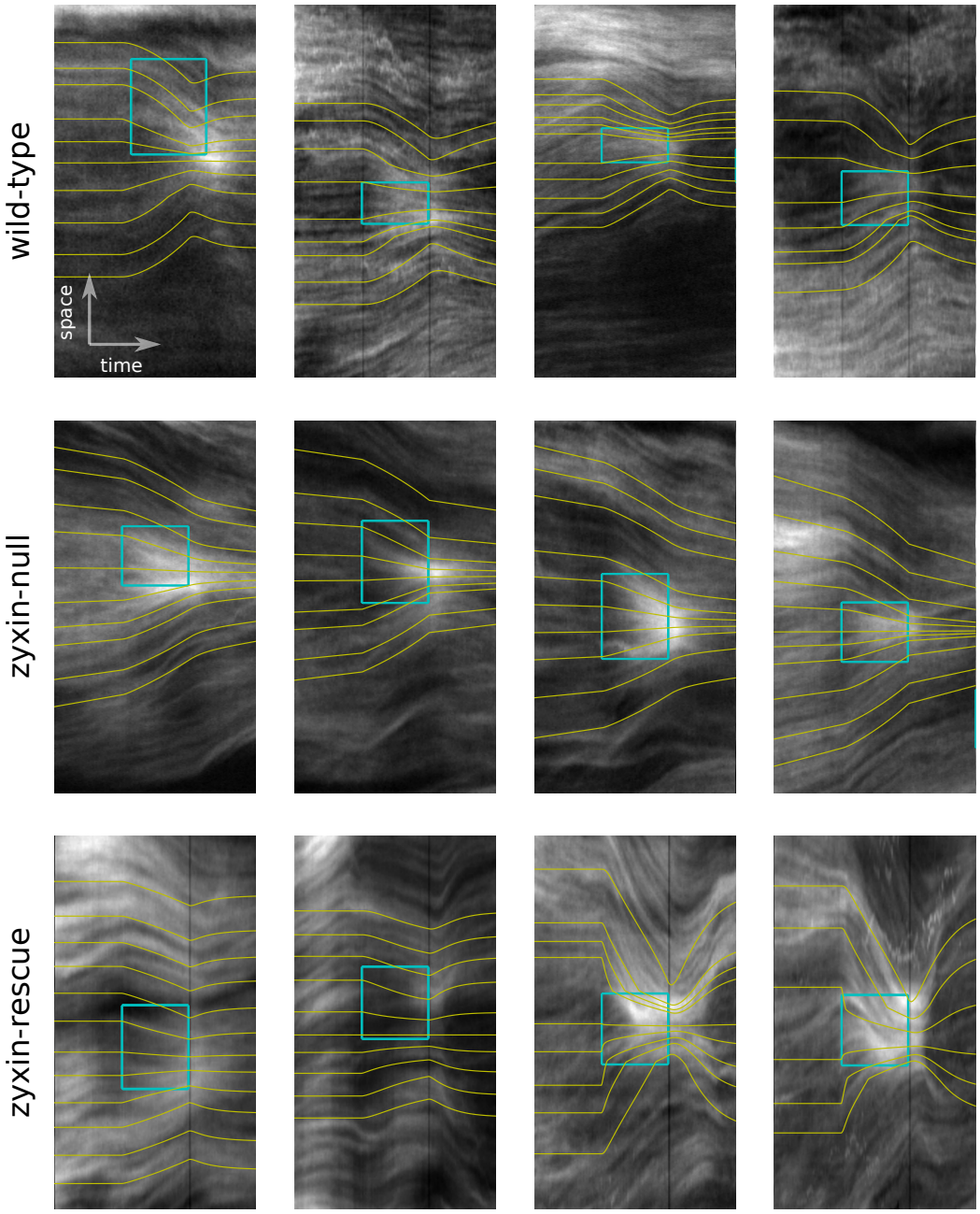

Figure 3.9: Representative kymographs showing the spatiotemporal evolution of fluorescently labelled myosin II filaments in single SFs during activation of RhoA for the three investigated cell types: wild-type, zyxin-null and zyxin-rescue cells, from top to bottom. Time is in horizontal and space in vertical direction. Overlayed *yellow lines* show the model fits. *Blue boxes* illustrate the original spatial extension (5 μm) and duration (15 min) of the photoactivation. Image adapted from *Oakes et al.* [2017].

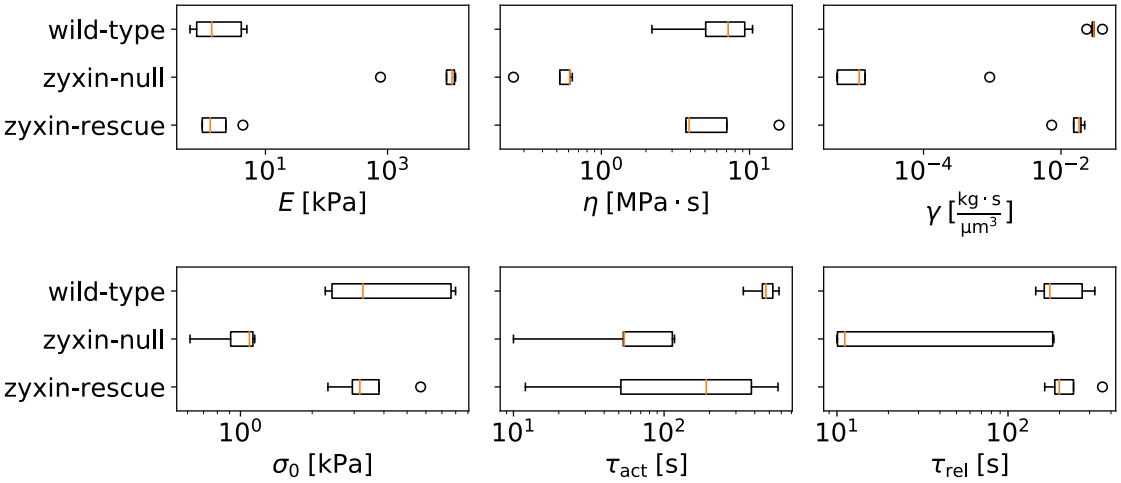

Figure 3.10: Parameters which result from the model fit to the SF dynamics extracted from the kymographs in Figure 3.9. *Yellow lines* denote the median values, *boxes* are the midspread, while *whiskers* contain 99.3 % of the data. *Circles* denote outliers. Image adapted from *Oakes et al.* [2017].

the kymographs. The resulting parameter values are in good accordance with the values we already deduced from the strain energy course in Table A.2. We can calculate a hydrodynamic length $\lambda = \sqrt{\eta_c/\gamma} \approx 15.0\,\mu$m, which is in good agreement with those of other cell types (compare e.g. *Saha et al.* [2016]).
The typical relaxation time constant for wild-type cells results to $\tau_c \approx 49.0$ min. This time scale determines the transition time from when the actin CSK behaves elastic-like to viscous-like. Thus, cells are predominantly elastic on a time scale of up to tens of minutes, and behave like a viscous fluid on times larger than one hour.
Furthermore, the kymographs reveal that the described optogenetic probe and protocol lead to a rather slow effect on the downstream effectors actin and myosin, which is reflected by the activation and relaxation time scales of $\tau_{\text{act}} \approx 7.9$ min and $\tau_{\text{rel}} \approx 3.9$ min, as compared e.g. with the optogenetic method presented in Chapter 4.
In Figure 3.10, we can clearly see the change in magnitudes if zyxin is absent: the stress fiber becomes stiffer and more fluid, the latter by both a decreased viscosity and a decreased viscous coupling to its environment. The apparently extreme stiffening of the cells can be explained based on the constitutive relation in Equation 3.8. With $E \to \infty$, the relation reduces to those of an active viscous fluid:

$$\sigma - \sigma_m = \eta_c \dot{\epsilon}\,. \tag{3.33}$$

As Figure A.4 demonstrates, however, fitting the dynamics of wild-type cells and setting $E \to \infty$ is not sufficient to describe the dynamics of zyxin-null cells, which reveals that zyxin has an effect on both the elasticity and the viscosity of a cell. In the absence of zyxin, also both the stress time constants τ_{act} and τ_{rel} as well as the magnitude of the motor stress σ_0 during activation decreases by almost an order of magnitude. This suggests that,

after depletion of zyxin, the cell is unable to exert its full contractile capabilities. Surprisingly, the recovery of zyxin also completely recovers the elastic property of cells, with relaxation times $\tau_c \approx 59.0\,\text{min}$ and a hydrodynamic length $\lambda \approx 20.4\,\mu\text{m}$ approaching those of wild-type cells. This result clearly demonstrates that the depletion of zyxin is a fully reversible process when considering the accompanied mechanical properties of the cell.

3.5 Relating Discrete and Continuum Viscoelastic Model via Discrete Homogenization

The one-dimensional active Maxwell model introduced so far offers an acceptable description of the dynamics of the actin CSK during local activation of RhoA. However, one should keep in mind that the model only unveils global, i.e. homogenized, parameters of the heterogeneous actin CSK. Furthermore, the presented continuum model does not consider the asymmetric cable-like mechanical behavior of actin filaments, which behave like springs upon pulling, but buckle with a negligible resisting force upon pushing.
A closer touch to experimental data can be gained by modeling the actin CSK as a mesh of discrete contractile viscoelastic cables representing actin filaments and myosin II motors, with stress fibers embedded as viscoelastic cable-element line structures into the mesh. This model approach has been investigated in *Brand* [2017] and unveils a powerful technique to fine-grainedly model the dynamics of actin CSK. Figure 3.12A shows an example how the actin CSK of a cell is translated to a discrete mesh of contractile cables of stiffness k, viscosity η and Stokes' drag γ, with discrete SFs embedded into the mesh as additional links of stiffness k_{SF}, viscosity η_{SF} and motor stress σ_{m}.
The active cable model, however, suffers from several disadvantages. First, with increasing detail the computational time drastically increases. On top of this, the parameter space grows, and thus, a direct parameter optimization with respect to experimental data becomes unfeasible. Furthermore, micromechanical parameters inside a cell can vary by orders of magnitude. Thus, microscopical parameters, such as the stiffness of single actin links, do not need to coincide with global properties of the cell, such as its global stiffness. Therefore, great interest arises in creating a link between the microscopic parameters and their contribution to macroscopic parameters.
In the following, we will use the so-called *discrete homogenization* technique, which was introduced by *Tollenaere and Caillerie* [1998], to relate an exemplar rectangular cell following the dynamics of the active cable model, as introduced by *Brand* [2017], and the continuum model introduced in the previous section. For this, we start with a two-dimensional extension of the continuum model, followed by calculating the relation between microscopic and macroscopic parameters.

3.5.1 Two-Dimensional Active Maxwell Model

We consider the two-dimensional problem of a rectangular, unidirectionally contracting cell of Maxwell type, spanning from $-L_x$ to L_x in x- and $-L_y$ to L_y in y-direction,

with fixed boundary (see Figure 3.12B). With regard to a comparison of a viscoelastic continuum model and a discrete cable Maxwell model, we have to modify the continuum cell as depicted in Figure 3.12C:

- We only consider a half cell, leaving the boundary adjacent to the activation region unfixed. Material can "vanish" through this free boundary.
- The part of the cell which is covered by the activation region is modeled as a purely viscous material in order to achieve the non-repelling character known from cables. Once material crosses the border to the activation region, it is converted from a Maxwell to a Newtonian fluid.

Indeed, material flow inside the activation region in the continuum model significantly differs from that of the cable Maxwell model. However, we are only interested in the flow close to the activation region, such that dynamics inside the activation region remain irrelevant for our purposes. We model the material outside the activation region, referred to as Ω_1, as a Maxwell fluid with constitutive relation

$$\frac{\sigma_{ij} - \sigma_{\mathrm{m}ij}}{\tau_{\mathrm{c}}} + (\dot{\sigma}_{ij} - \dot{\sigma}_{\mathrm{m}ij}) = \frac{\partial}{\partial t} \left(\lambda \delta_{ij} \epsilon_{kk} + 2\mu \epsilon_{ij}\right) , \tag{3.34}$$

or, in tensor form,

$$\frac{\boldsymbol{\sigma} - \boldsymbol{\sigma}_{\mathbf{m}}}{\tau_{\mathrm{c}}} + (\dot{\boldsymbol{\sigma}} - \dot{\boldsymbol{\sigma}}_{\mathrm{m}}) = \frac{\partial}{\partial t} \left(\lambda \mathrm{tr}\left(\boldsymbol{\epsilon}\right) \mathbb{1} + 2\mu \boldsymbol{\epsilon}\right) , \tag{3.35}$$

with Lamé coefficients

$$\lambda = \frac{E_{\mathrm{c}} h_{\mathrm{c}} \nu_{\mathrm{c}}}{1 - \nu_{\mathrm{c}}^2} , \tag{3.36}$$

and

$$\mu = \frac{E_{\mathrm{c}} h_{\mathrm{c}}}{2\left(1 + \nu_{\mathrm{c}}\right)} . \tag{3.37}$$

Material inside the activation region (Ω_2) is modeled as a Newtonian fluid

$$\frac{\boldsymbol{\sigma} - \boldsymbol{\sigma}_{\mathbf{m}}}{\tau_{\mathrm{c}}} = \frac{\partial}{\partial t} \left(\lambda \mathrm{tr}\left(\boldsymbol{\epsilon}\right) \mathbb{1} + 2\mu \boldsymbol{\epsilon}\right) . \tag{3.38}$$

In both equations, $\boldsymbol{\epsilon}$ denotes the strain tensor

$$\boldsymbol{\epsilon} = \frac{1}{2} \left(\nabla \mathbf{u} + (\nabla \mathbf{u})^T\right) . \tag{3.39}$$

Together with the multidimensional force balance equation

$$\nabla \cdot \boldsymbol{\sigma}\left(\mathbf{x}, t\right) = \gamma \dot{\mathbf{u}}(\mathbf{x}, t) , \tag{3.40}$$

we can calculate the evolution equations for both regions in analogy to Section 3.4.1, which yields

$$\gamma\ddot{\mathbf{u}} + \frac{\gamma}{\tau_c^{(1)}}\dot{\mathbf{u}} = \frac{\partial}{\partial t}\nabla\left(2\mu\epsilon + \lambda\mathrm{tr}\left(\epsilon\right)\mathbb{1}\right) \tag{3.41}$$

for region Ω_1 and

$$\frac{\gamma}{\tau_c^{(2)}}\dot{\mathbf{u}} = \frac{\partial}{\partial t}\nabla\left(2\mu\epsilon + \lambda\mathrm{tr}\left(\epsilon\right)\mathbb{1}\right) \tag{3.42}$$

for region Ω_2. We start with the initial conditions

$$\mathbf{u}(x, y, t = 0) = 0 \tag{3.43}$$

$$\frac{\partial \mathbf{u}(x, y, t = 0)}{\partial x} = 0\,. \tag{3.44}$$

The fixed cell boundary gives rise to the conditions

$$\mathbf{u}(x = L_x, t) = 0 \tag{3.45}$$

$$\mathbf{u}(x = \pm L_y, t) = 0\,. \tag{3.46}$$

Upon activation in a region of width l_1, we apply a piecewise active stress σ_{act} in x-direction according to Figure 3.12C:

$$\sigma_{\mathrm{act}} = \begin{cases} -\sigma_{\max}, & x \leq l_0 \\ -\sigma_{\max}\frac{l_1 - x}{l_1 - l_0}, & l_0 < x \leq l_1 \\ 0, & x > l_1 \end{cases}\,. \tag{3.47}$$

3.5.2 Weak Formulation of the Two-Dimensional Problem

As in the previous subsection, we use a FE approach with a backward difference scheme to compute the displacement $\mathbf{u}\left(x, y, t\right)$ in Equations 3.41 and 3.42 with the resulting temporal discretization in Equations 3.23.
The weak formulation of the evolution equations 3.41 and 3.42 yields

$$\begin{aligned}\tilde{\gamma}\int_{\Omega_1}\ddot{\mathbf{u}}\,\mathbf{v}\,\mathrm{d}\mathbf{x} + \frac{\tilde{\gamma}}{\tau_c^{(1)}}\int_{\Omega_1}\dot{\mathbf{u}}\,\mathbf{v}\,\mathrm{d}\mathbf{x} + \frac{\tilde{\gamma}}{\tau_c^{(2)}}\int_{\Omega_2}\dot{\mathbf{u}}\,\mathbf{v}\,\mathrm{d}\mathbf{x} + \int_{\Omega_1}\nabla\sigma_{\mathrm{act}}\,\mathbf{v}\,\mathrm{d}\mathbf{x} + \int_{\Omega_2}\nabla\sigma_{\mathrm{act}}\,\mathbf{v}\,\mathrm{d}\mathbf{x} \\ = \int_{\Omega_1}\nabla\left(2\mu\dot{\epsilon} + \lambda\mathrm{tr}\left(\dot{\epsilon}\right)\mathbb{1}\right)\,\mathbf{v}\,\mathrm{d}\mathbf{x} + \int_{\Omega_2}\nabla\left(2\mu\dot{\epsilon} + \lambda\mathrm{tr}\left(\dot{\epsilon}\right)\mathbb{1}\right)\,\mathbf{v}\,\mathrm{d}\mathbf{x}\,.\end{aligned} \tag{3.48}$$

We use the FE solver FEniCS to calculate the displacements in Equation 3.48 [*Alnæs et al.*, 2015]. The equations are solved separately for both regions with the boundary condition that the displacements resemble at the boundary between the two regions.

3.5.3 Relation Between Continuum and Discrete Model

We aim at creating a relation between a discrete cable Maxwell network and the introduced continuum model. In order to deduce continuum stresses from forces appearing at discrete

links of a triangular mesh, we need to compare the compressive energies. As *Brand* [2017] already described, the energy related with a line tension t at a link of length l is $E_t = 3/2 \cdot t \cdot l$, while the energy related with a surface tension σ at a triangle of surface area $A = \sqrt{3}/4 \cdot l^2$ yields $E_\sigma = \sqrt{3}/4 \cdot \sigma \cdot l^2$. Equating $E_t = E_\sigma$ results in the relation $\sigma = \sqrt{3} \cdot t/l$ between surface and line tension.
We furthermore use the so-called *discrete homogenization* method, as described in *Tollenaere and Caillerie* [1998] or *Caillerie et al.* [2006], in order to create a relation between the microscopic *spring constant* k and *viscosity* η_{mic} and macroscopic moduli E, η and the Poisson's ratio ν of the equivalent continuum material. For the calculation, we use the characteristic of the Maxwell model that the dynamics of springs and dashpots are independent of each other.
The reference cell of a triangular mesh consists of one node and three bars (see Figure 3.11). Since we only deal with a single node, the discrete homogenization calculation, if considering small displacements, reduces to the calculation of the 1st Piola-Kichhoff stress tensor directly from the reference configuration of the unit cell and the transformation to Euclidean coordinates. For unit cells containing more than one node, the calculation would become more calculated, as shown e.g. by *Mourad* [2003].
As in *Caillerie et al.* [2006], we start with defining the vectors which span the unit cell of a triangular mesh (see Figure 3.11):

$$\mathbf{y}_1 = l \cdot \begin{pmatrix} 1 \\ 0 \end{pmatrix}, \tag{3.49}$$

$$\mathbf{y}_2 = \frac{l}{2} \cdot \begin{pmatrix} 1 \\ \sqrt{3} \end{pmatrix}. \tag{3.50}$$

The reference configuration of a unit cell is then defined by

$$\mathbf{R}_R^0(\lambda_1, \lambda_2) = \lambda_1 \mathbf{y}_1 + \lambda_2 \mathbf{y}_2, \tag{3.51}$$

with the curvilinear coordinates $(\lambda_1, \lambda_2) \in \mathbb{R}^2$. The unit vectors of the three bars in a unit cell in the reference configuration are

$$\mathbf{e}_1^0 = \begin{pmatrix} 1 \\ 0 \end{pmatrix}, \tag{3.52}$$

$$\mathbf{e}_2^0 = \frac{1}{2} \cdot \begin{pmatrix} 1 \\ \sqrt{3} \end{pmatrix}, \tag{3.53}$$

$$\mathbf{e}_3^0 = \frac{1}{2} \cdot \begin{pmatrix} -1 \\ \sqrt{3} \end{pmatrix}, \tag{3.54}$$

with the bars numbered by $\mathcal{B}_R = \{1, 2, 3\}$ in clockwise direction (see Figure 3.11). We can write down the Jacobian $\mathbf{J}$ of the truss by computing

$$\mathbf{J} = \left[\frac{\partial \mathbf{R}^0}{\partial \lambda_1}, \frac{\partial \mathbf{R}^0}{\partial \lambda_2} \right](\lambda), \tag{3.55}$$

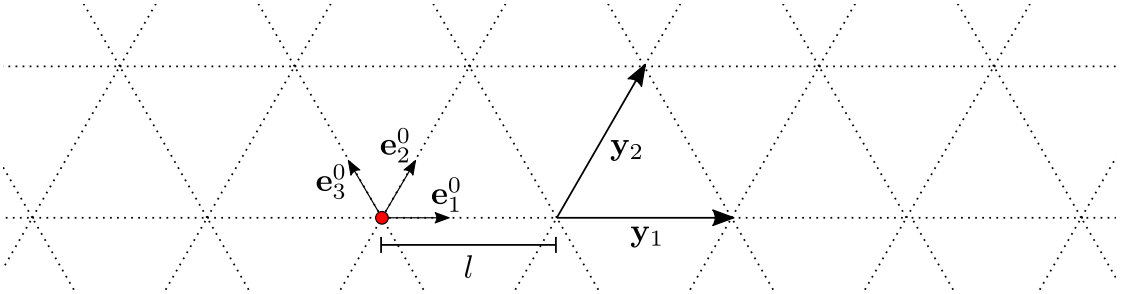

Figure 3.11: Discrete triangular mesh with a unit cell consisting of one node (*red*) and three bars of reference length l, which are represented by their unit vectors $\mathbf{e}_i^0$. The vectors $\mathbf{y}_1$ and $\mathbf{y}_2$ span the unit cell.

with $g = \det \mathbf{J}$ defining its determinant. Since we are assuming small deformations, the reference configuration stays approximately constant, yielding $\mathbf{R}^0 \approx \mathbf{R}_R^0$. Any strain defined in Euclidean coordinates can be transformed to the curvilinear coordinates via

$$\frac{\partial \mathbf{u}}{\partial \lambda} = \frac{\partial \mathbf{u}}{\partial \mathbf{x}} \cdot \mathbf{J} \,. \tag{3.56}$$

We can then calculate the internodal forces in the reference configuration via

$$N_b^0 = k \cdot \mathbf{e}_b^0 \cdot \frac{\partial \mathbf{u}}{\partial \lambda_i} \delta_{b,i} \tag{3.57}$$

with k being the stiffness of the microscopic link and $\delta_b = (\nu_1, \nu_2)^T \in \mathbb{N}^2$ indicating the node coordinate in which bar b ends, yielding

$$\delta_1 = \begin{pmatrix} 1 \\ 0 \end{pmatrix} , \tag{3.58}$$

$$\delta_2 = \begin{pmatrix} 0 \\ 1 \end{pmatrix} , \tag{3.59}$$

$$\delta_3 = \begin{pmatrix} -1 \\ 1 \end{pmatrix} . \tag{3.60}$$

The 1st Piola-Kichhoff stress tensor then yields

$$\mathbf{S}_i^0 = \sum_{b \in \mathcal{B}_R} N_b^0 \mathbf{e}_b^0 \delta_{b,i} \,, \tag{3.61}$$

which constitutes the Cauchy stress tensor σ via

$$\sigma = \frac{1}{g} \mathbf{S}^{i0} \otimes \frac{\partial \mathbf{R}^0}{\partial \lambda^i} \,. \tag{3.62}$$

This relation return a linear constitutive law between Cauchy stress and a particular

strain $\partial\mathbf{u}/\partial\mathbf{x}$. In the case of a triangular mesh, we get

$$\sigma = \frac{\sqrt{3}}{4} k \begin{pmatrix} 3 \cdot \frac{\partial u_x}{\partial x} + \frac{\partial u_y}{\partial y} & \frac{\partial u_x}{\partial y} + \frac{\partial u_y}{\partial x} \\ \frac{\partial u_x}{\partial y} + \frac{\partial u_y}{\partial x} & \frac{\partial u_x}{\partial x} + 3 \cdot \frac{\partial u_y}{\partial y} \end{pmatrix}, \tag{3.63}$$

if inserting Equations 3.51 and 3.61 into 3.62. The resulting Lamé coefficients are

$$\lambda = \frac{\sigma_{xx}}{\epsilon_{yy}} = \frac{\sqrt{3}}{4} k\,, \tag{3.64}$$

$$\mu = \frac{\sigma_{xy}}{\epsilon_{xy}} = \frac{\sqrt{3}}{4} k\,, \tag{3.65}$$

while the macroscopic constants of the continuum equivalent yield

$$E^{2\mathrm{D}} = \frac{4\mu\,(\lambda+\mu)}{\lambda+2\mu} = \frac{2\sqrt{3}}{3} k\,, \tag{3.66}$$

$$\nu^{2\mathrm{D}} = \frac{\lambda}{\lambda+2\mu} = \frac{1}{3}\,. \tag{3.67}$$

The same relation between microscopic and macroscopic parameters has also been calculated independently and using different techniques e.g. by *Boal* [2012] or *John et al.* [2013].

We can now introduce the resulting spring constants $k = \sqrt{3}/2h_\mathrm{c}E_\mathrm{c}$ in the discrete cable network, where $h_\mathrm{c} = 1\,\mu\mathrm{m}$ is the system height and E_c is the three-dimensional Young's modulus from the continuum model. Likewise, we evaluate $\eta_\mathrm{mic} = \sqrt{3}/2h_\mathrm{c}\eta_\mathrm{c}$ with the macroscopic viscosity η_c. We furthermore use a Nelder-Mead algorithm to fine tune the continuum model to the requirements of the discrete model [*Nelder and Mead*, 1965].

Figure 3.12E shows a comparison of the average material flow velocity in a region close to the activation region for the discrete and continuum model. In this example, the velocity calculated by means of the continuum model is a good approximation to those computed by means of the discrete model. Thus, using the scheme presented above, we can successfully map parameters between both models.

The graphs also show, especially during the relaxation phase, that the dynamics of both models can not be mapped completely. Here, the flow velocity during relaxation is about twice as large for the discrete compared to the continuum model. This can be explained by the Poisson effect, which is only present in the continuum model: In the continuum model, the material inflow during relaxation causes a perpendicular extension of the cell in order to preserve volume. This effect slows down the average flow velocity. In the discrete model, this mechanism does not show up due to the mechanical asymmetry of the cable links.

For the continuum model, we used the parameters listed in Table A.4. Details of the discrete cable model are described in *Brand* [2017].

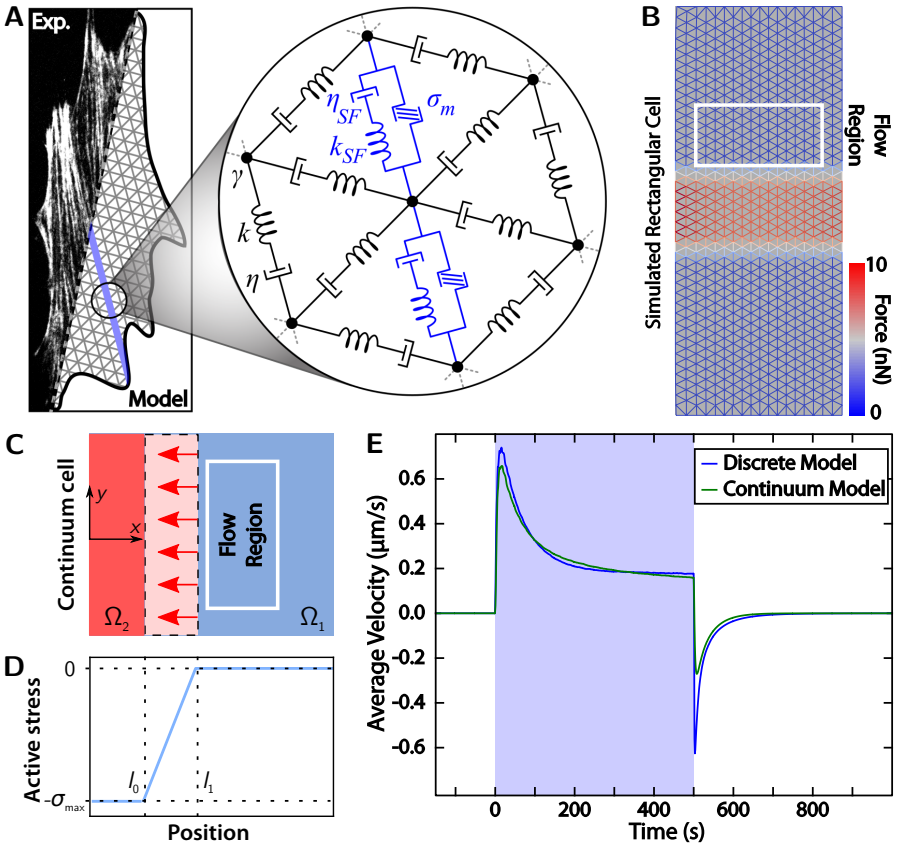

Figure 3.12: The dynamics of the introduced continuum model can be mapped to those of a discrete active viscoelastic cable network. **(A)** Representation of the actin cytoskeleton by a viscoelastic cable network. Stress fibers (*blue* symbols) are embedded as active viscoelastic cable elements into a passive network of Maxwell elements. **(B)** Rectangular model cell introduced to compare the viscoelastic flow in the cable network with the continuum model presented in **C**. The center of the rectangular cell is contractile. The averaged flow in the *white* box (termed *Flow Region*) is computed and mapped to the average flow in the continuum model. **(C)** In the continuum model, two modifications are accomplished in order to prevent from retracting forces: We simulate only half of a cell, i.e. with the activation region along the short side of the rectangle. Also, the continuum model is divided into a Maxwell fluid (*blue*) and a non-repelling Newtonian fluid (*red*). **(D)** For both models, the magnitude of the contractile stress is constant and non-zero inside activation region. Its absolute value decays linearly towards the non-activation regions. **(E)** Averaged flow velocity in the *Flow Region* for discrete and continuum model. Image adapted from *Oakes et al.* [2017].

3.6 Conclusion

This chapter showed that optogenetics can be used to locally and temporally affect the contractility of cells and, with this, help to determine mechanical properties of cells without using chemical drugs, genetic perturbations or severing experiments such as laser cutting.
We observed that a local activation of RhoA initiated an increase in actin concentration and myosin activity inside the activation region. This increase in local contractility induced a flow of actin and myosin towards the activation region and increased traction forces which propagated across the cell via SFs. Upon removal of the activating light, a flow of actin and myosin in the reverse direction was registered, resembling an elastic relaxation.
Measured global traction stresses and flows in the actin CSK allowed both to determine and constrain a one-dimensional viscoelastic continuum model of Maxwell type. The model not only allowed to explain the observed stress increase and elastic-like relaxation of SFs, but also helped to identify the protein zyxin as a key regulator of the elasticity of SFs. For wild-type cells, SFs were found to behave elastic-like on time scales smaller than tens of minutes, and fluid-like on time scales larger than tens of minutes. Without zyxin, the elasticity of cells vanishes and the fluidity increases.
The discrete homogenization technique was applied to find a relation between the introduced continuum model and a detailed cable Maxwell model introduced by *Brand* [2017]. We found a good correspondence in the flow dynamics between both models for an exemplar cell and were able to robustly map parameters between both models. However, the lack of pushing forces in the cable model lead to a slightly divergent behavior implying that, ideally, an equivalent continuum model has to be engineered from a separate analysis of the activated and relaxing cable network.
As compared to laser cutting experiments, such as those performed by *Colombelli et al.* [2009], the optogenetic method does not exploit the collapse of a SF, but effectively elevates the actin concentration and myosin activity, thus allowing to analyze the SF response to elevated tension over tens of minutes. Experiments conducted by *Colombelli et al.* [2009] probed the response to catastrophic damage resulting in large contractile strains over seconds. Here, we probed the response to a small perturbation in tension, resulting in smaller strains over tens of minutes. This explains the different modeling approach used to explain both experiments.

4 Influence of Cell Area and Actin Polarity on Cellular Contractility

Cellular contractility is not only determined by biochemical but also by physical cues of the cellular environment. In particular, cells tend to align their actin cytoskeleton (CSK) with respect to the shape of the adhesive environment to facilitate environmental sensing or protection from external forces [*Blanchoin et al.*, 2014]. The structure of the CSK is then a predominant determinant of the distribution of cellular traction stresses [*Schwarz and Safran*, 2013; *Scheiwe et al.*, 2015]. It is therefore essential to incorporate structural information of the cytoskeleton in the calculation of traction stresses to achieve both a better estimation of cellular stresses as compared to standard error-prone techniques, such as TFM, and a quantification of the internal stresses inside a cell.
For example, *Soiné et al.* [2015] introduced a technique which combines image analysis and biophysical modeling to allow for both a robust measurement of traction stresses, independent of sophisticated regularization algorithms, and the inference of the distribution of internal stresses inside the cell. For this, they adopted the discrete cable model established by *Torres* [2012] to be able to incorporate discrete force-generating elements, such as single SFs, into a distributed background actin mesh.
Another example is the model of *Deshpande et al.* [2006, 2007] which yields a dynamical modeling approach based on a continuum description of the cytoskeleton. Deshpande and colleagues model the adaptation of cells to the extracellular environment via a combined chemo-mechanical simulation of the molecular force-generating mechanisms. This enables the prediction of the distribution of internal stresses for a wide range of experiments. However, the model is in general highly non-linear, making the stability of the system dependent on the choice of parameters. Also, although their model is very detailed compared to other prominent methods, essential cytoskeletal phenotypes, like the crossing of stress fibers, cannot be represented appropriately due to the deficient averaging scheme [*Schwarz and Safran*, 2013].
In this chapter, we will approach the ansatz of *Soiné et al.* [2015] from the perspective of a continuum model by introducing anisotropy in the continuum model presented so far. We will use the model to investigate the influence of the cell area, the structure of the FN pattern and the duration of force regulation on the dynamic evolution of the contractile energy a cell invests and deduce the internal stresses inside the cell. Furthermore, we will show use TFM and FE simulations to demonstrate that cellular stresses indeed depend on the internal alignment of the cytoskeleton and not e.g. on contour of the cell as e.g. proposed by *Oakes et al.* [2014].
Our findings are supported by the quantification of cellular forces induced by means of optogenetic regulation via the CRY2/CIBN dimerizer system, which has been introduced

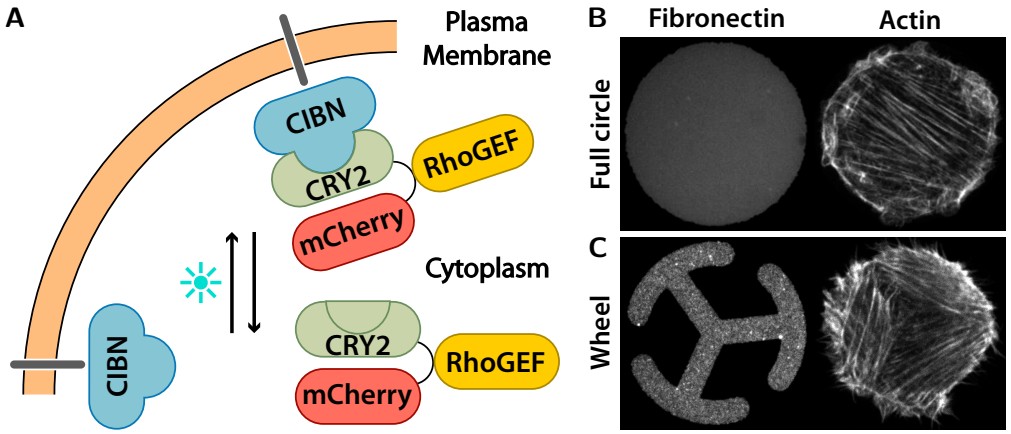

Figure 4.1: Optogenetic control of RhoA via the CRY2/CIBN dimerizer system and experimental setup to analyze the combined effect of the fibronectin coating and photoactivation on the arrangement of the actin cytoskeleton. **(A)** CIBN molecules are anchored to the plasma membrane and photorecruitable CRY2 molecules are distributed throughout the cytosol. Upon stimulation with blue light, CRY2, i.e. the *free* molecule, undergoes a conformational change, as opposed to the setup presented in Figure 3.1A. This reaction allows the recruitment of the attached RhoGEF to the plasma membrane, where it can activate RhoA. Removal of the activating light leads to a refolding of the CRY2 molecule and stops further recruitment of GEF to the membrane. **(B)** *Full circle* fibronectin pattern (*left*) and corresponding characteristic actin polarization after cell spreading (*right*). **(C)** *Wheel* fibronectin pattern (*left*) and corresponding characteristic actin polarization after cell spreading (*right*). Panels **B** and **C** by courtesy of Tomas Andersen, Université Grenoble Alpes.

by *Kennedy et al.* [2010] and established by *Valon et al.* [2017] to accomplish the regulation of cellular contractility. Both TFM and FE simulations help to predict a maximal photoactivation (PA) time above which the cellular stress response upon PA of the CRY2/CIBN-system saturates.

Identically to Chapter 3, we will find that both the time course of the chemical signal leading to the stress-generating mechanism and the viscosity of the system generates the characteristic energy response of the cells upon PA. However, the global optogenetic regulation will yield an effect which can be attributed rather to those of a viscoelastic solid than a viscoelastic fluid, which is in contrast to in Chapter 3.

The results presented in the following originate from a collaborative work together with Tomas Andersen and Martial Balland from the Université Grenoble Alpes, who conducted the optogenetic experiments.

4.1 Experimental Setup and Optogenetic Activation Protocol

We used the optogenetic setup introduced by *Kennedy et al.* [2010], who pioneered in the adaptation of the CRY2/CIB1 dimerizer system to regulate protein-protein interactions by means of photoactivation (PA). The CRY2/CIBN system, in which CIBN is a truncated version of CIB1, was then later elaborated by *Valon et al.* [2015] to allow for the optogenetic regulation of components of the actin CSK. The optogenetic system consists of two protein complexes that are channeled into the cell: a CIBN-GFP-CAAX-protein (or CIBN) anchored to the plasma membrane and CRY2PHR-mCherry (or CRY2) which is distributed throughout the cytosol.
Upon illumination of blue light, CRY2, i.e. the movable protein (which is in contrast to Chapter 3), undergoes a conformational change which allows for the association with CIBN molecules attached to the plasma membrane (see Figure 4.1A). The following steps are, in general, identical to Chapter 3: At the plasma membrane, a GEF, which is part of the CRY2 protein construct, triggers the phosphorylation of the inactive RhoA-GDP, which is particularly located in the immediate vicinity of the membrane. This boosts the concentration of active RhoA molecules which themselves prompt an increase of the concentration of actin and the activity of myosin in the illuminated region (see schematic in Figure 1.3E). When removing the activating light, the CRY2 molecules dissociate from the membrane-attached CIBN molecules and distribute again throughout the cytosol followed by a dispersal of the regions of increased actin and myosin II.
In contrast to Chapter 3, the PA protocol is modified on two counts: First, cells are illuminated globally in order to measure the effect of an overall increase of actin concentration and myosin activity on the total contractile energy invested by a cell. At this, different Fibronectin (FN) micropatterns are used, aiming at controlling the area and the contour of the adhering cell. This allows to investigate the contribution of the internal structure of the actin CSK to the cellular contractile energy under normalized experimental conditions (see Figures 1.6, 4.1B and C).
Second, the temporal illumination pattern distinctly differs from those used in Chapter 3. As before, cells are first left untouched for several hours to relax completely to a constant energy level. After that, cells are activated via single short photoactivation (PA) pulses of increasing duration in the range of $10 - 200\,\mathrm{ms}$ with an inter-pulse distance of $10 - 15\,\mathrm{min}$ between each pulse and, giving the cells enough time to relax to their baseline energy level.

4.2 Quantification of Traction Stresses Induced by Micropatterns and Optogenetics

In the following, we determined the effect of a global activation of RhoA on the overall contractility of the cells. For this, cells were plated on FN patterns of circular contour and circle area of $1000\,\mu\mathrm{m}^2$, on top of a PAA gel of Young's modulus $E_\mathrm{s} = 4.47\,\mathrm{kPa}$ and Poisson's ratio $\nu_\mathrm{s} = 0.5$. Contractile stresses were then quantified by means of FTTC, as

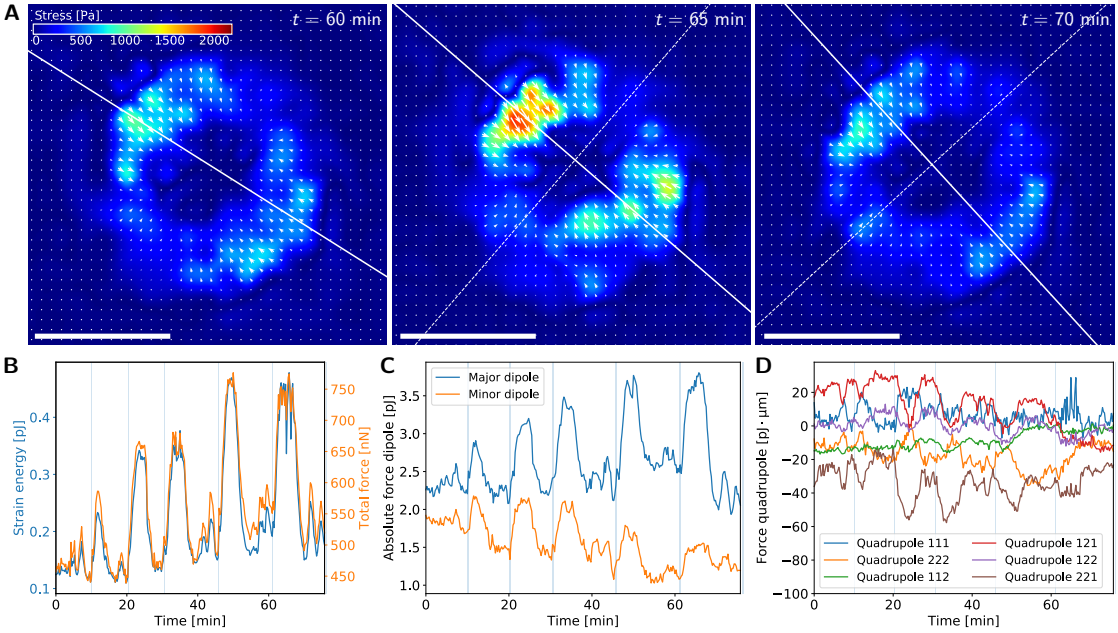

Figure 4.2: Global activation of RhoA leads to globally increased traction stresses in cells attached to a circular fibronectin pattern. **(A)** Exemplary time sequence of traction stresses during local RhoA activation and relaxation. Force dipole axes are depicted as *white lines*, of which *full lines* represent the dominant dipole axis. Scale bars are 25 μm. **(B)** Temporal evolution of the cellular strain energy and total force. Activation periods are depicted as *light blue lines*. **(C)** Temporal evolution of the major and minor force dipole moments of the cell. **(D)** Temporal evolution of the cellular force quadrupole moments w.r.t. the major dipole axis.

described earlier in Chapter 2.

Figures 4.2 and 4.3 illustrate representative traction stress patterns exerted by cells placed on the FN patterns shown in Figure 4.1B and C, respectively. We will, in the following, refer to the FN pattern in Figure 4.1B as *full circle pattern* and to the FN pattern in Figure 4.1C as *wheel pattern*.

In both cases, we can clearly observe that the global activation of RhoA elicits a temporally delayed global increase of traction stresses, in particular in the periphery of the cells. The energy and force levels reach a short-termed plateau about 2 min after the activating pulse. Afterwards, both levels decay to the original baseline within a time scale of minutes, entailing a symmetric response to a single PA (see Figures 4.2B and 4.3B). Compared to the contractile energy of the circle-patterned cell, the energy increase in wheel-patterned cells upon a single PA is lower by about 40 %.

Figures 4.2A and 4.3A further reveal that the resulting traction patterns are anisotropic, suggesting the contribution of the intracellular organization of the actin CSK as a response to the differing FN pattern shapes. This anisotropy is also reflected in the time course of the dipole and quadrupole moments depicted in Figures 4.2C-D and 4.3C-D, respectively

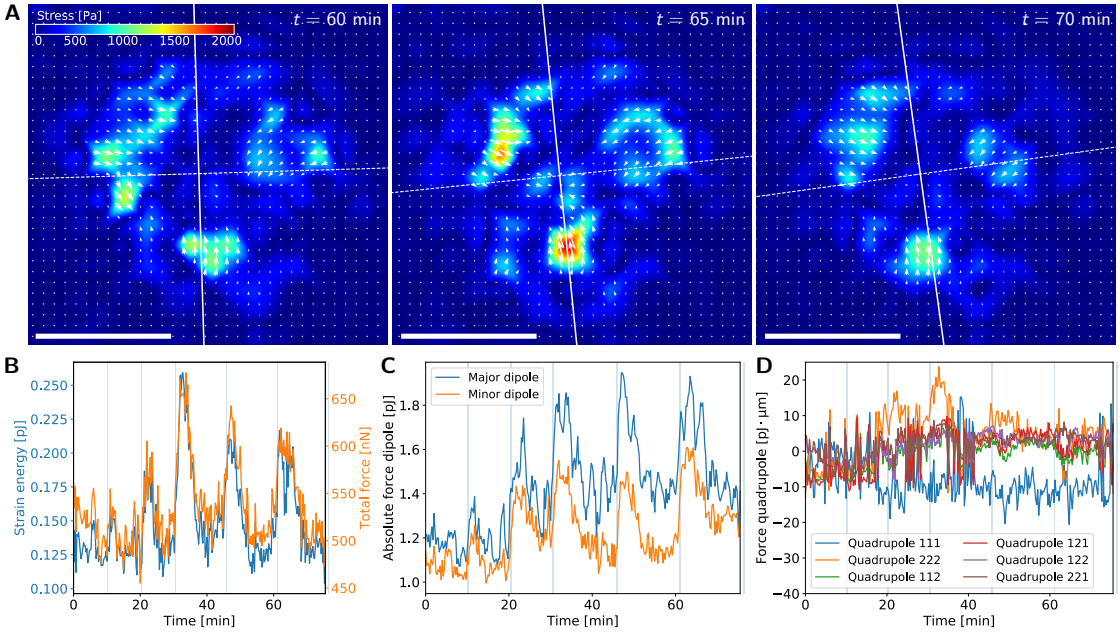

Figure 4.3: Global activation of RhoA leads to globally increased traction stresses for cells attached to the wheel fibronectin pattern. In contrast to Figure 4.2, stresses become more localized. **(A)** Exemplary time sequence of traction stresses during local RhoA activation and relaxation. Force dipole axes are depicted as *white lines*, of which *full lines* represent the dominant dipole axis. Scale bars are 25 μm. **(B)** Temporal evolution of the cellular strain energy and total force. Activation periods are depicted as *light blue lines*. **(C)** Temporal evolution of the major and minor force dipole moments of the cell. **(D)** Temporal evolution of the cellular force quadrupole moments w.r.t. the major dipole axis.

for the two FN patterns.

For the full circle pattern (FCP), we make out the formation of a clear major dipole, which is even amplified with progressing experimental time. The predominance of the quadrupole moment Q_{121} in the absence of PA reflects that the cell entails a stronger contraction in the half space right of the major dipole as compared to the left half space. Upon PA, this asymmetry vanishes. Furthermore, the quadrupole moment Q_{111} is positive and increases right after the PA, implying that a considerable amount of stresses points in the direction parallel to the major dipole axis. On the contrary, Q_{221} is negative and subject to decreasing jumps after the PA, which reveals that the traction pattern entails an asymmetry in favor of the direction antiparallel to the major dipole axis.

For the wheel pattern (WP), the force dipole ratio is much smaller, due to the asymmetric arrangement of the three traction stress accumulations, each of which is separated by an angle of about 120 ° with respect to the center of the circle. Here, the quadrupole moment Q_{222} dominates, indicating a considerable amount of traction stresses pointing perpendicular to the major dipole axis. This is even more confirmed by the predominant negativity of Q_{111}.

4.3 Simulation of the Cellular Contractile Energy

We can adapt the continuum model introduced in the previous chapter to capture the contractile dynamics of cells presented in Section 4.2 and extract mechanical properties from the data. In the following, we will start with a mathematical description of the model, which aims at reproducing the contractile behavior of the two representative cells presented in Figure 4.1B and C. In particular, we will introduce an anisotropic stress tensor to mimic the distribution of SFs on the different FN patterns and incorporate the geometry of the FN pattern into the simulation. Thereafter, we will use the time course of the cellular strain energy to constrain the continuum model. We conclude this section with the comparison of experimental and simulation results and the insights we gain from the model parameters.

4.3.1 Two-Dimensional Active Solid and Viscoelastic Models

From the experimental results presented so far, we obtain two indications which allow to find and constrain a physical model. First, we know from the analysis of time-lapse video of the actin-stained cells that the actin architecture is in a steady state and not affected by short PA pulses. Second, the strain energy response upon a single PA pulse shows a rounded off symmetric profile which, after some time span, returns back to the equilibrium energy state the cell adopted before stimulation.
The following one- or two-component rheological models come into question to fulfill the experimental requirements: a solid, a Kelvin-Voigt or a Maxwell model (see Figure 1.9). A pure viscous model is excluded right from the beginning as it will not allow to abide a steady energy state, even in the absence of a PA signal.
We start with the constitutive relation of the two-dimensional active solid model

$$\sigma_{ij} - \sigma_{ij}^{\mathrm{m}} = \lambda \epsilon_{kk} \delta_{ij} + 2\mu \epsilon_{ij} \,, \tag{4.1}$$

with stress tensor σ_{ij}, linearized strain tensor $\epsilon_{ij} = 1/2\,(\partial_i u_j + \partial_j u_i)$ and i^{th} component of the displacement vector u_i. Further, λ and μ denote the two-dimensional Lamé coefficients defined in Equations 3.36 and 3.37, respectively. σ^{m} denotes the anisotropic motors stress, which consists of two contributions: a constant background stress tensor, which is used to raise the cellular energy to its homeostatic level, and a PA stress tensor, describing the additional time-dependent stress during PA.
The constitutive relations of the active Kelvin-Voigt model and active Maxwell model are, respectively,

$$\sigma_{ij} - \sigma_{ij}^{\mathrm{m}} = \left(1 + \tau_{\mathrm{c}} \frac{\partial}{\partial t}\right) \cdot \left(\lambda \epsilon_{kk} \delta_{ij} + 2\mu \epsilon_{ij}\right) \,, \tag{4.2}$$

and

$$\frac{\sigma_{ij} - \sigma_{ij}^{\mathrm{m}}}{\tau_{\mathrm{c}}} + \left(\dot{\sigma}_{ij} - \dot{\sigma}_{ij}^{\mathrm{m}}\right) = \frac{\partial}{\partial t} \left(\lambda \epsilon_{kk} \delta_{ij} + 2\mu \epsilon_{ij}\right) \,, \tag{4.3}$$

with $\tau_{\mathrm{c}} = \eta_{\mathrm{c}}/E_{\mathrm{c}}$ and η_{c} being the material relaxation time and cell viscosity, respectively.

For all models, the force balance equation yields

$$\partial_j \sigma_{ij} = Y(\mathbf{x})\, u_i \,, \tag{4.4}$$

with Y denoting the spring stiffness density, which can be position-dependent in general. We can calculate Y using the force penetration length l_p introduced in Equation 3.15, which represents the length scale along which a point force is transmitted in an elastically coupled isotropic medium, via

$$Y = \frac{E_\mathrm{c} h_\mathrm{c}}{l_\mathrm{p}^2 \left(1 - \nu_\mathrm{c}^2\right)} \,. \tag{4.5}$$

All three models can be solved by means of a FE simulation. In each case, the weak formulation of Equation 4.4 is

$$\int_\Omega \boldsymbol{\sigma} : \left(\nabla \mathbf{v} + \nabla \mathbf{v}^\mathbf{T}\right) \mathrm{d}\mathbf{x} + \int_\Omega Y\, \mathbf{u}\mathbf{v}\, \mathrm{d}\mathbf{x} = 0 \,, \tag{4.6}$$

with Ω denoting the area of the viscoelastic disc and $\mathbf{v}$ a test function. We use the FE solver FEniCS to calculate the displacements of the disc [*Alnæs et al.*, 2015]. For reasons of stability, we apply the Dirichlet boundary condition $\mathbf{u} = (0, 0)$ at $\mathbf{x} = (0, 0)$. The strain energy U_s invested by the cell is then calculated from the substrate displacements $\mathbf{u}_\mathrm{s}$ and traction stresses $\mathbf{T} = Y\mathbf{u} = Y_\mathrm{s}\mathbf{u}_\mathrm{s}$ via

$$U_\mathrm{s} = \frac{1}{2} \int_A \mathbf{T}\mathbf{u}_\mathrm{s} \mathrm{d}A = \frac{1}{2} \int_A \frac{Y^2}{Y_\mathrm{s}}\, \mathbf{u}^2 \mathrm{d}A \,. \tag{4.7}$$

Here, Y_s denotes the contribution of the substrate properties to Y. We can use Equation 3.30 to estimate Y_s via

$$Y_\mathrm{s} = \frac{\pi E_\mathrm{s}}{h_\mathrm{eff}} \,, \tag{4.8}$$

with h_eff defined in Equation 3.31. With $E_\mathrm{s} = 4.47 \times 10^3\ ^N/_{\mathrm{m}^2}$, $h_\mathrm{s} = 50\,\mu\mathrm{m}$ and $L_\mathrm{s} \approx 40\,\mu\mathrm{m}$, we have approximately $Y_\mathrm{s} = 3.1 \times 10^8\ ^N/_{\mathrm{m}^3}$.
We can exploit the relation of the strain energy and the cell area to find a way to directly estimate l_p from the measurements. Assuming that the elastic disc of radius r_0 is approximately isotropically contractile, we can solve Equation 4.7 analytically. The radial displacement u_r for this special case yields [*Edwards and Schwarz*, 2011]

$$u_r(r) = -l_\mathrm{p} \frac{\sigma_0 h_\mathrm{c}}{\lambda + 2\mu} \cdot \frac{I_1\left(\frac{r}{l_\mathrm{p}}\right)}{I_0\left(\frac{r_0}{l_\mathrm{p}}\right) - \frac{2\mu}{\lambda+2\mu} \frac{l_\mathrm{p}}{r_0} I_1\left(\frac{r_0}{l_\mathrm{p}}\right)} \,, \tag{4.9}$$

with contractile stress σ_0, disc height h_c and modified Bessel functions of first kind I_0

and I_1. The strain energy then reduces to the integral

$$U_\mathrm{s} = \frac{Y^2}{2Y_\mathrm{s}} \int_0^{2\pi} \mathrm{d}\phi \int_0^{r_0} \mathrm{d}r r u_r^2$$
$$= \frac{\pi}{Y_\mathrm{s}} \cdot \left(\frac{Y l_\mathrm{p} \sigma_0 h_\mathrm{c} \left(1-\nu_\mathrm{c}^2\right)}{E_\mathrm{c} h_\mathrm{c}} \right)^2 \cdot \frac{\int_0^{r_0} \mathrm{d}r r I_1 \left(\frac{r}{l_\mathrm{p}}\right)^2}{\left(I_0\left(\frac{r_0}{l_\mathrm{p}}\right) - (1-\nu_\mathrm{c}) \frac{l_\mathrm{p}}{r_0} I_1\left(\frac{r_0}{l_\mathrm{p}}\right)\right)^2} = \frac{\pi \left(\sigma_0 h_\mathrm{c}\right)^2}{2Y_\mathrm{s}} \zeta\left(\frac{r_0}{l_\mathrm{p}}\right), \tag{4.10}$$

using the definition of Y in Equation 4.5 and

$$\zeta(x) = x^2 \cdot \frac{I_1(x)^2 + \frac{2}{x} I_0(x) I_1(x) - I_0(x)^2}{\left(I_0(x) - (1-\nu_\mathrm{c}) \frac{1}{x} I_1(x)\right)^2}. \tag{4.11}$$

We can find the two asymptotic trends of the energy by investigating ζ for the two limits $x \ll 1$ and $x \gg 1$. For $x \ll 1$, the modified Bessel functions can be approximated as

$$I_n(x) \xrightarrow[x \ll 1]{} \frac{1}{n!} \left(\frac{x}{2}\right)^n, \tag{4.12}$$

such that

$$\zeta(x) \xrightarrow[x \ll 1]{} \frac{x^4}{2\left(1+\nu_\mathrm{c}\right)^2} + \mathcal{O}\left(x^5\right), \tag{4.13}$$

and

$$U_\mathrm{s} \xrightarrow[r_0 \ll l_\mathrm{p}]{} \frac{\pi \left(\sigma_0 h_\mathrm{c}\right)^2}{4Y_\mathrm{s}\left(1+\nu_\mathrm{c}\right)^2} \left(\frac{r_0}{l_\mathrm{p}}\right)^4. \tag{4.14}$$

For $x \gg 1$, any modified Bessel function converges to

$$I_n(x) \xrightarrow[x \gg 1]{} \frac{\exp x}{\sqrt{2\pi x}}, \tag{4.15}$$

such that

$$\zeta(x) \xrightarrow[x \gg 1]{} 2x + \mathcal{O}\left(x^2\right), \tag{4.16}$$

and

$$U_\mathrm{s} \xrightarrow[r_0 \gg l_\mathrm{p}]{} \frac{\pi \left(\sigma_0 h_\mathrm{c}\right)^2}{Y_\mathrm{s}} \cdot \frac{r_0}{l_\mathrm{p}}. \tag{4.17}$$

Thus, the asymptotic behavior of the strain energy for $r_0 \gg l_\mathrm{p}$ is analogous to those of the total force, of which the latter was demonstrated by *Mertz et al.* [2012]. We will see in Chapter 5 that for $r_0 \ll l_\mathrm{p}$, the asymptotic behavior of the strain energy and the total force differ. Equation 4.10 will be used in the next Subsection 4.3.4 to estimate the parameters l_p and $\sigma_\mathrm{bck} h_\mathrm{c}$ from the relation of the cellular strain energy and its spread area.

4.3.2 Specification of the Photoactivation Stress Tensor

Both background stress tensor and the PA stress tensor depend on the shape of the FN pattern. Even in the absence of a PA, the orientation of the stress field remains unchanged, as Figures 4.2A and 4.3A point up, such that the background stress tensor can be assumed to pull in the same direction as the PA stress. We can calculate the anisotropic motor stress tensor σ^{m} directed along an arbitrary angle ϕ with respect to the x-axis via rotation of a stress tensor with its only non-zero component $\sigma_{xx} = \sigma_{\mathrm{bck}} + \sigma_{\mathrm{act}}(t)$. Here, σ_{bck} belongs to the background stress and σ_{act} to the time-dependent PA stress. One has

$$\begin{aligned}\sigma^{\mathrm{m}}(\phi) &= \begin{pmatrix}\cos\phi & -\sin\phi\\ \sin\phi & \cos\phi\end{pmatrix}\begin{pmatrix}\sigma_{\mathrm{bck}}+\sigma_{\mathrm{act}} & 0\\ 0 & 0\end{pmatrix}\begin{pmatrix}\cos\phi & \sin\phi\\ -\sin\phi & \cos\phi\end{pmatrix}\\ &= (\sigma_{\mathrm{bck}}+\sigma_{\mathrm{act}})\cdot\begin{pmatrix}\cos^2\phi & \frac{1}{2}\sin(2\phi)\\ \frac{1}{2}\sin(2\phi) & \sin^2\phi\end{pmatrix},\end{aligned} \tag{4.18}$$

Comparison with the orientation of SFs in Figure 4.1B and C lets us assume a motor stress tensor

$$\sigma^{\mathrm{m}}_{\mathrm{FC}} = \begin{pmatrix}0 & 0\\ 0 & \sigma_{\mathrm{bck}}+\sigma_{\mathrm{act}}\end{pmatrix} \tag{4.19}$$

in the case of the full circle pattern, as illustrated in Figure 4.5B (top), and

$$\sigma^{\mathrm{m}}_{\Omega 1} = (\sigma_{\mathrm{bck}}+\sigma_{\mathrm{act}})\cdot\begin{pmatrix}1 & 0\\ 0 & 0\end{pmatrix}, \tag{4.20}$$

$$\sigma^{\mathrm{m}}_{\Omega 2} = (\sigma_{\mathrm{bck}}+\sigma_{\mathrm{act}})\cdot\begin{pmatrix}\cos^2\left(\frac{2\pi}{3}\right) & \frac{1}{2}\sin\left(\frac{4\pi}{3}\right)\\ \frac{1}{2}\sin\left(\frac{4\pi}{3}\right) & \sin^2\left(\frac{2\pi}{3}\right)\end{pmatrix},$$

$$\sigma^{\mathrm{m}}_{\Omega 3} = (\sigma_{\mathrm{bck}}+\sigma_{\mathrm{act}})\cdot\begin{pmatrix}\cos^2\left(\frac{2\pi}{3}\right) & -\frac{1}{2}\sin\left(\frac{4\pi}{3}\right)\\ -\frac{1}{2}\sin\left(\frac{4\pi}{3}\right) & \sin^2\left(\frac{2\pi}{3}\right)\end{pmatrix},$$

for the respective regions Ω_1, Ω_2 and Ω_3 denoted in Figure 4.5C (top) in the case of the wheel pattern.
We consider three possible models for the time course of the PA stress component σ_{act}, which are depicted in Figure 4.4A from left to right. The simplest case is the rectangular profile

$$\sigma^{\mathrm{rec}}_{\mathrm{act}}(t) = \begin{cases}\sigma_0 & \text{for } t_0 \le t \le t_{\mathrm{act}}\\ 0 & \text{else}\end{cases}, \tag{4.21}$$

with peak activation stress σ_0, PA time point t_0 and duration t_{act}. To account for a delayed response of the activation stress, we introduce the exponential profile

$$\sigma^{\mathrm{exp}}_{\mathrm{act}}(t) = \begin{cases}\sigma_0\left(1-\exp\left(-\frac{t-t_0}{\tau_{\mathrm{act}}}\right)\right) & \text{for } t_0 \le t \le t_{\mathrm{act}}\\ \sigma_0\left(1-\exp\left(-\frac{t_{\mathrm{act}}-t_0}{\tau_{\mathrm{act}}}\right)\right)\exp\left(-\frac{t-(t_0+t_{\mathrm{act}})}{\tau_{\mathrm{rel}}}\right) & \text{else}\end{cases}, \tag{4.22}$$

with stress activation and relaxation times τ_{act} and τ_{rel}. The third stress profile is a

double sigmoid function

$$\sigma_{\text{act}}^{\text{sig}}(t) = \frac{\sigma_0}{1+\exp\left(-\frac{t-t_{\text{act}}}{\tau_{\text{act}}}\right)} \cdot \left(1 - \frac{1}{1+\exp\left(-\frac{t-t_{\text{rel}}}{\tau_{\text{rel}}}\right)}\right), \tag{4.23}$$

with the centers of the activating and relaxing sigmoid t_{act} and t_{rel}. Here, the four time time constants allow to combine a discontinuous jump at the ascending edge of the PA stress function and a flat stress plateau, as with the rectangular stress profile, with a damped activation and relaxation, as with the exponential stress profile.

4.3.3 Specification of the Shape of the Fibronectin Pattern

For the case of the full circle pattern, we represent the effect of the elastic substrate as well as the elastic contribution of the FAs via springs of constant spring stiffness density Y throughout the entire circle.
For the wheel pattern, we only introduce springs of stiffness density Y at those positions of the circle at which the cell can form connections to the substrate via its FAs, which is exactly the FN coated area. To simulate this fact, we determine the positions $(x,y)_{Y\neq 0}$, at which the stiffness density Y is non-zero, via:

$$\begin{aligned}(x,y)_{Y\neq 0} = \Big\{ x,y \,\Big|\, & \Big[R_{\text{in}} \leq \sqrt{x^2+y^2} \leq R \wedge \Big(\frac{\pi}{2} - \frac{\alpha_{\text{out}}}{2} \leq \arctan2(x,y) \leq \frac{\pi}{2} + \frac{\alpha_{\text{out}}}{2} \\ & \qquad \vee\ -\frac{\pi}{6} - \frac{\alpha_{\text{out}}}{2} \leq \arctan2(x,y) \leq -\frac{\pi}{6} + \frac{\alpha_{\text{out}}}{2} \\ & \qquad \vee\ -\frac{5\pi}{6} - \frac{\alpha_{\text{out}}}{2} \leq \arctan2(x,y) \leq -\frac{5\pi}{6} + \frac{\alpha_{\text{out}}}{2} \\ & \qquad \vee\ \pi - \alpha_{\text{overhang}} \leq \arctan2(x,y) \leq \pi\Big)\Big] \vee \\ & \Big[\sqrt{x^2+y^2} \leq R_{\text{in}} \wedge \Big(\Big(-\frac{w}{2} \leq x_1 \leq \frac{w}{2} \wedge y_1 \geq 0\Big) \\ & \qquad \vee \Big(-\frac{w}{2} \leq x_2 \leq \frac{w}{2} \wedge y_2 \geq 0\Big) \\ & \qquad \vee \Big(-\frac{w}{2} \leq x_3 \leq \frac{w}{2} \wedge y_3 \geq 0\Big)\Big)\Big] \Big\},\end{aligned}$$

with arm width $w = 5\,\mu\text{m}$, inner radius $R_{\text{in}} = R - w$ and $\alpha_{\text{out}} = \pi/2$. The remaining parameters are

$$\begin{aligned}(x_1,y_1) &= (x,\, y) \\ (x_2,y_2) &= \left(x\cdot\cos\left(\frac{2\pi}{3}\right) - y\cdot\sin\left(\frac{2\pi}{3}\right),\, x\cdot\sin\left(\frac{2\pi}{3}\right) + y\cdot\cos\left(\frac{2\pi}{3}\right)\right) \\ (x_3,y_3) &= \left(x\cdot\cos\left(\frac{2\pi}{3}\right) + y\cdot\sin\left(\frac{2\pi}{3}\right),\, -x\cdot\sin\left(\frac{2\pi}{3}\right) + y\cdot\cos\left(\frac{2\pi}{3}\right)\right),\end{aligned}$$

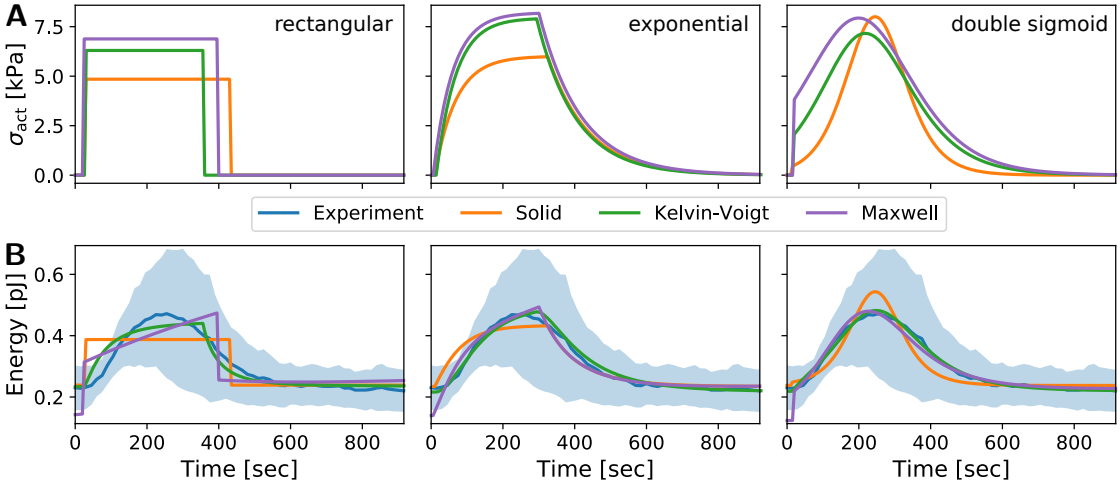

Figure 4.4: Photoactivation stress profile σ_{act} and the corresponding energy response for the case of a solid, Kelvin-Voigt and Maxwell model. **(A)** Photoactivation stress profiles σ_{act} used to reproduce the experimentally acquired cellular energy response: rectangular, exponential and double sigmoid profile from left to right. Different curves illustrate the optimized stress profiles for the three models. **(B)** Corresponding energy responses for the three different stress profiles and continuum models, illustrated on top of the experimental average. *Shaded regions* denote the standard deviation. A Kelvin-Voigt model with a double sigmoid stress profile fits best to the experimental curve. Corresponding parameter values are listed in Table A.5.

and

$$\alpha_{\text{overhang}} = \frac{5\pi}{6} + \frac{\alpha_{\text{out}}}{2} - \pi \text{ if } \frac{5\pi}{6} + \frac{\alpha_{\text{out}}}{2} > \pi, \text{ otherwise } 0\,. \tag{4.24}$$

Equation 4.24 accounts for the unsteady jump of the arctan2-function at the function values $-\pi$ and π.

4.3.4 Simulation Results

We will now start with the selection of an appropriate physical model which allows to capture the dynamics of the cellular energy. Thereafter, we will investigate the effects of the cell area, the shape of the FN pattern or the duration of the PA pulse on the cellular energy level and dynamics. To find the best model fits, we use the conjugate-gradient based parameter optimization method of *Nelder and Mead* [1965].

Model Choice Figure 4.4A shows the optimized PA stress profiles introduced in Section 4.3.2 to reproduce the experimentally acquired cellular strain energy response. The corresponding average experimental energy response and the simulated energy response for the three continuum models upon a single PA pulse of 50 ms duration are illustrated in Figure 4.4B.
A rectangular PA stress profile does not provide an adequate description of the cellular

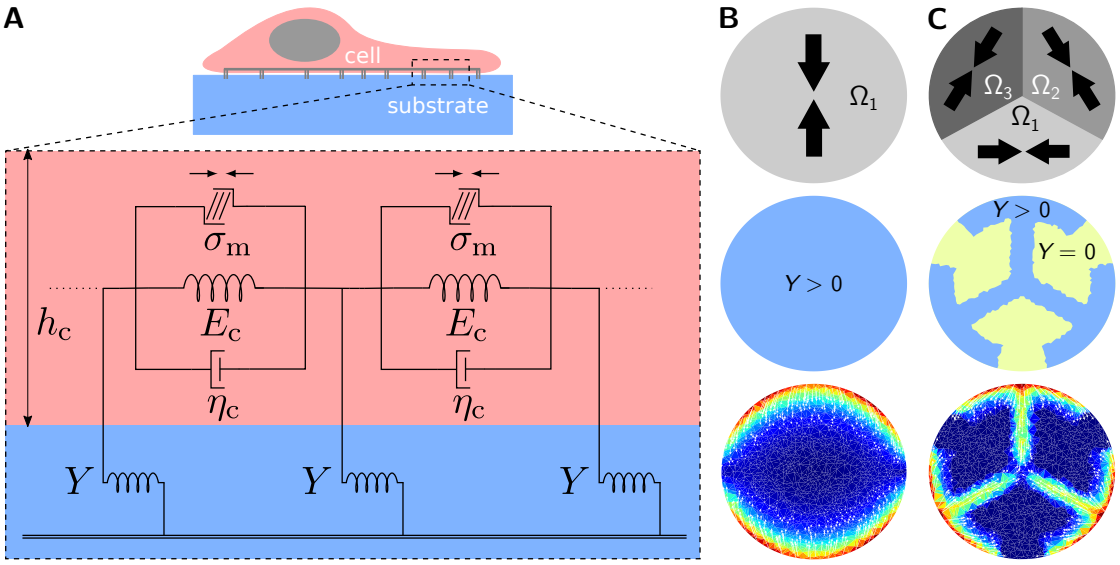

Figure 4.5: Effective physical representation of the cell and the elastic substrate on different fibronectin patterns and qualitative distribution of simulated traction stresses. **(A)** A Kelvin-Voigt model with active contractility and coupling to an elastic foundation is used to reconstruct the dynamic energy response of cells upon global optogenetic activation (*side view*). **(B-C)** From top to bottom: Principal directions of the stress tensor, distribution of the spring stiffness and a typical qualitative stress map during the simulated photoactivation of circle-patterned and wheel-patterned cells, respectively (*top view*).

dynamics as it introduces discontinuous features in the energy response which are not present in the experimental data. An exponential PA stress profile allows better fits to the experimental data, but can only establish an asymmetric energy response upon PA. The double sigmoid PA stress profile most likely resembles the predominant features of the experimental data.

For the solid model, the double sigmoid fit is inadequate since the stress profile entail a convex course almost over its full range. Due to the model dynamics, the energy profile instantaneously follows the stress profile. The experimental energy profile, however, comprises a lengthy concave course around its peak.

The Maxwell model with double sigmoid PA stress profile can closely capture the dynamics of the cellular contractile energy over the largest part of the time course. However, the ideal parameter values to reproduce the exact energy shape upon a single PA do not allow to keep a constant energy baseline after the PA pulse. This is due to the calculated material relaxation time, which yields $\tau_c^M = \eta_c^M / E_c^M = 147\,\mathrm{s}$ and is an order of magnitude lower than typical relaxation times deduced in Chapter 3. That is why, in the course of the energy response, which takes about $500\,\mathrm{s} > 3\tau_c^M$, a significant increase of the energy baseline is registered, which is not present in the experimental curve.

The Kelvin-Voigt model with a characteristic material relaxation time of $\tau_c^{KV} = \eta_c^{KV} / E_c^{KV} = 155\,\mathrm{s}$ provides the best fit results. It allows to correct for the shortcomings of the other

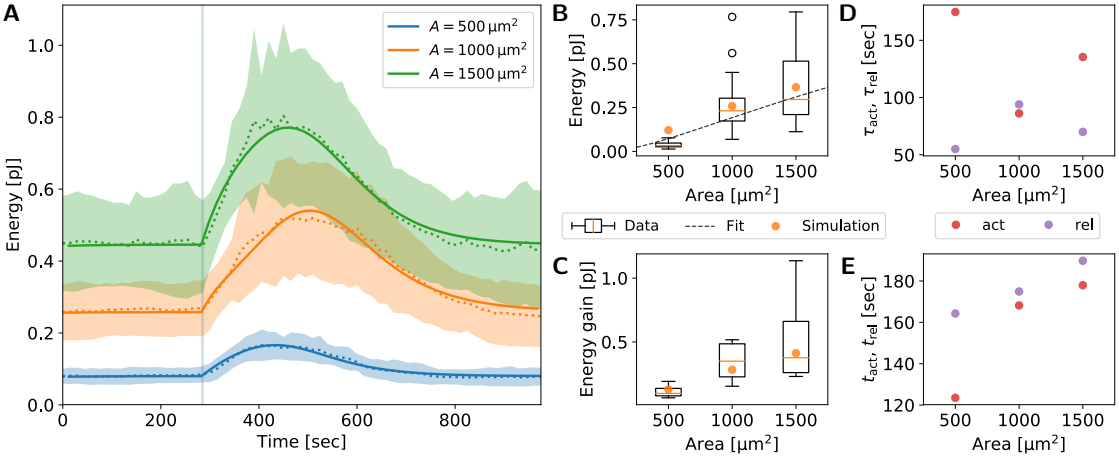

Figure 4.6: Effect of the cellular area on its energy level as well as its energy gain and dynamics upon photoactivation. **(A)** Time course of the strain energy. *Dotted lines* show mean values, *shaded regions* correspond to standard deviations and *full lines* show model fits. Each curve corresponds to an average of 9 , 11 and 11 cells, respectively, which are activated by a pulse of 100 ms duration. **(B)** Static strain energy level. With increasing spread area, the strain energy increases. *Boxes* denote the statistics of 29 , 23 and 23 cells, respectively. The *dashed* line shows the relation for an isotropically contractile disc derived in Equation 4.10. *Orange* dots show simulation results, with σ_{bck} kept constant for all patterns. **(C)** Strain energy gain upon photoactivation. With increasing spread area, the strain energy increases significantly. *Boxes* denote the statistics of 9 , 11 and 11 cells, respectively. *Orange* dots show simulation results, with σ_0 kept constant for all patterns. **(D-E)** PA stress activation and relaxation times τ_{act} and τ_{rel} and centers of the activating and relaxing sigmoid t_{act} and t_{rel}. The sum $\tau_{\mathrm{act}} + \tau_{\mathrm{rel}}$ stays approximately constant for all patterns. The onset t_{act} and offset t_{rel} of the stress plateau increase with the cell area, while the duration of the plateau $t_{\mathrm{rel}} - t_{\mathrm{act}}$ decreases.

models. Its parallel arrangement of springs and dashpots makes the material retard any instantaneous signal, such that convex stress profiles appear in a low-pass filtered fashion in the energy response. Further, as a solid model it allows a fast recovery to the energy baseline after optogenetic activation as compared with the Maxwell model.
We will therefore continue with the active Kelvin-Voigt model as a mechanical representation of the cell, as depicted in Figure 4.5A, and use a double sigmoid PA stress profile $\sigma_{\mathrm{act}}^{\mathrm{sig}}$. In particular, a double sigmoid profile, as illustrated by the green curve in Figure 4.4A, bears closest analogy to the experimentally acquired time course of the concentration of CRY2/CIBN-dimers upon PA, which was measured by *Valon et al.* [2015]: An instantaneous increase on the time scale of 2 s followed by a plateau of tens of seconds duration and a dissociation time of several hundreds of seconds. In general, a double sigmoid shape of the activation function fits better to the Michaelis-Menten kinetics which is a standard model to describe the association and dissociation dynamics of molecules [*Michaelis and Menten*, 1913].

Effect of the Cell Area on its Energy Level and Dynamics To enforce a varying spread area, circular shaped FN micropatterns of area $500\,\mu\text{m}^2$, $1000\,\mu\text{m}^2$ and $1500\,\mu\text{m}^2$ were manufactured. Cells plated on the patterns usually spread until the complete pattern was covered. Only cells which fully covered their patterns are considered in the following. Figure 4.6A illustrates the average strain energy level as well as the strain energy gain and dynamics as a response to a single PA pulse of 100 ms, both as a function of the cellular spread area. We find that the model dynamics allows to closely reproduce the mean time course of the experimental strain energy upon PA for each cell area.
Before treating the dynamics of the strain energy course in detail, we exploit the positive correlation of the static energy level and the cell area from Figure 4.6B to estimate the internal stress $\sigma_{\text{bck}}h_{\text{c}}$ and the force penetration length l_{p}. Fitting the analytical expression of an isotropically contracting disc from Equation 4.10 to the median energy value yields $\sigma_{\text{bck}}h_{\text{c}} = 7.1\,{}^{\text{nN}}/_{\mu\text{m}}$ and $l_{\text{p}} = 10.37\,\mu\text{m}$. If not explicitly stated, we will use the value for l_{p} in the remainder of this chapter. Since we model the cellular contractility via an anisotropic stress tensor which is different from the isotropic one, σ_{bck} and σ_0 are fitted once to the default case of a cell patterned on a FN circle of area $1000\,\mu\text{m}^2$ and left unchanged for the remaining cell areas, if investigating the full data set in Figure 4.6B and C. Only for the reduced data sets in Figure 4.6A, we will fit the stresses separately. From the fit of the energy curve belonging to cells patterned on a FN circle of area $1000\,\mu\text{m}^2$, we also obtain the stiffness $E_{\text{c}} = 716.0\,\text{Pa}$ and viscosity $\eta_{\text{c}} = 82.94\,\text{kPa}\cdot\text{s}$, if assuming a typical cell height of $h_{\text{c}} = 1\,\mu\text{m}$. These values yield a relaxation time constant $\tau_{\text{c}} = 115.84\,\text{s}$. We will keep these values fixed in the remainder of this chapter.
We find in Figure 4.6B that, in general, a pure increase of the cell radius, while leaving the background stress σ_{bck} constant, closely reproduces the full data set, which is indicated by the yellow dots. This suggests that SFs generate the same internal stress, independent of their length. In has to be noted that the orange dots represent the energy baseline found in Figure 4.6A, which only covers a reduced data set. Therefore, simulated energy values appear deviate from the medians of the experimental data, represented by the orange bars.
We find in Figure 4.6C shows that also the strain energy gain during PA positively scales with the spread area, uncovering a saturation of the energy gain at cell areas larger than $1000\,\mu\text{m}^2$. Simulations with a constant PA stress σ_0 can closely capture this relation, as indicated by the orange dots.
If considering the dynamics of stress generation and dissipation upon PA, we find a negative correlation of the average stress activation and relaxation times τ_{act} and τ_{rel} if varying the cell area, whereas the sum $\tau_{\text{act}} + \tau_{\text{rel}}$ stays approximately constant (see Figure 4.6D). This suggests that the effect of a single PA pulse on the cellular energy is of equal duration independent of the cell area.
The cell area has, however, a dominant impact on the onset, offset and duration of the stress plateau of the activation function, as illustrated in Figure 4.6E. With increasing cell area, both on- and offset times t_{act} and t_{rel} increase, while the duration of the stress plateau $t_{\text{rel}} - t_{\text{act}}$ decreases from 40 s for $500\,\mu\text{m}^2$ area to 10 s for a cell area larger than $1000\,\mu\text{m}^2$. Thus, for small cells, the saturation of the activating stress starts earlier and takes longer than for larger cells. This indicates that the molecular system evoking the

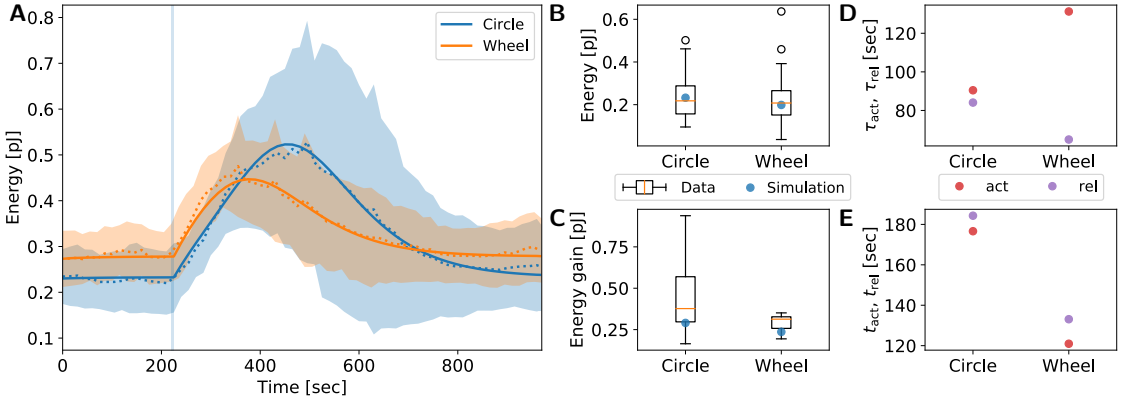

Figure 4.7: Effect of the FN pattern on the cellular energy level as well as its energy gain and dynamics upon photoactivation. **(A)** Time course of the strain energy. *Dotted lines* show mean values, *shaded regions* correspond to standard deviations and *full lines* show model fits. The curves represent averages of the reduced set of 7 circle-patterned and 5 wheel-patterned cells which are activated by a pulse of 100 ms duration. **(B)** Static strain energy level. The average energy baselines of circle- and wheel-patterned cells closely resemble. *Boxes* denote the statistics of 40 and 71 cells, respectively. *Blue* dots show simulation results, with σ_{bck} kept constant for both patterns. **(C)** Strain energy gain upon photoactivation. The energy gain of circle-patterned cells is significantly higher than for wheel-patterned cells. *Boxes* denote the statistics of 7 and 5 cells, respectively. *Blue* dots show simulation results, with σ_0 kept constant for both patterns. **(D-E)** PA stress activation and relaxation times τ_{act} and τ_{rel} and centers of the activating and relaxing sigmoid t_{act} and t_{rel}. The sum $\tau_{\mathrm{act}} + \tau_{\mathrm{rel}}$ stays approximately constant for both patterns. Wheel-patterned cells reach their plateau significantly faster, but the duration of the plateau remains unchanged for both patterns.

increase of the strain energy upon PA is non-uniformly distributed or activated for a different cell size.
Taken together, the cell area is a major determinant of both the static tensional efficiency of cells and the dynamics of force production.

Effect of the Actin Polarity on the Cellular Energy Level and Dynamics Figure 4.7 shows the effect of the actin polarity on the energy level as well as the strain energy gain and dynamics upon a single PA pulse of 100 ms duration. In particular, we compare the contractile dynamics of cells plated on one of the micropatterns presented in Figure 4.1B-C. As discussed in Section 4.1, the wheel pattern (WP) induces an actin polarity which is different from those induced by the full circle pattern (FCP), while keeping the cell area unchanged.
We find in Figure 4.7A that the model dynamics closely reproduces the experimental energy curves for both patterns. Figure 4.7B shows the energy baseline levels of experiment and model calculations required to maintain the energy level. On average, the strain

energy level of wheel-patterned cells equals those of circle-patterned cells, although the latter are allowed to adhere to a larger area, due to the designed pattern shape. It has to be noted that this is different for Figure 4.7A, which, however, only considers a fraction of the full data set. The continuum model with a constant background stress σ_{bck}, which is optimized with respect to the circle-patterned cells, can closely reproduce the median static energy level measured in the experiment.
Although the static energy level of cells on the WP equals those of cells on the FCP, their dynamic strain energy gain in response to a single PA pulse is less effective, as Figure 4.7C highlights. As before, a model with a constant PA stress σ_0 for both patterns closely recovers the experimentally deduced difference.
The experimental ratio of the median strain energy gains between both patterns yields 1.20 . From the simulation, we get a ratio of 1.23 , which is close to the experimental value.
Two aspects can explain the difference in the force production between both patterns, of which both arise from different arrangement of SFs.
On the one hand, SFs in circle-patterned cells usually reveal a parallel alignment across the full diameter of the cell. In the case of wheel-patterned cells, the width of a region of parallelly aligned SFs is only half as large. Assuming a constant SF density and each SF producing the same force, this difference can explain the differing force production for both patterns.
On the other hand, not all SFs in the wheel-patterned cells pull into the same direction. If assuming that each SF produces the same force magnitude F, we can compare the total force $F_{2\mathrm{SF}}$ exerted by two parallel SFs in the case of circle-patterned cells and the total force produced by two SFs from different subregions Ω_n of the wheel-patterned cells (compare Figure 4.5B-C, top). The magnitude of the sum of two force vectors $\mathbf{F}_1$ and $\mathbf{F}_2$ which originate from the same point and are separated by an angle α is

$$F_{2\mathrm{SF}} = |\mathbf{F}_1 + \mathbf{F}_2| = \left| \begin{pmatrix} F \\ 0 \end{pmatrix} + \begin{pmatrix} F\cos(\alpha) \\ F\sin(\alpha) \end{pmatrix} \right| = F\sqrt{2\,(1+\cos(\alpha))}\,. \tag{4.25}$$

For $\alpha = 0°$, which is the situation in circle-patterned cells, we have $F_{2\mathrm{SF}}^{\mathrm{FCP}} = 2F$. For $\alpha = 60°$, i.e. in the case of wheel-patterned cells, we get $F_{2\mathrm{SF}}^{\mathrm{WP}} = \sqrt{3}F$. The ratio of both numbers yields

$$\frac{F_{2\mathrm{SF}}^{\mathrm{FCP}}}{F_{2\mathrm{SF}}^{\mathrm{WP}}} = 1.16\,, \tag{4.26}$$

which is close to the experimentally and computationally obtained values stated above.
Figures 4.7D-E show the effect of the actin polarity on the dynamics of stress generation. We find that the stress activation and relaxation times τ_{act} and τ_{rel} for circle-patterned cells resemble each other, while for wheel-patterned cells, the stress activation time is twice as long as the relaxation time. However, in both cases, the sum $\tau_{\mathrm{act}} + \tau_{\mathrm{rel}}$ remains constant, indicating that the duration of the effect of a single PA pulse remains equal, independent of the actin polarity.
Wheel-patterned cells reach their strain energy plateau almost twice as fast than circle-patterned cells, but the duration of the plateau lies in the range of 10 s for both patterns

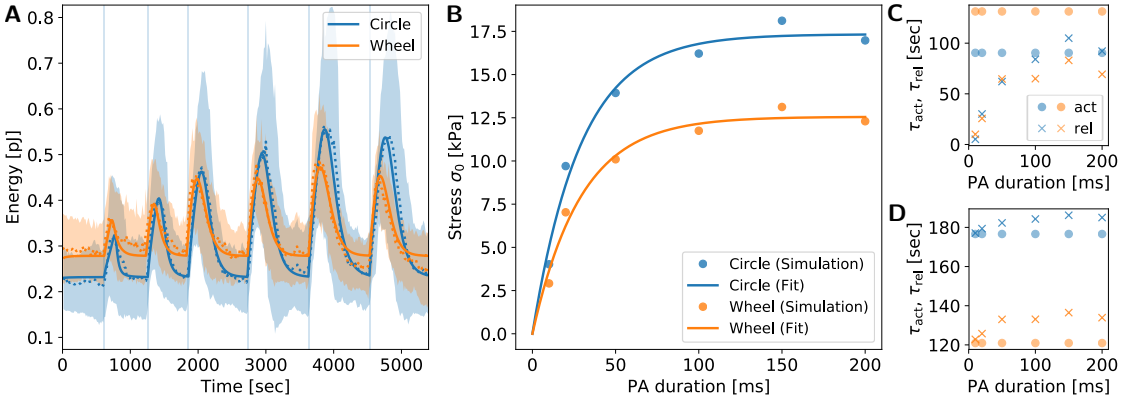

Figure 4.8: Effect of the PA pulse duration on the cellular energy gain and dynamics. **(A)** Time course of the strain energy. *Dotted lines* show mean values, *shaded regions* correspond to standard deviations and *full lines* show model fits. The curves represent averages of the reduced set of 7 circle-patterned cells and 5 wheel-patterned cells. **(B)** Calculated PA stress σ_0 for the two FN patterns (*dots*) and exponential fit (*lines*). The PA stress σ_0 increases with increasing PA duration and saturates above a PA duration of 29.1 ms independent of the FN pattern. For the reduced data set in Panel A, circle-patterned cells exert a higher stress than wheel-patterned cells. **(C-D)** PA stress activation and relaxation times τ_{act} and τ_{rel} and centers of the activating and relaxing sigmoid t_{act} and t_{rel}. Both τ_{act} and t_{act} are independent of the PA duration. τ_{rel} and t_{rel} increase in a saturating manner as a function of the PA duration, i.e. a longer PA duration has a longer impact on the contractility of cells. *Blue* dots and crosses correspond to the full circle pattern, while *orange* dots and crosses refer to the wheel pattern.

(see Figure 4.7E). This suggests that the arrangement of SFs has an impact on the inset of the force saturation in cells, but does not influence the duration of force saturation. Overall, actin polarity has hardly an effect on the homeostatic energy level of cells, but is a major determinant of the dynamic force production upon optogenetic regulation.

Effect of the PA Pulse Duration on the Strain Energy Gain and Dynamics Figure 4.8 demonstrates the impact of the PA pulse duration on the cellular strain energy gain and dynamics. We find in Figure 4.8A that an active Kelvin-Voigt model with σ_0-dependent stress relaxation time $\tau_{rel}(\sigma_0)$ a center $t_{rel}(\sigma_0)$ of the relaxing sigmoid closely resembles the experimental evolution of the cellular energy for both FCP and WP. It has to be noted that, in this paragraph, we fitted σ_{bck} and σ_0 separately for both FN patterns to meet the requirements of the reduced data set presented in Figure 4.8A. It is, however, expected that for the full data set, which was used to compile the statistics in Figure 4.7B and C, σ_{bck} and σ_0 will be consistent for both FN patterns.
Figure 4.8B reveals that an increase of the PA pulse duration leads to an increasing stress response. By fitting an exponentially saturating curve to the calculated stress σ_0 as a function of the PA pulse duration, we obtain a saturation time of 29.1 ms, irrespective of

the FN pattern, above which a prolongation of the PA pulse does not evoke an increase of σ_0. For the reduced data set in Figure 4.8A, we obtain a maximal stress $\sigma_0^{\max} = 17.33\,\mathrm{kPa}$ for cells on the FCP and $\sigma_0^{\max} = 12.56\,\mathrm{kPa}$ for cells on the WP.
Figures 4.8C-D show that, with increasing PA pulse duration, the stress relaxation time τ_{rel} increases for both FCP and WP proportionally to $(\sigma_0/\sigma_0^{\max})^2$, while the stress activation time τ_{act} remains unaffected. Thus, a prolonged PA pulse has a longer effect on the cellular force production. This is further verified by the rise of t_{rel} proportional to $(\sigma_0/\sigma_0^{\max})^2$, indicating that the plateau of maximal stress lasts longer for longer PA pulses. Taken together, the duration of the optogenetic activation determines both strength and duration of the cellular energy response, but the energy response saturates in terms of both strength and duration for PA pulses of 29.1 ms and longer.

4.4 Conclusion

In this chapter, we introduced anisotropic stress in our existing two-dimensional continuum model to analyze the influence of the composition of the FN pattern on the total contractile force of a cell. The anisotropic arrangement of stresses was engineered by exploiting the knowledge about the underlying architecture of the actin CSK and lead to a qualitatively agreement of the simulated and experimental traction stress patterns.
The continuum model could also reproduce the positive correlation of the contractile energy cells invest and their spread area as well as of the energy gain upon optogenetic activation and spread area. We will follow up this relation by means of an analytical calculation in the following chapter for the case of blood platelets.
The model helped to explain the different energy levels cells exert on differently shaped FN coatings, even if they adopt the same spreading area and area curvature. In this sense, the continuum model presented here outperforms existing continuum models such as *Edwards and Schwarz* [2011] or *Oakes et al.* [2014], which do not consider the internal structure of the CSK.
Simulation results further demonstrated that the global activation of RhoA rather causes the cell to behave like a viscoelastic solid than a viscoelastic fluid, which is in contrast to the case for local activation in Chapter 3. The characteristic relaxation time constant here lies at the order of 100 s, which is an order of magnitude lower than in Chapter 3. These results suggest that the cellular CSK interprets local and global regulation signals differently. A local RhoA signal triggers the local reconstruction of the CSK, while a global signal triggers a global contraction of cells, aiming at preserving its homeostatic energy state.
Also, we found that the activation stress profile required to reproduce the cellular energy response is different from the exponential profile assumed for the LOV-based system from the temporal evolution of its downstream effectors in Chapter 3. Here, the activation profile is found to be of double sigmoid shape with an instantaneous jump right after the PA. This closely resembles the asymmetric temporal course of the concentration of CRY2/CIBN-dimers measured by *Valon et al.* [2015]: A fast increase with a time constant of 2 s, a plateau of $10 - 100\,\mathrm{s}$ duration and an exponential decrease at the order of 100 s.

Finally, our model allowed to determine a PA time of about 30 ms, above which the effect of the activation of RhoA by means of the CRY2/CIBN-system saturates. PA pulses of duration longer than 30 ms will not significantly change the increase of the cellular force response. With increasing pulse duration, the cellular relaxation time and the duration of the force plateau increased, indicating that a cell needs a longer time to recover from a stronger activation.
Overall, we found that the cell size, the structure of the extracellular environment and the duration of the regulation of the RhoA signaling pathway are major determinants of the force production and dynamics of a cell, while the homeostatic energy level of cell is mainly influenced by its size. The latter finding confirms previous studies on the relation of cellular force production and spread area e.g. by *Reinhart-King et al.* [2005].

5 Force Generation by Spreading Blood Platelets

Blood platelets are the smallest cells found in the human body, featuring a typical diameter of about $2-5\,\mu$m. Due to the lacking nucleus, they exhibit a roughly constant thickness of about $1\,\mu$m in their resting state [*Sandmann et al.*, 2014]. Their major task is plugging of broken walls of blood vessels to prevent blood loss, in the course of which they generate clots via the interaction with the adhesive protein fibrin [*Michelson*, 2012].
In particular, platelets, once stimulated by the enzyme thrombin, adhere to the wounded site and spread to an area of about $30-40\,\mu\text{m}^2$, thus reducing their height to the order of 100 nm [*Aquino et al.*, 2011]. At the same time, the platelets form protrusions in terms of filopodia or lamellipodia [*Allen et al.*, 1979; *Sandmann and Köster*, 2016]. The filopodia are then used to sense the extracellular environment, which is communicated via traction forces [*Mattila and Lappalainen*, 2008].
Several studies have been conducted to measure the magnitude of these traction forces. Early measurements tried to infer the force per platelet by studying the maximum force exerted by blood clot, yielding forces below 1 nN [*Jen and McIntire*, 1982; *Carr and Zekert*, 1991]. In the recent time, technologies such as AFM or TFM improved, allowing the measurement of the forces exerted by single platelets. *Lam et al.* [2011] used AFM to find an average contractile force of 29 nN. This value was further confirmed by TFM measurements by *Henriques et al.* [2012], who obtained an average force of 34 nN, revealing that, in spite of their size, blood platelets are able to generate forces in the order of those exerted by the ten times larger fibroblast cells.
However, no study has investigated the temporal evolution of the force during clotting and the influence of environmental mechanics of the total force so far. In the following, we combine TFM and continuum mechanics to get an understanding of how platelets establish and maintain their contractile forces and whether force and cell organization depend of the mechanics of the environment.
In particular, we start in Section 5.1 with describing the optimization of the existing TFM procedure to accomplish requirements set by the blood platelets as compared to e.g. fibroblasts presented in the previous chapters: Blood platelets are an order of magnitude smaller, but exert stresses of up to an order of magnitude larger as compared to fibroblast cells. Therefore traction force measurements entail both a low bead density and a low signal-to-noise ratio, but at the same time large displacements.
In Section 5.2, we will find that the maximum stresses exerted by platelets can even exceed the above values by a factor of up to 10 and that platelets feature at least two different contractile modes to maintain their maximal force, either an oscillating or an non-oscillating mode.

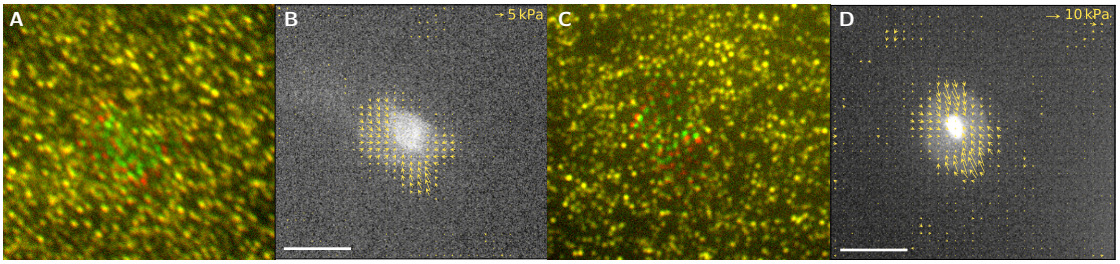

Figure 5.1: Although they are an order of magnitude smaller than typical fibroblasts, blood platelets exert higher forces on the elastic substrate, thus requiring more sophisticated algorithms to calculate their traction field. The figure shows exemplary bead images with overlayed color-coded displacement field in **A** and **C**. Panels **B** and **D** show the resulting traction fields on top of corresponding recordings of the membrane stained cells. Scale bars are 5 μm.

Finally, in Section 5.3, we will use the continuum model presented in Chapter 4 to explain the relation between the force exerted by blood platelets and their spread area during blood clot formation. The model will allow to explain the apparent lack of mechanosensitivity of platelets in the investigated range of substrate stiffnesses, by balancing the contributions of the substrate stiffness and the FA stiffness to the reach of cellular force transduction. The results presented in the following originate from a collaborative work together with Jana Hanke and Sarah Köster from the University of Göttingen, who conducted the experiments, and Assaf Zemel from the Hebrew University of Jerusalem, who contributed to the theoretical model.

5.1 Experimental Protocol

Blood platelets were extracted from the human blood plasma and placed on PAA substrates of variable stiffness ranging from $E_\mathrm{s} = 19\,\mathrm{kPa}$ to $E_\mathrm{s} = 83\,\mathrm{kPa}$ and a Poisson's ratio $\nu_\mathrm{s} = 0.3$. Softer substrates were not taken into account as considerable displacement components in z-direction were measured in this case, resulting from a large contraction in the (x, y)-plane. Fluorescent beads of 40 nm in diameter were embedded into the PAA substrates, which allowed to measure the displacements induced by the contractile force of the blood platelets.
The platelets were stimulated by means of the enzyme thrombin, which was also extracted from the human blood plasma. After the addition of thrombin, bead positions and the fluorescently stained cell membrane were imaged every 7.5 s for as total time of 30 min. During these 30 min, each of the cells attached at its individual time point t_0 to the substrate, which was inspected from fluorescent microscopy recordings of the cell membrane. The bead image before time point t_0 was taken as the relaxed undeformed reference image.
Figures 5.1A and 5.1C show exemplary bead images with the color-coded displacement field for substrates of stiffness $E_\mathrm{s} = 19\,\mathrm{kPa}$ and $E_\mathrm{s} = 41\,\mathrm{kPa}$, respectively. Figures 5.1B and 5.1D illustrate the corresponding membrane stained images overlayed with the cellular

traction field.
Due to the small cell size and large displacements at the same time, the calculation of displacements is far more challenging than for fibroblast in Chapters 3 and 4. Bead images exhibit a low absolute number of beads, with a bead density of about $^{1.5}/_{\mu m^2}$, and a low signal-to-noise ratio arising from typical limitations in the resolution of the microscope. We find the typical diameter of cells lying in the range $5-10\,\mu$m and maximal displacements of about $1\,\mu$m, yielding a ratio of displacement to cell size of $10-20\,\%$.
To compute the displacement field, we use the pyramidal KLT optical flow algorithm presented in Section 2.1.1, which yields robust displacement results for low bead densities as compared to PIV. Due to the low bead density and large bead displacements at the same time, we use differential measurements, i.e. displacements between time point t and $t+\Delta t$ are calculated and added up for the total image sequence. It has to be noted that a differential measurement leads to an amplification of the measurement error for the duration of the data set. To circumvent this artifact, we use Equation 2.11 to compute the displacement field.
To estimate the minimal window size for the KLT algorithm which we can use to prevent from the loss of information, we use the guidance presented by *Colin-York et al.* [2016]. Starting with a bead density of $^{1.5}/_{\mu m^2}$, we can read off an optimal resolution of traction stresses of $1.7\,\mu$m and a real resolution of traction stresses of $2.5\,\mu$m, of which the latter assumes the presence of noise. With a micrometer-to-pixel ratio of $0.076\,^{\mu m}/_{\text{pix}}$, we get a minimal window size of about 32 pix.
We finally use FTTC, as presented in Section 2.1.2, to compute the traction traction stresses of the platelets, the result of which will be outlined in the following section.

5.2 Quantification of the Total Force Exerted by Blood Platelets

In the following, we will calculate traction stresses exerted by blood platelets. We will start with a qualitative description and then turn to a quantitative specification of force exerted by platelets. The latter will motivate the introduction of a mathematical model.

5.2.1 Qualitative Analysis of Forces Exerted by Platelets

Figures 5.2A and 5.3A show typical traction stress patterns exerted by thrombin-stimulated platelets which were placed on substrates of stiffness 19 kPa and 41 kPa, respectively. In the following, we will refer to the cells as *cell 1* and *cell 2*.
In both cases, we find that the stimulation elicits a global increase of traction stresses mainly in the periphery of the cell, which correlates with the peripherally located actin network in wild-type platelets, as shown by *Pleines et al.* [2012] and in Figure 1.2E. The resulting traction patterns furthermore tend to be anisotropic, suggesting a predominantly unidirectional alignment of the actin CSK in general. This is also reflected in the time courses of the dipole moments, depicted in Figures 5.2C and 5.3C. After the contractile stresses completely formed, cell 1 reaches a dipole ratio of about 2, while the dipole

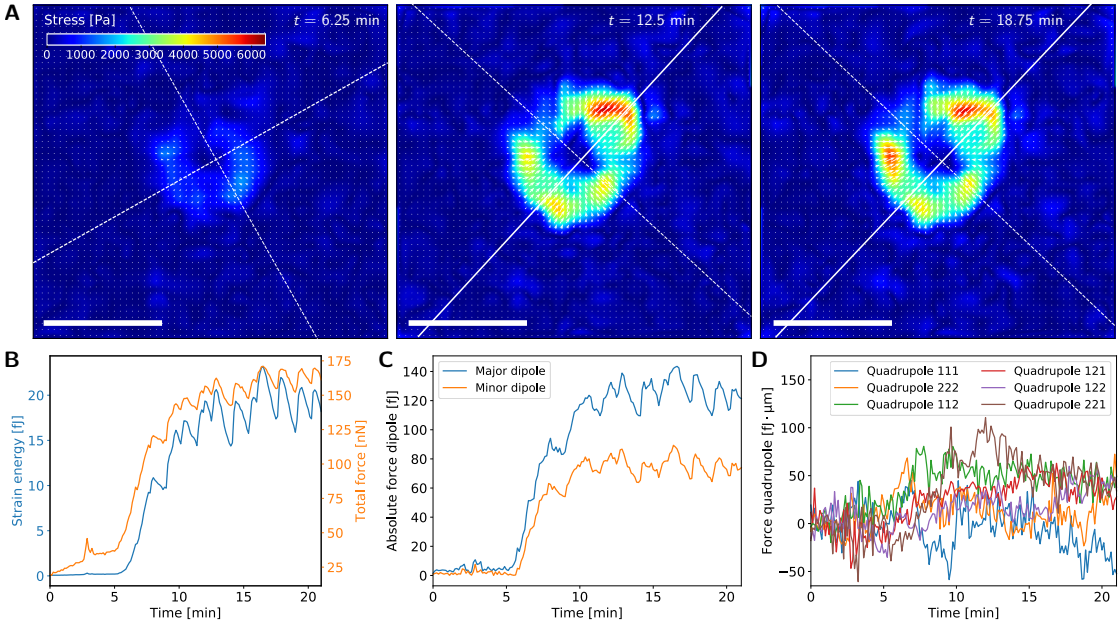

Figure 5.2: Features of the traction pattern of a blood platelet which exerts an oscillating and growing force magnitude. **(A)** Exemplary time sequence of traction stresses of a contracting blood platelet. Force dipole axes are depicted as *white lines*, of which *full lines* represent the dominant dipole axis. Scale bars are 5 μm. **(B)** Temporal evolution of the cellular strain energy and total force. **(C)** Temporal evolution of the major and minor force dipole moments of the cell. **(D)** Temporal evolution of the cellular force quadrupole moments w.r.t. the major dipole axis.

ratio of cell 2 increases to up to 10, indicating a dominant beam-like internal contractile element, similar to stress fibers in fibroblasts.

The build up of traction forces happens on a time scale of about 5 min, as Figures 5.2B and 5.3B demonstrate. Both cells reach strain energy maxima of about $20 - 30$ fJ, while the total force maxima are at the order of 100 nN. Surprisingly, both values are at the order of typical forces exerted by fibroblasts, which are about ten times larger than platelets (compare Chapters 3 and 4). Also, we find that the total force value is about an order of magnitude larger than the previously reported 30 nN by *Lam et al.* [2011] or *Henriques et al.* [2012]. However, *Seifert et al.* [2017] show that the dynamics of the cytoskeleton strongly depend on the thrombin concentration. Therefore, it is to be expected that in the earlier studies the concentration of thrombin might be lower than those used in our study.[1]

A striking difference between the two cells is the temporal evolution of both the total force and the contractile energy when maintaining their maximal force. For cell 1, we find that both force and energy oscillate with a frequency of about 17 mHz and amplitudes of about 10 nN and 2.5 fJ around their average values, respectively. Cell 2, on the contrary,

[1] In our case, the thrombin activity per volume was $4\,{}^{\mathrm{U}}/_{\mathrm{ml}} = 4\,{}^{\mu\mathrm{mol}}/_{\mathrm{min\,ml}}$.

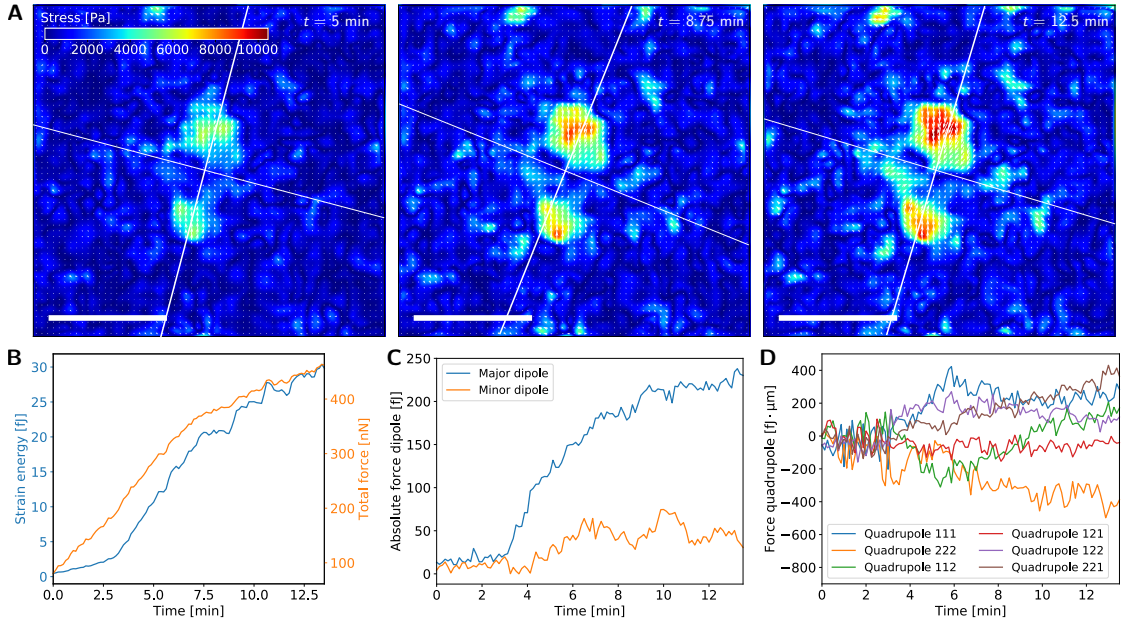

Figure 5.3: Features of the traction pattern of a blood platelet with a non-oscillating but growing force magnitude. **(A)** Exemplary time sequence of traction stresses of a contracting blood platelet. Force dipole axes are depicted as *white lines*, of which *full lines* represent the dominant dipole axis. Scale bars are 5 μm. **(B)** Temporal evolution of the cellular strain energy and total force. **(C)** Temporal evolution of the major and minor force dipole moments of the cell. **(D)** Temporal evolution of the cellular force quadrupole moments w.r.t. the major dipole axis.

does not reveal any oscillation, but maintains a monotonous increase in both force and energy with an initiating saturation.
The different levels of anisotropy of the traction stress field are also reflected by the time course of the quadrupole moments depicted in Figures 5.2D and 5.3D. In both cases, we find a positive correlation of the Q_{221} component with the time course of the contractile energy, suggesting a prevalent direction of the stress field parallel to the major dipole axis. For cell 1, also the quadrupole moment Q_{112}, which reflects stresses perpendicular to the major dipole axis, has a considerable contribution, expressing the approximately isotropic stress generation of cell 1. For cell 2, on the contrary, the quadrupole moment Q_{112} is underrepresented. Instead, the component Q_{111} contributes as a second dominant moment, emphasizing the strict unidirectionality of cell 2.

5.2.2 Quantitative Analysis of Forces Exerted by Platelets

We recorded the time course of the total force for about $N = 30$ platelets per substrate stiffness and averaged the curves for each stiffness value. Figure 5.4A shows the resulting average time course of the total force and its standard deviation, yielding average values

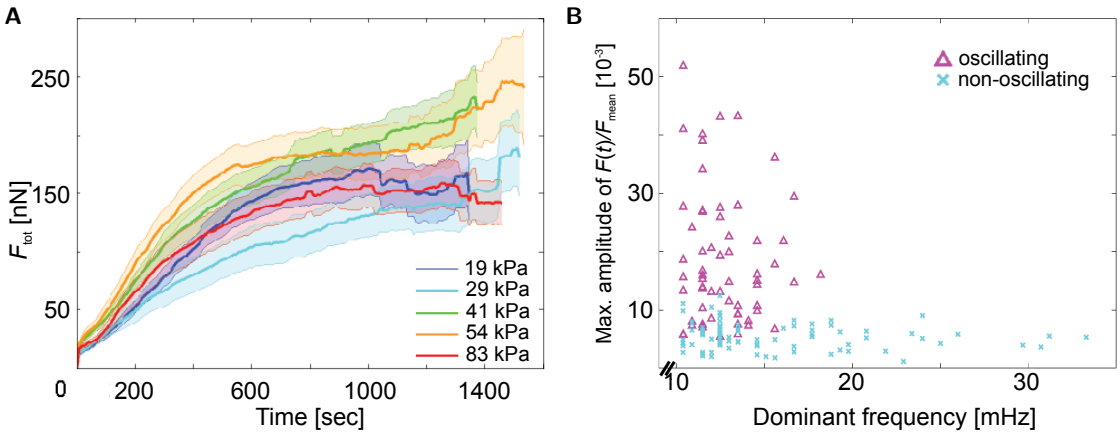

Figure 5.4: The average force magnitude platelets exert is independent of the substrate stiffness. Platelets can further be classified into an oscillating and non-oscillating type based on time course of the force magnitude. **(A)** Averaged temporal evolution of the total traction force. Lines denote mean values, while transparent regions denote standard errors of the mean. **(B)** Oscillation amplitude of the cell as a function of the oscillation frequency. Oscillating platelets exhibit a higher power amplitude in the Fourier domain compared to non-oscillating platelets. Cells were discriminated by means of visual inspection. Images by courtesy of Jana Hanke, University of Göttingen.

in the range $100 - 200\,\mathrm{nN}$.[2]

We do not find a systematic correlation of the force curves with increasing substrate stiffness, suggesting a lacking mechanosensitivity of blood platelets for substrate stiffnesses of the order of tens of kPa. This is in good agreement with the work by *Qiu et al.* [2014], who found out that the relative number of platelets adhering to the substrate at all is independent of the stiffness for substrate stiffnesses of tens of kPa and larger. Taking their results into account, a mechano-dependent force maximum would only be expected for a substrate stiffness of 5 kPa and below, which however is not considered experimentally in the course of this work, as described in Section 5.1.

Figure 5.4B shows the classification of cells into the categories *oscillating* and *non-oscillating*, yielding a ratio of 39 % to 61 % for 161 investigated cells.[2] For each point in the scatter plot, the plateaus of the force curves were divided by their mean value and filtered by means of a bandpass filter, leaving only oscillations in the frequency range $10 - 35\,\mathrm{mHz}$. Transforming the signal into Fourier space yielded a dominant frequency, which was assigned as the oscillation frequency of the cell. The magnitude of the dominant peak in Fourier space was then considered as a classification criterion.

As the total force curves in Figure 5.2B and 5.3B suggest, the maximal force a platelet exerts varies from cell to cell. To understand this variability, we analyze the relation between the final spread area A_0 and the maximal force F_{max} exerted by a platelet. Here, the spread area is determined by averaging the spread area in the last five frames of

[2]Quantification by courtesy of Jana Hanke, University of Göttingen.

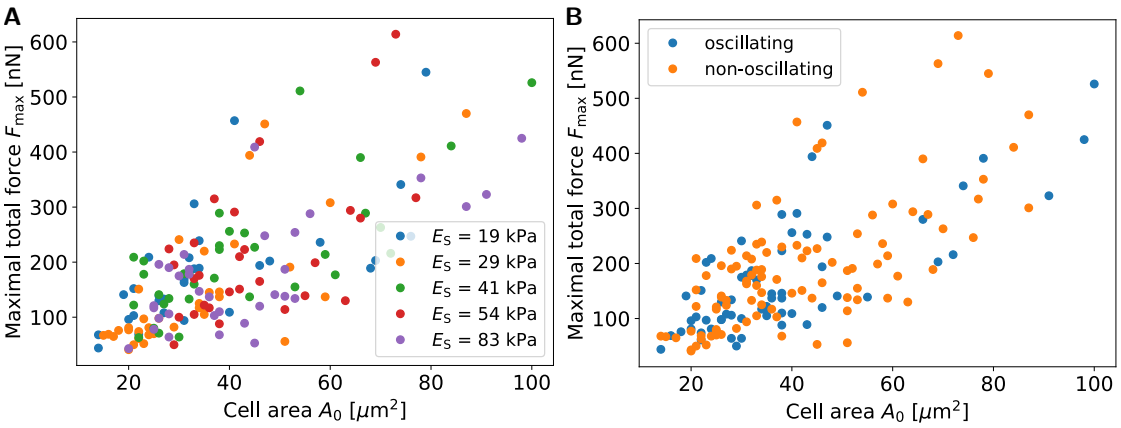

Figure 5.5: The maximal total force of a platelet is proportional to the cellular spread area, but independent of the substrate stiffness and the temporal evolution of the total force. **(A)** Maximal total force as a function of the cell area for different substrate stiffnesses. **(B)** Maximal total force as a function of the cell area for oscillating vs. non-oscillating cells. Data by courtesy of Jana Hanke, University of Göttingen.

the fluorescence recording of the membrane stained cell. Previous work by *Sandmann et al.* [2014] showed that cells reach their final area after a few minutes after thrombin-stimulation.

Figure 5.5 shows the relation between $F_{\max}$ and A_0 for all 161 cells. As for fibroblasts in Chapter 4, we find a positive correlation between $F_{\max}$ and A_0. In accordance with Figure 5.4A, we do not register a systematic difference of the force-area-relation for different substrate stiffnesses, (see Figure 5.5A). Figure 5.5B further indicates that also oscillating and non-oscillating cells do not differ with respect to their force-area-relation.

Also, the force anisotropy for the two contractile modes does not differ on average. Figure 5.6A and B show an exemplar experimental traction stress pattern with highlighted major and minor dipole axis and the corresponding temporal evolution of the dipoles as well as their ratio, respectively. As the histograms in Figure 5.6C reveal, we do not find a significant difference in the force anisotropy for the oscillating and non-oscillating mode. In both cases, the distribution of dipole ratios can be represented by a log-normal distribution with mean 2.3 , standard deviation 0.9 and median 2.1 , suggesting that cells tend to contract slightly anisotropically. We thus conclude that the platelet presented in Figure 5.3 only constitutes an exception.

We can reproduce the force anisotropy by means of a simulated traction patterns. Each simulated traction pattern consists of 8 elliptic stress spots which are placed on the same circle line to account for the peripheral location of traction hot spots in the experiments. Further, all force vectors are pointing towards the center of the image. The positions of the first 7 hot spots, of which each has the same stress magnitude 500 Pa, are sampled from a uniform distribution. The last force spot is placed at the opposite side of the average traction spot position. Its stress magnitude is chosen such that the overall net force becomes zero. Exemplary simulation traction patterns are illustrated in Figure 5.6E.

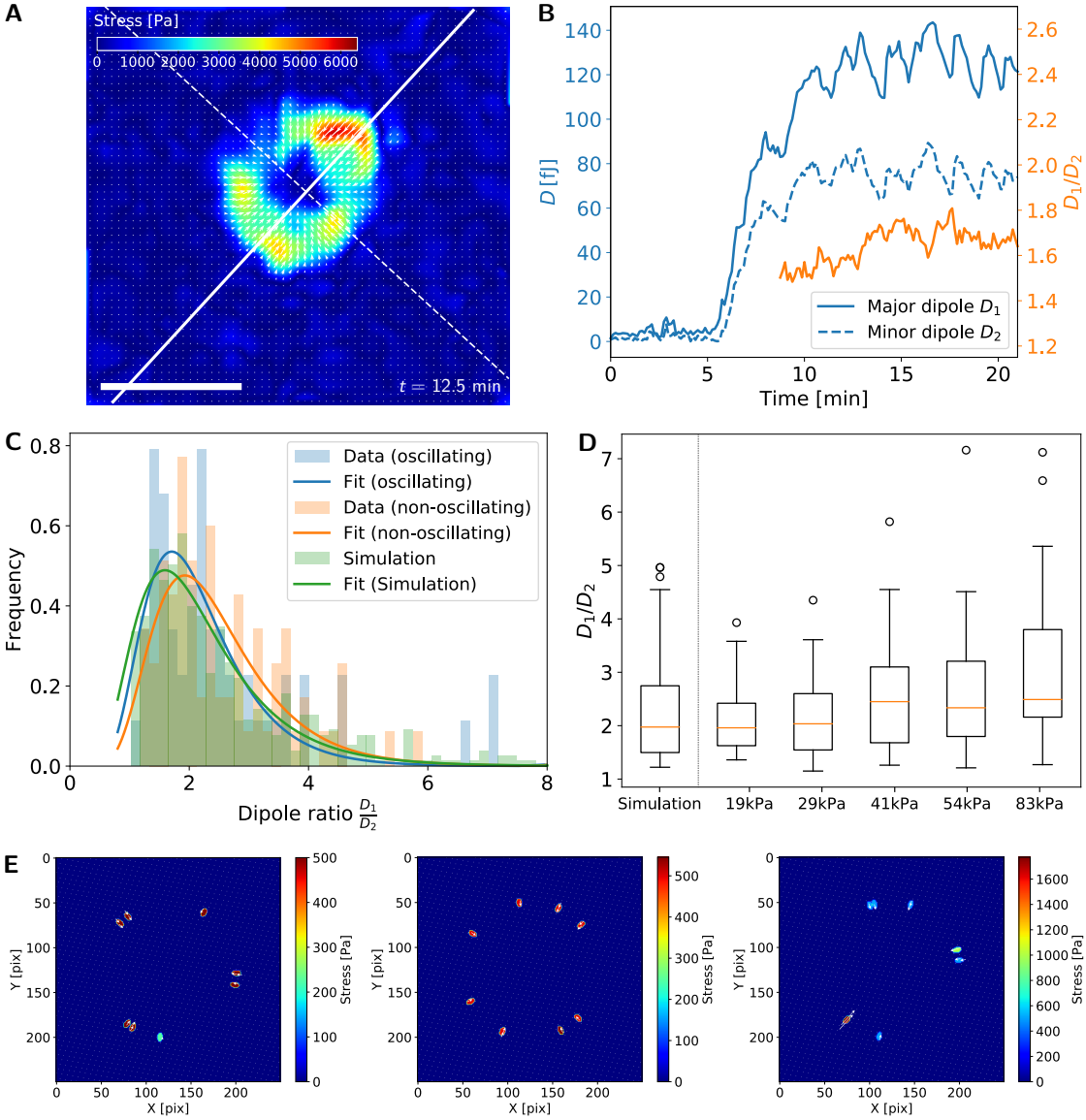

Figure 5.6: On average, platelets tend to contract with an average force dipole ratio of about 2 independent of the substrate stiffness and their contraction mode. **(A)** Exemplary traction pattern with the major (D_1, *full line*) and minor (D_2, *dashed line*) force dipole axis on top. **(B)** Temporal evolution of the major and minor dipole shown in *blue*, respectively. The *orange* curve displays the ratio D_1/D_2 of the two force dipoles. **(C)** Histogram of experimentally observed dipole ratios and results of the corresponding simulations for 8 randomly positioned force spots on a circular line, each of which is directed towards the center of the image. **(D)** Dipole ratio as a function of the substrate stiffness for experiment and simulation. One can observe a slight trend towards larger force anisotropy with increasing substrate stiffness. The simulation can well reproduce the experimental results. *Yellow lines* denote the median values, *boxes* are the midspread, while *whiskers* contain 99.3 % of the data. *Circles* denote outliers. **(E)** Exemplary simulated traction stress patterns used in Panels C and D.

Figure 5.6D shows the force dipole ratio as a function of the substrate stiffness for both experimental and simulated traction patterns. We find that with increasing substrate stiffness a slight, but insignificant, trend towards larger force anisotropy exists. The average dipole ratio for all analyzed platelets is 2.3 . The simulated traction patterns from Figure 5.6E can well reproduce the experimental results. In general, a reduction of the number of simulated traction spots will increase the average dipole ratio and vice versa, since fewer traction spots are more likely to generate a unidirectional traction pattern. Based on the available data, we cannot determine a difference both between oscillating and non-oscillating platelets or between platelets adhering to substrates of different stiffness neither in terms of the force-area-relation nor in terms of the dipole ratio. Therefore, we will pool the data in the following mathematical analysis.

5.3 Theoretical Investigation of the Total Force Exerted by Blood Platelets

We can use the continuum model presented in Chapters 3 and 4 to explain the force-area-relationship illustrated in Figure 5.5 and, with this, make out the origin of the apparent lack of mechanosensitivity observed in Figure 5.4A and 5.5A.
In the following, we will first calculate the relationship between the total force and the size of the system for both one- and two-dimensional active solid model (compare Figures 1.9A and B, both without viscosity). We will consider an isotropic model for two reasons: First, the average dipole ratio is close to that of an isotropic system, as shown in Figure 5.6, and second, an isotropic model facilitates an analytical expression for the total force in both cases. One should however be aware that some platelets exert a highly anisotropic traction stress field. Therefore, it is to be expected that an orthotropic material model, such as the model presented in Chapter 4, would yield the best correspondence between experiment and theory.
We will thereafter constrain the model parameters with respect to the experimental data by means of the conjugate-gradient based parameter optimization method of *Nelder and Mead* [1965]. The final parameters will be used to explain the origin of the lacking mechanosensitivity by considering a comparison of the contribution of the FAs and the substrate stiffness to the force penetration length l_p.

5.3.1 Total Traction Force in the One-Dimensional Active Solid Model

The displacement u of a one-dimensional elastic bar of elasticity E_c with coupling density Y, subjected to a constant contractile stress σ_0, yields [*Edwards and Schwarz*, 2011]

$$u\left(x\right) = -l_\mathrm{p}\frac{\sigma_0}{E_\mathrm{c}} \cdot \frac{\sinh\left(\frac{x}{l_\mathrm{p}}\right)}{\cosh\left(\frac{l_0}{l_\mathrm{p}}\right)}\,, \tag{5.1}$$

where $2l_0$ is the bar length (see Figure 1.9A). The quantity l_p denotes the force penetration length, which can be estimated by the expressions derived by *Banerjee and Marchetti*

[2012], as described in Section 3.4. It is composed of contributions l_a due to FAs and l_s due to the substrate stiffness. For fibroblast cells, we used

$$l_\mathrm{a} = \sqrt{\frac{E_\mathrm{c} h_\mathrm{c}}{Y_\mathrm{a}}}\,, \tag{5.2}$$

with

$$Y_\mathrm{a} = \frac{k_\mathrm{a}}{L_\mathrm{c} l_\mathrm{sarc}}\,, \tag{5.3}$$

where k_a is the stiffness of a FA, h_c the cell height, L_c the typical cell size and l_sarc the length of the sarcomeric unit. However, since the CSK of platelets is known to not consist of single contractile units, but is rather a dense peripheral network, as illustrated in Figure 1.2E, we cannot make out a sarcomeric length l_sarc, but rather estimate l_sarc via

$$l_\mathrm{sarc} = \frac{L_\mathrm{c}}{N_\mathrm{a}}\,. \tag{5.4}$$

Here, N_a is the total number of adhesions. This transforms the interpolation formula for l_p as

$$l_\mathrm{p} = \sqrt{\frac{E_\mathrm{c} h_\mathrm{c} L_\mathrm{c}^2}{N_\mathrm{a} k_\mathrm{a}} + \frac{E_\mathrm{c} h_\mathrm{c} h_\mathrm{eff}}{\pi E_\mathrm{s}}}\,, \tag{5.5}$$

with h_eff defined by Equation 3.31 and remaining parameters listed in Table A.6. With Equation 3.15, we obtain an expression for the effective spring stiffness density Y that describes the combined stiffness of the FA layer and the substrate:

$$Y = \frac{E_\mathrm{c} h_\mathrm{c}}{l_\mathrm{p}^2 \left(1 - \nu_\mathrm{c}^2\right)} = \frac{1}{1 - \nu_\mathrm{c}^2} \frac{{}^{\pi E_\mathrm{s} N_\mathrm{a} k_\mathrm{a}}/_{h_\mathrm{eff}}}{N_\mathrm{a} k_\mathrm{a} + {}^{\pi E_\mathrm{s} L_\mathrm{c}^2}/_{h_\mathrm{eff}}}\,. \tag{5.6}$$

From Equation 5.1, we can then directly calculate the traction force T_1D via

$$T_\mathrm{1D} = \int_{-l_0}^{l_0} Y|u|\mathrm{d}x = 2Y \int_0^{l_0} l_\mathrm{p} \frac{\sigma_0}{E_\mathrm{c}} \cdot \frac{\sinh\left(\frac{x}{l_\mathrm{p}}\right)}{\cosh\left(\frac{l_0}{l_\mathrm{p}}\right)} \mathrm{d}x = \frac{2\sigma_0}{1 - \nu_\mathrm{c}^2} \left(1 - \frac{1}{\cosh\left(\frac{l_0}{l_\mathrm{p}}\right)}\right)\,. \tag{5.7}$$

Figure 5.7A illustrates the traction force T_1D as a function of the system size l_0. With increasing l_0, the total force saturates at the maximal contractile force $T_\mathrm{1D,max} = {}^{2\sigma_0}/_{1-\nu_\mathrm{c}^2}$. Moreover, the total force decreases exponentially with increasing penetration length l_p. Around $l_0 \approx l_\mathrm{p}$, the traction force is a linear function of the system size. By expanding the force around $l_0 = l_\mathrm{p}$ as

$$T_\mathrm{1D}\left(l_0 = l_\mathrm{p}\right) = \frac{2\sigma_0}{1 - \nu_\mathrm{c}^2} \left(1 - \frac{1}{\cosh\left(1\right)}\right) + \frac{2\sigma_0}{l_\mathrm{p}\left(1 - \nu_\mathrm{c}^2\right)} \cdot \frac{\tanh\left(1\right)}{\cosh\left(1\right)} \left(l_0 - l_\mathrm{p}\right) + \mathcal{O}\left(l_0^2\right)\,, \tag{5.8}$$

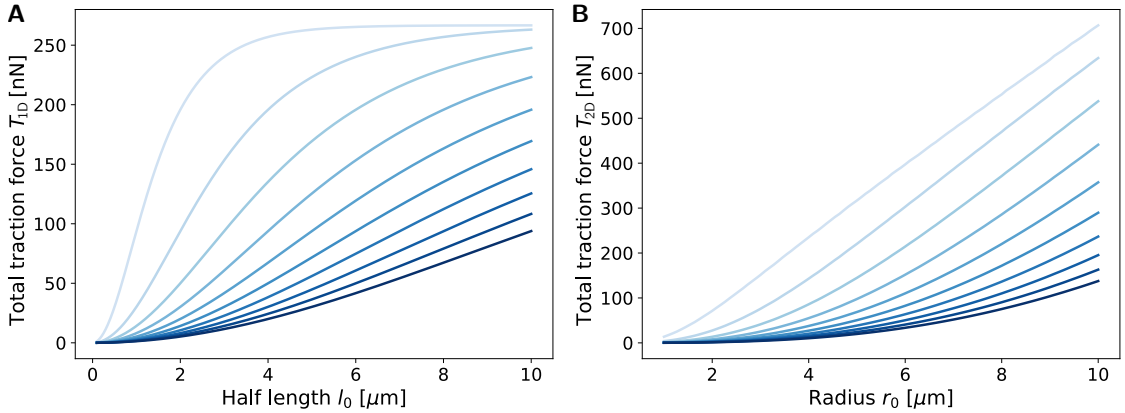

Figure 5.7: Relation between the total traction force T and half cell length l_0 or radius r_0 for both one- and two-dimensional thermo-elastic model. **(A)** and **(B)** show the relationship for the 1D model and 2D model, respectively. For both panels, l_p covers values from 1 μm (*light blue*) to 10 μm (*dark blue*). Default values are: $\sigma_0^{1\mathrm{D}} = 100\,\mathrm{nN}$, $\sigma_0^{2\mathrm{D}} = 120\,\mathrm{kPa}$, $E_\mathrm{c}^{2\mathrm{D}} = 10\,\mathrm{kPa}$ and $h_\mathrm{c}^{2\mathrm{D}} = 100\,\mathrm{nm}$.

we can find the slope m in this region to be

$$m = \frac{2\sigma_0}{l_\mathrm{p}\left(1-\nu_\mathrm{c}^2\right)} \cdot \frac{\tanh\left(1\right)}{\cosh\left(1\right)}\,, \tag{5.9}$$

which likewise is the maximal slope of the traction force.

5.3.2 Total Traction Force in the Two-Dimensional Active Solid Model

Parts of the following calculation were already conducted by *Mertz et al.* [2012] to describe the scaling of forces in cohesive cell colonies. For reasons of completeness, we will briefly reconsider the calculation and thereafter investigate the limit cases of the system.
As *Edwards and Schwarz* [2011] showed, one can analytically calculate the radial displacement u_r for the special case of a two-dimensional disc of radius r_0, which is elastically coupled to its environment and subjected to a constant isotropic contraction σ_0 (see Figure 1.9B). The radial displacement field u_r, which is the only non-zero component of the displacement field, yields

$$u_r\left(r\right) = -l_\mathrm{p}\frac{\sigma_0 h_\mathrm{c}}{\lambda+2\mu} \cdot \frac{I_1\left(\frac{r}{l_\mathrm{p}}\right)}{I_0\left(\frac{r_0}{l_\mathrm{p}}\right) - \frac{2\mu}{\lambda+2\mu}\frac{l_\mathrm{p}}{r_0}I_1\left(\frac{r_0}{l_\mathrm{p}}\right)}\,, \tag{5.10}$$

with the Lamé coefficients $\lambda = {\nu_\mathrm{c}E_\mathrm{c}h_\mathrm{c}}/{1-\nu_\mathrm{c}^2}$ and $\mu = {E_\mathrm{c}h_\mathrm{c}}/{2(1+\nu_\mathrm{c})}$, and the modified Bessel functions of first kind I_0 and I_1. The remaining parameters are explained in the previous subsection.
Equivalent to the one-dimensional model, the total fraction force $T_{2\mathrm{D}}$ can be calculated

by summing over all stress magnitudes:

$$\begin{aligned} T_{2\mathrm{D}} &= \int_{A_0} Y|u_r|\mathrm{d}A = Y\int_0^{2\pi}\mathrm{d}\phi\int_0^{r_0}\left(-u_r\left(r\right)\right)\cdot r\mathrm{d}r \\ &= \frac{2\pi Y l_\mathrm{p}\sigma_0 h_\mathrm{c}}{\lambda+2\mu}\cdot\frac{\int_0^{r_0} I_1\left(\frac{r}{l_\mathrm{p}}\right)\cdot r\mathrm{d}r}{I_0\left(\frac{r_0}{l_\mathrm{p}}\right)-\frac{2\mu}{\lambda+2\mu}\frac{l_\mathrm{p}}{r_0}I_1\left(\frac{r_0}{l_\mathrm{p}}\right)} \qquad (5.11) \\ &= \pi^2 r_0 h_\mathrm{c}\sigma_0\frac{I_1\left(\frac{r_0}{l_\mathrm{p}}\right)L_0\left(\frac{r_0}{l_\mathrm{p}}\right)-I_0\left(\frac{r_0}{l_\mathrm{p}}\right)L_1\left(\frac{r_0}{l_\mathrm{p}}\right)}{I_0\left(\frac{r_0}{l_\mathrm{p}}\right)-\left(1-\nu_\mathrm{c}\right)\frac{l_\mathrm{p}}{r_0}I_1\left(\frac{r_0}{l_\mathrm{p}}\right)}\,, \qquad (5.12) \end{aligned}$$

where $L_n\left(x\right)$ is the modified Struve function.[3] One has $L_0\left(0\right)=L_1\left(0\right)=0$, hence for soft substrates we get

$$l_\mathrm{p}\to\sqrt{\frac{E_\mathrm{c}h_\mathrm{c}h_\mathrm{eff}}{\pi E_\mathrm{s}}}\xrightarrow[E_\mathrm{s}\to 0]{}\infty\,, \qquad (5.13)$$

and thus $T_{2\mathrm{D}}\to 0$, as one would intuitively expect. For stiff substrates, l_p decreases to the minimal value

$$l_\mathrm{p}^{\min}=\sqrt{\frac{E_\mathrm{c}h_\mathrm{c}L_\mathrm{c}^2}{N_\mathrm{a}k_\mathrm{a}}}\,, \qquad (5.14)$$

and $T_{2\mathrm{D}}$ saturates at its maximal value given by Equation 5.12. The rate at which the total force increases towards the saturation value is dictated by the two distinct factors ${N_\mathrm{a}k_\mathrm{a}}/{L_\mathrm{c}^2}$ and $E_\mathrm{c}h_\mathrm{c}$.

In accordance with the calculations carried out in Chapter 4, we use the two asymptotic trends of the modified Bessel functions $I_n\left(x\right)$ to gain insight into the functional dependence of $T_{2\mathrm{D}}$ on r_0. For $x\gg 1$, one has

$$I_n\left(x\right)\xrightarrow[x\gg 1]{}\frac{\exp x}{\sqrt{2\pi x}}\,. \qquad (5.15)$$

By using this approximation in Equation 5.12 and expanding to first order in ${r_0}/{l_\mathrm{p}}$, we find

$$\frac{T_{2\mathrm{D}}}{2\pi r_0}\approx\sigma_0 h_\mathrm{c}\left[1+\left(\frac{1}{2}-\nu_\mathrm{c}\right)\frac{l_\mathrm{p}}{r_0}+\mathcal{O}\left(\left(\frac{l_\mathrm{p}}{r_0}\right)^2\right)\right]\,. \qquad (5.16)$$

Thus, for a two-dimensional system, the relation between the total force and radius r_0 is different from the one-dimensional case, as also Figure 5.7B demonstrates. Here, for increasing circle radius $r_0\gg l_\mathrm{p}$, the total force shows a linear dependence of the radius. For increasing penetration length l_p, this linear regime is delayed to larger radii.

In the opposite limit, $x\ll 1$, the Bessel functions can be approximated as

$$I_n\left(x\right)\xrightarrow[x\ll 1]{}\frac{1}{n!}\left(\frac{x}{2}\right)^n\,, \qquad (5.17)$$

[3] Relations 5.12, 5.16 and 5.18 obtained by courtesy of Assaf Zemel, Hebrew University of Jerusalem.

and in particular $I_0(x) \approx 1$ and $I_1(x) \approx x/2$. With this approximation, we find the following scaling of the total force using Equation 5.12:

$$\frac{T_{2D}}{2\pi r_0} \approx \frac{\sigma_0 h_c}{2(1+\nu_c)} \left(\frac{r_0}{l_p}\right)^2 . \tag{5.18}$$

Thus, different from the strain energy, the total force scales with the cubed radius of the disc (compare Equation 4.14).

5.3.3 Simulation Results

Figure 5.8A shows that both one- and two-dimensional model can explain the measured force-area-relation. For the one-dimensional model, we introduced a cell width $w_0 \approx 10\,\mu$m, yielding a cell area of $A = 2w_0 l_0$. The model unveils a slightly convex force-area-relation, which means that the region of the curve around $l_0 \lesssim l_p$ is selected as best fit. Indeed, the parameter optimization yields a penetration length $l_p = 10.77\,\mu$m (see Table A.6). The resulting fit value for the active stress amounts to $\sigma_0 = 1.25\,$MPa, which is about two orders of magnitude larger than usual stresses in fibroblasts (compare e.g. values in Table A.2).
We however argue in the following that the one-dimensional model offers an insufficient explanation in our situation. The idea in the 1D model, that the increase of an area A_0 can be represented as an increase of a length l_0 is wrong, because the anisotropy of the platelets is not large enough to neglect traction stresses which are far away from the major dipole axis and act perpendicular to it. We would, for example, get more realistic values if replacing l_0/l_p with $(l_0/l_p)^2$ in the total force function. This would yield fitting results in the order of $\sigma_0 \sim 100\,$kPa, which is closer to the stress magnitude inferred by means of the two-dimensional model (see below). Therefore, we prefer the 2D model in the following.
The two-dimensional model generates a concave fit due to the relationship $T_{2D} \propto \sqrt{A_0}$ for large A_0. The parameter optimization yields a force penetration length $l_p = 1.78\,\mu$m and a contractile stress $\sigma_0 = 162.70\,$kPa, i.e. the contractile stress is up to two orders of magnitude larger than the typical stiffness of platelets, which was measured to be $E_c = 5\,$kPa [*Lam et al.*, 2011]. This result distinctly differs from the ratio between stress and stiffness for fibroblasts, which is at the order of 1 (compare Table A.5). The fit curve of the two-dimensional model in Figure 5.8A displays the regime $l_0 \gtrsim l_p$, i.e. the transition regime towards a linear force-radius-relation.
Figure 5.8B shows the scaled maximal force $F_{max}/2\pi r_0$ as a function of the platelet radius r_0, which reveals two central cell characteristics. In the limit of large r_0, the curve slowly saturates at an asymptotic value $\sigma_0 h_c$, as calculated in Equation 5.16. In practice, we find that this saturation level is only reached at cell radii which are much larger than the typical platelet size. The scatter plot furthermore does not rule out the possibility that σ_0 is a function of the cell radius itself. In the limit of small r_0, the rate of increase of $F_{max}/2\pi r_0$ with r_0 is determined by $1/l_p^2$, as demonstrated in Equation 5.18.
We can validate our obtained value for the force penetration length by fitting the traction

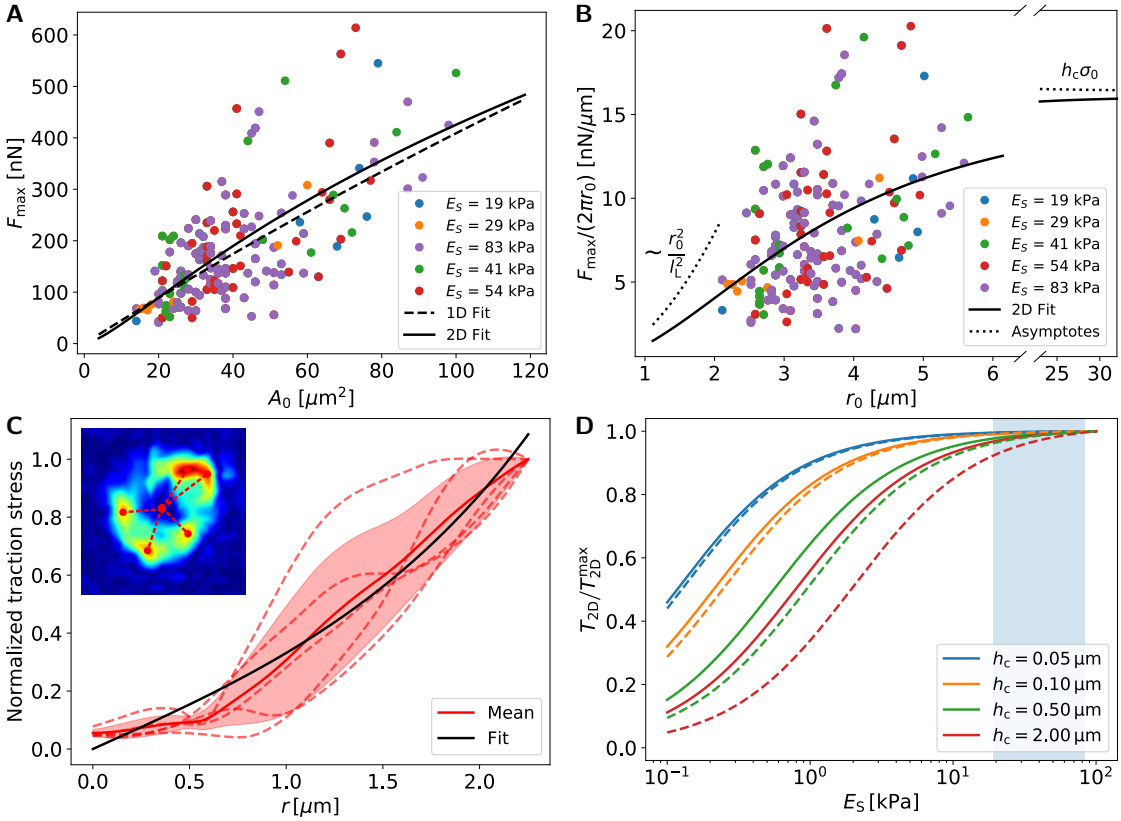

Figure 5.8: Both one- and two-dimensional active solid model can describe the relationship between final spreading area $A_0^\star$ and maximal force amplitude $F_{\max}$. **(A)** Data points and best fits for all measured cells. The *dashed* line shows the fit by the one-dimensional model, while the *solid* line refers to the two-dimensional model. **(B)** Scaled total force as a function of the platelet radius. The *solid* line provides the best fit of the two-dimensional model to the data. The *dotted* lines show the respective asymptotes to the mean cell behavior. **(C)** Determination of the force penetration length by means of the measured traction stress data. The *inset* shows, in *red* color, the lines along which we measured the traction stress profile. These are shown as *red dashed* lines in the main plot. The *red solid* line denotes the mean profile and the *shaded* region its standard deviation. The *black* line illustrates the model fit to the mean profile, yielding a penetration length $l_{\mathrm{p}} = 1.3\,\mu$m. **(D)** Effect of platelet thickness and the stiffness of the cell-substrate adhesion bonds on the regime of the mechanosensitivity of platelets. The *solid* lines correspond to an adhesion layer stiffness density ${}^{N_a k_a}/_{L^2} = 0.3\,{}^{nN}/_{\mu\mathrm{m}^3}$, which is an estimate from the experimentally acquired penetration length in Panel C. The *dashed* lines refer to ${}^{N_a k_a}/_{L^2} = 1.0\,{}^{nN}/_{\mu\mathrm{m}^3}$. The *light blue* rectangle shows the regime of substrate stiffnesses used in this chapter.

profile given by Equation 5.10 multiplied with Y to the reconstructed traction patterns, as illustrated in Figure 5.8C. Indeed, we find a typical value of $l_{\mathrm{p}}^{\mathrm{exp}} = 1.3\,\mu$m, which is close

to the theoretically obtained value and thus further supports our model assumptions.
We can now use the deduced force penetration length from the two-dimensional model to explain the apparent lack of mechanosensitivity shown in Figure 5.4A. With the measured $l_\mathrm{p}^\mathrm{exp}$ as well as E_c and h_c taken from Table A.6, and the assumption that we deal with stiff substrates as compared with the platelet stiffness, we can estimate the adhesion layer stiffness density from Equation 5.14, yielding

$$\frac{N_\mathrm{a} k_\mathrm{a}}{L_\mathrm{c}^2} \approx \frac{E_\mathrm{c} h_\mathrm{c}}{(l_\mathrm{p}^\mathrm{exp})^2} \approx 0.3\,{}^{\mathrm{nN}}/_{\mu\mathrm{m}^3}\,. \tag{5.19}$$

Figure 5.8D shows the relation between the theoretical total force T_2D and the substrate stiffness E_s for the parameter values given above and for a varying cell height h_c. For a typical height of $h_\mathrm{c} = 100\,\mathrm{nm}$, our model reveals that, in the investigated substrate stiffness regime, the total force does not vary with the substrate stiffness. Platelet mechanosensitivity would only occur at substrate stiffness values far below $E_\mathrm{s} = 1\,\mathrm{kPa}$. We find that a measurable mechanosensitivity in the investigated substrate stiffness regime will only be registered if a cell is either higher or stiffer by a factor of 10 , or if its adhesions are stiffer by a factor of 10 , as indicated by the dashed lines.

5.4 Conclusion

In this chapter, we used TFM to determine the temporal evolution of traction stresses exerted by human blood platelets when placed on an elastic substrate and stimulated via thrombin. We found that after a time span of several minutes, the platelets reached a plateau in the order of 10 fJ in terms of contractile energy and 100 nN in terms of total force, thus displaying contractile capabilities similar to those of the ten-times larger fibroblast cells.
An eigenvalue analysis of the platelet dipole tensor revealed a small anisotropy of the exerted force, which is compatible with a random distribution of a few force generating centers, in agreement with the observed shapes and traction patterns. In particular, we could estimate the average force anisotropy to be ${}^{D_1}/_{D_2} = 2.3$, with suggests a slightly anisotropic intracellular level of organization.
We further observed two distinct contractile behaviors of blood platelets: Cells which oscillate with a frequency of around 10 mHz during contraction and non-oscillating cells. The contractile behavior was, however, found to be unspecific with respect to the total force, the spread area, the substrate stiffness and the degree of force anisotropy.
Interestingly, both total force and spread area of the platelets were independent of the substrate stiffnesses used in the experiment, which were in the range $19 - 83\,\mathrm{kPa}$. This indicated a lacking mechanosensitivity of blood platelets, an observation which was already found by *Qiu et al.* [2014] for this particular range of substrate rigidity. However, the relation between total force and spread area exhibited a positive correlation, which was already observed in Chapter 4 for the case of fibroblasts.
We therefore used our two-dimensional active solid model to explain the force-area-relation, yielding a typical force penetration length of $l_\mathrm{p} \approx 1.8\,\mu\mathrm{m}$ and contractile stress

of $\sigma_0 \approx 163\,\mathrm{kPa}$. The ratio between the contractile stress and the typical stiffness of platelets thus turns out to be of the order of 100, which is in contrast to the typical ratio $\sigma_0/E_\mathrm{c} \approx 1$ in the case of fibroblast cells (see e.g. Chapters 3 and 4).
We could finally show that the small thickness of platelets allows to explain the observed lack of mechanosensitivity. For decreasing cell height, i.e. an effective softening of the cell, the stiffness sensitivity regime is shifted to lower values of substrate stiffness, which we demonstrated by means of our continuum model. In our case, this stiffness sensitivity regime is about two orders of magnitude lower than the stiffness regime used in the course of the experimental study. Due to the high dissimilarity of platelet and substrate stiffness, the platelets are not able to distinguish the existence of an elastic substrate from a completely rigid substrate. A similar decrease of cellular mechanosensitivity upon increasing dissimilarity of cell and substrate stiffness was found e.g. by *Abdalrahman et al.* [2017] by means of FE simulations of fibroblasts.

6 An Elastic Theory of Leader Cell Formation

Biological processes like organogenesis, wound healing or cancer invasion all have in common that they require the collective coordinated migration of a group of cells [*Friedl and Gilmour*, 2009; *Haeger et al.*, 2015]. In the course of this migration, instead of moving individually, many cells connect to assemblies like sheets or clusters while still preserving the actin CSK-based mechanisms of a single cells to generate the movement, which is then mediated via adherens junctions to the remaining cells. A particular example for collectively migrating cells are epithelial cells, which usually move in a dense supracellular sheet without letting single cells escape at the front edge of the tissue.
A characteristic feature of collective cell migration is the formation of leader cells at the free edge of the tissue [*Haeger et al.*, 2015]. During the collective migration of a monolayer of epithelial cells, which is a standard biological model for wound healing, leader cells exhibit a prominently large protrusion of the lamellipodium towards the free edge, feature large FAs and are usually highly polarized. Due to these properties, these cells accomplish a directed guidance for the group of migrating cells [*Mayor and Etienne-Manneville*, 2016]. The origin and the dynamics of the formation of leader cells is, however, still largely unexplored. In particular, it is still elusive at what level, monolayer bulk or interface, the formation of leader cells is triggered and why only a fraction of cells at the interface become leader cells.
An established fact is that, besides biochemical signaling like the differential activity of RhoA, cellular forces play an important role during e.g. the collective closure of a wound, with the largest forces usually attributed to the leader cells [*Brugués et al.*, 2014; *Reffay et al.*, 2014]. In this sense, any attempt to decipher the origin and dynamics of leader cells has to consider the stresses exerted during the collective migration.
Force-based modeling of collective cell migration is a dense field [*Hakim and Silberzan*, 2017], ranging from the collective modeling of single cells interacting via attracting or repelling cohesions, e.g. via the Cellular Potts Model [*Albert and Schwarz*, 2016], to continuum models, representing the monolayer either as a continuum solid [*Rausch et al.*, 2013; *Mertz et al.*, 2013] or fluid [*Blanch-Mercader et al.*, 2017]. When it comes to describe the cooperative formation and protrusion of leader cells at the free edge of the monolayer, in general either an *interface-based* or a *bulk-based* approach come into question, both encouraged by the underlying experimental evidence.
A prominent example for an interface-based theory is the work by *Mark et al.* [2010], who model leader cells as finger-like outgrowths originating from a continuous and active one-dimensional membrane representing the pluricellular actomyosin cable running along the layer interface [*Reffay et al.*, 2014]. In this model, the underlying local curvature of

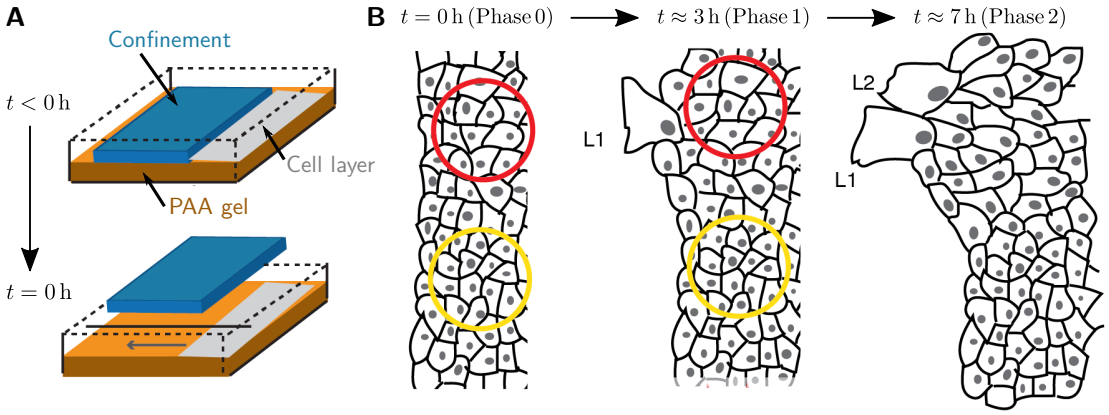

Figure 6.1: Experimental procedure and definitions of phases of leader cell formation. **(A)** At the beginning of the experiment, the cell monolayer is confined to a small region due to a PDMS sheet acting as a boundary. At time $t = 0\,\mathrm{h}$, the boundary is removed and the cell layer is allowed to spread on the elastic PAA substrate. **(B)** Definition of three characteristic phases during the formation of leader cells: *Phase 0* is characterized by high normal and traction stresses right behind the prospective leader cell (*red circle* as compared to *yellow circle*). During *Phase 1*, the leader cell (L1) and its follower cells evolve. In *Phase 2*, a second leader (L2) appears from the leader-follower-outgrowth. Courtesy of Medhavi Vishwakarma, MPI Stuttgart, with minor modifications.

the cell layer front determines about the ability of the cells to generate motility, giving rise to a dynamic instability. A locally highly curved surface leads to a high cellular motility, preventing neighboring regions along the membrane from adopting a larger velocity. *Tarle et al.* [2015] further build up on this model by coupling a particle-based simulation to the existing model, allowing the authors to closely reproduce crucial parts of the dynamics of leader cells. However, their model requires a highly detailed and complicated numerical simulation, involving hand-made local rules and a large parameter space with parameters which are not directly tangible from the experiments. Furthermore, their model rather aims at precisely describing the protrusion of the leader cells than pursuing their origin, allowing a spontaneous formation of leader cells.

In the following, we will show by means of TFM and a bulk-based continuum approach, allying previous work e.g. by *Rausch et al.* [2013], that the position of emerging leader cells is known from the mechanical activity of the would-be follower cells at their back even before their emergence and that the origin, maintenance and splitting of leader cells can be deduced from simple mechanisms known from elasticity theory (see Sections 6.2 and 6.3). Our approach will be based on collaborative work together with Medhavi Vishwakarma, Jacopo Di Russo, Tamal Das and Joachim Spatz from the Max-Planck-Institute for Complex Systems in Stuttgart, who conducted the experiments and analyzed the experimental data, which is briefly described in Section 6.1.

In particular, we will use our two-dimensional continuum model introduced in the previous three chapters to explain that a leader cell will emerge only if the lateral distance

to neighboring leader cells is such that both cells do not mechanically interact. By means of our modeling approach, we will be able to elucidate the dependence of the characteristic distance between neighboring cells upon chemical and physical modulations of the monolayer. We will finally, in Section 6.4, introduce an exactly solvable one-dimensional model which will allow to interpret experimental findings based on analytical calculations, but will also reveal that a purely mechanical one-dimensional description is not capable to fully explain the benefit of sticking to characteristic distances in an epithelial monolayer.
It has to be noted here, that, since we will focus on the very early time points of the expansion of the monolayer and are not aiming at predicting the dynamical expansion of the boundary, but rather the propagation of mechanical stress through the cell monolayer, a purely elastic model is fully justified for the purpose of the following work. In general, one might combine our model with a viscous model, such as the work by *Blanch-Mercader et al.* [2017], to obtain a dynamical description of the monolayer expansion.

6.1 Quantification of Characteristic Distances during Collective Cell Migration

Confluent monolayers of MDCK epithelial cells were grown within an initially confined rectangular area on a PAA gel of stiffness $E_\mathrm{s} = 11\,\mathrm{kPa}$ and Poisson's ratio $\nu = 0.5$, as illustrated in Figure 6.1A. At time $t = 0$, the confinement was lifted off, inducing a quasi-two-dimensional migration of the epithelial sheet.
Figure 6.1B schematically depicts the characteristic dynamics at the wound margin after removing the confinement. During approximately the first hour, we did not observe any noticeable lamellipodial protrusion along the wound margin. This time span will be referred to as *Phase 0* in the following discussion. During the subsequent about three hours, the first lamellipodial protrusions of the would-be leader cell appeared and, as the migration continued, the leader cell generated an outgrowth by pulling against its follower cells. This period will be denoted as *Phase 1* in the following. Finally, after about four hours, during the so-called *Phase 2*, additional leader cells started to appear at the front of the existing outgrowth, thereby splitting the total group of follower cells. We identified these three phases as a general mechanism during the formation of leader cells along the wound margin.
By analyzing the margin of the epithelial layer during Phase 1 by means of image analysis of phase-contrast microscopy images, we found that neighboring leader cells exhibit a surprisingly constant distance of about $150\,\mu\mathrm{m}$, which we denote as leader-to-leader distance d_LL (see Figure 6.2A).
We then were interested in the influence of the geometry of the confinement on the distance d_LL. For this, we used different confinement profiles with introduced invaginations, aiming at triggering the evagination of emerging leader cells at the predefined positions (see Figure 6.2B). However, we found that, after some time span of about 1 h, the preexisting outgrowth vanished and new outgrowths appeared, featuring the typical leader-to-leader distance of the unbiased case, as shown in Figure 6.2C. This suggests that the distance

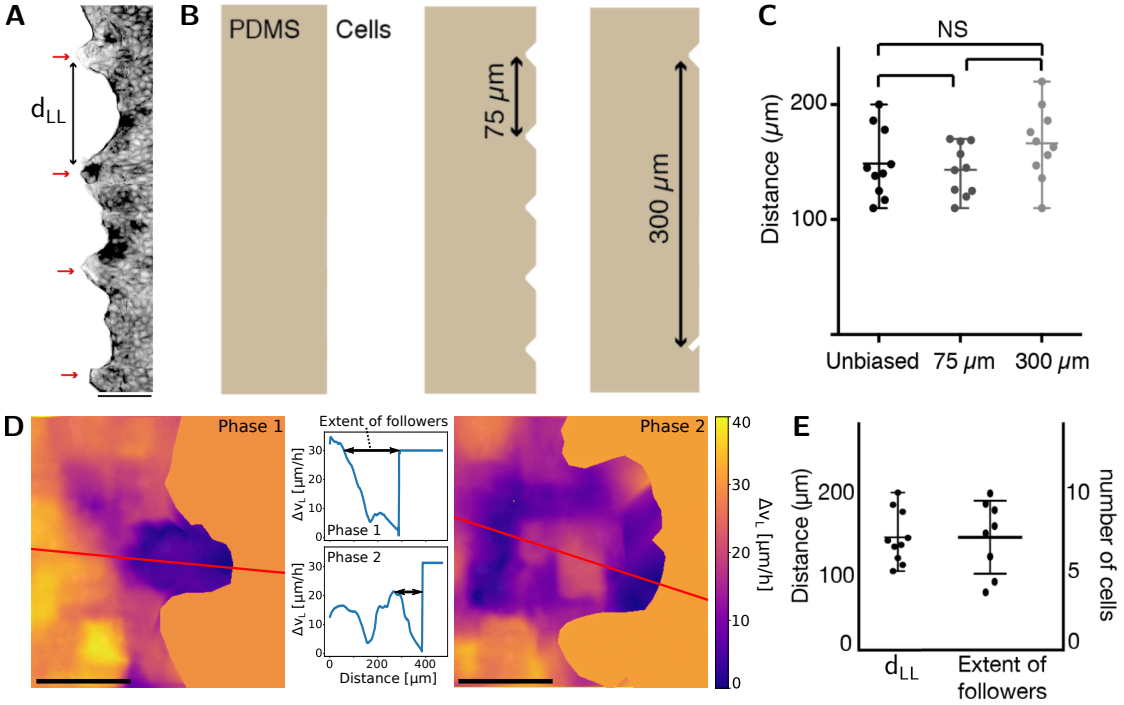

Figure 6.2: The lateral leader-to-leader distance d_{LL} as well as the transversal outreach of the leader cell are both equal and constant along the margin of the cellular monolayer. **(A)** Representative image of the margin of the cellular monolayer during collective cell migration. The characteristic leader-to-leader distance d_{LL} is constant along the margin. **(B)** Confinement profiles with differently spaced notches have been used in order to induce leader cells at pre-defined positions. **(C)** Irrespective of the introduced geometrical bias, leader cells emerge at constant distances d_{LL}. **(D)** *Color maps* show the absolute deviation Δv_{L} of the local velocity $\mathbf{v}$ of the monolayer from the leader velocity $\mathbf{v}_{\mathrm{L}}$ for Phase 1 and 2. The extent of followers is defined as the size of the interval in which Δv_{L} is smaller than $|\mathbf{v}_{\mathrm{L}}|$ and increases with increasing distance from the leader cell. *Inset* plots show Δv_{L} as a function of the position along the *red line* highlighted in the respective color map. In both cases, the red line is oriented along the direction of $\mathbf{v}_{\mathrm{L}}$. **(E)** During Phase 1, average transversal and lateral characteristic distances of the cell layer coincide, i.e. also the transversal evagination induced by a single leader cell is in the range of the lateral leader-to-leader distance d_{LL}. Scale bars are 100 μm. Courtesy of Medhavi Vishwakarma, MPI Stuttgart, with minor modifications.

between neighboring leader cells is rather a property of the cell layer and the substrate than of the geometry of the wound margin.

We then turned to the quantification of the predominant transversal distance during the formation of leader cells, defining the spatial extent of the outgrowth evoked by a leader cell. For this, we measured the cellular velocities in the vicinity of the margin relative to the velocity $\mathbf{v}_{\mathrm{L}}$ of the leader cell between Phase 1 and 2. In particular, we

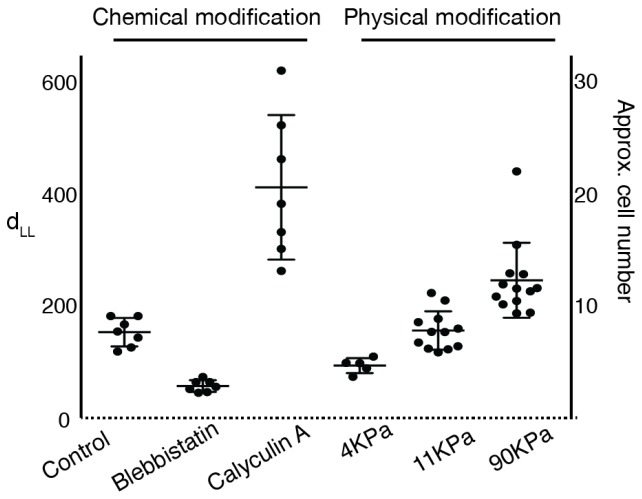

Figure 6.3: Both a drug treatment and an increase of the substrate stiffness have an influence the leader-to-leader distance d_{LL}. Addition of blebbistatin reduces the distance, while addition of Calyculin A increases d_{LL}. Increasing the substrate stiffness also increases d_{LL}. In each case, the resulting leader-to-leader distance remains constant throughout the monolayer. Courtesy of Medhavi Vishwakarma, MPI Stuttgart.

used the optical flow algorithm, presented in Section 2.1.1, to calculate velocities $\mathbf{v}\,(x, y)$ from the phase-contrast images and introduced the deviation from the leader velocity $\Delta v_{\mathrm{L}} = \|\mathbf{v} - \mathbf{v}_{\mathrm{L}}\|_2^2$ to quantify the similarity of the cellular velocity with respect to the leader cell, defining $\Delta v_{\mathrm{L}}^{\max} = \|\mathbf{v}_{\mathrm{L}}\|_2$ as the maximal deviation for which a cell is still counted as a follower cell. It has to be noted that, in general, one could also use an autocorrelation measure here.

Figure 6.2D and 6.2E show both qualitatively and quantitatively that, in the direction perpendicular to the wound margin, the characteristic length in the cell layer is at the order of 150 μm. This omnipresence of the characteristic distance d_{LL} within the cell layer suggests that, macroscopically and irrespectively of the heterogeneity of the single cells, the cell layer can be treated as a bulk with isotropic mechanical properties to the first order. We also find that the velocity decay length drastically decreases after the transition from Phase 1 to 2, suggesting that the leader cell and its outgrowth mechanically decouple from the remaining layer.

We finally wondered whether the magnitude of d_{LL} remains constant if manipulating the properties of the actin CSK either chemically by means of drugs or physically by means of regulating the stiffness of the substrate on top of which the cell layer is grown. For chemical modification, we treated the cells either with the non-muscle myosin-II inhibitor blebbistatin (concentration: 5 μM) or the myosin-light-chain phosphatase inhibitor calyculin A (concentration: 1 nM). For physical modulation, we changed the substrate stiffnesses from 11 kPa (control case) either to 4 kPa or to 90 kPa.

Figure 6.3 illustrates that the chemical and physical modulation significantly influence

the leader-to-leader distance d_{LL}. The addition of blebbistatin leads to a decrease of d_{LL} by a factor of about 2, while adding calyculin A on average doubles d_{LL}, of which both however depend on the concentration of the drug. Furthermore, we measured a positive correlation between the substrate stiffness and d_{LL}, thus increasing the substrate stiffness decreases the propensity of the cells to become a leader cell and vice versa.
These results indicate that both chemical and physical parameters of the cell layer and its environment influence the characteristic length scales in the cell layer. In the following sections, we will therefore examine these observations in more detail by means of TFM and computational modeling.

6.2 Quantification of Cellular Stresses during Collective Cell Migration

We used TFM to determine the traction stresses exerted by the cell monolayer in the first phases of collective migration introduced in the previous section. For this, monolayers were grown on the substrates of a typical stiffness of $E_{\mathrm{s}} = 11\,\mathrm{kPa}$ and Poisson's ratio $\nu = 0.5$ containing fluorescent beads of diameter $0.5\,\mu\mathrm{m}$. In particular, we determined the displacements by means of PIV and used regularized FTTC to determine traction stresses (see Chapter 2.1 for a detailed description).
We then applied Monolayer Stress Microscopy (MSM) to infer the internal stresses inside the cell layer, as described by *Tambe et al.* [2011]. In this method, we make the simple assumption that the cell layer is a two-dimensional elastic sheet and obtain internal stresses $\sigma_{ij}(x, y)$ by enforcing the two-dimensional force balance equation $\sigma_{ij,j} = T_i$. Here, T_i represent the measured local traction stresses along the free boundary of the layer and, due to Newton's third law, at the same time, components of the shear stress exerted by the cell layer. Enforcing zero-stress boundary conditions at the boundary of the layer and zero-displacement boundary conditions at the edge of the field of view, we then use a FE simulation to deduce the internal stresses from the minimization of the potential energy per unit thickness $\iint_\Omega (1/2\sigma_{ij}\epsilon_{ij} - T_j u_j)\,\mathrm{d}x\mathrm{d}y$ with respect to the displacements u_j. Here, ϵ_{ij} is the linearized strain tensor and Ω the area of the layer.
From the displacements, we can calculate the components of the stress tensor by using the constitutive relation of a passive two-dimensional elastic medium $\sigma_{ij} = \lambda\epsilon_{kk}\delta_{ij} + 2\mu\epsilon_{ij}$, with Lamé coefficients λ and μ. The stress tensor is further diagonalized, yielding the eigenvalues $\sigma_{\max}$ and $\sigma_{\min}$, which determine the quantity $\sigma_{\max}+\sigma_{\min}/2$ to be the *local average normal stress* (or abbreviated *normal stress*) and $\sigma_{\max}-\sigma_{\min}/2$ to be the *maximum shear stress*. The direction of the eigenvector belonging to the largest absolute eigenvalue is used as the *principal stress orientation*, while the direction of the shear stress is rotated by 45 ° to this axis.
In the following discussion, we will illustrate the negative of the normal stress, such that all material compressions are positive, while extensions become negative.

Cellular Stresses during Leader Cell Formation Figure 6.4A, C and D show representative images of the traction stress and inferred normal and shear stress, respectively,

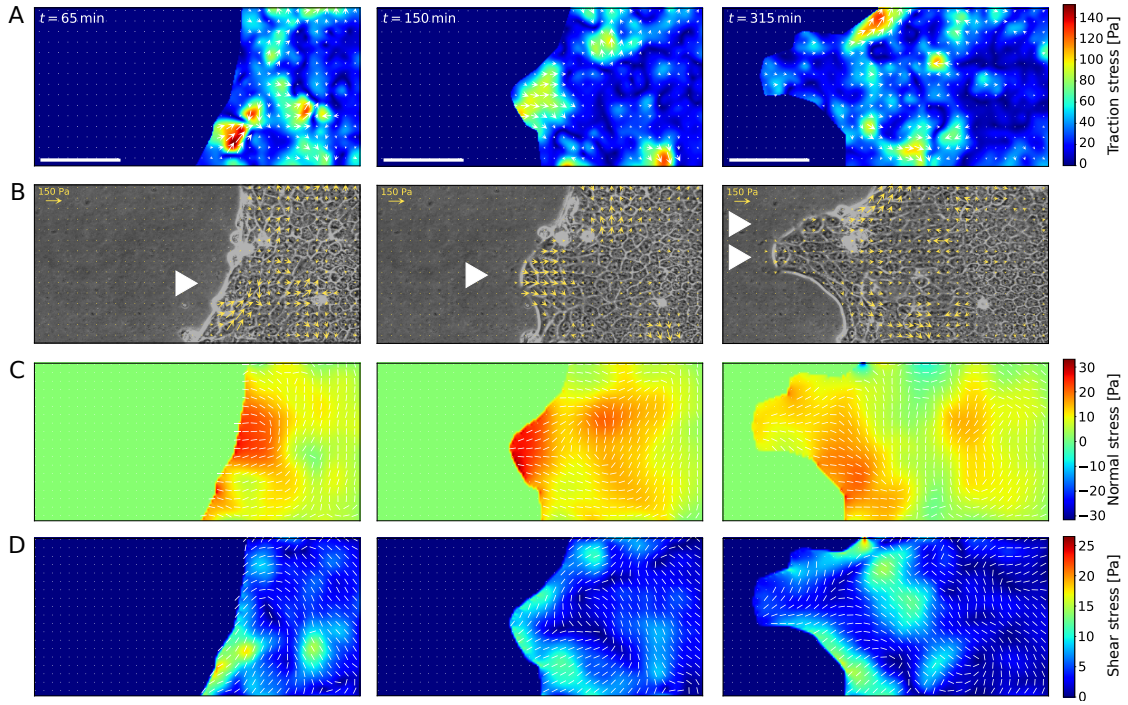

Figure 6.4: Follower cells behind the prospective leader cell exert highest stresses during Phase 0. During Phase 1, the outgrowth containing the leader cell exerts the highest stresses. Panels **A-D** show exemplary traction stress magnitudes, traction stresses on top of phase-contrast images of the monolayer, normal and shear stresses, respectively. In Panel **C**, positive values denote compressed regions, while negative values represent tensed regions. From *left* to *right*, representative images for Phase 0, 1 and 2 are depicted. Leader cell outgrowths are indicated by *white triangles*. Scale bars are 100 μm.

which are exerted by an advancing monolayer for the three phases of leader cell formation described so far. In Figure 6.4B, we further see the traction stress on top of the corresponding phase-contrast image of the monolayer, with emerging or advancing outgrowths indicated by a white triangle.

The left column of Figure 6.4 illustrates the traction and monolayer stress during Phase 0, i.e. shortly before the appearance of a leader cell. Apparently, even before a leader cell emerges, we find both increased traction and monolayer stresses in the region behind the future leader cell, as compared to peripheral regions. This suggests that even before the appearance of the outgrowth, the follower cells use mechanical cues to decide about their prospective leader cell (compare with stress magnitudes in non-leader regions, shown in Figure A.3).

We can further observe from the traction stress pattern in Figure 6.4 that the stress tends to increase again at a distance of about 200 μm above the appearing leader cell, indicating that a second leader cell is about to emerge at the top edge of the image (compare also Figure A.3). This distance approximately coincides with the typical distance d_{LL} between

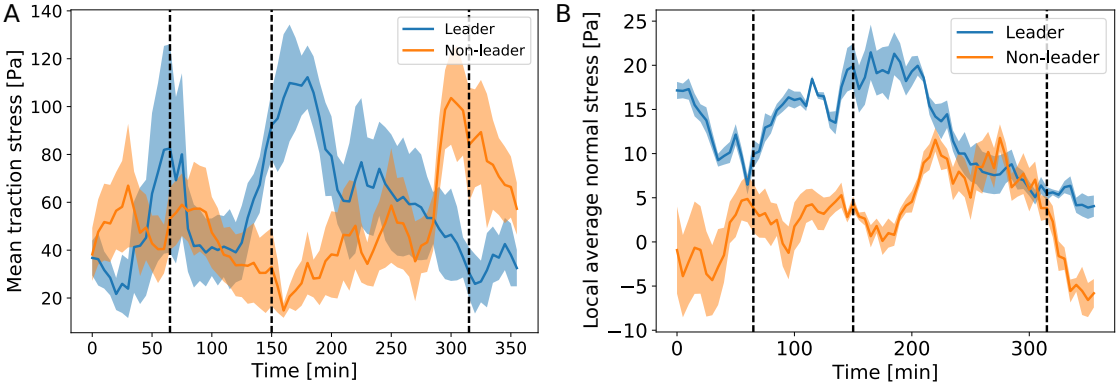

Figure 6.5: Mean traction stress **(A)** and normal stress **(B)** around the leader cell and a non-leader cell at the monolayer front show that the highest stresses during leader cell emergence are exerted by the cells in the vicinity of the leader cell. The averaged stresses were determined from all stresses, which are larger than 10 Pa for the traction stress or larger than 1 Pa for the normal stress, within a circular region of radius 25 μm around the leader or non-leader cell, respectively. *Full lines* denote mean values, while *shaded regions* are standard deviations. *Dashed lines* show the time points corresponding to the representative images for Phase 0, 1 and 2 from Figure 6.4.

neighboring leaders which we found in Section 6.1. In the following, we will refer to this typical force correlation length as d_{FC}.

The central column of Figure 6.4 depicts the traction and monolayer stresses during Phase 1. Here, we can clearly see that the leader-follower-outgrowth generates the largest stress and, with this, pulls against the remaining bulk towards the cell-free region. Regions along the layer boundary apart from the outgrowth seem to exert negligibly small stresses. For the leader cell, we find maximal traction stresses in the order of 100 Pa and normal stresses of about 30 Pa, which are in good accordance with e.g. an earlier study by *Rausch et al.* [2013].

The right column of Figure 6.4 finally shows the traction and monolayer stresses during Phase 2. We now find two traction stress hot spots directly underneath the two leader cells emerging from the outgrowth, although the stress magnitude drastically decreased by a factor of 2. This effect can be explained by the fact that the outgrowth is now mechanically decoupled from the remaining bulk and, thus, exhibits a much smaller size as compared with the full layer. We will discuss this observation in the following section by means of our continuum model.

At the same time, other even larger stress hot spots appear, indicating that, due to the advancement of the outgrowth, the remaining layer is pulled to proceed into the direction of the cell-free region. As both the traction and monolayer stress patterns demonstrate, these hot spots are located along the interface of the layer at the transitions of the outgrowth to the outgrowth-free region, which suggests a mediation of the direction of movement towards the outgrowth. This force mediation is very likely to be established by means of a pluricellular actin cable, which is usually present in monolayers along the

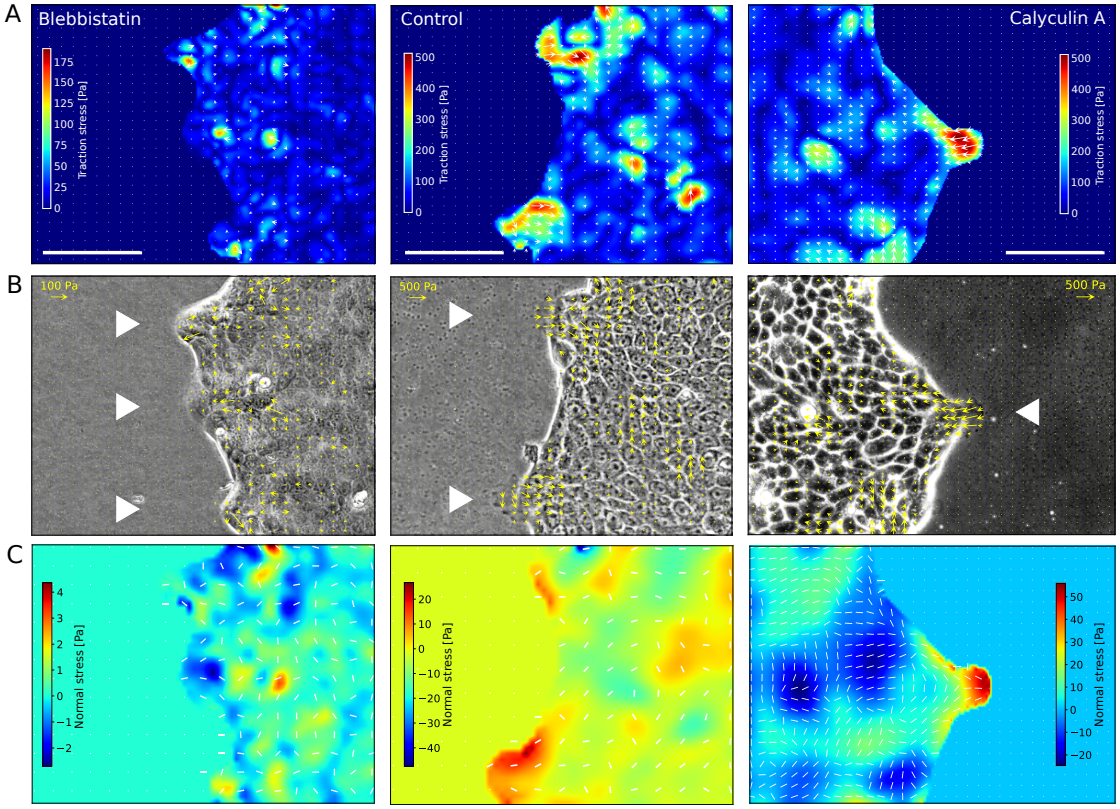

Figure 6.6: Addition of blebbistatin decreases both the overall stresses in the monolayer and the distance between leader cells, while addition of Calyculin A leads to an increase of both quantities. Panels **A-C** show exemplary traction stress magnitudes, traction stresses on top of phase-contrast images of the monolayer and normal stress magnitudes, respectively. In Panel **C**, positive values denote compressed regions, while negative values represent tensed regions. Leader cell outgrowths are indicated by *white triangles*. Scale bars are 100 μm.

leading edge [*Reffay et al.*, 2014].

We can quantify the mean traction and monolayer stress in the vicinity of the leader cell as compared to those in non-leader regions by averaging all traction stresses larger than 10 Pa and normal stresses larger than 1 Pa in a circular region of radius 25 μm around the leader cell and in a non-leader region. Figure 6.5 illustrates the resulting average stress over time.

We find that shortly before the leader cell appears, which is at about $t = 75$ min, the stresses in its vicinity increase and exceed those in the non-leader region. The deduced contractile stresses are significantly larger in the region around the leader cell, even before the leader cell emerges. With the advancement of the leader cell, both traction and contractile normal stresses around the leader cell increase even further, reaching a peak of about 100 Pa and 20 Pa after 3 h, respectively. Thereafter, the stresses decrease again to their baseline level, which can be mainly explained by the fact that the outgrowth steadily

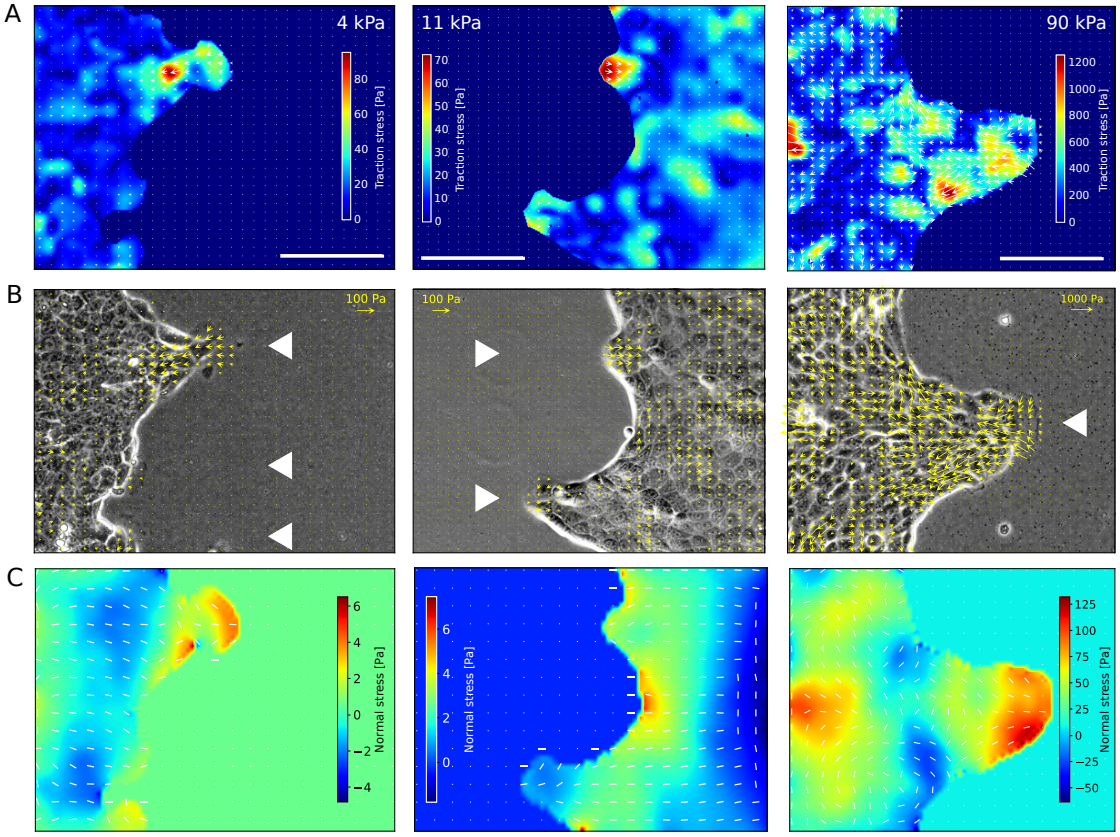

Figure 6.7: A decrease of the substrate stiffness decreases both the overall stresses in the monolayer and the distance between leader cells, while an increase of the substrate stiffness leads to an increase of both quantities. Panels **A-C** show exemplary traction stress magnitudes, traction stresses on top of phase-contrast images of the monolayer and normal stress magnitudes, respectively. In Panel **C**, positive values denote compressed regions, while negative values represent tensed regions. Leader cell outgrowths are indicated by *white triangles*. Scale bars are 100 μm.

decouples from the remaining bulk and, thus, lower stress magnitudes are required to effectively pull at the reduced number of cells. The remaining bulk is then pulled towards the outgrowth, which is indicated by the stress increase in the non-leader region.

Effect of Chemical and Physical Modulation on Leader Cell Formation We further compared traction and monolayer stresses in the advancing cell monolayers upon chemical modulation by means of blebbistatin or calyculin A with those of the unperturbed cell layer (see Figure 6.6). Here, we find that chemical modulation not only affects the typical distance between leader cells, but also the typical spatial variation of stresses, i.e. force correlation length d_{FC}. Addition of blebbistatin leads to a reduction of both d_{LL} and d_{FC} to about 100 μm, while treatment with calyculin A causes an increase of both

lengths. Moreover, the overall stress magnitudes decrease upon blebbistatin treatment and increase upon treatment with calyculin A. In the case of blebbistatin treatment, the stress field rather looks like a random pool of uncorrelated stresses, which indicates that the mechanical collaboration of cells is of short range. On the other hand, cells treated with calyculin A form a clear outgrowth whose contractile activity outweighs those of the remaining monolayer by far.
A similar modulation can be observed for a physical modification of the monolayer via changing the substrate stiffness (see Figure 6.7). Here, decreasing the substrate stiffness leads to a decreasing distance between both neighboring leader cells and neighboring traction and normal stress hot spots along the interface of the layer. Increasing the substrate stiffness not only increases the distances d_{LL} and d_{FC} dramatically, but also the stress magnitude exerted by the outgrowth by a factor of about 10. Furthermore, the spatial extension of the outgrowth is an order of magnitude larger than in the control case, such that several prospective leader cells can be found in one single outgrowth.
Overall, we find that typical distances between neighboring leader cells and neighboring stress hot spots coincide, which indicates that traction stresses are involved in leader cell formation during Phase 0, in the communication between leader cells in Phase 1 as well as in the splitting of outgrowths during Phase 2. We further conclude from the previous section that the cell monolayer can be considered as a continuum with isotropic material properties, since characteristic length scales coincide in both lateral and transversal direction of the layer. Therefore, we will introduce an active solid model in the following, which was already used in the previous chapters, to come up with a possible origin of these typical mechanical length scales.

6.3 Computational Investigation of the Formation of Leader Cells

The equality of both the characteristic distance d_{LL} between neighboring leader cells and the transversal maximal size of an outgrowth induced by a single leader cell, on the one hand, and the typical distances between traction stress peaks, on the other hand, suggests that mechanical forces are likely to play an important role in the process of leader cell formation, i.e. their origin, maintenance and splitting. Therefore, a good model aiming for the description of the system should consider the mechanistic influence of both the monolayer and its environment. In particular, the model should incorporate an elastic interaction with the environment representing the influence of the FAs and the substrate stiffness, and with this, allowing for forces to decay on a characteristic length scale, while making the largest traction stresses appear at the position of a leader cell.
For this, we will use the elastic continuum model we already introduced for single cells in Chapters 3–5, treating the whole monolayer as one single continuum bulk. As discussed above, we will skip the viscoelastic part, since we are not interested in the precise dynamics of the system, but only in internal and environmental influences on the penetration width of forces. A more complete mechanistic description would have to combine our model with a purely viscous model, such as those introduced by *Blanch-Mercader et al.* [2017].

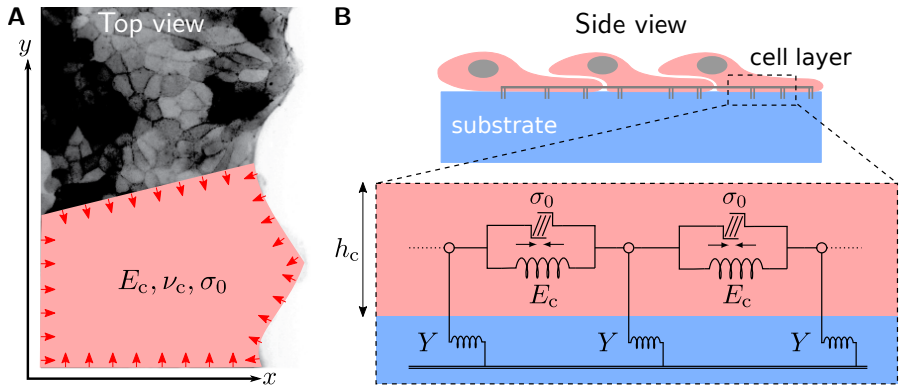

Figure 6.8: The cell monolayer is represented as a two-dimensional elastic sheet of elastic modulus E_c and negligible height h_c, Poisson's ratio ν_c and isotropic contraction stress σ_0. The parameter Y denotes the spring stiffness density, which describes the combined influence of focal adhesions and the substrate on the dynamics of the layer. **(A)** Top view and **(B)** side view of the modeled cell layer and its coupling to the environment.

We will, in the following, start with the description of the full model, and mainly specify on the description of Phase 1 and 2, followed by a discussion about the incorporation of chemical and physical modulations into the model. Although a full description of Phase 0 should contain biochemical elements which are triggering the emergence of large traction stresses exerted by the would-be followed cells, we will show by means of our model, why the origin of leader cells separated by a characteristic distance d_{LL} is mechanically favorable. We will finally conclude with simulation results, showing that our simple model can serve as a good description of the initiation of leader cell formation.

6.3.1 A Continuum Bulk-Based Model of the Epithelial Cell Layer

As Figure 6.8 depicts, we model the epithelial monolayer as an elastic continuum of stiffness E_c, Poisson's ratio ν_c, height h_c and active isotropic contractile stress σ_0. Furthermore, the elastic layer is elastically coupled to the environment via springs of constant spring stiffness density Y, as introduced by *Edwards and Schwarz* [2011]. The elastic coupling represents the contribution of both the focal adhesions and the elastic substrate to the mechanics of the cell layer. In the following, we will first derive the central equations of the model. The equations will then be solved numerically by means of the finite element software FEniCS [*Alnæs et al.*, 2015].
We can describe our model by using the two-dimensional force balance equation

$$\sigma_{ij,j} - Y u_i = 0\,, \tag{6.1}$$

with the stress tensor σ_{ij} and displacement u_i. By analogy with Chapters 3–5, the constitutive relation of the model is assumed to be

$$\sigma_{ij} = 2\mu\epsilon_{ij} + (\lambda\epsilon_{kk} + \sigma_0)\,\delta_{ij}\,, \tag{6.2}$$

with the linearized strain $\epsilon_{ij} = \frac{1}{2}(u_{i,j} + u_{j,i})$ and the two-dimensional Lamé coefficients λ and μ defined in Equations 3.36 and 3.37, respectively.
Inserting Equation 6.2 into 6.1 yields the differential equation

$$\sigma_{ij,j} = \lambda u_{k,ki} + \mu(u_{i,jj} + u_{j,ij}) + \sigma_{0,i} = Y u_i\,, \tag{6.3}$$

or

$$\frac{\lambda+\mu}{\lambda+2\mu}u_{j,ij} + \frac{\mu}{\lambda+2\mu}u_{i,jj} + \frac{1}{\lambda+2\mu}\sigma_{0,i} = \frac{u_i}{l_p^2}\,, \tag{6.4}$$

Since we assume a constant isotropic stress σ_0, its derivative will vanish within the bulk and appear as Neumann boundary condition of the elastic problem, which is why we term σ_0 also as the effective boundary stress. The parameter l_p denotes the *force penetration length*

$$l_\mathrm{p} = \sqrt{\frac{E_\mathrm{c}h_\mathrm{c}}{Y(1-\nu_\mathrm{c}^2)}}\,, \tag{6.5}$$

analogous to the expression in Equation 3.15. As described earlier in Chapters 3–5, we can use the calculations of *Banerjee and Marchetti* [2012] to express l_p as a function of the bulk and substrate parameters and, with this, estimate the stiffness density Y. Here, we use the formula

$$l_\mathrm{p} = \sqrt{\frac{E_\mathrm{c}h_\mathrm{c}L_\mathrm{L}L_\mathrm{c}}{k_\mathrm{a}} + \frac{E_\mathrm{c}h_\mathrm{c}h_\mathrm{eff}}{\pi E_\mathrm{s}}} \tag{6.6}$$

and

$$h_\mathrm{eff}^{-1} = \frac{1}{h_\mathrm{s}2\pi(1+\nu_\mathrm{s})} + \frac{1}{L_\mathrm{L}} \tag{6.7}$$

with parameters taken from Table A.7. In particular, we use as typical cell height $h_\mathrm{c} = 5\,\mu$m, which was deduced experimentally e.g. by *Tambe et al.* [2011]. The cell length is set to the typical length of $L_\mathrm{c} = 20\,\mu$m measured in the phase-contrast images, while the overall dimension of the monolayer is fixed to $L_\mathrm{L} = 1\,$mm.
So far, we have considered the mechanics of the bulk of the cell layer and will now incorporate the emergence of single leader cells into the model.
We simulate the formation of a leader cell via a two-step process, as sketched in Figure 6.9A-B. In both steps, we impose zero-displacement boundary conditions at the left boundary of the layer, periodic boundary conditions at the top and bottom boundary and zero-stress boundary conditions at the right, i.e. free, boundary.
First, the contractile layer is split into 2 parts, Ω_1 with horizontal extension $0.05L_x$ and Ω_1 with horizontal extension $0.95L_x$, where L_x is the total horizontal width of the layer. We decouple Ω_1 from the substrate and switch off the internal contractility, while Ω_2 remains contractile and elastically coupled. Leader cells are then initiated by pulling against two points at the boundary, represented via two-dimensional Gaussian-shaped forces of magnitude

$$F(x,y) = \frac{F_\mathrm{L}}{2\pi\sigma_x\sigma_y}\cdot\exp\left[-\left(\frac{(x-\mu_x)^2}{2\sigma_x^2} + \frac{(y-\mu_y)^2}{2\sigma_y^2}\right)\right]\,, \tag{6.8}$$

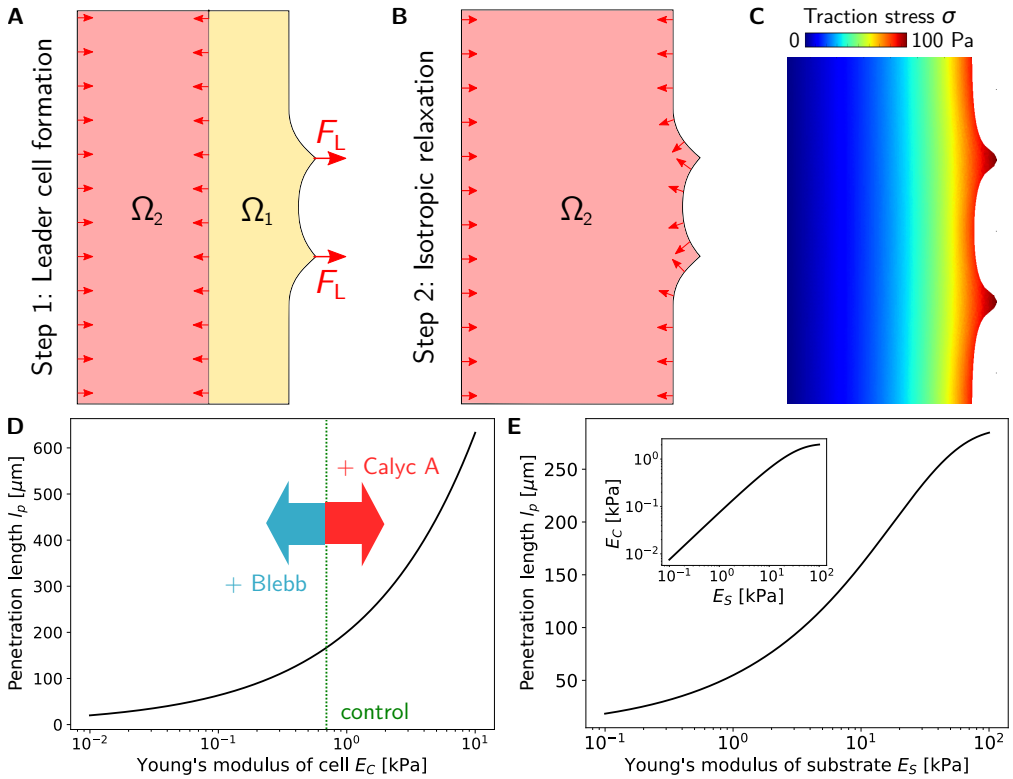

Figure 6.9: Simulation steps to model the leader cell formation experiments. **(A)** We first decouple the part Ω_1 of the elastic contractile bulk from the substrate. Only Ω_2 remains elastically attached to the substrate and isotropically contractile. The leader cells are initiated via pulling at two boundary points which are separated by a distance d_{LL}. **(B)** In the resulting stretched situation, we couple part Ω_1 elastically to the substrate and let the whole layer contract isotropically. **(C)** Typical traction stress pattern in a finite element simulation. Due to the isotropic contraction, larger stress peaks automatically appear in regions with the highest curvature. Panels **D** and **E** show the estimated relation between the localization length l_{p} and the cell stiffness E_{c} **(D)** or the gel stiffness E_{s} **(E)**, both in a semi-logarithmic plot. Both increasing cell stiffness and increasing gel stiffness lead to a increasing force localization length. Addition of Blebbistatin decreases the penetration length, while addition of Calyculin A increases the penetration length. The inset in Panel **E** shows the relation between cell and gel stiffness based on the experiments by *Solon et al.* [2007].

as shown in Figure 6.9A. The total force of the leader cell was set to $F_{\mathrm{L}} = 100\,\mathrm{nN}$, which is a typical force exerted by an MDCK cell (compare e.g. *Maruthamuthu et al.* [2011]). We further choose the leader cell positions μ_x and μ_y to be separated by the desired leader-to-leader distance, while their widths are chosen to be $\sigma_x = 5\,\mu\mathrm{m}$ and $\sigma_y = 10\,\mu\mathrm{m}$. We use different widths in both dimensions for two reasons. First, from the computational perspective, we want to assure that the maximum of the Gaussian force does not lie exactly between two nodes of the FE mesh, such that the mesh remains unaffected by the

force and the simulation result gets distorted. Second, from the biological perspective, a larger leader cell width parallel to the boundary is also justified, since leader cells usually exhibit a broad lamellipodium at their leading edge (see e.g. Figure 6.4).
This first simulation step serves as a simple model for the protrusion of leader cells via the creation of lamellipodia. In the second simulation step, also called the *relaxation step*, the complete bulk is coupled to the environment again and contracts isotropically (see Figure 6.9B), representing the pulling of the outgrowth containing both leader and follower cells against the remaining bulk, mediated by the newly created FAs at the tip of the leader cells. The magnitude of the traction stress at a position (x, y) is then computed via $T = Y|\mathbf{u}|$.
Figure 6.9C depicts a typical traction stress pattern after relaxation of the cell layer. We can see that the largest traction stresses appear along the free boundary of the layer. In particular, the evaginated regions, i.e. the modeled leader cells, exert the highest stresses, which results from the geometry of the layer and the fact that σ_0 is perpendicular to the boundary at the free edge.
Before presenting the simulation results in detail, we will discuss the influence of a chemical and physical modulation on the force penetration length l_p.

6.3.2 Incorporation of Chemical and Physical Modulation in the Model

We can exploit the dependence of the force localization length l_p on the cell stiffness E_c and the substrate stiffness E_s to explain the influence of chemical and physical modulation on the characteristic lengths in the monolayer.
Using the relation derived by *Banerjee and Marchetti* [2012], we find that $l_\mathrm{p} \propto \sqrt{E_\mathrm{c}}$. Figure 6.9D illustrates this relation with the remaining parameters fixed as listed in Table A.7. For the control case, we can now determine those value of E_c, for which $l_\mathrm{p} = 150\,\mu\mathrm{m}$, i.e. the characteristic length derived in Sections 6.1 and 6.2, yielding $E_\mathrm{c} = 700\,\mathrm{Pa}$, which is in good agreement with values determined experimentally e.g. by *Brückner and Janshoff* [2015].
Furthermore, we know, on the one hand, that addition of blebbistatin decreases the elastic modulus of the cell layer. This is because, on the molecular scale, blebbistatin is known to block myosin-II in an actin-detached state [*Kovács et al.*, 2004], such that fewer motors are bound to actin filaments. On the level of single cells, this is known to lead to a decrease of the mechanical the effective elastic modulus [*Schillers et al.*, 2010; *Schlosser et al.*, 2015]. Therefore, we can also assume that the blebbistatin treatment effectively decreases the elastic modulus of the cell layer. Going back to Figure 6.9D, this implies a decrease of l_p, which is also observed in the experimental results in Sections 6.1 and 6.2. More precisely, if using the measured value for d_LL from Figure 6.3, we find an elastic modulus of $E_\mathrm{c} \approx 100\,\mathrm{Pa}$ for the experiment with blebbistatin-treated cells.
On the other hand, calyculin A is known to inhibit the myosin phosphatase, and with this, leaving myosin-II in a hyperactivated state such that, effectively, more motors are bound to the actin filaments as known e.g. from experiments by *Fabian et al.* [2007] or *Gutzman and Sive* [2010]. This is known to lead to an effective increase of E_c and implies an increase of l_p (see e.g. *Haghparast et al.* [2015] and Figure 6.9D, respectively).

Introducing the measured value from Figure 6.3, we find an elastic modulus of $E_c \approx 5\,\mathrm{kPa}$ for the cells treated with calyculin A.
Regarding the influence of physical modulation on l_p, we know from measurements conducted by *Solon et al.* [2007] that cells become stiffer with increasing substrate stiffness. Therefore, the cell layer stiffness E_c can not be treated independently from the substrate stiffness E_s. The experiments by *Solon et al.* [2007] yield a monotonically increasing E_c with increasing E_s, with a saturation for both very small and very large substrate stiffnesses. By fitting the data from our experiments to a saturating function, as shown in the inset of Figure 6.9E,

$$E_c = E_{C0} + B_C \left(1 - \exp\left(-\frac{E_s}{E_{S0}}\right)\right) , \tag{6.9}$$

we can assign the parameter values to $B_C \approx 2.1\,\mathrm{kPa}$, $E_{C0} \approx 0.0\,\mathrm{kPa}$ and $E_{S0} \approx 27.5\,\mathrm{kPa}$. With these values, we get the relationship of l_p and E_s shown in Panel 6.9E An increasing substrate stiffness E_s thus leads to an increasing force penetration length l_p, i.e. a decreasing propensity of leader cells, which we have also measured experimentally. As for the chemical modification, we can use the relation between l_p and E_s to estimate the cell stiffness to be $E_c \approx 250\,\mathrm{Pa}$ for $E_s = 4\,\mathrm{kPa}$, $E_c \approx 700\,\mathrm{Pa}$ for the control case $E_s = 11\,\mathrm{kPa}$ and $E_c \approx 2\,\mathrm{kPa}$ for $E_s = 90\,\mathrm{kPa}$.
It has to be noted here, that we do not claim to have measured exact values of E_c, but these values are inferred from our purely elastic model by assuming a constant cell height h_c and length L_c. It is, however, very likely that not only E_c, but also h_c and L_c change upon chemical or physical modulation, which has not been considered in the course of this study.
In the FE simulations of the chemical and physical modulation, we do not only modulate E_c, but also the isotropic stress σ_0 and the protrusion force F_L, in order to keep the overall displacement of the cell layer in the same order, irrespective of the cell stiffness. These values, however, do not modulate the force penetration length in our model.

6.3.3 Simulation Results

In the following, we quantify the effect of the force penetration length l_p on the coherence of two neighboring leader cells and, from this, conclude that the penetration length determines the optimum distance two neighboring leader cell have. Also, we will find that the force penetration length is involved in the decision about the transversal extent of an outgrowth before it splits in Phase 2.

Simulation Results for Phase 0 and Phase 1 We can define a measure for the coherence of two leader cells by comparing the displacement x_C of the center between the two outgrowths after the relaxation of the layer with respect to the baseline displacement x_B far away from the protrusions (see Figure 6.10A). We then vary the distance d_{LL} between the two outgrowths and compute the distance $|x_C - x_B|$ as a function of d_{LL}, as shown in Figure 6.10B for different values of l_p. It has to be noted here, that x_B is a purely

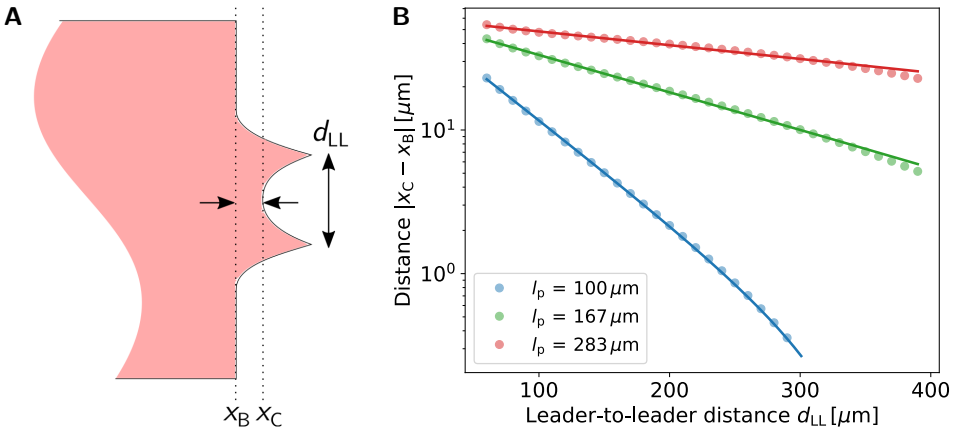

Figure 6.10: The evagination of the contact point between two simulated leader cells decreases exponentially with the decay length equaling the force penetration length l_p. **(A)** We measure the spatial difference between the strained position of the layer boundary between the "leader cells" x_C and the baseline x_B as a function of d_{LL}. **(B)** The transversal strain between the leader cells is an exponential function of the leader-to-leader distance d_{LL} with a characteristic length scale l_p. *Circles* are simulation results, while *solid lines* present exponential fits with decay constant l_p. Simulation results suggest that the force localization length l_p is the closest distance between two neighboring leader cells at which the cells do not cohere.

conceptional value which can be calculated from simulations but will never be measured experimentally.
The simulation results yield an exponential dependence of $|x_C - x_B|$ on the distance d_{LL} with the characteristic decay length l_p

$$|x_C - x_B| \propto \exp\left(-\frac{d_{LL}}{l_p}\right), \tag{6.10}$$

indicating that the coherence of the leader cells stops at $d_{LL} = l_p$. Deviations between the simulation results and the exponential fits reveal simulation artifacts due to the finite total size of the mesh and the minimal mesh size.
Our result can be interpreted in the following way with respect to the experiments from Section 6.1: The length l_p determines the distance above which the mechanical communication of two point forces, or leader cells, ends. Below $d_{LL} = l_p$, two leader cells would rather cohere to a single outgrowth which will then be interpreted as an outgrowth following a single leader cell. At and above $d_{LL} = l_p$, two leader cells will not interact and thus will "survive". For $d_{LL} > l_p$, the neighboring leader cells will allow the appearance of a third leader cell in between, which would finally yield only leader cells with a constant leader-to-leader distance $d_{LL} = l_p$, as observed in the experiments.
The disadvantage of the model, so far, is the fact that it does not allow to create a bridge between Phase 0 and Phase 1. As we have observed in Section 6.2, we can measure

regions of increased traction stresses at the back of the leader cells even before it emerges. In our model, however, we do not exclude a primarily random distribution of leader cells which then cohere if they are closer than l_p as described above. Furthermore, by comparing the actual traction stress patterns in Section 6.2 with the qualitative simulated pattern in Figure 6.9C, we find that the assumption of an isotropic contractile stress, and consequently a higher leader stress due to an increased evagination of the cell layer, does not fully capture the observe traction stress pattern. Instead, we find single stress hot spots exerted by the leader cells or their would-be follower cells, which are embedded in a rather passive layer.
Therefore, we can alternatively think of a model for Phase 0 in which the would-be follower cells are the only stress-generating entities in the layer, as Figure 6.11A illustrates. We start from a rectangular elastic bulk with elastic coupling to its environment, as described above, but now the traction stress exerted by would-be follower cells is represented as two force spots at the boundary of the layer separated by a distance d_LL and pulling towards the interior of the layer. The remaining cell layer is assumed to be passive and the remaining boundary conditions remain the same as before.
For each distance d_LL, we can now calculate the total energy U_tot of the cell layer by computing its contributions from the elastic coupling

$$U_\mathrm{Y} = \frac{1}{2}\int_\Omega Y\mathbf{u}^2\mathrm{d}\Omega\,, \tag{6.11}$$

and the strain energy in the two-dimensional cell layer

$$\begin{aligned} U_\mathrm{E} &= \frac{1}{2}\int_\Omega \sigma_{ij}\epsilon_{ij}\mathrm{d}\Omega \\ &= \frac{1}{2}\int_\Omega \left(\sigma_{xx}\epsilon_{xx} + \sigma_{xy}\epsilon_{xy} + \sigma_{yx}\epsilon_{yx} + \sigma_{yy}\epsilon_{yy}\right)\mathrm{d}\Omega \\ &= \frac{1}{2}\int_\Omega \left[\lambda\left(\epsilon_{xx}+\epsilon_{yy}\right)^2 + 2\mu\left(\epsilon_{xx}^2+\epsilon_{yy}^2\right) + 4\mu\epsilon_{xy}^2\right]\mathrm{d}\Omega\,, \end{aligned} \tag{6.12}$$

using the passive part of the constitutive relation in Equation 6.2. The total energy of the cell layer then reads $U_\mathrm{tot} = U_\mathrm{Y} + U_\mathrm{E}$.
Figure 6.11B shows that the resulting total energy exhibits a minimum close to $d_\mathrm{LL} = l_\mathrm{p}$. In fact, d_LL is always slightly smaller than l_p. In this context, we can argue that l_p is the distance between two neighboring leader cells at which the whole cell layer invests a minimal amount of energy while initiating a protrusion into the cell free region.
Intuitively, we can picture this fact as follows. A single force vector exerted in the cell layer will propagate by l_p in the direction of its orientation and, due to $\nu_\mathrm{c} \approx 0.5$, by $l_\mathrm{p}/2$ in both directions perpendicular to its orientation. At the distance $l_\mathrm{p}/2$ perpendicular to the direction of the force vector, the induced displacement vectors will be perpendicular to the force vector. If two parallel point forces are exerted at a

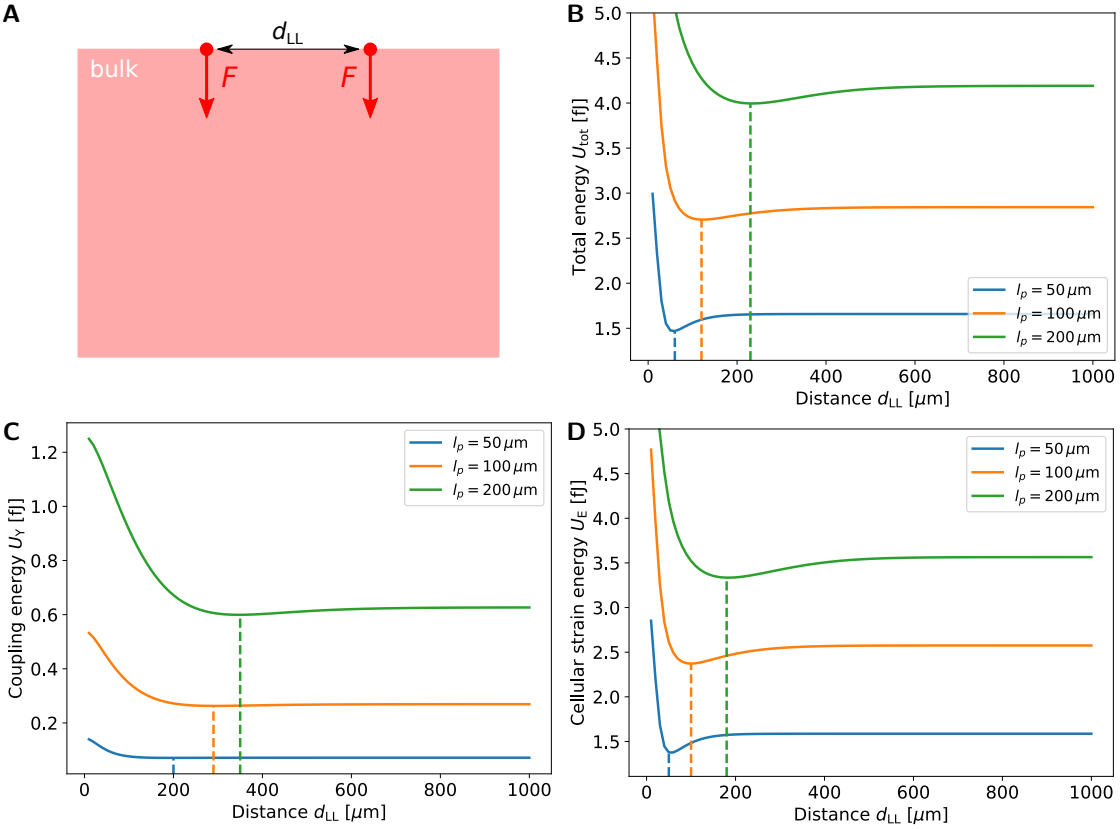

Figure 6.11: Representation of leader cell forces as two parallel point forces at a distance d from each other acting perpendicularly to the boundary of a semi-infinite two-dimensional elastic sheet with elastic coupling with the environment. **(A)** Schematic of the orientation of forces. **(B)** Total energy U_{tot} and its contributions **(C)** coupling energy U_{Y} and **(D)** strain energy U_{E} as a function of the distance d between two point forces. The minimum of the total energy is located at $d \approx l_{\mathrm{p}}$. The total energy is dominated by the strain energy.

lateral distance of $d_{\mathrm{LL}} \approx l_{\mathrm{p}}$, as depicted in Figure 6.11A, the displacement vectors at the center line between the force spots will annihilate each other and not contribute to the mechanical energy of the system. If $d_{\mathrm{LL}} < l_{\mathrm{p}}$, the displacement vectors induced at the center line will have considerable components parallel and perpendicular to the force direction. The perpendicular components will annihilate each other, but the perpendicular components will sum up, which yields a larger contribution to the total energy. If $d_{\mathrm{LL}} > l_{\mathrm{p}}$, displacements induced by the force spots do not affect each other and the total energy of the system is twice the energy expended by a single force vector. This explains why $d_{\mathrm{LL}} \approx l_{\mathrm{p}}$ leads to an energy minimum.
Figures 6.11C and 6.11D further show that also U_{Y} and U_{E} contain characteristic minima at an increasing leader-to-leader distance with increasing force penetration length. The coupling energy U_{Y} is always minimal for some $d_{\mathrm{LL}} > l_{\mathrm{p}}$, while the strain energy U_{E} is

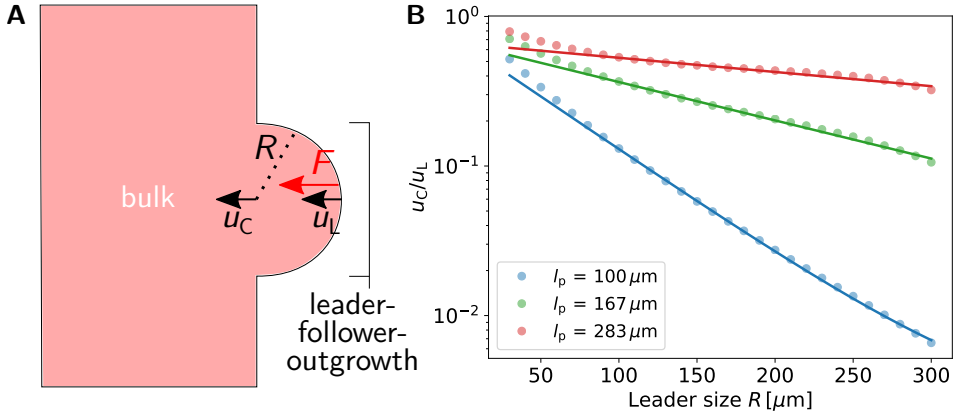

Figure 6.12: Simple model of leader cell splitting (i.e. Phase 2) during collective cell migration. **(A)** The pre-existing outgrowth is modeled as a circular protrusion with radius R. The displacement u_C of the center of the circle is a measure for the influence of a force exerted by the leader cell on the bulk. **(B)** With increasing radius of the circular protrusion, the displacement u_C, i.e. the communication between leader cell and bulk, decreases exponentially with characteristic length scale l_p.

also minimal for $d_{LL} \approx l_p$. Moreover, U_E is always the dominant contribution to the total energy. We will discuss this fact in more detail in Section 6.4, where we will reduce the two-dimensional to a one-dimensional model. This will allow to analytically analyze the energetic contributions from the cell layer and the substrate. With the reduced model, however, we will not be able to describe the formation of leader cells based on the energy argument we used here in two dimensions.

Simulation Results for Phase 2 To model Phase 2, we start with a cell layer which already exhibits a single outgrowth, represented by the idealized circular evagination of radius R in Figure 6.12A. We then exert a Gaussian-shaped point force of magnitude F, equivalent to Equation 6.8), at the farther protrusion of the outgrowth, as a model for a force exerted by the leader cell. We can then quantify the effective force registered by the bulk by means of comparing the displacement u_L of the leader cell itself with the displacement u_C of the center of the circle, which lies at the boundary between outgrowth an bulk.
By varying the outgrowth radius R, we find that the ratio u_C/u_L is an exponentially decaying function of the radius R with the decay length scale

$$\frac{u_C}{u_L} \propto \exp\left(-\frac{R}{l_p}\right), \tag{6.13}$$

indicating that for outgrowth radii $R > l_p$, outgrowth and bulk become mechanically decoupled (see Figure 6.12B).
The outgrowth itself can now be treated as its own bulk with a spatial extension $L_O \ll L_L$.

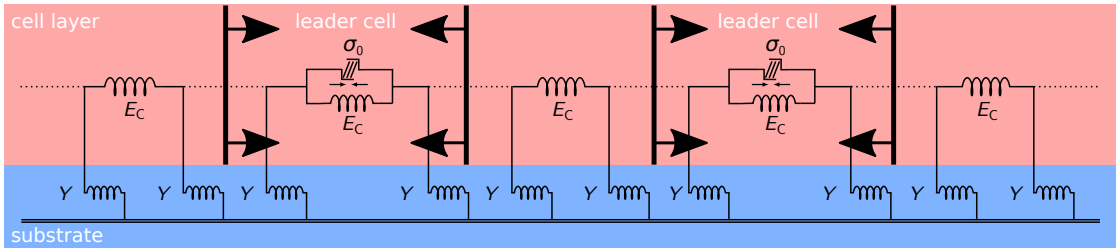

Figure 6.13: One-dimensional model of leader cell formation. The leader cells are represented by two contractile areas in an elastic medium. The outer boundaries are stress-free boundaries.

Since the force penetration length l_p positively correlates with L_O via $l_\mathrm{p} \propto \sqrt{L_\mathrm{O}}$, the penetration length in the outgrowth dramatically decreases, allowing the emergence of further leader cells, which we also observe in the experiments.

6.4 A Minimal One-Dimensional Model of the Formation of Leader Cells

So far, we showed that the characteristic distances in the course of leader cell formation can be described by means of a two-dimensional continuum model. However, the complicated boundary conditions, involved in this mathematical problem, did not allow to treat the problem analytically.
Therefore, we now introduce a one-dimensional model of the monolayer, which will allow a full analytical treatment of the problem. As Figure 6.13 illustrates, leader cells are modeled as uniformly contractile regions within a one-dimensional bar, embedded in a comparably passive elastic layer with negligible active stress. Focal adhesions and the extracellular environment are incorporated into the model as an elastic foundation with links of spring stiffness area density Y [*Edwards and Schwarz*, 2011; *Banerjee and Marchetti*, 2012].
In the following calculations, we will derive the equations for the displacement u and the inner stress σ of the medium. As discussed earlier, we will try to keep the model as simple as possible, but do not claim that the model comprises the full dynamics of a spreading cell monolayer. However, the model can serve as a basis for further computations involving a viscous contribution, such as the model by *Blanch-Mercader et al.* [2017], or a separate modeling of cadherin junctions, as proposed by *Mertz et al.* [2013].

6.4.1 One-Dimensional Model of Leader Cell Formation

We start with the constitutive equation of a one-dimensional active elastic bar with contraction σ_0

$$\sigma = E_\mathrm{c}\epsilon - \sigma_0\,, \tag{6.14}$$

with the one-dimensional strain $\epsilon = {}^{\partial u}/_{\partial x}$. Together with the force balance equation

$$\frac{\partial \sigma}{\partial x} - Yu = 0\,, \tag{6.15}$$

we find that the displacement u yields

$$\frac{\partial^2 u}{\partial x^2} - \frac{u}{l_\mathrm{p}^2} = \frac{1}{E_\mathrm{c}} \frac{\partial \sigma_0}{\partial x}\,, \tag{6.16}$$

with the *force penetration length*

$$l_\mathrm{p} = \sqrt{\frac{E_\mathrm{c}}{Y}}\,. \tag{6.17}$$

As the layer contracts piecewise uniformly, σ_0 is piecewise constant and can be left out from Equation 6.16, leading to

$$\frac{\partial^2 u}{\partial x^2} - \frac{u}{l_\mathrm{p}^2} = 0\,. \tag{6.18}$$

It will, however, appear in the solution via the internal boundary conditions.
In Section 6.4.1.1, we will deal with the two relevant subproblems which appear in our model, each with its own boundary conditions, before we combine both solutions to get a solution for the full model in Section 6.4.1.2.

6.4.1.1 Calculation of Relevant Subproblems

Before addressing the full problem, we will first solve the two subproblems

- elastically coupled elastic bar with stress load at one end and the other end fixed
- elastically coupled elastic bar with stress loads at both ends

separately and combine the solutions in the succeeding subsection.

Constant Stress Boundary and Fixed Boundary We consider the situation illustrated in Figure 6.14. Here, we have to solve Equation 6.18 with the two boundary conditions $u(x = 0) = 0$ and $\sigma(x = L) = E_\mathrm{c}\, \frac{\partial u}{\partial x}\big|_{x=L} = \sigma_0$.
We start with the ansatz

$$u(x) = A \exp\left(\frac{x}{l_\mathrm{p}}\right) + B \exp\left(-\frac{x}{l_\mathrm{p}}\right)\,. \tag{6.19}$$

The zero-displacement boundary condition $u(x = 0) = 0$ leads to $A = -B$, such that

$$u(x) = 2A \sinh\left(\frac{x}{l_\mathrm{p}}\right) \quad \text{and} \quad \sigma(x) = \frac{2AE_\mathrm{c}}{l_\mathrm{p}} \cosh\left(\frac{x}{l_\mathrm{p}}\right)\,. \tag{6.20}$$

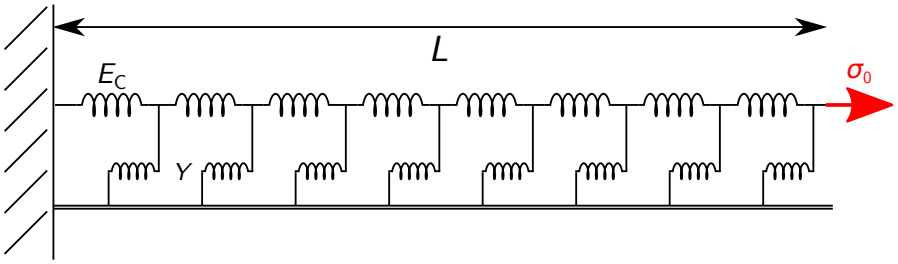

Figure 6.14: Subproblem of the model: Elastically coupled elastic bar with stress load at one end and the other end fixed.

The stress boundary condition $\sigma(x = L) = \sigma_0$ then yields $A = \frac{\sigma_0 l_\mathrm{p}}{2E_\mathrm{c}\cosh\left(\frac{L}{l_\mathrm{p}}\right)}$, such that

$$u(x) = \frac{\sigma_0 l_\mathrm{p}}{E_\mathrm{c}} \frac{\sinh\left(\frac{x}{l_\mathrm{p}}\right)}{\cosh\left(\frac{L}{l_\mathrm{p}}\right)} \quad \text{and} \quad \sigma(x) = \sigma_0 \frac{\cosh\left(\frac{x}{l_\mathrm{p}}\right)}{\cosh\left(\frac{L}{l_\mathrm{p}}\right)} = E_\mathrm{c}\epsilon\left(x\right) . \tag{6.21}$$

Equivalent results were already derived by *Edwards and Schwarz* [2011]. We can use them to calculate the energies involved in the problem. First, we have the coupling energy U_Y which is stored in the elastic foundation:

$$U_\mathrm{Y} = \frac{Y}{2}\int_0^L u^2\left(x\right)\mathrm{d}x \tag{6.22}$$

$$= \frac{\sigma_0^2}{8E_\mathrm{c}\cosh^2\left(\frac{L}{l_\mathrm{p}}\right)}\left(l_\mathrm{p}\sinh\left(\frac{2L}{l_\mathrm{p}}\right) - 2L\right) . \tag{6.23}$$

The second energy sink is due to the energy U_E which is stored in the elastic bar:

$$U_\mathrm{E} = \frac{E_\mathrm{c}}{2}\int_0^L \epsilon^2\left(x\right)\mathrm{d}x \tag{6.24}$$

$$= \frac{\sigma_0^2}{8E_\mathrm{c}\cosh^2\left(\frac{L}{l_\mathrm{p}}\right)}\left(l_\mathrm{p}\sinh\left(\frac{2L}{l_\mathrm{p}}\right) + 2L\right) . \tag{6.25}$$

In total, we get the energy

$$\begin{aligned} U_\mathrm{tot} = U_\mathrm{Y} + U_\mathrm{E} &= \frac{\sigma_0^2 l_\mathrm{p}}{4E_\mathrm{c}\cosh^2\left(\frac{L}{l_\mathrm{p}}\right)}\sinh\left(\frac{2L}{l_\mathrm{p}}\right) \\ &= \frac{\sigma_0^2 l_\mathrm{p}}{2E_\mathrm{c}\cosh^2\left(\frac{L}{l_\mathrm{p}}\right)}\sinh\left(\frac{L}{l_\mathrm{p}}\right)\cosh\left(\frac{L}{l_\mathrm{p}}\right) \\ &= \frac{1}{2}\sigma_0 \cdot u\left(L\right) . \end{aligned} \tag{6.26}$$

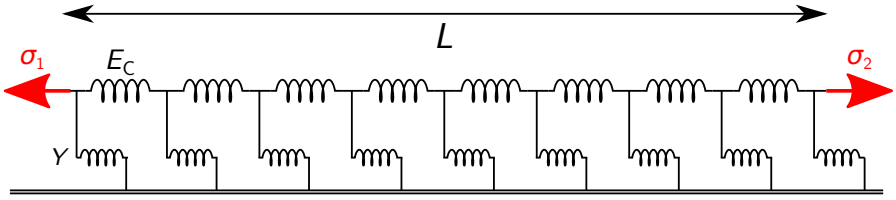

Figure 6.15: Subproblem of the model: Elastically coupled elastic bar with stress load σ_1 at one end and stress load σ_2 at the other end.

Thus, the total energy is the product of the half stress exerted at L and the displacement of the bar at the position $x = L$. This is equivalent to the energy $U = {}^1\!/\!_2 Fx$ upon extension of a spring by a force F to a new extension x. Note that here, the total energy is not $U = Fx$, as one would expect, since the assumption that a spring, or an elastic bar in our case, is extended by means of a constant force F, or stress σ_0, is wrong. Indeed, the force needed to extend the spring to a new extension x is always $F = k \cdot x \neq \text{const}$, since it must satisfy Newton's third law.

Two Constant Stress Boundaries We now consider the situation illustrated in Figure 6.15. Here, we have to solve Equation 6.18 with the two boundary conditions $\sigma(x = l_1) = \sigma_1$ and $\sigma(x = l_2) = \sigma_2$, with $L = l_2 - l_1$.
With the ansatz from Equation 6.19, we get the general form for the internal stress

$$\sigma(x) = E_\mathrm{c}\left(\frac{A}{l_\mathrm{p}}\exp\left(\frac{x}{l_\mathrm{p}}\right) - \frac{B}{l_\mathrm{p}}\exp\left(-\frac{x}{l_\mathrm{p}}\right)\right). \tag{6.27}$$

The first boundary condition $\sigma(x = l_1) = \sigma_1$ leads to

$$B = A\exp\left(\frac{2l_1}{l_\mathrm{p}}\right) - \frac{\sigma_1 l_\mathrm{p}}{E_\mathrm{c}}\exp\left(-\frac{l_1}{l_\mathrm{p}}\right), \tag{6.28}$$

while the second boundary condition $\sigma(x = l_2) = \sigma_2$ yields

$$A = \frac{l_\mathrm{p}}{E_\mathrm{c}} \cdot \frac{\sigma_2 - \sigma_1 \exp\left(\frac{l_1 - l_2}{l_\mathrm{p}}\right)}{\exp\left(\frac{l_2}{l_\mathrm{p}}\right) - \exp\left(\frac{2l_1 - l_2}{l_\mathrm{p}}\right)}. \tag{6.29}$$

Inserting these relations into Equations 6.19 and 6.27 yields

$$\begin{aligned} u(x) &= \frac{l_\mathrm{p}}{E_\mathrm{c}}\left[\left(\sigma_2 - \sigma_1\exp\left(\frac{l_1 - l_2}{l_\mathrm{p}}\right)\right)\frac{\exp\left(\frac{x}{l_\mathrm{p}}\right) + \exp\left(\frac{2l_1 - x}{l_\mathrm{p}}\right)}{\exp\left(\frac{l_2}{l_\mathrm{p}}\right) - \exp\left(\frac{2l_1 - l_2}{l_\mathrm{p}}\right)} - \sigma_1\exp\left(\frac{l_1 - x}{l_\mathrm{p}}\right)\right] \\ &= \frac{l_\mathrm{p}}{E_\mathrm{c}} \cdot \frac{\sigma_2\cosh\left(\frac{l_1 - x}{l_\mathrm{p}}\right) - \sigma_1\cosh\left(\frac{l_2 - x}{l_\mathrm{p}}\right)}{\sinh\left(\frac{l_2 - l_1}{l_\mathrm{p}}\right)}, \end{aligned} \tag{6.30}$$

and

$$\sigma(x) = \frac{\sigma_1 \sinh\left(\frac{l_2-x}{l_\mathrm{p}}\right) - \sigma_2 \sinh\left(\frac{l_1-x}{l_\mathrm{p}}\right)}{\sinh\left(\frac{l_2-l_1}{l_\mathrm{p}}\right)} \,. \tag{6.31}$$

As in the previous case, we can calculate the energies involved in the problem. First, we have the coupling energy U_Y which is

$$\begin{aligned} U_\mathrm{Y} &= \frac{Y}{2}\int_0^L u^2(x)\,\mathrm{d}x \\ &= \frac{1}{2E_\mathrm{c}\sinh^2\left(\frac{l_2-l_1}{l_\mathrm{p}}\right)} \left[\frac{\sigma_1^2}{4}\left(l_\mathrm{p}\sinh\left(\frac{2(l_2-l_1)}{l_\mathrm{p}}\right) + 2(l_2-l_1)\right)\right. \\ &\qquad + \frac{\sigma_2^2}{4}\left(l_\mathrm{p}\sinh\left(\frac{2(l_2-l_1)}{l_\mathrm{p}}\right) + 2(l_2-l_1)\right) \\ &\qquad \left. - \sigma_1\sigma_2\left((l_2-l_1)\cosh\left(\frac{l_2-l_1}{l_\mathrm{p}}\right) + l_\mathrm{p}\sinh\left(\frac{l_2-l_1}{l_\mathrm{p}}\right)\right)\right] . \end{aligned}$$

Second, the elastic energy U_E yields:

$$\begin{aligned} U_\mathrm{E} &= \frac{E_\mathrm{c}}{2}\int_0^L \epsilon^2(x)\,\mathrm{d}x \\ &= \frac{1}{2E_\mathrm{c}\sinh^2\left(\frac{l_2-l_1}{l_\mathrm{p}}\right)} \left[\frac{\sigma_1^2}{4}\left(l_\mathrm{p}\sinh\left(\frac{2(l_2-l_1)}{l_\mathrm{p}}\right) - 2(l_2-l_1)\right)\right. \\ &\qquad + \frac{\sigma_2^2}{4}\left(l_\mathrm{p}\sinh\left(\frac{2(l_2-l_1)}{l_\mathrm{p}}\right) - 2(l_2-l_1)\right) \\ &\qquad \left. - \sigma_1\sigma_2\left((l_1-l_2)\cosh\left(\frac{l_2-l_1}{l_\mathrm{p}}\right) + l_\mathrm{p}\sinh\left(\frac{l_2-l_1}{l_\mathrm{p}}\right)\right)\right] . \end{aligned}$$

In total, we get the energy

$$\begin{aligned} U_\mathrm{tot} &= U_\mathrm{Y} + U_\mathrm{E} \\ &= \frac{l_\mathrm{p}}{2E_\mathrm{c}\sinh^2\left(\frac{l_2-l_1}{l_\mathrm{p}}\right)} \left[\frac{\sigma_1^2}{2}\sinh\left(\frac{2(l_2-l_1)}{l_\mathrm{p}}\right) + \frac{\sigma_2^2}{2}\sinh\left(\frac{2(l_2-l_1)}{l_\mathrm{p}}\right)\right. \\ &\qquad \left. - 2\sigma_1\sigma_2\sinh\left(\frac{l_2-l_1}{l_\mathrm{p}}\right)\right] \\ &= \frac{l_\mathrm{p}}{2E_\mathrm{c}\sinh\left(\frac{l_2-l_1}{l_\mathrm{p}}\right)} \left[\left(\sigma_1^2+\sigma_2^2\right)\cosh\left(\frac{l_2-l_1}{l_\mathrm{p}}\right) - 2\sigma_1\sigma_2\right] \\ &= \frac{1}{2}\left(-u(l_1)\cdot\sigma(l_1) + u(l_2)\cdot\sigma(l_2)\right) . \end{aligned} \tag{6.34}$$

The last equality was found by reverse evaluating the functions $u(x)$ and $\sigma(x)$ at the positions l_1 and l_2. The different signs in the last expression are due to the (one-dimensional) normal vectors, which are oppositely directed.

6.4.1.2 Analytical Solution of the Full Problem

Figure 6.16 shows a simplified sketch of the full problem. Since the problem is symmetric, we can skip the dynamics of the left half of the bar by using the boundary condition $u(x=0)=0$. We now deal with two internal active stresses $\sigma(l_1)=\sigma_0$ and $\sigma(l_2)=-\sigma_0$. The problem at hand is linear, such that the full solution will be a superposition of the subproblems $\sigma(l_1)=\sigma_0$ and $\sigma(l_2)$ unprescribed and vice versa. Therefore, we will first calculate the solution w.r.t. the boundary conditions $u(x=0)=0$, $\sigma(x=l_1)=\sigma_0$ and $\sigma(x=L)=0$.

Single Internal Stress Boundary We label the region $0 \leq x \leq l_1$ with I and the region $l_1 < x \leq L$ with II. The lengths of the two sub-bars are now

$$L_{\mathrm{I}} = l_1 \,, \tag{6.35}$$

and

$$L_{\mathrm{II}} = L - l_1 \,. \tag{6.36}$$

We can split the stress σ_0 at l_1 into two sub-stresses σ_{I} and σ_{II} which pull at bar I and II and lead to displacements u_{I} and u_{II}, respectively. The following two conditions have to be fulfilled

$$\begin{cases} \sigma_0 &= \sigma_{\mathrm{I}} - \sigma_{\mathrm{II}} \\ 0 &= u_{\mathrm{I}}(L_{\mathrm{I}}) - u_{\mathrm{II}}(L_{\mathrm{I}}) \end{cases} . \tag{6.37}$$

We know from Equations 6.21 and 6.30, that

$$u_{\mathrm{I}}(L_{\mathrm{I}}) = \frac{\sigma_{\mathrm{I}} l_{\mathrm{p}}}{E_{\mathrm{c}}} \frac{\sinh\left(\frac{L_{\mathrm{I}}}{l_{\mathrm{p}}}\right)}{\cosh\left(\frac{L_{\mathrm{I}}}{l_{\mathrm{p}}}\right)} \coloneqq \frac{\sigma_{\mathrm{I}} l_{\mathrm{p}}}{E_{\mathrm{c}}}\, g\left(L_{\mathrm{I}}\right) \,, \tag{6.38}$$

and

$$u_{\mathrm{II}}(L_{\mathrm{I}}) = -\frac{\sigma_{\mathrm{II}} l_{\mathrm{p}}}{E_{\mathrm{c}}} \frac{\cosh\left(\frac{L_{\mathrm{II}}}{l_{\mathrm{p}}}\right)}{\sinh\left(\frac{L_{\mathrm{II}}}{l_{\mathrm{p}}}\right)} \coloneqq -\frac{\sigma_{\mathrm{II}} l_{\mathrm{p}}}{E_{\mathrm{c}}}\, h\left(L_{\mathrm{II}}\right) \,. \tag{6.39}$$

We can summarize Equations 6.37–6.39 by means of the linear system

$$\begin{pmatrix} \sigma_0 \\ 0 \end{pmatrix} = \begin{pmatrix} 1 & -1 \\ \frac{l_{\mathrm{p}}}{E_{\mathrm{c}}} g\left(L_{\mathrm{I}}\right) & \frac{l_{\mathrm{p}}}{E_{\mathrm{c}}} h\left(L_{\mathrm{II}}\right) \end{pmatrix} \begin{pmatrix} \sigma_{\mathrm{I}} \\ \sigma_{\mathrm{II}} \end{pmatrix} . \tag{6.40}$$

Since we are interested in σ_{I} and σ_{II}, we invert Equation 6.40, which leads to

$$\begin{pmatrix} \sigma_{\mathrm{I}} \\ \sigma_{\mathrm{II}} \end{pmatrix} = \frac{E_{\mathrm{c}}/l_{\mathrm{p}}}{g\left(L_{\mathrm{I}}\right) + h\left(L_{\mathrm{II}}\right)} \begin{pmatrix} \frac{l_{\mathrm{p}}}{E_{\mathrm{c}}} h\left(L_{\mathrm{II}}\right) & 1 \\ -\frac{l_{\mathrm{p}}}{E_{\mathrm{c}}} g\left(L_{\mathrm{I}}\right) & 1 \end{pmatrix} \begin{pmatrix} \sigma_0 \\ 0 \end{pmatrix} , \tag{6.41}$$

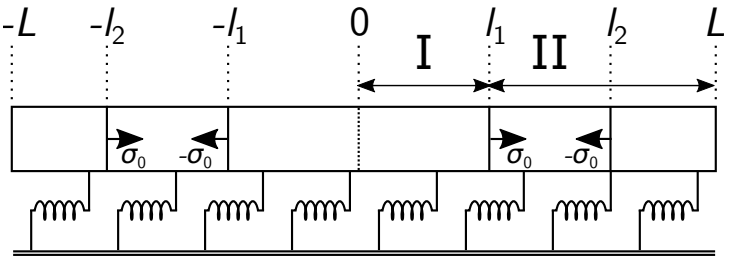

Figure 6.16: Simplified sketch of the full problem: Leader cells are represented by two contractile areas each of length $l_2 - l_1$ in the elastic bar of length $2L$. The outer boundaries are stress-free boundaries.

such that

$$\begin{cases} \sigma_{\mathrm{I}} & = \frac{\sigma_0 h(L_{\mathrm{II}})}{g(L_{\mathrm{I}})+h(L_{\mathrm{II}})} \\ \sigma_{\mathrm{II}} & = -\frac{\sigma_0 g(L_{\mathrm{I}})}{g(L_{\mathrm{I}})+h(L_{\mathrm{II}})} \end{cases} , \tag{6.42}$$

and

$$\begin{cases} u_{\mathrm{I}}(L_{\mathrm{I}}) & = \frac{\sigma_0 h(L_{\mathrm{II}})}{g(L_{\mathrm{I}})+h(L_{\mathrm{II}})} g\left(L_{\mathrm{I}}\right) \\ u_{\mathrm{II}}(L_{\mathrm{I}}) & = \frac{\sigma_0 g(L_{\mathrm{I}})}{g(L_{\mathrm{I}})+h(L_{\mathrm{II}})} h\left(L_{\mathrm{II}}\right) \end{cases} . \tag{6.43}$$

The denominator yields

$$g\left(L_{\mathrm{I}}\right) + h\left(L_{\mathrm{II}}\right) = \frac{\sinh\left(\frac{L_{\mathrm{I}}}{l_{\mathrm{p}}}\right)}{\cosh\left(\frac{L_{\mathrm{I}}}{l_{\mathrm{p}}}\right)} + \frac{\cosh\left(\frac{L_{\mathrm{II}}}{l_{\mathrm{p}}}\right)}{\sinh\left(\frac{L_{\mathrm{II}}}{l_{\mathrm{p}}}\right)} = \frac{\cosh\left(\frac{L}{l_{\mathrm{p}}}\right)}{\cosh\left(\frac{L_{\mathrm{I}}}{l_{\mathrm{p}}}\right)\sinh\left(\frac{L_{\mathrm{II}}}{l_{\mathrm{p}}}\right)} , \tag{6.44}$$

which leads to the displacements

$$u_{\mathrm{I}}(x) = \frac{\sigma_0 l_{\mathrm{p}}}{E_{\mathrm{c}}} \frac{\cosh\left(\frac{L-l_1}{l_{\mathrm{p}}}\right)}{\cosh\left(\frac{L}{l_{\mathrm{p}}}\right)} \sinh\left(\frac{x}{l_{\mathrm{p}}}\right) , \tag{6.45}$$

for $0 \leq x \leq l_1$ and

$$u_{\mathrm{II}}(x) = \frac{\sigma_0 l_{\mathrm{p}}}{E_{\mathrm{c}}} \frac{\sinh\left(\frac{l_1}{l_{\mathrm{p}}}\right)}{\cosh\left(\frac{L}{l_{\mathrm{p}}}\right)} \cosh\left(\frac{x-L}{l_{\mathrm{p}}}\right) , \tag{6.46}$$

for $l_1 < x \leq L$. We arrive at the piecewise solutions

$$u(x) = \begin{cases} \frac{\sigma_0 l_{\mathrm{p}}}{E_{\mathrm{c}}} \frac{\cosh\left(\frac{L-l_1}{l_{\mathrm{p}}}\right)}{\cosh\left(\frac{L}{l_{\mathrm{p}}}\right)} \sinh\left(\frac{x}{l_{\mathrm{p}}}\right) & , \text{ for } 0 < x < l_1 \\ \frac{\sigma_0 l_{\mathrm{p}}}{E_{\mathrm{c}}} \frac{\sinh\left(\frac{l_1}{l_{\mathrm{p}}}\right)}{\cosh\left(\frac{L}{l_{\mathrm{p}}}\right)} \cosh\left(\frac{x-L}{l_{\mathrm{p}}}\right) & , \text{ for } l_1 \leq x \leq L \end{cases} , \tag{6.47}$$

for the displacement u and

$$\sigma(x) = E_\mathrm{c}\frac{\partial u}{\partial x} = \begin{cases} \sigma_0 \frac{\cosh\left(\frac{L-l_1}{l_\mathrm{p}}\right)}{\cosh\left(\frac{L}{l_\mathrm{p}}\right)} \cosh\left(\frac{x}{l_\mathrm{p}}\right) & \text{, for } 0 < x < l_1 \\ \sigma_0 \frac{\sinh\left(\frac{l_1}{l_\mathrm{p}}\right)}{\cosh\left(\frac{L}{l_\mathrm{p}}\right)} \sinh\left(\frac{x-L}{l_\mathrm{p}}\right) & \text{, for } l_1 \leq x \leq L \end{cases}, \tag{6.48}$$

for the stress σ.
In analogy to the previous subsections, we can calculate the energies involved in the system. For reasons of comparability with previous results, we will hold to the calculation of the energy of a half bar. The coupling energy amounts to

$$\begin{aligned} U_\mathrm{Y} &= \frac{Y}{2}\int_0^L u^2(x)\,\mathrm{d}x = \frac{Y}{2}\left[\int_0^{l_1} u_\mathrm{I}^2(x)\,\mathrm{d}x + \int_{l_1}^L u_\mathrm{II}^2(x)\,\mathrm{d}x\right] \\ &= \frac{\sigma_0^2}{8E_\mathrm{c}\cosh^2\left(\frac{L}{l_\mathrm{p}}\right)}\left[\cosh^2\left(\frac{L-l_1}{l_\mathrm{p}}\right)\left(l_\mathrm{p}\sinh\left(\frac{2l_1}{l_\mathrm{p}}\right) - 2l_1\right)\right. \\ &\qquad \left. + \sinh^2\left(\frac{l_1}{l_\mathrm{p}}\right)\left(2L - 2l_1 + l_\mathrm{p}\sinh\left(\frac{2(L-l_1)}{l_\mathrm{p}}\right)\right)\right]. \end{aligned} \tag{6.49a}$$

The elastic energy yields

$$\begin{aligned} U_\mathrm{E} &= \frac{E_\mathrm{c}}{2}\int_0^L \epsilon^2(x)\,\mathrm{d}x = \frac{E_\mathrm{c}}{2}\left[\int_0^{l_1} \epsilon_\mathrm{I}^2(x)\,\mathrm{d}x + \int_{l_1}^L \epsilon_\mathrm{II}^2(x)\,\mathrm{d}x\right] \\ &= \frac{\sigma_0^2}{8E_\mathrm{c}\cosh^2\left(\frac{L}{l_\mathrm{p}}\right)}\left[\cosh^2\left(\frac{L-l_1}{l_\mathrm{p}}\right)\left(l_\mathrm{p}\sinh\left(\frac{2l_1}{l_\mathrm{p}}\right) + 2l_1\right)\right. \\ &\qquad \left. + \sinh^2\left(\frac{l_1}{l_\mathrm{p}}\right)\left(-2L + 2l_1 + l_\mathrm{p}\sinh\left(\frac{2(L-l_1)}{l_\mathrm{p}}\right)\right)\right]. \end{aligned} \tag{6.50a}$$

In total, we get the energy

$$\begin{aligned} U_\mathrm{tot} &= U_\mathrm{Y} + U_\mathrm{E} \\ &= \frac{\sigma_0^2 l_\mathrm{p}}{4E_\mathrm{c}\cosh^2\left(\frac{L}{l_\mathrm{p}}\right)}\left[\cosh^2\left(\frac{L-l_1}{l_\mathrm{p}}\right)\sinh\left(\frac{2l_1}{l_\mathrm{p}}\right) + \sinh^2\left(\frac{l_1}{l_\mathrm{p}}\right)\sinh\left(\frac{2(L-l_1)}{l_\mathrm{p}}\right)\right] \\ &= \frac{\sigma_0^2 l_\mathrm{p}}{2E_\mathrm{c}}\cdot\left[\frac{\cosh\left(\frac{L-l_1}{l_\mathrm{p}}\right)\cosh\left(\frac{L-l_1}{l_\mathrm{p}}\right)\sinh\left(\frac{l_1}{l_\mathrm{p}}\right)\cosh\left(\frac{l_1}{l_\mathrm{p}}\right)}{\cosh^2\left(\frac{L}{l_\mathrm{p}}\right)}\right. \\ &\qquad \left. + \frac{\cosh\left(\frac{L-l_1}{l_\mathrm{p}}\right)\sinh\left(\frac{L-l_1}{l_\mathrm{p}}\right)\sinh\left(\frac{l_1}{l_\mathrm{p}}\right)\sinh\left(\frac{l_1}{l_\mathrm{p}}\right)}{\cosh^2\left(\frac{L}{l_\mathrm{p}}\right)}\right] \end{aligned}$$

$$
\begin{aligned}
&= \frac{1}{2} \cdot \Bigg[\underbrace{\frac{\sigma_0 \cosh\left(\frac{L-l_1}{l_\mathrm{p}}\right)\cosh\left(\frac{l_1}{l_\mathrm{p}}\right)}{\cosh\left(\frac{L}{l_\mathrm{p}}\right)}}_{\sigma_\mathrm{I}(l_1)} \cdot \underbrace{\frac{\sigma_0 l_\mathrm{p}}{E_\mathrm{c}} \cdot \frac{\cosh\left(\frac{L-l_1}{l_\mathrm{p}}\right)\sinh\left(\frac{l_1}{l_\mathrm{p}}\right)}{\cosh\left(\frac{L}{l_\mathrm{p}}\right)}}_{u_\mathrm{I}(l_1)} \\
&\qquad + \underbrace{\frac{\sigma_0 \sinh\left(\frac{L-l_1}{l_\mathrm{p}}\right)\sinh\left(\frac{l_1}{l_\mathrm{p}}\right)}{\cosh\left(\frac{L}{l_\mathrm{p}}\right)}}_{-\sigma_\mathrm{II}(l_1)} \cdot \underbrace{\frac{\sigma_0 l_\mathrm{p}}{E_\mathrm{c}} \cdot \frac{\cosh\left(\frac{L-l_1}{l_\mathrm{p}}\right)\sinh\left(\frac{l_1}{l_\mathrm{p}}\right)}{\cosh\left(\frac{L}{l_\mathrm{p}}\right)}}_{u_\mathrm{II}(l_1)} \Bigg] \\
&= \frac{1}{2}\left(\sigma_\mathrm{I}\left(l_1\right) \cdot u_\mathrm{I}\left(l_1\right) - \sigma_\mathrm{II}\left(l_1\right) \cdot u_\mathrm{II}\left(l_1\right)\right) \\
&= \frac{1}{2}\left[\lim_{x \to l_1^-}\left(\sigma\left(x\right) \cdot u\left(x\right)\right) - \lim_{x \to l_1^+}\left(\sigma\left(x\right) \cdot u\left(x\right)\right)\right], \qquad \text{(6.51a)}
\end{aligned}
$$

with the one-sided limits $\lim_{x\to a^-}$, as x approaches the value a from below, and $\lim_{x\to a^+}$, as x approaches the value a from above.

Full Model Since the stresses evoked by both contractile regions in Figure 6.16 superpose, the solution of the full model is a superposition of Equations 6.47 and 6.48, reading

$$
u(x) = \begin{cases}
-\frac{\sigma_0 l_\mathrm{p}}{E_\mathrm{c}} \frac{\sinh\left(\frac{l_1}{l_\mathrm{p}}\right) - \sinh\left(\frac{l_2}{l_\mathrm{p}}\right)}{\cosh\left(\frac{L}{l_\mathrm{p}}\right)} \cosh\left(\frac{x+L}{l_\mathrm{p}}\right) & , \text{ for } -L \le x \le -l_2 \\
-\frac{\sigma_0 l_\mathrm{p}}{E_\mathrm{c}} \frac{\sinh\left(\frac{l_1}{l_\mathrm{p}}\right)\cosh\left(\frac{x+L}{l_\mathrm{p}}\right) + \cosh\left(\frac{L-l_2}{l_\mathrm{p}}\right)\sinh\left(\frac{x}{l_\mathrm{p}}\right)}{\cosh\left(\frac{L}{l_\mathrm{p}}\right)} & , \text{ for } -l_2 < x \le -l_1 \\
\frac{\sigma_0 l_\mathrm{p}}{E_\mathrm{c}} \frac{\cosh\left(\frac{L-l_1}{l_\mathrm{p}}\right) - \cosh\left(\frac{L-l_2}{l_\mathrm{p}}\right)}{\cosh\left(\frac{L}{l_\mathrm{p}}\right)} \sinh\left(\frac{x}{l_\mathrm{p}}\right) & , \text{ for } -l_1 < x < l_1 \\
\frac{\sigma_0 l_\mathrm{p}}{E_\mathrm{c}} \frac{\sinh\left(\frac{l_1}{l_\mathrm{p}}\right)\cosh\left(\frac{x-L}{l_\mathrm{p}}\right) - \cosh\left(\frac{L-l_2}{l_\mathrm{p}}\right)\sinh\left(\frac{x}{l_\mathrm{p}}\right)}{\cosh\left(\frac{L}{l_\mathrm{p}}\right)} & , \text{ for } l_1 \le x < l_2 \\
\frac{\sigma_0 l_\mathrm{p}}{E_\mathrm{c}} \frac{\sinh\left(\frac{l_1}{l_\mathrm{p}}\right) - \sinh\left(\frac{l_2}{l_\mathrm{p}}\right)}{\cosh\left(\frac{L}{l_\mathrm{p}}\right)} \cosh\left(\frac{x-L}{l_\mathrm{p}}\right) & , \text{ for } l_2 \le x \le L
\end{cases}, \qquad \text{(6.52)}
$$

for the displacement u and

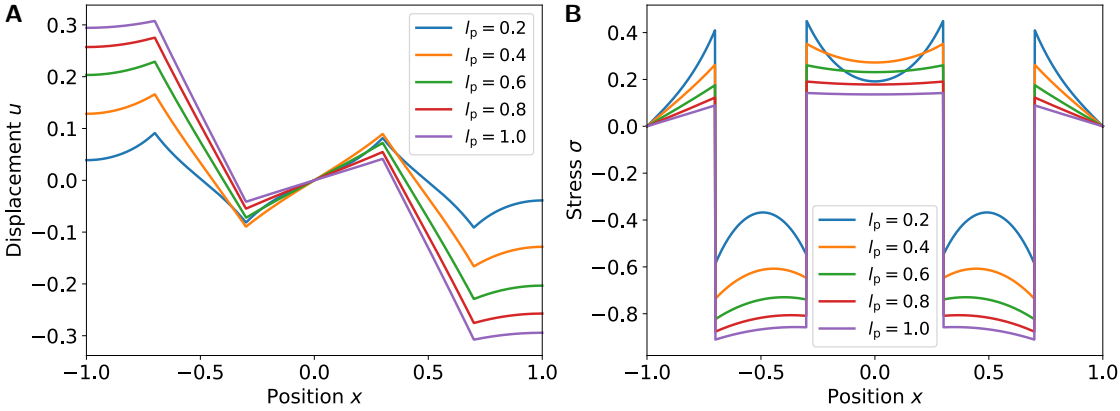

Figure 6.17: Exemplary displacement field u **(A)** and internal stress field σ **(B)** of an elastic bar with $E_c = 1.0$ in the full model for a varying force penetration length l_p. Parameters are: $\sigma_0 = 1.0$, $l_1 = 0.3$ and $l_2 = 0.7$, i.e. $p = 0.5$ and $w = 0.4$. Lengths and displacements are given in μm, while stress and stiffness are in nN.

$$\sigma(x) = \begin{cases} -\sigma_0 \frac{\sinh\left(\frac{l_1}{l_p}\right) - \sinh\left(\frac{l_2}{l_p}\right)}{\cosh\left(\frac{L}{l_p}\right)} \sinh\left(\frac{x+L}{l_p}\right) & , \text{ for } -L \le x \le -l_2 \\ -\sigma_0 \frac{\sinh\left(\frac{l_1}{l_p}\right) \sinh\left(\frac{x+L}{l_p}\right) + \cosh\left(\frac{L-l_2}{l_p}\right) \cosh\left(\frac{x}{l_p}\right)}{\cosh\left(\frac{L}{l_p}\right)} & , \text{ for } -l_2 < x \le -l_1 \\ \sigma_0 \frac{\cosh\left(\frac{L-l_1}{l_p}\right) - \cosh\left(\frac{L-l_2}{l_p}\right)}{\cosh\left(\frac{L}{l_p}\right)} \cosh\left(\frac{x}{l_p}\right) & , \text{ for } -l_1 < x < l_1 \\ \sigma_0 \frac{\sinh\left(\frac{l_1}{l_p}\right) \sinh\left(\frac{x-L}{l_p}\right) - \cosh\left(\frac{L-l_2}{l_p}\right) \cosh\left(\frac{x}{l_p}\right)}{\cosh\left(\frac{L}{l_p}\right)} & , \text{ for } l_1 \le x < l_2 \\ \sigma_0 \frac{\sinh\left(\frac{l_1}{l_p}\right) - \sinh\left(\frac{l_2}{l_p}\right)}{\cosh\left(\frac{L}{l_p}\right)} \sinh\left(\frac{x-L}{l_p}\right) & , \text{ for } l_2 \le x \le L \end{cases} , \tag{6.53}$$

for the stress σ. Figure 6.17 shows exemplary displacement and stress fields as a function of the penetration length for a bar length of $2\,\mu$m and the contractile region spanning between $l_1 = 0.3\,\mu$m and $l_2 = 0.7\,\mu$m. Interestingly, the stress σ in the center of the bar exhibits a maximum for a penetration length between $0.2\,\mu\text{m} < l_p < 0.6\,\mu\text{m}$. We will consider this observation further in Section 6.4.2.
Instead of the lengths l_1 and l_2, we can define the quantities *width of the leader cell*

$$w = l_2 - l_1\,, \tag{6.54}$$

and *position of the leader cell*

$$p = \frac{l_1 + l_2}{2}\,, \tag{6.55}$$

such that we can introduce the *distance between two leader cells* $d = 2p$. The internal

stress at position $x = 0$ as a function of the width w and position p of a leader cell is

$$\sigma(x=0) = \sigma_0 \frac{\cosh\left(\frac{L-l_1}{l_\mathrm{p}}\right) - \cosh\left(\frac{L-l_2}{l_\mathrm{p}}\right)}{\cosh\left(\frac{L}{l_\mathrm{p}}\right)} = \sigma_0 \frac{2\sinh\left(\frac{L-p}{l_\mathrm{p}}\right)\sinh\left(\frac{w}{2l_\mathrm{p}}\right)}{\cosh\left(\frac{L}{l_\mathrm{p}}\right)}\,. \tag{6.56}$$

From Equation 6.52, we can finally calculate the energy U_Y, which is stored in the elastic foundation, and U_E, which is stored in the elastic bar (see Appendix A.4.1). By adding U_Y and U_E, we get the total energy

$$\begin{aligned} U_\mathrm{tot} = \frac{\sigma_0^2 l_\mathrm{p}}{2E_\mathrm{c}\cosh^2\left(\frac{L}{l_\mathrm{p}}\right)} \cdot \Bigg[& 2\sinh\left(\frac{L}{l_\mathrm{p}}\right) - \sinh\left(\frac{L-2l_1}{l_\mathrm{p}}\right) \\ & -4\cosh\left(\frac{L-l_2}{l_\mathrm{p}}\right)\sinh\left(\frac{l_1}{l_\mathrm{p}}\right) - \sinh\left(\frac{L-2l_2}{l_\mathrm{p}}\right)\Bigg] \\ = \lim_{x\to l_1^-}(\sigma(x)\cdot u(x)) - \lim_{x\to l_1^+}(\sigma(x)\cdot u(x)) + \lim_{x\to l_2^-}(\sigma(x)\cdot u(x)) - \lim_{x\to l_2^+}(\sigma(x)\cdot u(x)) \end{aligned} \tag{6.57a}$$

Note that, in the last line, the factor 1/2 is missing if comparing with Equation 6.51 because we now expressed the energy with respect to the full bar.

6.4.2 Analytical Results

Figure 6.18 illustrates the internal stress $\sigma(x=0)$ in the center of the layer, as given by Equation 6.56, as a function of the model parameters. We find in Figures 6.18A and 6.18C that with increasing leader cell distance $2p$, the stress between the cells exponentially decreases with a length constant l_p, which is similar to the isotropically contracting two-dimensional model described in Section 6.3. Thus, this behavior can be interpreted in the way that two leader cells emerge only at a position $p > l_\mathrm{p}$, at which they do not feel each other.

Further on, the stress $\sigma(x=0)$ increases linearly with the leader cell width w, indicating that a larger part of the elastic bar and, with this, larger displacements are involved (see Figure 6.18B). As one would expect, this fact implies that a larger leader cell is a stronger leader cell.

Interestingly, we find in Figure 6.18D that the internal stress at $\sigma(x=0)$ becomes maximal for $l_\mathrm{p} = p$, which we already observed in the stress pattern in Figure 6.17B. We can explain this maximum by analyzing Equation 6.56 for the limit cases $p, w, l_\mathrm{p} \ll L$ and $w \ll l_\mathrm{p}$. The derivative of $\sigma(x=0)$ with respect to l_p yields

$$\begin{aligned} \frac{\partial\sigma(x=0)}{\partial l_\mathrm{p}} = \frac{\sigma_0}{l_\mathrm{p}^2\cosh\left(\frac{L}{l_\mathrm{p}}\right)} \cdot \Bigg[& \frac{\sinh\left(\frac{w}{2l_\mathrm{p}}\right)}{\cosh\left(\frac{L}{l_\mathrm{p}}\right)} \cdot \left(p\cosh\left(\frac{2L-p}{l_\mathrm{p}}\right) + (p-2L)\cosh\left(\frac{p}{l_\mathrm{p}}\right)\right) \\ & - w\cosh\left(\frac{w}{2l_\mathrm{p}}\right)\sinh\left(\frac{L-p}{l_\mathrm{p}}\right)\Bigg]\,. \end{aligned} \tag{6.58}$$

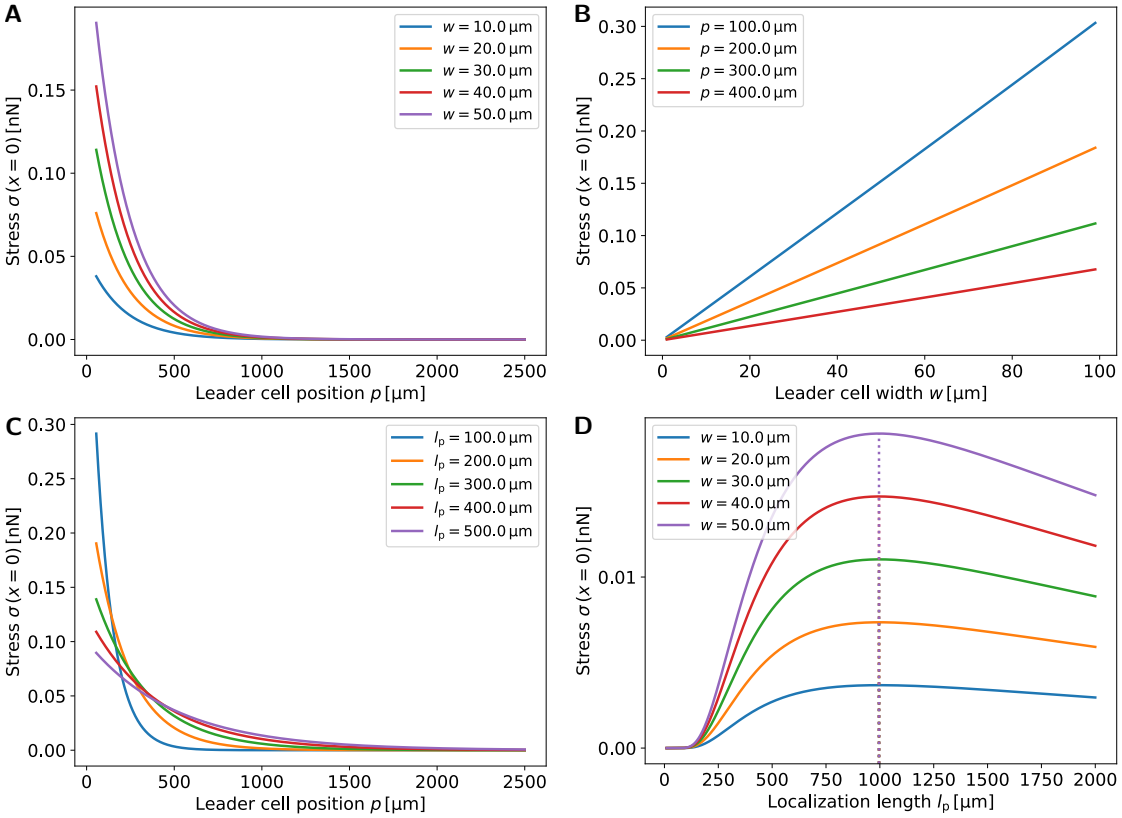

Figure 6.18: Internal stress $\sigma\,(x=0)$ as a function of the model parameters. **(A)** Internal stress $\sigma\,(x=0)$ as a function of the leader cell position p for different widths w. The internal stress at $x=0$ increases with increasing leader cell width w, while it decreases exponentially with increasing leader cell distance $2p$. **(B)** The internal stress at $x=0$ is a linearly increasing function of the leader cell width w. **(C)** Internal stress $\sigma\,(x=0)$ as a function of the position p for different localization lengths l_p. The internal stress at $x=0$ drops faster with decreasing l_p. **(D)** Internal stress $\sigma\,(x=0)$ as a function of the localization length l_p for different widths w. The internal stress at $x=0$ is maximal for $l_\mathrm{p}=p$, independent of width w. Default values are: $\sigma_0=1\,\mathrm{nN}$, $E_\mathrm{c}=1\,\mathrm{nN}$, $L=5000\,\mu\mathrm{m}$, $w=50\,\mu\mathrm{m}$, $p=1000\,\mu\mathrm{m}$ and $l_\mathrm{p}=200\,\mu\mathrm{m}$.

Equaling the derivative with zero yields the trivial minima at $l_\mathrm{p}\to 0$ and $l_\mathrm{p}\to\infty$, and the maximum lies at l_p fulfilling the following equation:

$$p\cosh\left(\frac{2L-p}{l_\mathrm{p}}\right)+(p-2L)\cosh\left(\frac{p}{l_\mathrm{p}}\right)-\frac{w\cosh\left(\frac{L}{l_\mathrm{p}}\right)\sinh\left(\frac{L-p}{l_\mathrm{p}}\right)}{\tanh\left(\frac{w}{2l_\mathrm{p}}\right)}=0\,. \tag{6.59}$$

With the addition theorem

$$\cosh\left(\frac{2L-p}{l_\mathrm{p}}\right) = \cosh\left(\frac{L}{l_\mathrm{p}}\right)\cosh\left(\frac{L-p}{l_\mathrm{p}}\right) + \sinh\left(\frac{L}{l_\mathrm{p}}\right)\sinh\left(\frac{L-p}{l_\mathrm{p}}\right), \tag{6.60}$$

and $\cosh(p/l_\mathrm{p})/\cosh(L/l_\mathrm{p}) \approx 0$, we can reduce the equation to

$$p\left(\frac{1}{\tanh\left(\frac{L-p}{l_\mathrm{p}}\right)} + \tanh\left(\frac{L}{l_\mathrm{p}}\right)\right) - \frac{w}{\tanh\left(\frac{w}{2l_\mathrm{p}}\right)} = 0\,. \tag{6.61}$$

With $\tanh(L-p/l_\mathrm{p}) \approx \tanh(L/l_\mathrm{p})$ and the limits

$$\tanh\left(\frac{w}{2l_\mathrm{p}}\right) \xrightarrow[w \ll 2l_\mathrm{p}]{} \frac{w}{2l_\mathrm{p}}\,, \tag{6.62}$$

and

$$\tanh\left(\frac{L}{l_\mathrm{p}}\right) \xrightarrow[l_\mathrm{p} \ll L]{} 1\,, \tag{6.63}$$

we finally get the equality $l_\mathrm{p} = p$.
Figure 6.19 shows the energy contributions involved in the system. In particular, we find in Figure 6.19A that the coupling energy becomes minimal at $p = l_\mathrm{p}$, implying that a leader cell distance of $2l_\mathrm{p}$ is ideal if cell dynamics is dominated by the mechanical properties of the environment.
Conversely, Figure 6.19B reveals that the minimal strain energy is always reached at the limit $p \to 0$, independent of l_p. The elastic bar, however, has a characteristic maximal strain energy at $p = 2l_\mathrm{p}$.
Figure 6.19C shows the total energy of the elastic bar as a function of the leader cell position. The course of the curve is similar to those of the strain energy, since, for the complete range of p, the strain energy is up to an order of magnitude larger than the coupling energy, as illustrated by Figure 6.19D. However, the total energy does not contain a maximum at finite position p, but the maximum of the strain energy is flattened by means of the coupling energy contribution.
Compared to the total energy of a two-dimensional elastic layer in Figure 6.11, the total energy does not become minimal for $p = l_\mathrm{p}/2$, but independently of l_p for $p \to 0$. In this sense, the model is insufficient to serve as a mechanistic explanation of the experimental observations from Sections 6.1 and 6.2. This indicates that the two-dimensional description of the cell layer is a prerequisite to explain the emergence of leader cells from a pure mechanical perspective, as was accomplished in Section 6.3.

6.5 Conclusion

Although cellular mechanical activity in the process of collective cell migration is very diverse and complex, we could show by means of our continuum model that the origin, maintenance and splitting of leader cells can be explained based on simple mechanical

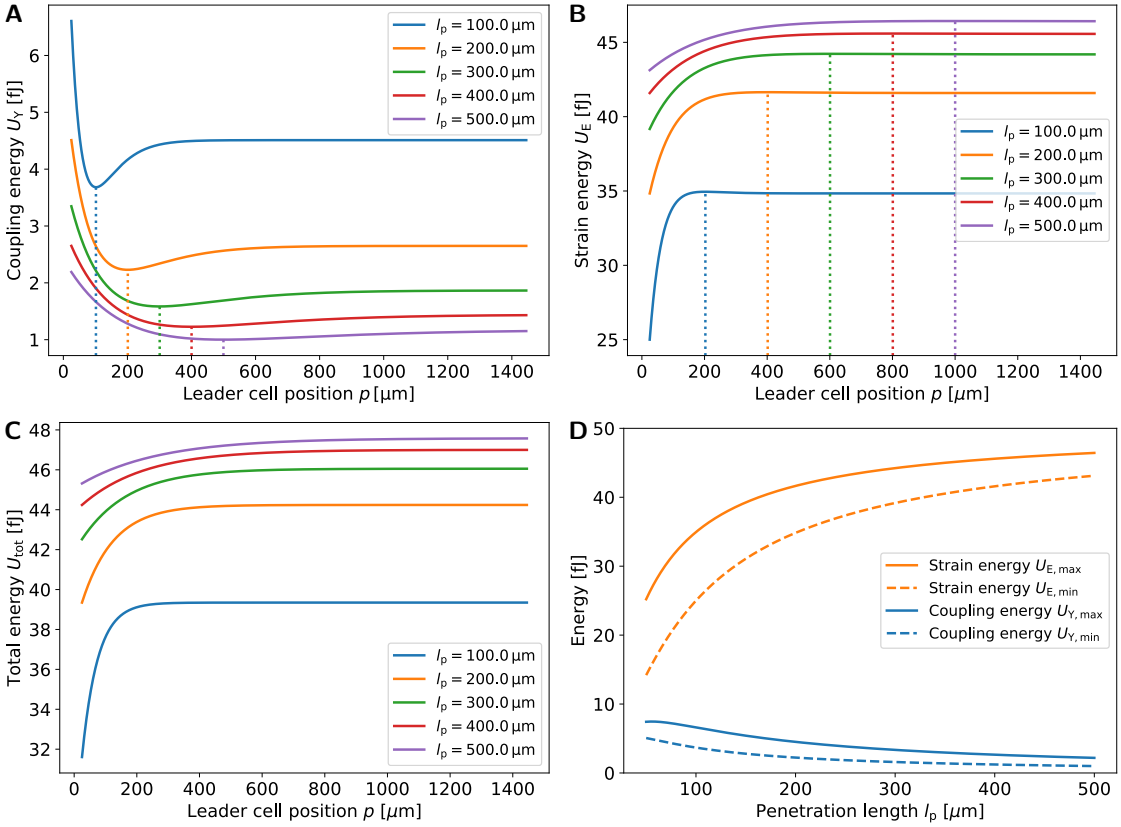

Figure 6.19: Comparison of energy contributions as a function of the position p and localization length l_p. **(A)** Coupling energy U_Y: As indicated by the dotted lines, the coupling energy is minimal for $p = l_p$. **(B)** Strain energy U_E: As indicated by the dotted lines, the strain energy is maximal for $p = 2 \cdot l_p$ and minimal for $p \to 0$, independent of l_p. **(C)** The total energy U_{tot} is minimal for $p \to 0$, independent of l_p. **(D)** Over a large range of l_p, the strain energy U_E is an order of magnitude larger than the coupling energy U_Y. For small $l_p \approx w$, both energy contributions approach each other. Default values are: $\sigma_0 = 1\,\text{nN}$, $E_c = 1\,\text{nN}$, $L = 5000\,\mu\text{m}$ and $w = 50\,\mu\text{m}$.

arguments, such as the localization of forces in elastic solids whose dynamics is subject to elastic coupling with a fixed foundation.

In particular, we used our two-dimensional continuum model to derive a purely mechanical explanation of leader cell formation. We could explain the fact that neighboring leader cells express a surprisingly constant distance between each other and that this length scale is preserved in the transversal direction of the cell layer during the splitting process of an outgrowth into two cell groups, each of which is guided by a different leader cell.

We further used TFM to find that leader cells exert the largest forces and that the characteristic distance between two neighboring force peaks approximately equals the distance between two neighboring leader cells. Surprisingly, these specific traction stresses already exist before the initiation of a leader cell, suggesting that leader cells are selected

by their would-be follower cells by means of pulling forces.
We incorporated the results deduced by means of TFM into our model, representing the mechanical activity of leader cells as single force spots embedded in a mechanically passive bulk. This facilitated to deduce an explanation of the observed characteristic distances based on the total mechanical energy in the system: The characteristic distance between two neighboring leader cells minimizes the total energy of the system.
We finally introduced a one-dimensional model which allowed an analytical treatment of the mechanisms involved during the first steps of leader cell formation. Although we found that a one-dimensional description of the process is not sufficient to allow a reasoning based on minimal energy arguments, it still allows to compare contributions from the layer and the substrate to the total energy and serves as a good starting point for further computation involving e.g. a viscous component, chemical gradients or physical heterogeneities.
Taken together, a migrating layer of cells exhibits a characteristic distance at which forces and velocities decay, which equals the typical distance between two neighboring leader cells at the onset of migration. Finite element simulations of a two-dimensional elastic sheet with elastic foundation showed that this typical distance can be explained by the spatial limit of force transduction in the elastic sheet. A reduction of the finite element model to one dimension revealed that the mechanically-guided emergence of leader cells can only be captured by the two-dimensional description.

Part III

From Macroscopic Models to Microscopic Composition - Multiscale Modeling of the Actin Cytoskeleton

7 Relating Scales of Cellular Contractility via Asymptotic Homogenization

So far, we only considered the actin cytoskeleton (CSK) as a homogeneous bulk of contractile viscoelastic material with homogeneous coupling to its environment. However, on a microscopic scale, the actin CSK is an assembly of string-like dynamically polymerizing and depolymerizing actin filaments and discrete filaments of myosin motors organized in various architectures, such as actin cortex or stress fibers, depending on their location and function in the cell [*Blanchoin et al.*, 2014].
For example, stress fibers (SFs) exhibit a muscle-cell-like sarcomeric arrangement of active and passive elements, while in the actin cortex, the number of actin and myosin filaments tends to decrease with decreasing distance from the cell edge. The discrete actomyosin mesh is further mechanically coupled to the cellular environment at discrete focal adhesion (FA) sites. It is therefore inevitable to take the microscopic structure of the actin CSK into consideration in order to understand the basics of actomyosin contractility on a global scale.
The mathematical formalism to establish a connection between local and global material properties is the so-called *asymptotic homogenization* (AH). Briefly worded, we introduce a local scale parameter ϵ which captures the microscopic variations of the system and, by investigating the limit case $\epsilon \to \infty$, we arrive at a homogeneous model which, at first order, behaves equivalently as compared to the complex microscopic material [*Hornung*, 1997; *Cioranescu and Donato*, 1999]. In this context, AH crucially differs from the simple spatial averaging of local parameters. Typical fields of application of AH range from the propagation of acoustic waves through heterogeneous media [*Capdeville et al.*, 2010] to porous flow of fluids in sheets of plant cells [*Chavarría-Krauser and Ptashnyk*, 2010]. However, a corresponding formal treatment of the actin CSK in order to relate macroscopic with microscopic mechanics in unknown so far.
In this chapter, we apply the one-dimensional asymptotic homogenization technique to the problem of actomyosin-generated contractility to create a relation between the microscopic composition of the cellular cytoskeleton and macroscopic properties. We will see in Section 7.1 that the global stiffness and stress strongly depends on the microscopic arrangement of springs and motors, while the global adhesion strength is independent of the arrangement of single adhesions. In Section 7.2, we will then use the analytical relation between macroscopic and microscopic model to deduce microscopic parameters from global stiffness and stress ranges measured in the particular case of single SFs. SFs are known to be the stiffest and strongest elements in epithelial cells, thus it is of particular interest to create a relation between their global forces and the local dynamics of the sarcomeric subunits. Our calculations will allow to assign local stiffness and stress

values to the sarcomeric subregions using from experimentally acquired macroscopic parameters and reevaluate a current study by *Livne and Geiger* [2016], who suggested that the actomyosin contractility is unlikely to generate the full SF contractility. Indeed, we will find that the macroscopic behavior of SFs can only emerge from a local negative compressibility, a property which is usually attributed to metamaterials.

7.1 One-Dimensional Homogenization of Active Viscoelastic Material

In the following, we will start with an introduction of the asymptotic homogenization technique in one dimension and apply the technique to the particular problem of an actively contractile viscoelastic bar of Maxwell or Kelvin-Voigt type with elastic coupling in Section 7.1.1. In Section 7.1.2, we will establish the relation between micro- and macromechanical properties for mechanobiologically relevant arrangements of springs, dashpots and motors.

7.1.1 Homogenization of Active Viscoelastic Models

We will now calculate the asymptotic behavior of a contractile viscoelastic bar of Maxwell or Kelvin-Voigt type with elastic coupling, subject to a rapid spatial variation of its coefficients. For reasons of analytical computability, we will consider the case of temporally fixed parameters, which is sufficient for the problems we approach in the remainder of this chapter. For time-dependent problems, the reader is referred e.g. to *Orlik* [1998] for the particular case of a Maxwell model and *Abdessamad et al.* [2009] for the particular case of a Kelvin-Voigt model.

Homogenization of the Active Maxwell Model We start with a one-dimensional viscoelastic bar of Maxwell-type (see Figure 1.9D) with a periodically varying elasticity E_ϵ, viscosity η_ϵ and motor stress $\sigma_{\mathrm{m}\epsilon}$, with variations occurring on a microscopic length scale l with respect to the length of the bar L, such that $\epsilon = {}^{l}/_{L} \ll 1$. We further assume a constant cross-section area A_0 throughout the entire bar. We can write down the constitutive relation of the model by retrieving Equation 3.8

$$\frac{\sigma_\epsilon - \sigma_{\mathrm{m}\epsilon}}{\tau_\epsilon} + (\dot{\sigma}_\epsilon - \dot{\sigma}_{\mathrm{m}\epsilon}) = E_\epsilon \frac{\partial \dot{u}_\epsilon}{\partial x} \,, \tag{7.1}$$

with the Maxwell time constant $\tau_\epsilon = {}^{\eta_\epsilon}/_{E_\epsilon}$. The equation of motion is then determined by the elastic coupling of the bar to its environment

$$\frac{\partial \sigma_\epsilon}{\partial x} = Y_\epsilon u_\epsilon - f_{\mathrm{ext}} \,, \tag{7.2}$$

with varying coupling strength Y_ϵ and additional external stresses represented by the force f_{ext}. In general, we can also introduce a friction term in this equation, as we did in

Equation 3.9, but we will see that we can treat any other component which is in series to Y_ϵ in an equivalent manner.
Since we deal with time-independent parameters, we can simplify the following calculation by transforming the problem into the Laplace domain, in a similar fashion to e.g. *Francfort and Suquet* [1986]. Laplace transformation of Equation 7.1 yields

$$\tilde{\sigma}_\epsilon(s) = \tilde{A}_\epsilon(s)\frac{\partial \tilde{u}_\epsilon}{\partial x} + \tilde{\sigma}_{\mathrm{m}\epsilon}\,, \tag{7.3}$$

with the frequency parameter s and the material parameter

$$\tilde{A}_\epsilon(s) = \frac{E_\epsilon s}{s + \frac{1}{\tau_\epsilon}}\,. \tag{7.4}$$

Here, without loss of generality, we set the initial displacement and stress to zero. Equation 7.3 has now the form of the standard asymptotic problem of an elastic bar subject to a thermo-elastic stress, as treated e.g. by *Sanchez-Palencia* [1983] or *Hornung* [1997]. The Laplace transform of Equation 7.2 yields

$$\frac{\partial}{\partial x}\left[\tilde{A}_\epsilon \frac{\partial \tilde{u}_\epsilon}{\partial x}\right] + \frac{\partial}{\partial x}\tilde{\sigma}_{\mathrm{m}\epsilon} = \tilde{Y}_\epsilon \tilde{u} - \tilde{f}_{\mathrm{ext}}\,. \tag{7.5}$$

Since $\epsilon \ll 1$, we are not interested in the exact calculation of the displacement $\tilde{u}_\epsilon(x,s)$, but in the effective behavior of the elastic bar in the limit $\epsilon \to 0$. With this in mind, in addition to the global spatial variable x, we now introduce a second variable $y = x/\epsilon$, which, by design, captures the local variability of the material on the length scale l. Any function $f_\epsilon(x)$ then turns into a function of two variables $f(x,y) = f(x, x/\epsilon)$. The change of variables changes the derivative of function $f_\epsilon(x)$, due to the chain rule, to

$$\frac{\partial}{\partial x} f_\epsilon(x) = \frac{\partial f(x,y)}{\partial x}\frac{\partial x}{\partial x} + \frac{\partial f(x,y)}{\partial y}\frac{\partial y}{\partial x} = \left(\frac{\partial}{\partial x} + \frac{1}{\epsilon}\frac{\partial}{\partial y}\right) f(x,y)\,. \tag{7.6}$$

Thus, any derivative with respect to x transforms to

$$\frac{\partial}{\partial x} \to \frac{\partial}{\partial x} + \frac{1}{\epsilon}\frac{\partial}{\partial y}\,. \tag{7.7}$$

We then expand the displacement as

$$\tilde{u}_\epsilon(x,s) = \sum_{i=0}^{\infty} \epsilon^i \tilde{u}_i(x,y,s)\,. \tag{7.8}$$

Introducing Equations 7.7 and 7.8 into Equation 7.5 leads to

$$\left(\frac{\partial}{\partial x}+\frac{1}{\epsilon}\frac{\partial}{\partial y}\right)\left[\tilde{A}_\epsilon\left(\frac{\partial}{\partial x}+\frac{1}{\epsilon}\frac{\partial}{\partial y}\right)\left(\tilde{u}_0+\epsilon\tilde{u}_1+\epsilon^2\tilde{u}_2+...\right)\right] = -\left(\frac{\partial}{\partial x}+\frac{1}{\epsilon}\frac{\partial}{\partial y}\right)\tilde{\sigma}_{\mathrm{m}\epsilon}+\tilde{Y}_\epsilon\left(\tilde{u}_0+\epsilon\tilde{u}_1+\epsilon^2\tilde{u}_2+...\right)-\tilde{f}_{\mathrm{ext}}\,. \quad (7.9)$$

We now separate the equation by orders of ϵ, which yields

$$\left[\epsilon^{-2}\partial_y\left(\tilde{A}_\epsilon\partial_y\right)+\epsilon^{-1}\left(\partial_y\tilde{A}_\epsilon\partial_x+\partial_x\tilde{A}_\epsilon\partial_y\right)+\partial_x\tilde{A}_\epsilon\partial_x\right]\left(\tilde{u}_0+\epsilon\tilde{u}_1+\epsilon^2\tilde{u}_2+...\right)\equiv \left[\epsilon^{-2}T_0+\epsilon^{-1}T_1+T_2\right]\left(\tilde{u}_0+\epsilon\tilde{u}_1+\epsilon^2\tilde{u}_2+...\right)= -\left(\partial_x+\epsilon^{-1}\partial_y\right)\tilde{\sigma}_{\mathrm{m}\epsilon}+\tilde{Y}_\epsilon\left(\tilde{u}_0+\epsilon\tilde{u}_1+\epsilon^2\tilde{u}_2+...\right)-\tilde{f}_{\mathrm{ext}}\,. \quad (7.10)$$

Since $\epsilon \ll 1$, we can subdivide Equation 7.10 into infinitely many equations, depending on the order in ϵ, and take only the lowest orders of ϵ into account. For $\mathcal{O}\left(\epsilon^{-2}\right)$, we have

$$T_0\tilde{u}_0=\partial_y\left(\tilde{A}_\epsilon\partial_y\tilde{u}_0\right)=0\,, \quad (7.11)$$

which yields

$$\partial_y\tilde{u}_0=0 \iff \tilde{u}_0\left(x,y\right)=\tilde{u}_0\left(x\right)\,, \quad (7.12)$$

since $\tilde{A}_\epsilon$ is, in general, a function of y. Thus, $\tilde{u}_0$ is only a function of the macroscopic variable x, irrespective of the microscopic variations. For $\mathcal{O}\left(\epsilon^{-1}\right)$, we get

$$T_0\tilde{u}_1+T_1\tilde{u}_0=-\partial_y\tilde{\sigma}_{\mathrm{m}\epsilon}\,, \quad (7.13)$$

yielding

$$\begin{aligned}\partial_y\left(\tilde{A}_\epsilon\partial_y\tilde{u}_1\right) &= -\partial_y\tilde{\sigma}_{\mathrm{m}\epsilon}-\left(\partial_y\tilde{A}_\epsilon\partial_x+\partial_x\tilde{A}_\epsilon\partial_y\right)\tilde{u}_0\\ \Leftrightarrow\ \partial_y\left(\tilde{A}_\epsilon\partial_y\tilde{u}_1\right) &\overset{(7.12)}{=} -\partial_y\tilde{\sigma}_{\mathrm{m}\epsilon}-\partial_y\left(\tilde{A}_\epsilon\partial_x\tilde{u}_0\right)\,,\end{aligned} \quad (7.14)$$

which means that $u_1(x,y)$ is a sum of 2 independent functions of y:

$$\tilde{u}_1(x,y)=\chi_1(y)\partial_x\tilde{u}_0(x)+\chi_2(y)+\langle\tilde{u}_1\rangle_\Omega(x)\,. \quad (7.15)$$

Here, χ_1 and χ_2 are the so-called *first-order periodic correctors*. Uniqueness is enforced by imposing $\langle\chi_1\rangle_\Omega=0$ and $\langle\chi_2\rangle_\Omega=0$ with

$$\langle h\rangle_\Omega=\frac{1}{|\Omega|}\int_\Omega h(x,y)\mathrm{d}y\,, \quad (7.16)$$

where Ω denotes the unit cell. Introducing $\tilde{u}_1$ from Equation 7.15 into Equation 7.14

yields

$$\partial_y \left(\tilde{A}_\epsilon \partial_y \tilde{u}_1 \right) = \partial_y \left[\tilde{A}_\epsilon \left(\partial_y \left(\chi_1 \partial_x \tilde{u}_0 + \chi_2 \right) \right) \right] \stackrel{!}{=} -\partial_y \tilde{\sigma}_{\mathrm{m}\epsilon} - \partial_y \left(\tilde{A}_\epsilon \partial_x \tilde{u}_0 \right) . \tag{7.17}$$

By comparison, we find two independent cell problems

$$\begin{cases} \partial_y \left[\tilde{A}_\epsilon \left(\partial_y \chi_1 + 1 \right) \right] = 0 \\ \partial_y \left[\tilde{A}_\epsilon \left(\partial_y \chi_2 \right) + \tilde{\sigma}_{\mathrm{m}\epsilon} \right] = 0 \end{cases} , \tag{7.18}$$

which can be solved for χ_1 and χ_2 for any given profile of $\tilde{A}_\epsilon$ and $\tilde{\sigma}_{\mathrm{m}\epsilon}$. Finally, the equation which results from considering only terms of order $\mathcal{O}(1)$ in Equation 7.10 yields

$$T_0 \tilde{u}_2 + T_1 \tilde{u}_1 + T_2 \tilde{u}_0 = -\partial_x \tilde{\sigma}_{\mathrm{m}\epsilon} + \tilde{Y}_\epsilon \tilde{u}_0 - \tilde{f}_{\mathrm{ext}} . \tag{7.19}$$

or, written-out,

$$\partial_y \left(\tilde{A}_\epsilon \partial_y \tilde{u}_2 \right) + \left(\partial_y \tilde{A}_\epsilon \partial_x + \partial_x \tilde{A}_\epsilon \partial_y \right) \tilde{u}_1 + \partial_x \left(\tilde{A}_\epsilon \partial_x \tilde{u}_0 \right) = -\partial_x \tilde{\sigma}_{\mathrm{m}\epsilon} + \tilde{Y}_\epsilon \tilde{u}_0 - \tilde{f}_{\mathrm{ext}} . \tag{7.20}$$

By averaging Equation 7.20 over the unit cell, we can eliminate the first two terms due to their Ω-periodicity. We can now introduce Equation 7.15 into 7.20 yielding

$$\begin{aligned} \partial_x \left\langle \tilde{A}_\epsilon \partial_y \chi_1 \right\rangle_\Omega \partial_x \tilde{u}_0 + \partial_x \left\langle \tilde{A}_\epsilon \partial_x \chi_2 \right\rangle_\Omega + \partial_x \left\langle \tilde{A}_\epsilon \right\rangle_\Omega \partial_x \tilde{u}_0 \\ = -\partial_x \left\langle \tilde{\sigma}_{\mathrm{m}\epsilon} \right\rangle_\Omega + \left\langle \tilde{Y}_\epsilon \right\rangle_\Omega \tilde{u}_0 - \tilde{f}_{\mathrm{ext}} , \end{aligned} \tag{7.21}$$

where we find the *homogenized equation of motion*

$$\partial_x \left[\tilde{A}^* \partial_x \tilde{u}_0 \right] = -\partial_x \tilde{\sigma}^*_{\mathrm{m}} + \tilde{Y}^*_\epsilon - \tilde{f}_{\mathrm{ext}} , \tag{7.22}$$

with the *homogenized moduli*

$$\begin{cases} \tilde{A}^* = \left\langle \tilde{A}_\epsilon \left(\partial_y \chi_1 + 1 \right) \right\rangle_\Omega \\ \tilde{\sigma}^*_{\mathrm{m}} = \left\langle \tilde{A}_\epsilon \left(\partial_y \chi_2 \right) + \tilde{\sigma}_{\mathrm{m}\epsilon} \right\rangle_\Omega \\ \tilde{Y}^*_\epsilon = \left\langle \tilde{Y}_\epsilon \right\rangle_\Omega \end{cases} , \tag{7.23}$$

representing the effective parameters of the viscoelastic bar.
We can solve the resulting cell problems in Equation 7.18 for χ_1 and χ_2 for the general one-dimensional case [*Capdeville et al.*, 2010]. The solution of the first ODE denotes

$$\partial_y \chi_1 = \frac{a}{\tilde{A}_\epsilon(y)} - 1 , \tag{7.24}$$

and, thus,

$$\chi_1 = -y + a \int_0^y \frac{1}{\tilde{A}_\epsilon(y')} \mathrm{d}y' + b\,, \tag{7.25}$$

with constants $a = \langle \tilde{A}_\epsilon^{-1} \rangle_\Omega^{-1}$ from $\langle \partial_y \chi_1 \rangle_\Omega = 0$ and b from the uniqueness condition $\langle \chi_1 \rangle_\Omega = 0$. With Equation 7.24, the homogenized elastic modulus is exactly the harmonic average of E_ϵ

$$\tilde{A}^* = a = |\Omega| \left(\int_\Omega \frac{1}{\tilde{A}_\epsilon(y')} \mathrm{d}y' \right)^{-1} . \tag{7.26}$$

We can consider the same procedure for solving the second ODE of Equation 7.18 in order to compute the homogenized active stress, yielding

$$\partial_y \chi_2 = \frac{c}{\tilde{A}_\epsilon(y)} - \frac{\tilde{\sigma}_{\mathrm{m}\epsilon}(y)}{\tilde{A}_\epsilon(y)}\,, \tag{7.27}$$

and, thus,

$$\chi_2 = c \int_0^y \frac{1}{\tilde{A}_\epsilon(y')} \mathrm{d}y' + \int_0^y \frac{\tilde{\sigma}_{\mathrm{m}\epsilon}(y')}{\tilde{A}_\epsilon(y')} \mathrm{d}y' + d\,, \tag{7.28}$$

with constants c and d. Using the assumption of periodicity and vanishing average of χ_2 in the unit cell, finally yields the homogenized active stress

$$\tilde{\sigma}_{\mathrm{m}}^* = c = \left(\int_\Omega \frac{1}{\tilde{A}_\epsilon(y')} \mathrm{d}y' \right)^{-1} \cdot \int_\Omega \frac{\tilde{\sigma}_{\mathrm{m}\epsilon}(y')}{\tilde{A}_\epsilon(y')} \mathrm{d}y' \,. \tag{7.29}$$

In contrast to $\tilde{A}^*$, which is only affected by $\tilde{A}_\epsilon$, the homogenized value $\tilde{\sigma}_{\mathrm{m}}^*$ depends on both $\tilde{A}_\epsilon$ and $\tilde{\sigma}_{\mathrm{m}\epsilon}$. Finally, we have the homogenized adhesive strength, which is simply the average

$$\tilde{Y}^* = \frac{1}{|\Omega|} \int_\Omega \tilde{Y}_\epsilon(y') \mathrm{d}y' \,, \tag{7.30}$$

independent of the internal moduli of the bar.

Homogenization of the Active Kelvin-Voigt Model We continue with a one-dimensional viscoelastic bar of Kelvin-Voigt-type (see Figure 1.9C) with a periodically varying elasticity E_ϵ, viscosity η_ϵ and motor stress $\sigma_{\mathrm{m}\epsilon}$, where again the index ϵ indicates variations occurring on a microscopic length scale l with respect to the length of the bar L, such that $\epsilon = l/L \ll 1$. As before, we assume a constant cross-section area A_0 throughout the entire bar. We can write down the constitutive relation of the Kelvin-Voigt model [*Howell et al.*, 2009]:

$$\sigma_\epsilon - \sigma_{\mathrm{m}\epsilon} = E_\epsilon \frac{\partial u_\epsilon}{\partial x} + \eta_\epsilon \frac{\partial \dot{u}_\epsilon}{\partial x} \,. \tag{7.31}$$

Here, the relaxation time constant is defined by $\tau_\epsilon = \eta_\epsilon / E_\epsilon$. The equation of motion remains as in Equation 7.2. In the same manner as was done in the previous paragraph, we can Laplace-transform the two equations before computing the homogenized moduli,

yielding the equation

$$\frac{\partial}{\partial x}\left[\tilde{A}_\epsilon \frac{\partial \tilde{u}_\epsilon}{\partial x}\right] + \frac{\partial}{\partial x}\tilde{\sigma}_{\mathrm{m}\epsilon} = \tilde{Y}_\epsilon \tilde{u} - \tilde{f}_{\mathrm{ext}}\,, \tag{7.32}$$

now with the material parameter

$$\tilde{A}_\epsilon(s) = \tilde{E}_\epsilon + \tilde{\eta}_\epsilon \cdot s\,, \tag{7.33}$$

as compared to the material parameter for the Maxwell model in Equation 7.4. The remaining mathematical procedure is equivalent those of the previous paragraph.

7.1.2 Analytical Calculation of Macroscopic from Microscopic Properties

We can use the relations for the Maxwell and Kelvin-Voigt model derived in Equations 7.23 to calculate the macroscopic properties of a viscoelastic bar based on microscopic variations. In particular, we will start with the simplest case of a periodic rectangular profile, for which we can calculate the homogenized coefficients analytically in the case of the viscoelastic bar. We will thereafter solve Equations 7.23 for the stiffness and stress profiles depicted in Figure 7.1A for a purely elastic bar.

7.1.2.1 Periodic Rectangular Profile in the Active Maxwell Model

We consider a periodic rectangular profile as illustrated by the blue curve in Figure 7.1A for the material parameter $\tilde{A}_\epsilon$, the motor stress $\tilde{\sigma}_{\mathrm{m}\epsilon}$ and the coupling strength $\tilde{Y}_\epsilon$, yielding

$$\tilde{\sigma}_\epsilon = \begin{cases} \tilde{A}^{(1)}\partial_y \tilde{u}_\epsilon + \tilde{\sigma}_{\mathrm{m}}^{(1)} & ,\ \text{for } 0 < y < \alpha \\ \tilde{A}^{(2)}\partial_y \tilde{u}_\epsilon + \tilde{\sigma}_{\mathrm{m}}^{(2)} & ,\ \text{for } \alpha < y < 1 \end{cases}\,, \tag{7.34}$$

with the ratio parameter $0 < \alpha < 1$. We will skip the particular treatment of the coupling strength $\tilde{Y}_\epsilon$, since the homogenized strength $\tilde{Y}^*$ is simply the average value of $\tilde{Y}_\epsilon$.
We can calculate the homogenized material parameter $\tilde{A}^*$ by solving Equation 7.26, yielding

$$\tilde{A}^* = \left(\int_0^\alpha \frac{1}{\tilde{A}^{(1)}}\mathrm{d}y' + \int_\alpha^1 \frac{1}{\tilde{A}^{(2)}}\mathrm{d}y'\right)^{-1} = \frac{\tilde{A}^{(1)}\tilde{A}^{(2)}}{(1-\alpha)\,\tilde{A}^{(1)} + \alpha\tilde{A}^{(2)}}\,, \tag{7.35}$$

with the particular limit

$$\tilde{A}^* \xrightarrow[\tilde{A}^{(2)}\to\infty]{} \frac{\tilde{A}^{(1)}}{\alpha}\,. \tag{7.36}$$

We further find for the motor stress

$$\begin{aligned}\tilde{\sigma}_{\mathrm{m}}^* = \left(\int_0^\alpha \frac{1}{\tilde{A}^{(1)}}\mathrm{d}y' + \int_\alpha^1 \frac{1}{\tilde{A}^{(2)}}\mathrm{d}y'\right)^{-1} \cdot \left(\int_0^\alpha \frac{\tilde{\sigma}^{(1)}}{\tilde{A}^{(1)}}\mathrm{d}y' + \int_\alpha^1 \frac{\tilde{\sigma}^{(2)}}{\tilde{A}^{(2)}}\mathrm{d}y'\right) \\ = \frac{\alpha\tilde{\sigma}^{(1)}\tilde{A}^{(2)} + (1-\alpha)\,\tilde{\sigma}^{(2)}\tilde{A}^{(1)}}{(1-\alpha)\,\tilde{A}^{(1)} + \alpha\tilde{A}^{(2)}}\,,\end{aligned} \tag{7.37}$$

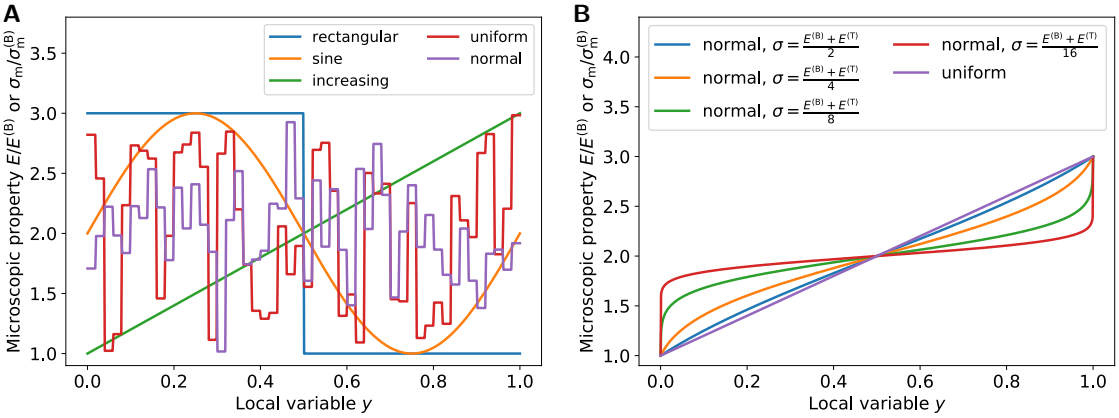

Figure 7.1: Inhomogeneous one-dimensional stiffness and motor stress profiles. **(A)** Different one-dimensional stiffness and motor stress profiles for which the homogenized coefficients are computed. All profiles entail the same average stiffness or motor stress. **(B)** If ordering the randomly distributed moduli from Panel **A**, the profiles turn to the inverse of the cumulative distribution function of the respective probability distribution. Default values are: $E^{(T)} = 3E^{(B)}$ and mean $\mu = \frac{E^{(B)}+E^{(T)}}{2}$ of the truncated normal distribution, equivalent for σ_m.

with the limit

$$\tilde{\sigma}^*_\mathrm{m} \xrightarrow[\tilde{A}^{(2)}\to\infty]{} \tilde{\sigma}^{(1)} \,. \tag{7.38}$$

We can now introduce the relation for $\tilde{A}_\epsilon$ from Equation 7.4 to calculate the homogenized stiffness, viscosity and motor stress for the Maxwell model. For the material parameter, we initially get

$$\tilde{A}^* = \frac{\tilde{E}^{(1)}\tilde{E}^{(2)}}{(1-\alpha)\,\tilde{E}^{(1)} + \alpha\tilde{E}^{(2)}} \cdot \left(1 - \frac{\frac{(1-\alpha)\frac{\tilde{E}^{(1)}}{\tilde{\tau}^{(2)}} + \alpha\frac{\tilde{E}^{(2)}}{\tilde{\tau}^{(1)}}}{(1-\alpha)\tilde{E}^{(1)} + \alpha\tilde{E}^{(2)}}}{s + \frac{(1-\alpha)\frac{\tilde{E}^{(1)}}{\tilde{\tau}^{(2)}} + \alpha\frac{\tilde{E}^{(2)}}{\tilde{\tau}^{(1)}}}{(1-\alpha)\tilde{E}^{(1)} + \alpha\tilde{E}^{(2)}}} \right) \,. \tag{7.39}$$

By inversely transforming this relation to the real domain, we get the Maxwell stress relaxation kernel

$$A^*(t) = E^* \cdot \left(\delta(t) - \frac{1}{\tau^*} \exp\left(-\frac{t}{\tau^*} \right) \right) \,, \tag{7.40}$$

with the homogenized stiffness extracted from the initial instantaneous jump of the kernel

$$E^* = \frac{E^{(1)}E^{(2)}}{(1-\alpha)\,E^{(1)} + \alpha E^{(2)}} \,, \tag{7.41}$$

equaling the homogenized stiffness of a purely elastic bar (compare e.g. *Fish et al.* [2002]). The homogenized viscosity can be deduced from the homogenized decay time constant of

the stress relaxation function

$$\tau^* = \frac{(1-\alpha)\,E^{(1)} + \alpha E^{(2)}}{(1-\alpha)\,\frac{E^{(1)}}{\tau^{(2)}} + \alpha\frac{E^{(2)}}{\tau^{(1)}}}\,, \tag{7.42}$$

such that

$$\eta^* = \tau^* E^* = \frac{\eta^{(1)}\eta^{(2)}}{(1-\alpha)\,\eta^{(1)} + \alpha\eta^{(2)}}\,, \tag{7.43}$$

confirming the fact that the springs and dashpots deform independently in the Maxwell model. With Equation 7.37, we get in a similar manner the inverse Laplace transform of the motor stress

$$\sigma^*_{\mathrm{m}}(t) = \sigma^*_{\mathrm{m0}} \cdot \left(\delta(t) - \left(\frac{1}{\tau^*} - \frac{1}{\tau^*_{\mathrm{m}}}\right)\exp\left(-\frac{t}{\tau^*}\right)\right)\,, \tag{7.44}$$

with the motor stress

$$\sigma^*_{\mathrm{m0}} = \frac{\alpha\sigma^{(1)}E^{(2)} + (1-\alpha)\,\sigma^{(2)}E^{(1)}}{(1-\alpha)\,E^{(1)} + \alpha E^{(2)}}\,, \tag{7.45}$$

independent of the viscosity and the motor stress decay time constant

$$\tau^*_{\mathrm{m}} = \frac{\alpha\sigma^{(1)}E^{(2)} + (1-\alpha)\,\sigma^{(2)}E^{(1)}}{\alpha\frac{\sigma^{(1)}E^{(2)}}{\tau^{(1)}} + (1-\alpha)\,\frac{\sigma^{(2)}E^{(1)}}{\tau^{(2)}}}\,. \tag{7.46}$$

For the case $E^{(\mathrm{i})} \propto \eta^{(\mathrm{i})}$, we have $\tau^* = \tau^*_{\mathrm{m}}$ and the motor stress in the homogenized model stays constant.

Figure 7.2 shows the resulting homogenized moduli as a function of the microscopic rectangular profile. Panel A illustrates the rectangular profiles for different ratio parameters α. For each for these profiles, the minimal stiffness is kept constant, to represent some minimal stiffness required to withstand typical stresses. Also, the mean value is kept constant to symbolize that in each case we deal with the same total amount of springs. With increasing α, both the width of the region of lower stiffness and the magnitude of the region with higher stiffness increase. In the following, we denote the region of lower stiffness by the superscript (B), for *bottom*, and the region of higher stiffness by the superscript (T), for *top*.

Figure 7.2B shows that the homogenized elastic modulus E^* increases with the magnitude of the microscopic modulus $E^{(\mathrm{T})}$, following a concavely shaped function for $0 < \alpha < 1$. With increasing α, i.e. with increasing region (B), E^* decreases, highlighting that the width of the region of lower stiffness outweighs the magnitude of the region of higher stiffness. Further, with increasing $E^{(\mathrm{T})}$, $E^*/E^{(\mathrm{B})}$ approaches the value $1/\alpha$ as expected from Equation 7.36. We have to note here, that according to Equation 7.43, the homogenized viscosity η^* will have the same dependency of the microscopic viscosity.

As Panels 7.2C and 7.2D indicate, the homogenized motor stress σ^*_{m} decreases with increasing stiffness $E^{(\mathrm{T})}$ and increases linearly with increasing motor stress $\sigma^{(\mathrm{T})}_{\mathrm{m}}$. As

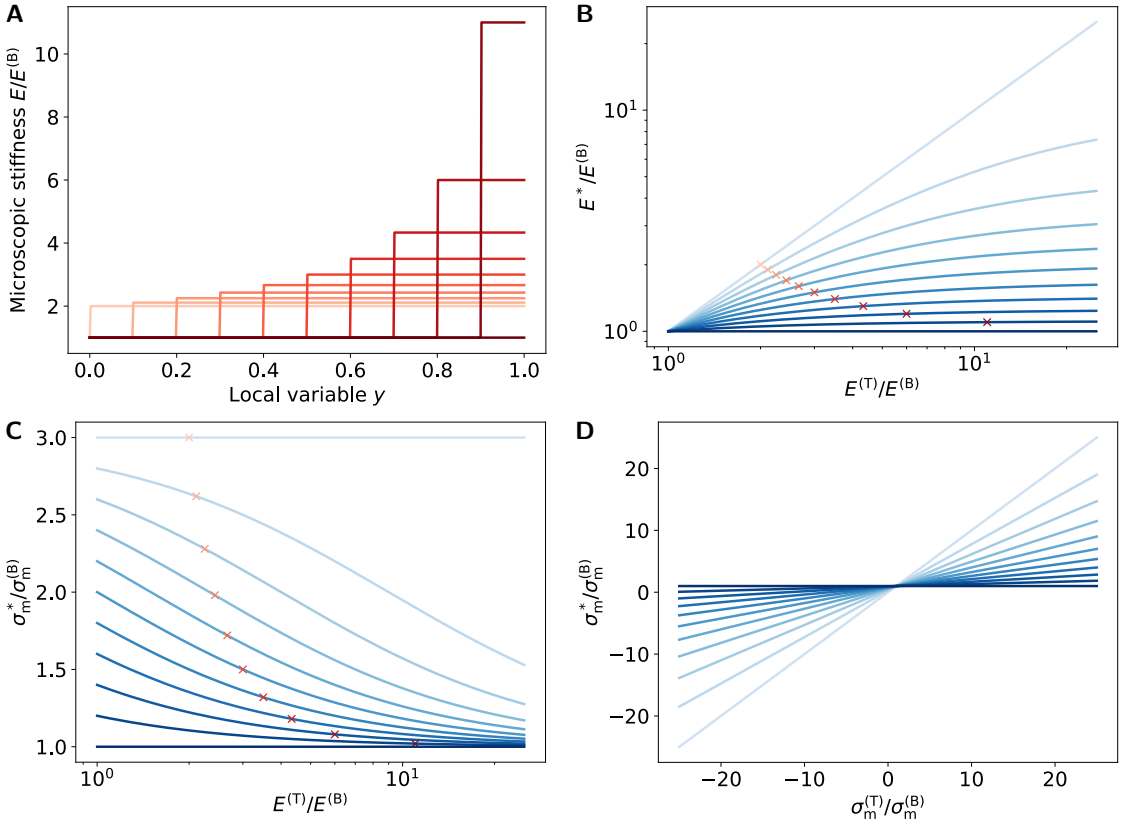

Figure 7.2: One-dimensional homogenized stiffness and stress moduli for an active Maxwell model with a rectangular stiffness, viscosity and stress profile as a function of the fraction parameter α. **(A)** Stiffness profiles as a function of α. With increasing α, both the maximal stiffness value $E^{(T)}$ and the size of the region with $E^{(B)}$ increase. For all profiles, we use $\bar{E} = 2E^{(B)}$. **(B)** Macroscopic stiffness $E^\star$ as a function of $E^{(T)}$. For $0 < \alpha < 1$, $E^\star$ is a concave, monotonically increasing function of $E^{(T)}$. With increasing α, $E^\star$ decreases. *Red crosses* refer to the profiles in Panel **A**. **(C)** Macroscopic stress $\sigma_m^\star$ as a function of $E^{(T)}$. For $0 < \alpha < 1$, $\sigma_m^\star$ is a monotonically decreasing function of $E^{(T)}$. With increasing α, $\sigma_m^\star$ decreases. *Red crosses* refer to the profiles in Panel **A**. **(D)** Macroscopic stress $\sigma_m^\star$ as a function of $\sigma_m^{(T)}$. The stress $\sigma_m^\star$ is a linearly increasing function of $\sigma_m^{(T)}$. With increasing α, the magnitude of $\sigma_m^\star$ decreases. For all profiles, we assume a constant minimal stiffness $E^{(B)}$. *Colors* range from $\alpha = 0.0$ (*light*) to $\alpha = 1.0$ (*dark*) in equidistant manner.

expected from Equation 7.38, σ_m^* approaches $\sigma_m^{(T)}$ for $E^{(B)} \to \infty$ and $\sigma_m^{(B)}$ for $E^{(T)} \to \infty$. With increasing α, $\sigma_m^\star$ decreases.

7.1.2.2 Periodic Rectangular Profile in the Active Kelvin-Voigt Model

We continue with solving the homogenization problem for a Kelvin-Voigt bar for the periodic rectangular profile, as illustrated by the blue curve in Figure 7.1A, with material parameter $\tilde{A}_\epsilon$, the motor stress $\tilde{\sigma}_{\mathrm{m}\epsilon}$ and the coupling strength $\tilde{Y}_\epsilon$. As before, we will skip the particular treatment of the coupling strength $\tilde{Y}_\epsilon$, since the homogenized strength $\tilde{Y}^*$ is simply the average value of $\tilde{Y}_\epsilon$.
Combining Equation 7.33 with both Equations 7.35 and 7.37 yields

$$\tilde{A}^*_\epsilon = \frac{\left(\tilde{E}^{(1)} + \tilde{\eta}^{(1)} s\right) \cdot \left(\tilde{E}^{(2)} + \tilde{\eta}^{(2)} s\right)}{(1-\alpha) \cdot \left(\tilde{E}^{(1)} + \tilde{\eta}^{(1)} s\right) + \alpha \left(\tilde{E}^{(2)} + \tilde{\eta}^{(2)} s\right)}, \tag{7.47}$$

and

$$\tilde{\sigma}^*_{\mathrm{m}\epsilon} = \frac{\alpha \tilde{\sigma}^{(1)}_{\mathrm{m}} \left(\tilde{E}^{(2)} + \tilde{\eta}^{(2)} s\right) + (1-\alpha)\, \tilde{\sigma}^{(2)}_{\mathrm{m}} \left(\tilde{E}^{(1)} + \tilde{\eta}^{(1)} s\right)}{(1-\alpha) \cdot \left(\tilde{E}^{(1)} + \tilde{\eta}^{(1)} s\right) + \alpha \left(\tilde{E}^{(2)} + \tilde{\eta}^{(2)} s\right)}, \tag{7.48}$$

with the respective inverse Laplace transforms

$$A^*(t) = E^* \cdot \delta(t) + \eta^* \cdot \delta'(t) - \frac{1}{\tau^*_A} \exp\left(-\frac{t}{\tau^*}\right), \tag{7.49}$$

and

$$\sigma^*_{\mathrm{m}}(t) = \sigma^*_{\mathrm{m}0} \cdot \delta(t) - \frac{1}{\tau^*_\sigma} \exp\left(-\frac{t}{\tau^*}\right). \tag{7.50}$$

Here, the coefficients denote the homogenized stiffness

$$E^* = \frac{(1-\alpha)\, E^{(2)} \left(\eta^{(1)}\right)^2 + \alpha E^{(1)} \left(\eta^{(2)}\right)^2}{\left((1-\alpha)\, \eta^{(1)} + \alpha \eta^{(2)}\right)^2}, \tag{7.51}$$

which, as compared with the Maxwell model, depends on the viscosity, the homogenized viscosity

$$\eta^* = \frac{\eta^{(1)} \eta^{(2)}}{(1-\alpha)\, \eta^{(1)} + \alpha \eta^{(2)}}, \tag{7.52}$$

which is the solution of the standard problem of a purely viscous bar, and the homogenized motor stress

$$\sigma^*_{\mathrm{m}0} = \frac{\alpha \sigma^{(1)} \eta^{(2)} + (1-\alpha)\, \sigma^{(2)} \eta^{(1)}}{(1-\alpha)\, \eta^{(1)} + \alpha \eta^{(2)}}, \tag{7.53}$$

which has the same form as for the Maxwell model, but with the stiffness replaced by viscosity coefficients. The decay kernel of σ_{m} has the magnitude

$$\frac{1}{\tau^*_\sigma} = \frac{(1-\alpha)\, \alpha \left(\sigma^{(1)} - \sigma^{(2)}\right) \left(E^{(1)} \eta^{(2)} - E^{(2)} \eta^{(1)}\right)}{\left((1-\alpha)\, \eta^{(1)} + \alpha \eta^{(2)}\right)^2}, \tag{7.54}$$

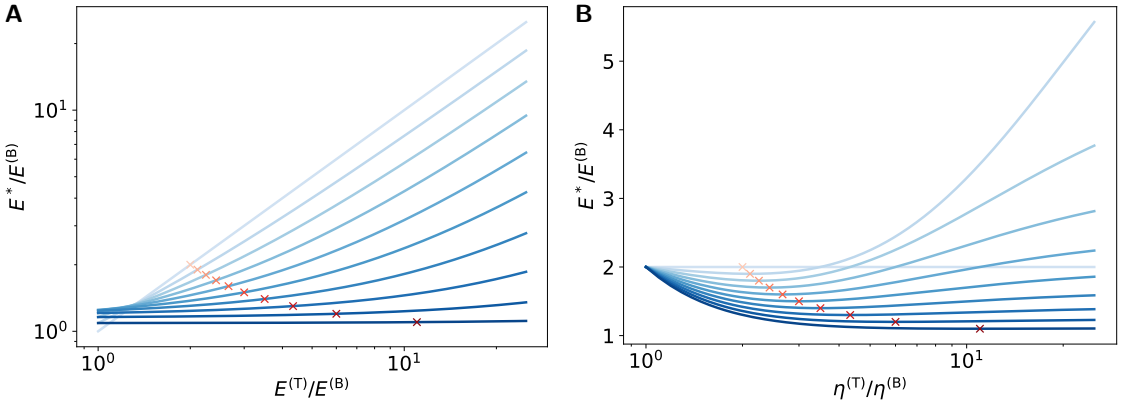

Figure 7.3: One-dimensional homogenized stiffness and stress moduli for an active Kelvin-Voigt model with a rectangular stiffness, viscosity and stress profile as a function of the fraction parameter α. **(A)** Macroscopic stiffness $E^\star$ as a function of $E^{(T)}$. For $0 < \alpha < 1$, $E^\star$ is a convex, monotonically increasing function of $E^{(T)}$. With increasing α, $E^\star$ decreases. *Red crosses* refer to the profiles in Figure 7.2A and $E^{(T)}/E^{(B)} = \eta^{(T)}/\eta^{(B)}$. **(B)** Macroscopic stiffness $E^\star$ as a function of $\eta^{(T)}$. For $0 < \alpha < 1$, $E^\star$ reaches a minimal value. For all profiles, we assume a constant minimal stiffness $E^{(B)}$ and viscosity $\eta^{(B)}$. *Colors* range from $\alpha = 0.0$ (*light*) to $\alpha = 1.0$ (*dark*) in equidistant manner.

and decay time constant

$$\tau^* = \frac{(1-\alpha)\,E^{(1)} - \alpha E^{(2)}}{(1-\alpha)\,\eta^{(1)} - \alpha\eta^{(2)}}\,. \tag{7.55}$$

Interestingly, the material parameter in Equation 7.49 contains a long-term memory term, as was already observed by *Palencia* [1980] for the general case, indicating that, due to the variation of parameters, the effective behavior of the Kelvin-Voigt bar on the micro-level comprises a mixture of Maxwell and Kelvin-Voigt-type dynamics on the macro-level. The magnitude of the additional memory term denotes

$$\frac{1}{\tau_A^*} = \frac{(1-\alpha)\,\alpha\left(E^{(1)}\eta^{(2)} - E^{(2)}\eta^{(1)}\right)^2}{\left((1-\alpha)\,\eta^{(1)} + \alpha\eta^{(2)}\right)^3}\,. \tag{7.56}$$

The long-term memory terms of both the material parameter and the motor stress vanish for the case $E^{(\mathrm{i})} \propto \eta^{(\mathrm{i})}$, for which the homogenized stiffness E^* further yields the result obtained in Equation 7.41. In general, Equation 7.55 can be used as starting point to constitute a relation between the Kelvin-Voigt type dynamics of SFs deduced in *Colombelli et al.* [2009] and the Maxwell type dynamics of SFs presented in Chapter 3. This, however, requires the quantification of the microscopic profiles of stiffness and viscosity along a SF, which are unknown yet.
Figure 7.3 illustrates the dependence of the homogenized stiffness E^* on the maximal microscopic stiffness $E^{(\mathrm{T})}$ (see Panel A) and the maximal microscopic viscosity $\eta^{(\mathrm{T})}$ (see Panel B) for the case of the rectangular profiles from Figure 7.2A.

As for the Maxwell model, the homogenized stiffness decreases with increasing α, but here, we have a *convex* monotonically increasing relation between E^* and $E^{(\mathrm{T})}$ for $0 < \alpha < 1$. The dependence of E^* on the viscosity $\eta^{(\mathrm{T})}$ is more complicated, exhibiting a minimum for

$$\frac{\eta^{(\mathrm{T})}}{\eta^{(\mathrm{B})}} = \frac{E^{(\mathrm{T})}}{E^{(\mathrm{B})}} \cdot \left(\frac{1-\alpha}{\alpha}\right)^2 . \tag{7.57}$$

and $0 < \alpha < 1$. For $\eta^{(\mathrm{T})} \to \infty$, ${}^{E^*}\!/_{E^{(\mathrm{B})}}$ approaches ${}^{1}\!/_{\alpha}$.

7.1.2.3 Homogenization of Stiffness and Stress Profiles in the Active Solid Model

Beyond the rectangular profile, the analytical derivation of macroscopic from microscopic moduli in the context of viscoelastic models presented so far is, in general, not feasible. Therefore, we will turn to an active solid model, for which analytical formulae for different biologically relevant profiles can be derived. We can find the homogenized formulae directly from the active Maxwell model by taking the limit $\eta^{(i)} \to \infty$, such that $\tau^* \to \infty$ and $\tau^*_{\mathrm{m}} \to \infty$, and consequently $\sigma^*_{\mathrm{m}} = \sigma^*_{\mathrm{m0}}$. We can now insert the profiles depicted in Figure 7.1 into Equations 7.41 and 7.45 and calculate the homogenized values E^* and σ^*_{m}, respectively.

Periodic Rectangular Profile with Phase Shift δ between Stiffness and Stress We start with the microscopic stiffness and stress profiles

$$E(y) = \begin{cases} E^{(\mathrm{B})} & , \text{ for } 0 \le y < \alpha \\ E^{(\mathrm{T})} & , \text{ for } \alpha \le y < 1 \end{cases} , \tag{7.58}$$

and

$$\sigma_{\mathrm{m}}(y) = \begin{cases} \sigma^{(\mathrm{B})}_{\mathrm{m}} & , \text{ for } \delta \le y < \alpha + \delta \\ \sigma^{(\mathrm{T})}_{\mathrm{m}} & , \text{ for } 0 \le y < \delta \text{ or } \alpha + \delta \le y < 1 \end{cases} , \tag{7.59}$$

with $0 \le \delta \le \alpha$ and $\alpha + \delta \le 1$. Introducing into Equation 7.26 yields for the homogenized stiffness value

$$E^* = \frac{E^{(\mathrm{B})} E^{(\mathrm{T})}}{(1-\alpha)\, E^{(\mathrm{B})} + \alpha E^{(\mathrm{T})}} , \tag{7.60}$$

which remains unaffected by the shift δ. With Equation 7.29, we get for the homogenized motor stress

$$\begin{aligned} \sigma^*_{\mathrm{m}} &= E^* \cdot \left(\int_0^{\delta} \frac{\sigma^{(\mathrm{T})}_{\mathrm{m}}}{E^{(\mathrm{B})}} \mathrm{d}y + \int_{\delta}^{\alpha} \frac{\sigma^{(\mathrm{B})}_{\mathrm{m}}}{E^{(\mathrm{B})}} \mathrm{d}y + \int_{\alpha}^{\alpha+\delta} \frac{\sigma^{(\mathrm{B})}_{\mathrm{m}}}{E^{(\mathrm{T})}} \mathrm{d}y + \int_{\alpha+\delta}^{1} \frac{\sigma^{(\mathrm{T})}_{\mathrm{m}}}{E^{(\mathrm{T})}} \mathrm{d}y \right) \\ &= \frac{1}{(1-\alpha)\, E^{(\mathrm{B})} + \alpha E^{(\mathrm{T})}} \cdot \\ &\quad \left(\delta \sigma^{(\mathrm{T})}_{\mathrm{m}} E^{(\mathrm{T})} + (\alpha - \delta)\, \sigma^{(\mathrm{B})}_{\mathrm{m}} E^{(\mathrm{T})} + \delta \sigma^{(\mathrm{B})}_{\mathrm{m}} E^{(\mathrm{B})} + (1 - \alpha - \delta)\, \sigma^{(\mathrm{T})}_{\mathrm{m}} E^{(\mathrm{B})} \right) . \end{aligned} \tag{7.61}$$

For $\delta = 0$, we get the solution from Equation 7.45. For $\delta = \alpha$, we have

$$\sigma_{\mathrm{m}}^{*} = \frac{\alpha\left(\sigma_{\mathrm{m}}^{(\mathrm{T})} E^{(\mathrm{T})} + \sigma_{\mathrm{m}}^{(\mathrm{B})} E^{(\mathrm{B})}\right) + (1-2\alpha)\,\sigma_{\mathrm{m}}^{(\mathrm{T})} E^{(\mathrm{B})}}{(1-\alpha)\,E^{(\mathrm{B})} + \alpha E^{(\mathrm{T})}}\,, \tag{7.62}$$

and, in particular for the special case $\alpha = 1/2$, we obtain the solution from Equation 7.45 with $\sigma_{\mathrm{m}}^{(\mathrm{T})}$ and $\sigma_{\mathrm{m}}^{(\mathrm{B})}$ exchanged. In this case, σ_{m}^{*} will always be larger for $\delta = \alpha$ than for $\delta = 0$.

Periodic Sine Profile with Phase Shift δ between Stiffness and Stress The shape of the microscopic stiffness and stress profile can be described by

$$E(y) = E^{(1)} + E^{(2)} \sin(2\pi y) = \frac{E^{(\mathrm{T})} + E^{(\mathrm{B})}}{2} + \frac{E^{(\mathrm{T})} - E^{(\mathrm{B})}}{2} \sin(2\pi y)\,, \tag{7.63}$$

and

$$\sigma_{\mathrm{m}}(y) = \sigma_{\mathrm{m}}^{(1)} + \sigma_{\mathrm{m}}^{(2)} \sin(2\pi y + \delta)\,, \tag{7.64}$$

with $E^{(2)} < E^{(1)}$. Introducing these relations into Equation 7.26 yields for the homogenized stiffness value

$$\begin{aligned} E^{*} &= \left(\left[\frac{\arctan\left(\frac{E^{(1)} \tan(\pi y) + E^{(2)}}{\sqrt{\left(E^{(1)}\right)^2 - \left(E^{(2)}\right)^2}} \right)}{\pi \sqrt{\left(E^{(1)}\right)^2 - \left(E^{(2)}\right)^2}} \right]_{y=-0.5}^{y=0.5} \right)^{-1} \\ &= \sqrt{\left(E^{(1)}\right)^2 - \left(E^{(2)}\right)^2} = \sqrt{\left(E^{(1)} - E^{(2)}\right)\left(E^{(1)} + E^{(2)}\right)} \\ &= \sqrt{E^{(\mathrm{T})} E^{(\mathrm{B})}}\,. \end{aligned} \tag{7.65}$$

For the homogenized motor stress, we obtain via Equation 7.29

$$\begin{aligned} \sigma_{\mathrm{m}}^{*} = \frac{E^{*}}{E^{(2)}} \Bigg[& \frac{\left(E^{(2)}\sigma_{\mathrm{m}}^{(1)} - E^{(1)}\sigma_{\mathrm{m}}^{(2)} \cos(\delta)\right) \arctan\left(\frac{E^{(1)} \tan(\pi y) + E^{(2)}}{\sqrt{\left(E^{(1)}\right)^2 - \left(E^{(2)}\right)^2}} \right)}{\pi \sqrt{\left(E^{(1)}\right)^2 - \left(E^{(2)}\right)^2}} + \\ & \frac{\sigma_{\mathrm{m}}^{(2)}}{2\pi} \left(2\pi y \cos(\delta) + \log\left(E^{(1)} + E^{(2)} \sin(2\pi y)\right) \sin(\delta)\right) \Bigg]_{y=-0.5}^{y=0.5} \\ = \frac{1}{E^{(2)}} \cdot & \left[\sigma_{\mathrm{m}}^{(1)} E^{(2)} - \sigma_{\mathrm{m}}^{(2)} \cos(\delta) \left(E^{(1)} - \sqrt{\left(E^{(1)}\right)^2 - \left(E^{(2)}\right)^2} \right) \right] \end{aligned} \tag{7.66}$$

$$= \frac{1}{2\left(E^{(\mathrm{T})} - E^{(\mathrm{B})}\right)} \cdot \Big[2E^* \left(\sigma_{\mathrm{m}}^{(\mathrm{T})} - \sigma_{\mathrm{m}}^{(\mathrm{B})}\right) + \left(E^{(\mathrm{T})} - E^{(\mathrm{B})}\right)\left(\sigma_{\mathrm{m}}^{(\mathrm{T})} + \sigma_{\mathrm{m}}^{(\mathrm{B})}\right) - \left(E^{(\mathrm{T})} + E^{(\mathrm{B})}\right)\left(\sigma_{\mathrm{m}}^{(\mathrm{T})} - \sigma_{\mathrm{m}}^{(\mathrm{B})}\right)\cos(\delta)\Big] . \tag{7.67}$$

such that for $\delta = 0$, we get

$$\sigma_{\mathrm{m}}^* = \frac{E^*\left(\sigma_{\mathrm{m}}^{(\mathrm{T})} - \sigma_{\mathrm{m}}^{(\mathrm{B})}\right) + E^{(\mathrm{T})}\sigma_{\mathrm{m}}^{(\mathrm{B})} - E^{(\mathrm{B})}\sigma_{\mathrm{m}}^{(\mathrm{T})}}{E^{(\mathrm{T})} - E^{(\mathrm{B})}} , \tag{7.68}$$

for $\delta = \pi$,

$$\sigma_{\mathrm{m}}^* = \frac{E^*\left(\sigma_{\mathrm{m}}^{(\mathrm{T})} - \sigma_{\mathrm{m}}^{(\mathrm{B})}\right) + E^{(\mathrm{T})}\sigma_{\mathrm{m}}^{(\mathrm{T})} - E^{(\mathrm{B})}\sigma_{\mathrm{m}}^{(\mathrm{B})}}{E^{(\mathrm{T})} - E^{(\mathrm{B})}} , \tag{7.69}$$

and for the intermediate case $\delta = \pm\pi/2$,

$$\sigma_{\mathrm{m}}^* = \frac{2E^*\left(\sigma_{\mathrm{m}}^{(\mathrm{T})} - \sigma_{\mathrm{m}}^{(\mathrm{B})}\right) + \left(E^{(\mathrm{T})} - E^{(\mathrm{B})}\right)\left(\sigma_{\mathrm{m}}^{(\mathrm{T})} + \sigma_{\mathrm{m}}^{(\mathrm{B})}\right)}{2\left(E^{(\mathrm{T})} - E^{(\mathrm{B})}\right)} . \tag{7.70}$$

For $0 < E^{(\mathrm{B})} \leq E^{(\mathrm{T})}$, σ_{m}^* will always be larger for $\delta = \pi$ than for $\delta = 0$.

Non-Periodic Linearly Increasing Profile and Uniformly Random Profile Here, we consider the stiffness and stress profiles given by

$$E(y) = E^{(1)} + \frac{E^{(2)}}{l} y . \tag{7.71}$$

and

$$\sigma_{\mathrm{m}}(y) = \sigma_{\mathrm{m}}^{(1)} + \frac{\sigma_{\mathrm{m}}^{(2)}}{l} y . \tag{7.72}$$

with l being the length of the elastic bar. Although the functions are not periodic, we can still apply the homogenization theory by assuming that the whole bar is one unit cell. Intuitively, one can think of the non-periodic homogenization as a special case of a bar with material properties sampled from a uniform distribution and ordered with respect to their strength, as illustrated in Figure 7.1B.[1] Thus, with the following equations, we derive the moduli not only of the linearly increasing profile, but also a profile in which the microscopic moduli are sampled from a uniform distribution given by

$$E(y) \in \mathcal{U}\left(E^{(\mathrm{B})}, E^{(\mathrm{T})}\right) , \tag{7.73}$$

and

$$\sigma_{\mathrm{m}}(y) \in \mathcal{U}\left(\sigma_{\mathrm{m}}^{(\mathrm{B})}, \sigma_{\mathrm{m}}^{(\mathrm{T})}\right) . \tag{7.74}$$

[1] Homogenization of random structures has been investigated e.g. by *Papanicolaou and Varadhan* [1979].

With Equation 7.41, we get for the homogenized stiffness

$$E^* = \frac{E^{(2)}}{\log\left(\frac{E^{(1)}+E^{(2)}}{E^{(1)}}\right)} = \frac{E^{(\mathrm{T})} - E^{(\mathrm{B})}}{\log\left(E^{(\mathrm{T})}\right) - \log\left(E^{(\mathrm{B})}\right)}\,. \tag{7.75}$$

while Equation 7.29 yields for the homogenized motor stress

$$\begin{aligned}\sigma_{\mathrm{m}}^* &= \frac{\left(E^{(2)}\sigma_{\mathrm{m}}^{(1)} - E^{(1)}\sigma_{\mathrm{m}}^{(2)}\right)\log\left(\frac{E^{(1)}+E^{(2)}}{E^{(1)}}\right) + E^{(2)}\sigma_{\mathrm{m}}^{(2)}}{E^{(2)}\log\left(\frac{E^{(1)}+E^{(2)}}{E^{(1)}}\right)} \\ &= \frac{\left(\sigma_{\mathrm{m}}^{(\mathrm{B})} - \frac{\sigma_{\mathrm{m}}^{(\mathrm{T})}-\sigma_{\mathrm{m}}^{(\mathrm{B})}}{E^{(\mathrm{T})}-E^{(\mathrm{B})}}E^{(\mathrm{B})}\right)\log\left(\frac{E^{(\mathrm{T})}}{E^{(\mathrm{B})}}\right) + \left(\sigma_{\mathrm{m}}^{(\mathrm{T})} - \sigma_{\mathrm{m}}^{(\mathrm{B})}\right)}{\log\left(\frac{E^{(\mathrm{T})}}{E^{(\mathrm{B})}}\right)}\end{aligned} \tag{7.76}$$

Random Truncated Gaussian Profile We finally consider the stiffness and stress profiles given by

$$E(y) \in \mathcal{T}\left(E^{(\mathrm{B})}, E^{(\mathrm{T})}, \mu = \frac{E^{(\mathrm{B})}+E^{(\mathrm{T})}}{2}, \sigma_E\right)\,, \tag{7.77}$$

$$\sigma_{\mathrm{m}}(y) \in \mathcal{T}\left(\sigma_{\mathrm{m}}^{(\mathrm{B})}, \sigma_{\mathrm{m}}^{(\mathrm{T})}, \mu = \frac{\sigma_{\mathrm{m}}^{(\mathrm{B})}+\sigma_{\mathrm{m}}^{(\mathrm{T})}}{2}, \sigma_\sigma\right)\,. \tag{7.78}$$

where $\mathcal{T}(a, b, \mu, \sigma)$ is a truncated normal distribution with minimum a, maximum b, mean μ and standard deviation σ (see Figure 7.1A). In similar manner to the previous paragraph, we can reorder the moduli sampled from the distribution, yielding a non-periodic profile given by the inverse of the cumulative distribution function of the truncated normal distribution

$$E(y) = \sqrt{2}\sigma\cdot\mathrm{erfinv}\left[2\left(y\left(\Phi\left(\frac{b-\mu}{\sigma}\right) - \Phi\left(\frac{a-\mu}{\sigma}\right)\right) + \Phi\left(\frac{a-\mu}{\sigma}\right)\right) - 1\right] + \mu\,, \tag{7.79}$$

and equally for $\sigma_{\mathrm{m}}(y)$, with the cumulative distribution function of the normal distribution

$$\Phi(x) = \frac{1}{2}\left(1 + \mathrm{erf}\left(\frac{x-\mu}{\sqrt{2}x}\right)\right)\,. \tag{7.80}$$

Figure 7.1B illustrates the resulting equivalent profile for different standard deviations, whereas a linear profile is the limit case for $\sigma \to \infty$. In the case of Equation 7.79, however, an analytical solution does not exist. We will therefore calculate the effective moduli by numerical integration.

Figure 7.4 shows the calculated homogenized stiffness, stress and coupling strength as a function of the profiles. For both, homogenized stiffness and stress, we find that the rectangular periodic profile yields the overall softest material, since the profile contains the largest number of springs of minimal stiffness. It is followed by the sine profile and

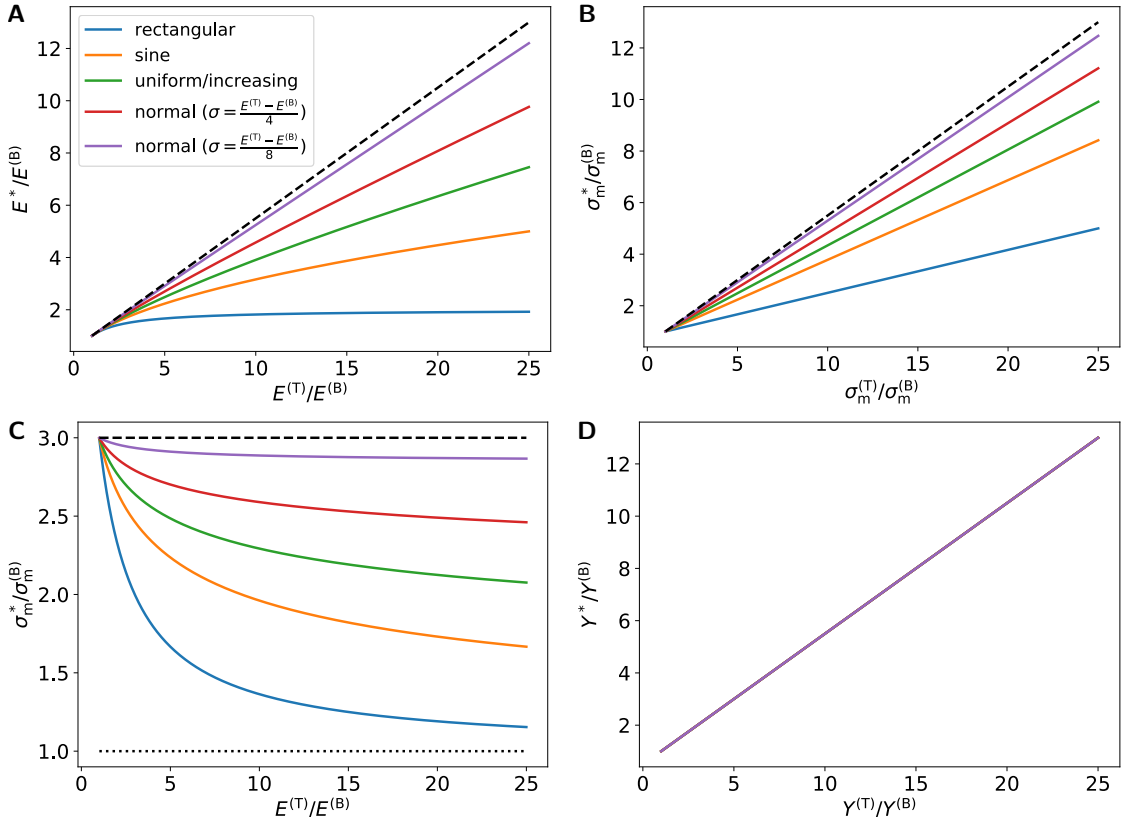

Figure 7.4: One-dimensional homogenized moduli $E^\star$, $\sigma_\mathrm{m}^\star$ and $Y^\star$ as a function of microscopic parameters. **(A)** Homogenized stiffness $E^\star$ as a function of the maximal stiffness $E^{(\mathrm{T})}$. The *dashed* curve indicates the mean value $\left(E^{(B)}+E^{(T)}\right)/2$. **(B)** Homogenized motor stress $\sigma_\mathrm{m}^\star$ as a function of the maximal motor stress $\sigma_\mathrm{m}^{(\mathrm{T})}$. The *dashed* curve indicates the mean value $\left(\sigma_\mathrm{m}^{(\mathrm{B})}+\sigma_\mathrm{m}^{(\mathrm{T})}\right)/2$. **(C)** Homogenized motor stress $\sigma_\mathrm{m}^\star$ as a function of the maximal stiffness $E^{(\mathrm{T})}$. The *dashed* line illustrates the maximal stress level, achieved via $E^{(B)} = E^{(T)}$, while the *dotted* line shows the minimal stress. **(D)** Homogenized adhesion strength $Y^\star$ as a function of the maximal adhesion strength Y_T. The function is independent of the profile, as long as the mean value stays constant. Default values are: $E^{(T)} = 5E^{(B)}$, $\sigma_\mathrm{m}^{(\mathrm{T})} = 5\sigma_\mathrm{m}^{(\mathrm{B})}$ and $Y^{(T)} = 5Y^{(B)}$.

the profile consisting of uniformly sampled moduli, whereas the latter profile is the softest of the sheaf of truncated Gaussian profiles. As shown in Equation 7.36, the homogenized stiffness of the rectangular profile approaches $2E^{(\mathrm{B})}$, as $E^{(\mathrm{T})} \to \infty$.
Figure 7.4C shows the homogenized motor stress as a function of the microscopic stiffness. For the particular case of a rectangular profile, we get the limit values

$$\frac{\sigma_\mathrm{m}^*}{\sigma_\mathrm{m}^{(\mathrm{B})}} = \frac{\sigma_\mathrm{m}^{(\mathrm{T})} + \sigma_\mathrm{m}^{(\mathrm{B})}}{2} \tag{7.81}$$

for $E^{(\mathrm{T})} = E^{(\mathrm{B})}$, and, as Equation 7.38 reveals, $\sigma_{\mathrm{m}}^{*} \to \sigma_{\mathrm{m}}^{(\mathrm{B})}$ for $E^{(\mathrm{T})} \to \infty$. For all profiles, the homogenized motor stress is a convex function of the microscopic stiffness.
Finally, Figure 7.4D shows the homogenized adhesive strength Y^{*} for the analyzed profiles. As Equation 7.30 demonstrates, the homogenized modulus is simply the average value of the microscopic distribution, thus yielding the same value for all analyzed profiles.

7.2 One-Dimensional Homogenization Applied to Stress Fiber Mechanics

In the following, we will apply the asymptotic homogenization technique to the particular example of stress fibers. We first start with a parameterization of stress fibers in Section 7.2.1. Thereafter in Section 7.2.2, we will apply the formulae derived in the previous subsection to the periodic architecture of SFs, aiming at calculating microscopic stiffnesses in the myosin and myosin-free regions along a SFs from the known macroscopic properties.

7.2.1 Microscopic and Macroscopic Parameterization of Stress Fibers

We start with a simplified molecular model of the stress fiber (SF) as illustrated in Figure 7.5. Here, the SF is composed of three major elements: The passive "substrate" composed of rigid actin filaments along which myosin heads walk and generate contractile forces. In addition, the actin filaments are interconnected by passive crosslinkers like α-actinin [*Langanger et al.*, 1986], in the vicinity of which the actin polymerization is accomplished [*Hu et al.*, 2017]. In the following, we will denote the motor-free region by the index (A) and the motor-occupied region by the index (M).
As *Hu et al.* [2017] further demonstrate, multiple SFs are often aligned in a parallel fashion, such that myosin filaments of neighboring SFs combine into stacks in perpendicular direction to the SFs (see Figure 7.5A). These parallel SFs are assumed to share the same focal adhesion (FA) (compare e.g. *Peterson et al.* [2004]).
Table 7.1 lists measured and inferred mechanical parameters of stress fibers. Using PALM super-resolution microscopy, *Livne and Geiger* [2016] show that the cross-section area of SFs is of the order of $0.001 - 0.04\,\mu\mathrm{m}^2$. Comparing these numbers with the experimental data of *Beach et al.* [2014] and *Hu et al.* [2017], we hypothesize in the remainder of this section that the typical cross-section area of a single SF lies in the order of the cross-section area of a myosin II minifilament, which is around $0.001 - 0.01\,\mu\mathrm{m}^2$. SFs with a larger cross-section area will be denoted as stacks of multiple SFs (see Figure 7.5B).
Livne and Geiger [2016] also show that the cross-section of SFs is two orders of magnitude lower than the related area of the focal adhesion (FA) site and that the SF area scales linearly with the FA area. From their (yet unpublished) data, we can extract a dependency between SF or stack area A_{stack} and FA area A_{FA} of about

$$A_{\mathrm{stack}} \approx \frac{A_{\mathrm{FA}}}{100} - 0.008\,\mu\mathrm{m}^2\,. \tag{7.82}$$

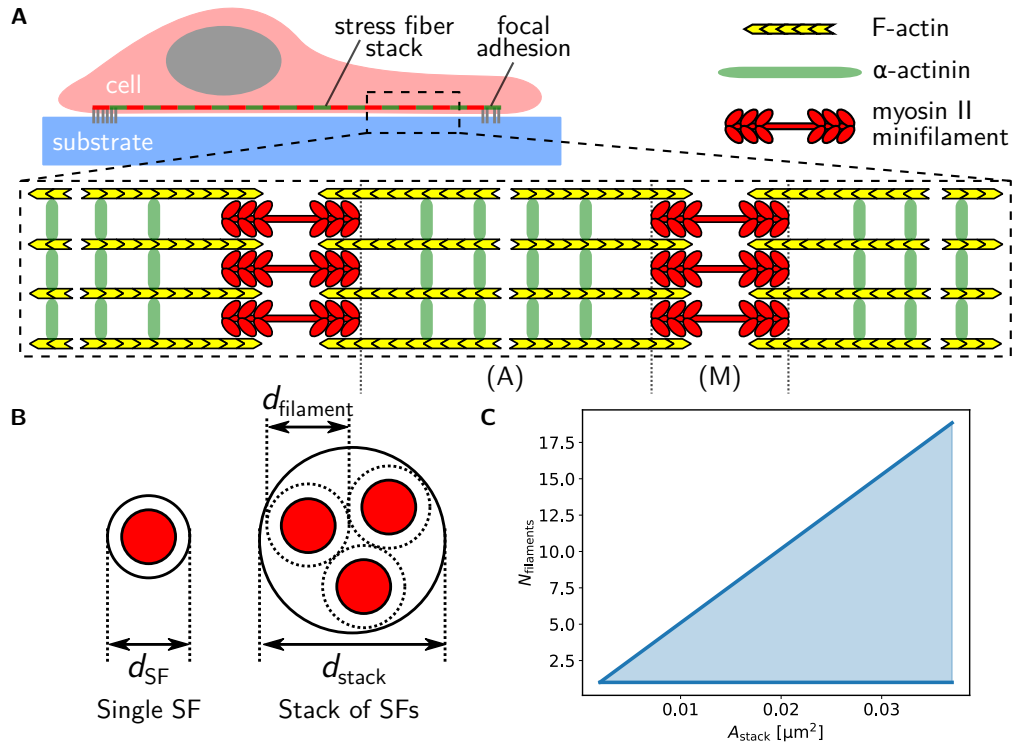

Figure 7.5: Simplified molecular model of stress fibers, assuming actomyosin contractility as the driving process of cellular force generation. **(A)** Major components of a stress fiber (SF) and their stacked interaction. Both actin and myosin minifilaments are organized in a parallel fashion. We find repetitive regions, in which we denote the myosin-free region by (A) and the myosin-occupied region by (M). **(B)** Models of cross-sectional myosin filament packing within a stress fiber, with the SF cross-section diameter d_{SF}, the diameter of a SF stack d_{stack} and the effective diameter d_{filament} of a myosin filament. In the *left* sub-image, we have $d_{\text{filament}} \approx d_{\text{SF}} = d_{\text{stack}}$. **(C)** Number of parallel myosin filaments as a function of the cross-section area A_{stack} of a stress fiber stack. The *blue* region marks the permissible number of parallel myosin filaments per stack.

We further know from traction force measurements either by cells pulling on adhesive sites or model-based traction force reconstruction, that typical stresses exerted by SFs via their FAs are at the order of $\sigma_{\text{m}} = 5 - 20\,\text{kPa}$ [*Balaban et al.*, 2001; *Soiné et al.*, 2015]. As *Livne and Geiger* [2016] estimated, with these stresses and the typical strains of SFs of $2 - 20\,\%$, measured by in vitro manipulation of isolated SFs with AFM cantilevers, the resulting Young's modulus of SFs in of the order of at least $E^* = 3 - 10\,\text{MPa}$ [*Deguchi et al.*, 2006]. This value agrees well with the Young's modulus of $1 - 10\,\text{kPa}$ determined in Chapter 3 via optogenetic manipulation of SFs, where we assumed a cell height of $1\,\mu\text{m}$, which is however about two orders of magnitude larger than the typical diameter of SFs. Since we deal with different cross-section areas, we normalize the calculations by consid-

Stress fiber property	Value range	Reference
FA area A_{FA} [μm^2]	$1-4$	*Livne and Geiger* [2016]
SF stack area A_{stack} [μm^2]	$0.001-0.04$	*Livne and Geiger* [2016]
SF stress $\sigma_{\mathrm{m}}^{\star}$ [kPa]	$5-20$	*Balaban et al.* [2001]
SF stiffness $E^{\star}$ [MPa]	$3-10$	*Livne and Geiger* [2016]
Motors per filament N_{motors}	$20-30$	*Thoresen et al.* [2013]
Stall force per motor head F_{head} [pN]	$2.2-2.9$	*Thoresen et al.* [2013]
Force in non-myosin region $F_{\mathrm{m}}^{(\mathrm{A})}$ [pN]	0	
Ratio of non-myosin region α	$0.6-0.8$	*Hu et al.* [2017]

Table 7.1: SF parameters known from the literature.

ering one-dimensional stiffnesses k and stresses F_{m} instead of E and σ_{m}, respectively. On the macroscopic scale, we thus have a homogenized stiffness of

$$k^* = E^* \cdot A_{\mathrm{stack}} \approx 6 - 320\,\mathrm{nN}\,, \tag{7.83}$$

and a homogenized contractile stress of

$$F_{\mathrm{m}}^* = \sigma_{\mathrm{m}}^* \cdot A_{\mathrm{FA}} \approx 5 - 80\,\mathrm{nN}\,. \tag{7.84}$$

We assume that both quantities scale linearly with the respective area. Since both quantities are approximately of the same order, we will use the relation $k^* \approx F_{\mathrm{m}}^*$ in the following. On the microscopic level, we know from experiments by e.g. *Norstrom et al.* [2010] that a non-muscle myosin-II motor pulls with a maximal force of about 2.2 pN. Experiments by *Thoresen et al.* [2013] reveal a linear relationship between the number of motor heads and the total force, with the slope yielding a value of 2.9 pN for the stall force per motor head.
We further know from multiple experimental studies, such as those by *Kaunas et al.* [2011], *Thoresen et al.* [2013] or *Billington et al.* [2013], that, in non-muscle cells, myosin motors in SFs are typically organized in filaments of $20-30$ motors per filament, giving a maximal force of about 90 pN per filament, if all motors are assumed to work in parallel. The typical thickness of an extracted myosin filament lies in the range of about $10-20$ nm [*Billington et al.*, 2013]. In action, myosin heads are however expected to occupy a width of about $40-50$ nm, which we will define in the following as effective cross-section thickness of a single myosin filament. Figure 7.5C shows the permissible number of parallelly arranged myosin filaments as a function of the cross-section area of a SF stack. With a typical length of a myosin filament of 300 nm and a sarcomeric length in the range of $0.8-1.6\,\mu$m, we can estimate the ratio α of myosin-free region to total sarcomeric length to $0.6-0.8$ (see *Russell et al.* [2011] and *Niederman and Pollard* [1975], respectively). We finally assume that the myosin-free region does not contain a force-generating mechanism, yielding $F_{\mathrm{m}}^{(\mathrm{A})} = 0\,\mathrm{pN}$.

7.2.2 Relation between Microscopic and Macroscopic Parameters of Stress Fibers

We will now compute the microscopic stiffnesses and stresses of the subunits of stress fibers (i.e. the sarcomeres) starting from two different extreme cases: a periodic rectangular profile without motors in region (A) and all motors in region (M), or, a periodic sine profile with a smooth transition of stiffness and motor strength between both regions.

Model 1: Rectangular Profile of Alternating Myosin-Occupied and Myosin-Free Regions We assume the simplest possible structure of a stress fiber: a rectangular profile of alternating myosin and non-myosin regions. We can therefore use Equations 7.41 and 7.45 to establish a relation between micro- and macroscopic quantities. Introducing quantities from Table 7.1, we have

$$k^* = \frac{k^{(\mathrm{A})} k^{(\mathrm{M})}}{(1-\alpha)\, k^{(\mathrm{A})} + \alpha k^{(\mathrm{M})}}\,, \tag{7.85}$$

and

$$F_{\mathrm{m}}^* = \frac{(1-\alpha)\, F_{\mathrm{m}}^{(\mathrm{M})} k^{(\mathrm{A})}}{(1-\alpha)\, k^{(\mathrm{A})} + \alpha k^{(\mathrm{M})}}\,. \tag{7.86}$$

Division of Equations 7.85 and 7.86 yields the approximate stiffness of the myosin-occupied region of a single SF

$$k^{(\mathrm{M})} = \frac{k^*}{F_{\mathrm{m}}^*} \cdot (1-\alpha)\, F_{\mathrm{m}}^{(\mathrm{M})} \approx (1-\alpha)\, F_{\mathrm{m}}^{(\mathrm{M})} \approx 30\,\mathrm{pN}\,, \tag{7.87}$$

if we assume that all motors pull synchronously and in parallel. The stiffness of the non-myosin region can then be calculated by reorganizing Equation 7.85:

$$k^{(\mathrm{A})} = \frac{\alpha k^{(\mathrm{M})} k^*}{k^{(\mathrm{M})} - (1-\alpha)\, k^*} \underset{k^{(\mathrm{M})} \ll k^*}{\approx} -\frac{\alpha}{1-\alpha} k^{(\mathrm{M})} \approx -k^{(\mathrm{M})}\,. \tag{7.88}$$

Figure 7.6 illustrates the numerical values for $k^{(\mathrm{A})}$ and $k^{(\mathrm{M})}$ for the parameter range constrained by the given experimental results, as listed in Table 7.1. We find that, for the given parameter range, the stiffness $k^{(\mathrm{A})}$ in the myosin-free region can have a positive and a negative value. However, we expect that the maximal microscopic force should cause the maximal macroscopic stress in a SF stack of maximal size, suggesting that the stiffness $k^{(\mathrm{A})}$ has to be negative to enable stresses of 5 kPa and larger (see white solid line in Figure 7.6). In contrast to this, the stiffness $k^{(\mathrm{M})}$ in the myosin-occupied region is found to be positive independently of the macroscopic parameters, yielding a value in the range $0.01 - 1\,\mathrm{nN}$.
Apparently, the parameter $N_{\mathrm{filaments}}$ is the critical parameter when relating micro- and macroscale. Figures 7.6C and 7.6D demonstrate that, if assuming the thickness of a single myosin filament to be $d_{\mathrm{filament}} = 50\,\mathrm{nm}$ and all motors of the filaments in the same stack working in parallel, $k^{(\mathrm{A})}$ becomes negative yielding about $-(0.01 - 1)$ nN. For more parallel filaments per stack or, in other words, a reduced effective filament thickness

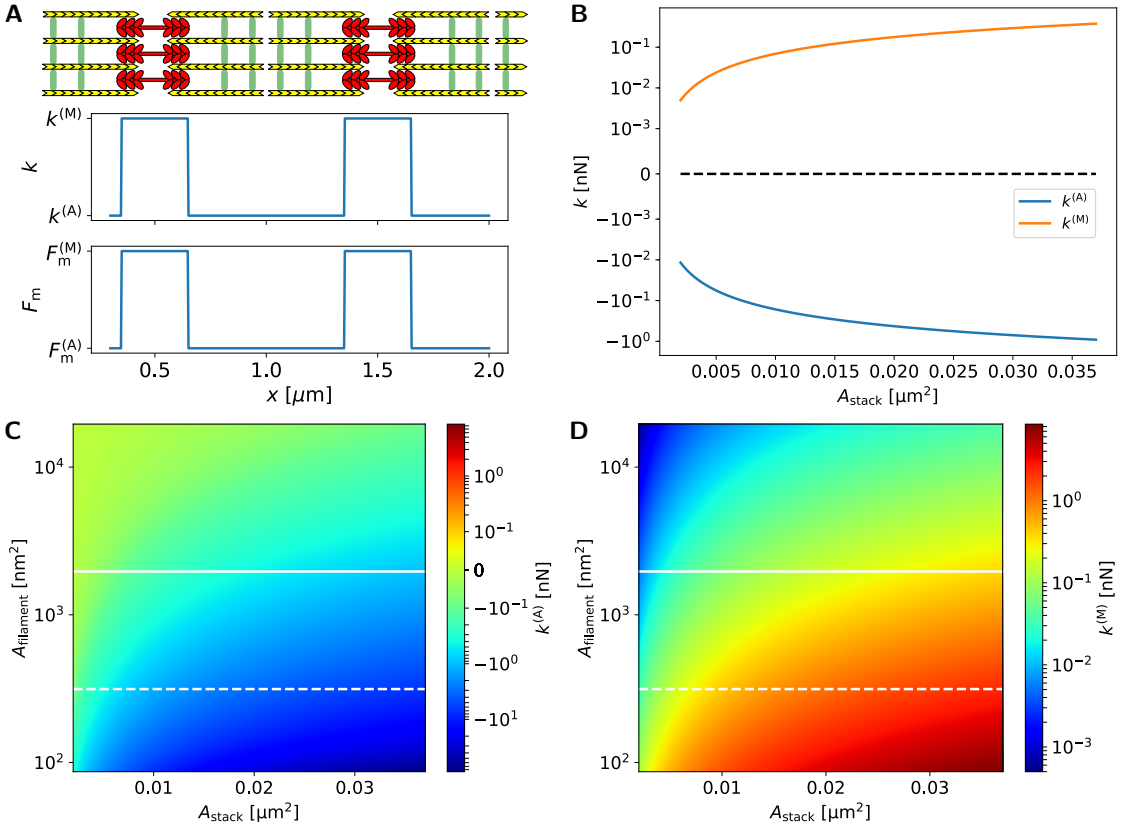

Figure 7.6: Microscopic stiffnesses $k^{(\mathrm{A})}$ and $k^{(\mathrm{M})}$ as a function of both micro- and macroscopic parameters if assuming *rectangular* stiffness and stress profiles and a vanishing motor stress in the motor-free region. **(A)** Stiffness and stress profiles along the stack of stress fibers. **(B)** Stiffness $k^{(\mathrm{A})}$ and $k^{(\mathrm{M})}$ as a function of the cross-section area A_{stack} of the SF stack if assuming a thickness of single myosin filaments of $d_{\mathrm{filament}} = 50\,\mathrm{nm}$. **(C,D)** $k^{(\mathrm{A})}$ and $k^{(\mathrm{M})}$ as a function of the cross-section area A_{stack} of the SF stack and the effective cross-section area of a myosin minifilament A_{filament}. The *white solid line* highlights the curves from Panel B, respectively, while the *white dashed line* shows the result for a maximal packing density with $d_{\mathrm{filament}} = 20\,\mathrm{nm}$. Default values are: $k^{\star} = 10\,\mathrm{nN}$, $F_{\mathrm{m}}^{\star} = 10\,\mathrm{nN}$, $\alpha = 0.7$, $F_{\mathrm{head}} = 2.9\,\mathrm{pN}$ and $N_{\mathrm{motors}} = 28$.

$d_{\mathrm{filament}} = 20\,\mathrm{nm}$, the stiffness $k^{(\mathrm{A})}$ would decrease to $-(1-100)$ nN. This packing density can however not be verified experimentally (see e.g. the study by *Langanger et al.* [1986]).

We can interpret these results as follows. The stiffness $k^{(\mathrm{M})}$ is much smaller compared to the macroscopic stiffness because actin filaments buckle under the myosin stress and depolymerize, thus, it takes only a little energy to compress these filaments by a high amount. The negative compressibility in the myosin-free region indicates that the actin filaments are highly pre-stretched otherwise one would obtain a stiffness $k^{(\mathrm{A})}$ close to $k^{(\mathrm{M})}$. An external tensile stress leads to a decrease of stretch in this region.

This is different from the situation in the sarcomeric subunits of a muscle cell. There, myosin filaments contain the tenfold number of motors, which would effectively move the white solid line from Figure 7.6C-D in the negative y-direction. One explanation for the uncommon mechanical properties of SFs in fibroblast cells derived here, in comparison to muscle cells, is as follows. Fibroblast cells need to be adaptive to the environmental needs and therefore rely on the steady polymerization and depolymerization of the actin CSK. Muscle cells, on the contrary, are, by natural design, dimensionally stable once they are incorporated into the muscle.
A further interesting point in Figure 7.6C-D is the fact that the absolute values of $k^{(\mathrm{A})}$ and $k^{(\mathrm{M})}$ are very close, which might militate for a coordinated degradation of actin in the myosin region and assembly in the non-myosin region upon active external stress.

Model 2: Sinusoidal Profile of Alternating Myosin-Occupied and Myosin-Free Regions Another extreme case of a periodic distribution of myosin motors is a sinusoidal profile. Here, we can use the relations 7.65 and 7.68 to establish a connection between micro- and macroscopic quantities. Introducing quantities from Table 7.1, we get

$$k^* = \sqrt{k^{(\mathrm{A})} k^{(\mathrm{M})}}\,, \tag{7.89}$$

and

$$F_{\mathrm{m}}^* = \frac{F_{\mathrm{m}}^{(\mathrm{M})}\left(k^* - k^{(\mathrm{A})}\right)}{k^{(\mathrm{M})} - k^{(\mathrm{A})}}\,. \tag{7.90}$$

We can reorganize both equations to get the microscopic values

$$k^{(\mathrm{A})} = \frac{\left(k^*\right)^2}{k^{(\mathrm{M})}}\,, \tag{7.91}$$

and

$$\begin{aligned} k^{(\mathrm{M})} &= \left(\frac{1}{2}\frac{F_{\mathrm{m}}^{(\mathrm{M})}}{F_{\mathrm{m}}^*} \pm \sqrt{\frac{1}{4}\left(\frac{F_{\mathrm{m}}^{(\mathrm{M})}}{F_{\mathrm{m}}^*}\right)^2 + 1 - \frac{F_{\mathrm{m}}^{(\mathrm{M})}}{F_{\mathrm{m}}^*}} \right) k^* \\ &= \left(\frac{1}{2}\frac{F_{\mathrm{m}}^{(\mathrm{M})}}{F_{\mathrm{m}}^*} \pm \sqrt{\left(1 - \frac{1}{2}\frac{F_{\mathrm{m}}^{(\mathrm{M})}}{F_{\mathrm{m}}^*}\right)^2} \right) k^*\,. \end{aligned} \tag{7.92}$$

These relations yields two different results for $k^{(\mathrm{A})}$ and $k^{(\mathrm{M})}$:

$$k^{(\mathrm{A})} = k^* \;\text{ and }\; k^{(\mathrm{M})} = k^*\,, \tag{7.93}$$

or

$$k^{(\mathrm{A})} = \frac{k^*}{\frac{F_{\mathrm{m}}^{(\mathrm{M})}}{F_{\mathrm{m}}^*} - 1} < 0 \;\text{ and }\; k^{(\mathrm{M})} = \left(\frac{F_{\mathrm{m}}^{(\mathrm{M})}}{F_{\mathrm{m}}^*} - 1\right) k^* < 0\,. \tag{7.94}$$

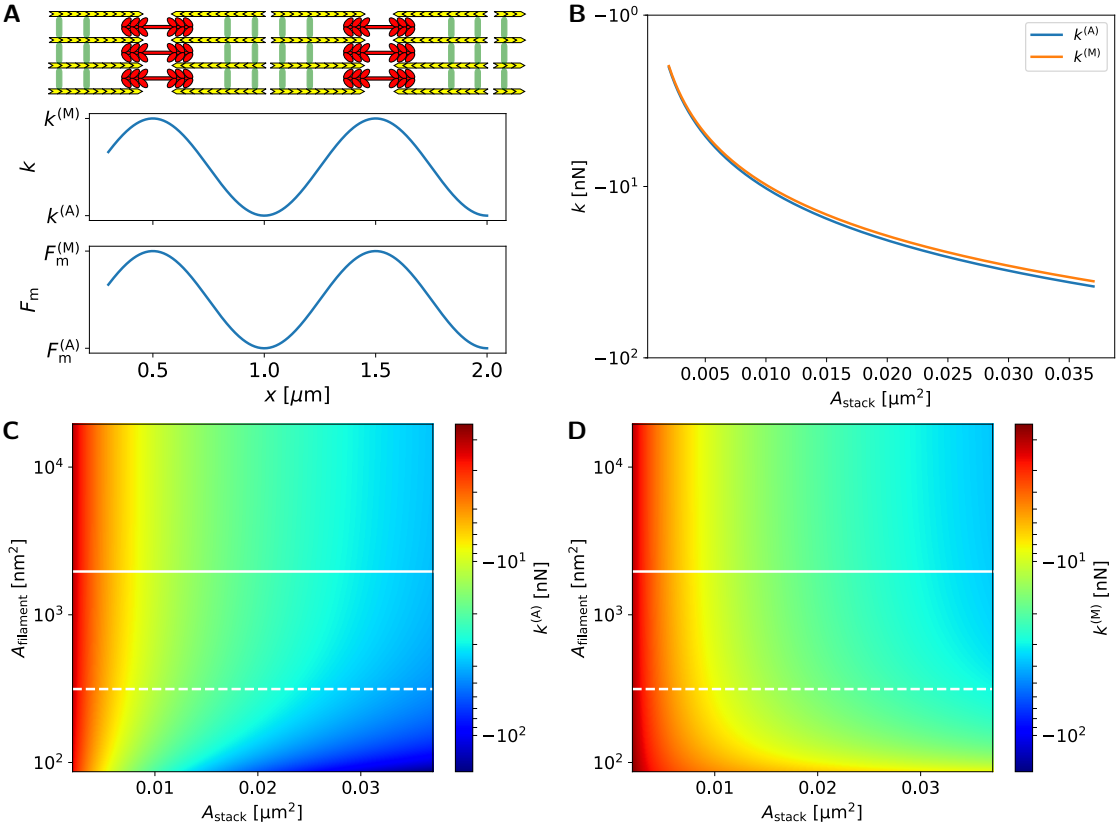

Figure 7.7: Microscopic stiffnesses $k^{(\mathrm{A})}$ and $k^{(\mathrm{M})}$ as a function of both micro- and macroscopic parameters if assuming *sinusoidal* stiffness and stress profiles and a vanishing motor stress in the motor-free region. **(A)** Stiffness and stress profiles along the stack of stress fibers. **(B)** Stiffness $k^{(\mathrm{A})}$ and $k^{(\mathrm{M})}$ as a function of the cross-section area A_{stack} of the SF stack if assuming a thickness of single myosin filaments of $d_{\mathrm{filament}} = 50\,\mathrm{nm}$. **(C,D)** $k^{(\mathrm{A})}$ and $k^{(\mathrm{M})}$ as a function of the cross-section area A_{stack} of the SF stack and the effective cross-section area of a myosin minifilament A_{filament}. The *white solid line* highlights the curves from Panel B, respectively, while the *white dashed line* shows the result for a maximal packing density with $d_{\mathrm{filament}} = 20\,\mathrm{nm}$. Default values are: $k^{\star} = 10\,\mathrm{nN}$, $F_{\mathrm{m}}^{\star} = 10\,\mathrm{nN}$, $F_{\mathrm{head}} = 2.9\,\mathrm{pN}$ and $N_{\mathrm{motors}} = 28$.

Equation 7.93 yields the ill-defined result $F_{\mathrm{m}}^{*} = F_{\mathrm{m}}^{(\mathrm{M})} \cdot \frac{0}{0}$ if introducing into Equation 7.90. The second result is also not consistent because both stiffnesses are negative for our special case $F_{\mathrm{m}}^{(\mathrm{M})}/F_{\mathrm{m}}^{*} \approx 0.01$, as Figure 7.7 demonstrates. One would, however, intuitively expect that the non-stretched region labeled by (M) has a positive stiffness.
The magnitudes of the microscopic stiffnesses $k^{(\mathrm{A})}$ and $k^{(\mathrm{M})}$ for the special case depicted in Figure 7.7B have a similar dependence on A_{stack} for the given filament thickness $d_{\mathrm{filament}} = 50\,\mathrm{nm}$ as compared to the stiffnesses in Figure 7.6B. Comparing Figure 7.7C and D, we find that $k^{(\mathrm{M})}$ approaches zero for decreasing d_{filament}, while $k^{(\mathrm{A})}$ increases in magnitude for decreasing d_{filament}, which is similar to Figure 7.6C and D.

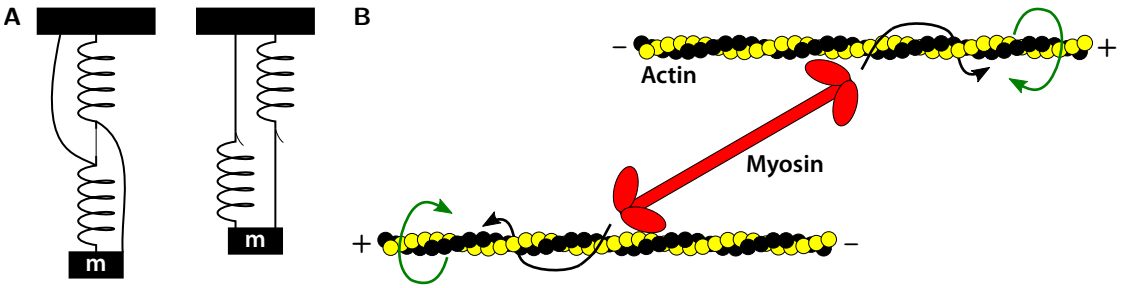

Figure 7.8: Two possible micromechanical scenarios which could contribute to the local negative compressibility of a stress fiber. **(A)** As demonstrated by *Cohen and Horowitz* [1991], a special arrangement of springs and strings can lead to a global contraction upon breaking stretched bonds in the network. **(B)** As *Fürthauer et al.* [2013] propose, chiral activity of myosin motors due to the helical structure of F-actin could lead to a torque in the actin filament. This might induce a shortening due to torsional stresses perpendicular to the filament axis. Figures adapted from *Cohen and Horowitz* [1991] and *Fürthauer et al.* [2013], respectively.

7.2.3 Potential Metamaterial-Invoking Mechanisms in Stress Fibers

The results from the previous section show that, given that the parameter values in Table 7.1 are correct, actomyosin contractility on its own cannot be the only force-generating mechanism in the SF. Instead, our model suggests a negative stiffness in the myosin-free region to be responsible for the large stresses observed on the global scale. Such a property is typically attributed to mechanical metamaterials (see e.g. *Nicolaou and Motter* [2012]).
Since filamentous actin is present in both regions (A) and (M), we can conclude that actin by itself is not the material responsible for the negative stiffness. Rather, the junction between actin and α-actinin is a candidate for this uncommon material property. This can also be expected from the fact that G-actin is predominantly incorporated into the existing filaments at exactly this junction, as indicated by the large concentration of G-actin in the vicinity of α-actinin [*Hu et al.*, 2017]. Indeed, the involved association and dissociation rates are very likely to be affected by tension [*Ye et al.*, 2014; *Livne and Geiger*, 2016]. In this context, different physical mechanisms besides actomyosin-based force generation might contribute to the contractility of the stress fiber, as illustrated in Figure 7.8. In both of the depicted scenarios, the myosin motors would rather represent the trigger for the force generation than entailing the mechanism itself, comparable with the small base-emitter current regulating a much larger collector–emitter current in a bipolar junction transistor.

Stress Fiber Contraction based on Braess's Paradox A possible force-generating mechanism establishing a contraction of SFs could be based on the so-called *Braess's paradox* in its mechanical manifestation, as introduced by *Cohen and Horowitz* [1991]. In their thought experiment, which is shown in Figure 7.8A, they reveal that for specific

arrangements of springs and strings in a mechanical network, the local removal of a central element and the following relaxation of the full network could paradoxically lead to a global contraction. This arises due to the fact that a predominantly serial arrangement of springs is replaced by a parallel one. By exploiting the asymmetric mechanical behavior of an actin filament, which exhibits spring-like behavior upon elongation and string-like behavior upon contraction, it is conceivable that the arrangement of actin filaments in SFs is driven by the exact same process.

We can use the numbers listed in Subsection 7.2.1 to estimate the contraction length upon removal of a stretched actin filament which is interconnected in a parallel network with N buckled filaments. After the link removal, the latter will bear the full load evoked by the pulling of the myosin motors. With a maximal force per myosin filament of $F_{\mathrm{m}}^{(\mathrm{M})} \approx 100\,\mathrm{pN}$ and a spring constant in the myosin-free region of $k^{(\mathrm{A})} \approx -1\,\mathrm{nN}$, we get an average strain $\epsilon = {}^{F_{\mathrm{m}}^{(\mathrm{M})}}\!/_{k^{(\mathrm{A})}} \approx -0.1$ per contraction of the myosin filament. With a spacing of $S_0 = 500\,\mathrm{nm}$ between two neighboring myosin filaments along the axis of the SF, this yields an overall length change of $|\Delta S| = 50\,\mathrm{nm}$, or a length change of $|\Delta S_{\mathrm{motor}}| = 1.7\,\mathrm{nm}$ per motor cycle.

On the microscopic scale, we know that the maximal force per motor cycle is $F_{\mathrm{head}} \approx 3\,\mathrm{pN}$ and that a single actin filament has a spring constant of $k_{\mathrm{actin}} = E_{\mathrm{actin}} A_{\mathrm{actin}} = 45\,\mathrm{nN}$, with $E_{\mathrm{actin}} = 1.8\,\mathrm{GPa}$ and $A_{\mathrm{actin}} = 25\,\mathrm{nm}^2$ measured by *Kojima et al.* [1994]. With these numbers, we get for each of the two stretched springs in the left panel of Figure 7.8A the strain

$$\epsilon_{\mathrm{ser}} = \frac{F_{\mathrm{head}}}{k_{\mathrm{actin}}} = 6.7 \times 10^{-5}\ . \tag{7.95}$$

After removing the connection between these springs, the load is, for simplicity, distributed among $N \to \infty$ parallel springs, such that the new strain of the arrangement goes to

$$\epsilon_{\mathrm{par}} = \frac{F_{\mathrm{head}}}{N k_{\mathrm{actin}}} \to 0\,. \tag{7.96}$$

The total length change in this situation would be $|\epsilon_{\mathrm{par}} - \epsilon_{\mathrm{ser}}| \cdot S_0 = 0.03\,\mathrm{nm}$ which is orders of magnitude lower than $|\Delta S|$.

An outlet to this discrepancy could be the fact that the combination of actin filaments and passive crosslinkers, such as α-actinin, and the involved association and dissociation dynamics could lead to a reduced effective stiffness of single actin filaments in the myosin-free region. As Chapter 3 further reveals, the effective material properties of a SF is not only determined by actin, myosin and passive crosslinkers, but also by numerous regulator proteins such as zyxin. With the desired length change per motor cycle of $\epsilon_{\mathrm{des}} = {}^{|\Delta S_{\mathrm{motor}}|}\!/_{S_0} = 0.0034$, we find an upper boundary for the effective stiffness of a single actin filament of

$$k_{\mathrm{actin/SF}} \lesssim \frac{F_{\mathrm{head}}}{\epsilon_{\mathrm{des}}} \approx 880\,\mathrm{pN}\,, \tag{7.97}$$

or $E_{\mathrm{actin/SF}} \lesssim 35\,\mathrm{MPa}$.

Experimentally, one could test for this hypothesis by correlating the amount of targeted depletion of F-actin in a bundle of parallel interconnected actin filaments and the

corresponding contraction or elongation of the bundle.

Stress Fiber Contraction based on Shortening upon Torsion A second possible force-generating mechanism in SF contraction could arise from the helical architecture of single actin filaments. Upon walking along the actin filaments, the myosin motors are likely to induce a torque in the actin filaments, yielding a force perpendicular to the movement direction of the myosin filaments (see Figure 7.8B). This feature was already used as a predominant force-generating mechanism e.g. in the model of *Fürthauer et al.* [2013]. In this situation, a contractile force arising from myosin motor activity would lead to a shortening rather than elongation of the actin filament.
We can estimate the contraction ΔS of a single actin filament upon a torque induced by the force $F_{\text{head}} \approx 3\,\text{pN}$ of a myosin motor head by calculating the total pitch of a helix as a function of the angular twist introduced by the torque. Here, the helix is representing the actin filament and has an arc length of $S_0 \approx 500\,\text{nm}$. With the parameterization

$$\mathbf{x}(t) = \begin{pmatrix} R\cos(t) \\ R\sin(t) \\ ht \end{pmatrix}, \tag{7.98}$$

with the radius $R = 2.8\,\text{nm}$ of the actin filament and $2\pi h$ the pitch of a single helix loop, we get the arc length

$$S_0 = \int_0^{\phi} \sqrt{R^2 + h^2}\mathrm{d}t = \phi\sqrt{R^2 + h^2}\,, \tag{7.99}$$

with the angular twist ϕ. Defining the total height of the helix by $S = h \cdot \phi$, we have the relation

$$S = S_0 - \Delta S = \sqrt{S_0^2 - R^2\phi^2}\,, \tag{7.100}$$

between height and arc length of the helix. With $\Delta S_{\text{motor}} = 1.7\,\text{nm}$, as was estimated in the previous paragraph, we have $\phi = 14.7 = 4.7\pi$. Assuming a uniform cross-section for the full actin filament, we can use the relation

$$\tau = FR = \frac{\kappa}{S_0}\phi\,, \tag{7.101}$$

between the torque τ and the angular twist ϕ to calculate the force F required to establish the twist ϕ. Here, $\kappa = 5.8 \times 10^{-26}\,\text{Nm}^2$ is the torsional rigidity measured by *Tsuda et al.* [1996]. With the above values, we get $F \approx 200\,\text{pN}$, which is about two orders of magnitude larger than the maximal force of a single myosin motor F_{head}.
Similar to the previous paragraph, this discrepancy can be explained by the fact that the actual torsional rigidity κ of the combination of actin filaments, passive crosslinkers and the involved association and dissociation dynamics could be orders of magnitude lower than the value measured by *Tsuda et al.* [1996] for single actin filaments. A measurement of κ on natural conditions in a stress fiber is however not known so far.

7.3 Conclusion

In this chapter, we applied the one-dimensional asymptotic homogenization to the problem of actomyosin-generated contractility to create a relation between the microscopic composition of the cytoskeleton and the macroscopic mechanical properties of the cell.
We found that the arrangement of elastic, viscous and contractile elements along a one-dimensional bar are major determinants of the global stiffness, viscosity and contractile stress. By keeping both the total energy and the minimal stiffness of the bar constant, we found that, when considering only point-symmetric profiles, the rectangular profile yields the overall softest and weakest material. As opposed to this, the global adhesive strength is, in first order, independent on the arrangement of single adhesion bonds as long as the total number of bonds stays constant.
We applied the asymptotic homogenization technique to the particular problem of stress fibers in order to relate microscopic and microscopic scales, thereby complying with recent experimentally deduced global parameters. The homogenization result helped to estimate the range of the microscopic stiffness based on these global properties. Both the homogenization of rectangular and sinusoidal stiffness and stress profiles suggest that the mechanics of stress fibers is mainly determined by a local negative compressibility, prescribing a negative stiffness value to those stress fiber region in which α-actinin accumulates. In particular, we found that the local stiffness in the myosin-free region equals approximately the negative of the local stiffness in the contractile region in order to fulfill the requirements set on the global scale.
We finally discussed micromechanical mechanisms which might contribute to this uncommon mechanistic behavior, showing that the contractility of a stress fiber on a local scale can only be captured by a non-linear material model, which contemplates the dynamics of permanently associating and dissociating actin filaments.

8 Two-Dimensional Homogenization for Continuum Model-Based TFM

In chapters 4-6, we modeled the actin CSK of adhering cells as an, at least piecewise, two-dimensional homogeneous elastic medium with elastic foundation, based on the continuum model introduced by *Edwards and Schwarz* [2011]. We showed that it is possible to reproduce experimentally acquired scaling laws for the total force or the strain energy as a function of the cell or layer size.
However, in reality the actin CSK is far from being a homogeneous continuum. Depending on the location within the cell, it is indeed composed of a complicated arrangement of discrete filamentous ensembles, like the actin cortex or stress fibers (see Section 1.1). A discrete modeling approach, thus, has to account for this structural inhomogeneity, as well as for the asymmetric cable-like nature of single actin filaments. Both properties are incorporated e.g. in the active cable model introduced by *Torres et al.* [2012]. Beyond that, *Soiné et al.* [2015] show that this kind of modeling allows to quantify cellular traction stresses to a high precision by exploiting information about the location of focal adhesions and stress fibers and assuming a that stress fibers are the dominant force-generating structures in cells.
The discrete modeling approach, however, comes with the drawback of a huge parameter space, including a time-consuming parameter optimization and, with this, making an efficient application of the method infeasible. In this regard, a continuum approach prevails the discrete method, yielding a small parameter space, with the advantage that parameters at the cellular scale can be directly characterized without the detour over a detailed specification of single links within a discrete mesh of filaments. The two-dimensional asymptotic homogenization, in this context, allows to form a bridge between discrete and continuum model.
An application of the asymptotic homogenization technique to deduce a continuum model of the actin CSK based on its structural information is not known so far. A prominent continuum model exploiting the architecture of the CSK is those of *Deshpande et al.* [2006], who study the dynamic reorganization of the cytoskeleton by modeling key biochemical processes in the context of stress fiber generation and tension mediated by myosin. The authors use an averaging scheme over stress fiber directions in a volume element of the cell to obtain an approximate continuum description, which is, however, preceded by a rather complicated computation of distributions of stress fiber directions. Also, although their model is very detailed compared to other prominent methods, essential cytoskeletal phenotypes, like the crossing of stress fibers, cannot be represented appropriately due to the deficient averaging scheme [*Schwarz and Safran*, 2013].
In this chapter, we will instead follow the imaging-based ansatz of *Soiné et al.* [2015] and use

the asymptotic homogenization technique to generate a connection between model-based TFM and the continuum model of *Edwards and Schwarz* [2011]. In particular, we start with the computation of homogenized parameters in a two-dimensional heterogeneous active solid medium in Section 8.1. In Section 8.2, we extend the continuum model presented in the previous chapters to the framework of anisotropic materials by coupling the information about the local architecture of the actin CSK with two-dimensional asymptotic homogenization, to predict the pattern of internal and traction stresses of a cell. We will accomplish a parametric characterization of the method and then use the data presented in Chapter 4 as benchmark to constrain our method. The new technique will allow to predict cellular traction stresses in good qualitative agreement to stresses calculated by means of TFM, showing that our model outperforms previously developed continuum models, such as those by *Edwards and Schwarz* [2011] or *Oakes et al.* [2014].

8.1 Two-Dimensional Asymptotic Homogenization Formalism Applied to Active Elastic Media

In the following, we will start in Section 8.1.1 with an introduction of the asymptotic homogenization technique in two dimensions and apply the method to the particular problem of an actively contractile elastic sheet of vanishing height compared to its planar dimensions, which further experiences an elastic coupling to its environment. In Section 8.1.2, we will outline the scheme used to compute the homogenized parameters of the elastic disc and its numerical implementation.

8.1.1 Two-Dimensional Asymptotic Homogenization of an Elastic Contractile Sheet

In analogy to Section 7.1.1, we can derive the effective material parameters for the case of a two-dimensional actively contractile elastic sheet. Multiple studies have already addressed the problem, like *Bensoussan et al.* [1978]; *Sánchez-Palencia* [1980]; *Fish et al.* [1994]; *Sigmund and Torquato* [1997]; *Hassani and Hinton* [1998]. In the following, we will summarize the problem and its solution by taking these studies as a basis.
We start with the constitutive relation of a two-(or three-)dimensional elastic sheet with active contraction

$$\sigma_{ij} = C^{\epsilon}_{ijkl}\epsilon_{kl} + \sigma^{\epsilon}_{\mathrm{m}ij}\,, \tag{8.1}$$

with the fourth-order stiffness tensor C^{ϵ}_{ijkl}, the second-order active stress tensor $\sigma^{\epsilon}_{\mathrm{m}ij}$ as well as the material stress and strain tensors σ_{ij} and ϵ_{kl}, respectively. The material coefficients are assumed to be locally varying at a length scale l which is much smaller than the overall system size L, which is reflected in the superscript index $\epsilon = {}^{l}/_{L}$.
In analogy to Section 7.1.1, we can introduce Equation 8.1 in the force balance equation and reorder the equation for different orders of the microscopic parameter ϵ, which yields the *cell problem* within a microscopic cell Ω of length l: Find $\chi^{kl} \in V$ and $\Gamma \in V$, with

$V = \{v : v \text{ is } \Omega\text{-periodic}\}$, such that

$$\int_\Omega C_{ijpq} \frac{\partial \chi_p^{kl}}{\partial y_q} \frac{\partial v_i}{\partial y_j} \mathrm{d}\Omega = \int_\Omega C_{ijpq} \epsilon_{pq}^{0(kl)} \frac{\partial v_i}{\partial y_j} \mathrm{d}\Omega \tag{8.2}$$

$$\int_\Omega C_{ijkl} \frac{\partial \Gamma_k}{\partial y_l} \frac{\partial v_i}{\partial y_j} \mathrm{d}\Omega = -\int_\Omega \sigma_{\mathrm{m}ij} \frac{\partial v_i}{\partial y_j} \mathrm{d}\Omega \,, \tag{8.3}$$

$\forall v \in V$ with test function v, microscopic variable y_j and $\epsilon_{pq}^{0(kl)}$ being three linearly independent test strain fields, e.g. $\epsilon_{pq}^{0(11)} = (1,0,0)$, $\epsilon_{pq}^{0(22)} = (0,1,0)$ and $\epsilon_{pq}^{0(12)} = (0,0,1)$ using Voigt's notation. The cell problems 8.2 and 8.3 are then solved for these three pre-strain cases, using the FE method with periodic boundary conditions. We will outline this step in the following subsection.
After the discretization of the unit cell into N finite elements e of size Ω_e, we can compute the effective material parameters $C_{ijkl}^\star$ and $\sigma_{\mathrm{m}ij}^\star$ via

$$C_{ijkl}^* = \frac{1}{|\Omega|} \sum_{e=1}^{N} \int_{\Omega_e} C_{pqrs}^e \left(\epsilon_{pq}^{0(kl)} - \epsilon_{pq}^{(*)}\left(\chi^{kl}\right)\right)\left(\epsilon_{rs}^{0(ij)} - \epsilon_{rs}^{(*)}\left(\chi^{ij}\right)\right) \mathrm{d}\Omega_e \tag{8.4}$$

$$\sigma_{\mathrm{m}ij}^* = \frac{1}{|\Omega|} \sum_{e=1}^{N} \int_{\Omega_e} C_{pqkl}^e \left(\alpha_{pq} - \epsilon_{pq}^C(\Gamma)\right)\left(\epsilon_{kl}^{0(ij)} - \epsilon_{kl}^{(*)}\left(\chi^{ij}\right)\right) \mathrm{d}\Omega_e \,, \tag{8.5}$$

with

$$\epsilon_{pq}^{(*)}\left(\chi^{kl}\right) = \frac{1}{2}\left(\frac{\partial \chi_p^{kl}}{\partial y_q} + \frac{\partial \chi_q^{kl}}{\partial y_p}\right) , \tag{8.6}$$

$$\epsilon_{pq}^C(\Gamma) = \frac{1}{2}\left(\frac{\partial \Gamma_p}{\partial y_q} + \frac{\partial \Gamma_q}{\partial y_p}\right) , \tag{8.7}$$

$$C_{ijpq}\alpha_{pq} = \sigma_{\mathrm{m}ij} \,, \tag{8.8}$$

where α_{pq} is the active strain [*Sigmund and Torquato*, 1997].

8.1.2 Numerical Implementation of Two-Dimensional Asymptotic Homogenization Technique

Hassani and Hinton [1998] show that for many two-dimensional patterns it is possible to calculate the effective material parameters analytically. For the general setting, however, the homogenization has to be performed numerically by means of a FE simulation [*Guedes and Kikuchi*, 1990; *Fish et al.*, 1994]. In this case, the cell problems in Equations 8.2 and 8.3 are discretized into the linear equations

$$\mathbf{K}\chi^i = \mathbf{f}^i \,, \tag{8.9}$$

and

$$\mathbf{K}\boldsymbol{\Gamma} = \mathbf{f}_\alpha \,, \tag{8.10}$$

with *stiffness matrix*

$$\mathbf{K} = \sum_{e=1}^{N} \int_{\Omega_e} \mathbf{B}_e^T \mathbf{C}_e \mathbf{B}_e \mathrm{d}\Omega_e \,, \tag{8.11}$$

as well as *load vectors*

$$\mathbf{f}^i = \sum_{e=1}^{N} \int_{\Omega_e} \mathbf{B}_e^T \mathbf{C}_e \epsilon^i \mathrm{d}\Omega_e \,, \tag{8.12}$$

and

$$\mathbf{f}_\alpha = \sum_{e=1}^{N} \int_{\Omega_e} \mathbf{B}_e^T \mathbf{C}_e \alpha_e \mathrm{d}\Omega_e \,. \tag{8.13}$$

Here, $\mathbf{B}_e^{(j)}$ represents the *strain-displacement matrix* of node j of the finite element e, defined as

$$\mathbf{B}_e^{(j)} = \begin{pmatrix} \frac{\partial N_e^{(j)}}{\partial y_1} & 0 \\ 0 & \frac{\partial N_e^{(j)}}{\partial y_2} \\ \frac{\partial N_e^{(j)}}{\partial y_2} & \frac{\partial N_e^{(j)}}{\partial y_1} \end{pmatrix} , \tag{8.14}$$

with associated *shape function* $N_e^{(j)}$. Further, ϵ^i denotes the pre-strain case $i \in \{1, 2, 3\}$ and α the unit active (or thermal) strain. Periodic boundary conditions within a unit cell Y are imposed by eliminating degrees of freedom for corresponding nodes on two opposite faces, as implemented by *Andreassen and Andreasen* [2014].

8.2 Application of Two-Dimensional Asymptotic Homogenization to Predict Cellular Stresses

We will now use the two-dimensional homogenization technique to establish a method based on continuum mechanics to predict cellular internal and traction stresses based on the structure of the actin CSK within a cell. In Section 8.2.1, we will introduce the algorithm to calculate stresses from actin-stained images of the cell. This is then followed by a specification of involved parameters in Section 8.2.2 based on preliminary TFM results. Finally, we will perform exemplary predictions of cellular stresses in Section 8.2.3 to verify the method.

8.2.1 Homogenization-Based Algorithm to Calculate Cellular Stresses

We can use the two-dimensional asymptotic homogenization technique introduced in Section 8.1.1 to formulate a detailed continuum model of the actin CSK of a cell starting from the internal composition of actin inside the cell. In the following listing, we will present the algorithm to deduce a FE description of the actin CSK from raw actin-stained images, which is illustrated in Figure 8.1:

1. We start the algorithm by segmenting the stress fibers (SFs) from the actin-stained images by means of the software package *Filament Sensor* [*Eltzner et al.*, 2015].

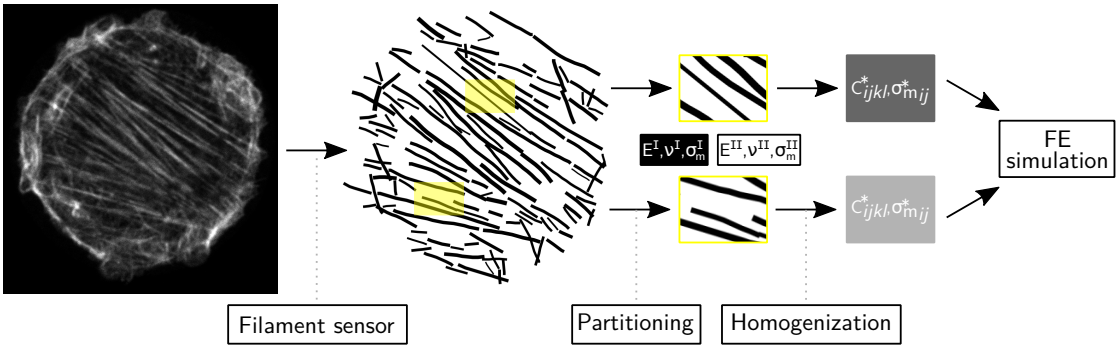

Figure 8.1: Algorithm to introduce structural information of the actin cytoskeleton in a two-dimensional continuum model. Filamentous structures of the actin cytoskeleton are extracted from actin stained images of the adhering cell. A binary coding scheme is prescribed to the segmented image: *Black* means "stress fiber" with isotropic properties E^{I}, ν^{I} and $\sigma^{\mathrm{I}}_{\mathrm{m}}$, while *white* means "void" with isotropic properties E^{II}, ν^{II} and $\sigma^{\mathrm{II}}_{\mathrm{m}}$. The segmented image is subdivided into patches of equal size. For each patch, homogenized coefficients C^*_{ijkl} and $\sigma^*_{\mathrm{m}ij}$ are computed by means of asymptotic homogenization. The resulting homogenized force balance equation is finally solved by means of a FE simulation. Actin-stained cell image by courtesy of Tomas Andersen, Université Grenoble Alpes.

Table A.8 lists the parameters for the image filtering and postprocessing which were used to extract filamentous structures from the images. The output of this first step is a list of detected filaments ordered by means of length, width and angles of its segments. We can now transform the original image into a binary image, in which black pixels represent SFs and white pixels represent void.

2. The segmented image is partitioned into square patches of length w. In general, the patch width w can be chosen arbitrarily. However, in Section 8.2.2, we will find that a preferred w should be large enough to contain several SFs, but much smaller than the overall cell size. The choice $w = 1$ will not work well, which shows that indeed the homogenization approach is essential.

3. We homogenize each local image patch separately using the methods from the previous section. On the microscopic scale, we assume the simplest possible model: A pixel which belongs to a SF is accredited with an isotropic stiffness E^{I}, Poisson's ratio $\nu^{\mathrm{I}} = 0.5$ and isotropic motor stress $\sigma^{\mathrm{I}}_{\mathrm{m}}$, while the remaining (i.e. void) pixels have an isotropic stiffness $E^{\mathrm{II}} = {}^{E^{\mathrm{I}}}/_{1000}$, Poisson's ratio $\nu^{\mathrm{II}} = 0.5$ and motor stress $\sigma^{\mathrm{II}}_{\mathrm{m}} = 0$. In Section 8.2.2, we will specify E^{I} and $\sigma^{\mathrm{I}}_{\mathrm{m}}$ by comparing the resulting macroscopic quantities with those obtained by means of TFM in Chapter 4. The result of this step is a single orthotropic stiffness tensor $C^\star_{ijkl}$ and stress tensor $\sigma^\star_{\mathrm{m}ij}$ per image patch.

4. We introduce the resulting stiffness and motor stress properties into a FE simulation and solve the locally homogenized force balance equation. By estimating the effective

spring stiffness density Y of the elastic connections between the two-dimensional sheet and its environment from experimental parameters (see Section 8.2.2), we can calculate traction stresses $\mathbf{T} = Y\mathbf{u}$ from the material displacements $\mathbf{u}$. A comparison of traction stresses deduced by means of our homogenization-based method and TFM finally allows to constrain the parameters involved in our algorithm.

8.2.2 Parameter Specification

The algorithm introduced in the previous section comprises several degrees of freedom which we will address in the following: the spring stiffness density Y, the image patch size w, and the microscopic stiffness $E^{\mathtt{I}}$ and active stress $\sigma_{\mathrm{m}}^{\mathtt{I}}$. In particular, we will constrain these parameters by using the experimental results acquired by means of TFM in Chapter 4 as a baseline.

Estimation of the Spring Stiffness Density Y We can make a rough estimation of the global spring stiffness density Y by estimating its contributions from the adhesion stiffness density Y_{a} and the substrate stiffness density Y_{s} from Equation 5.5, which yields the relations

$$Y_{\mathrm{a}} = \frac{N_{\mathrm{a}} k_{\mathrm{a}}}{A_{\mathrm{c}}}\,, \tag{8.15}$$

and

$$Y_{\mathrm{s}} = \frac{\pi E_{\mathrm{s}}}{h_{\mathrm{eff}}}\,, \tag{8.16}$$

with number of adhesions N_{a}, spring stiffness of a single FA site k_{a}, total cell area A_{c}, substrate stiffness E_{s} and effective substrate height h_{eff} from Equation 3.31. With roughly 10 stress fibers per cell, we have a number of $N_{\mathrm{a}} = 20$ adhesion sites per cell area $A_{\mathrm{c}} = 1000\,\mu\mathrm{m}^2$, each with a spring stiffness $k_{\mathrm{a}} \approx 1\,{}^{nN}/_{\mu\mathrm{m}}$ [*Balaban et al.*, 2001], yielding $Y_{\mathrm{a}} = 2 \times 10^7\,{}^{N}/_{\mathrm{m}^3}$.
On the other hand, we have $E_{\mathrm{s}} = 5 \cdot 10^3\,{}^{N}/_{\mathrm{m}^2}$, $h_{\mathrm{s}} = 50\,\mu\mathrm{m}$ and $L_{\mathrm{s}} \approx 40\,\mu\mathrm{m}$, yielding $Y_{\mathrm{s}} = 3 \times 10^8\,{}^{N}/_{\mathrm{m}^3}$. Together, we get

$$Y = \left(\frac{1}{Y_{\mathrm{a}}} + \frac{1}{Y_{\mathrm{s}}}\right)^{-1} \approx 2 \times 10^7\,{}^{N}/_{\mathrm{m}^3}\,, \tag{8.17}$$

where we used Equation 5.5 as an estimation for the global spring stiffness density Y. It has to be noted here that Y crucially depends on the involved parameters and the above results has to be interpreted with care. An alternative, but at the same time computationally much more expensive, method would involve continuum substrates, in which a Green's function replaces discrete springs, as suggested by *Banerjee and Marchetti* [2012]. This will be considered in follow-up studies (see Chapter 10).

Estimation of the Image Patch Size w Figure 8.2 shows both qualitatively and quantitatively the influence of the sub-image patch size w on the resulting traction stress

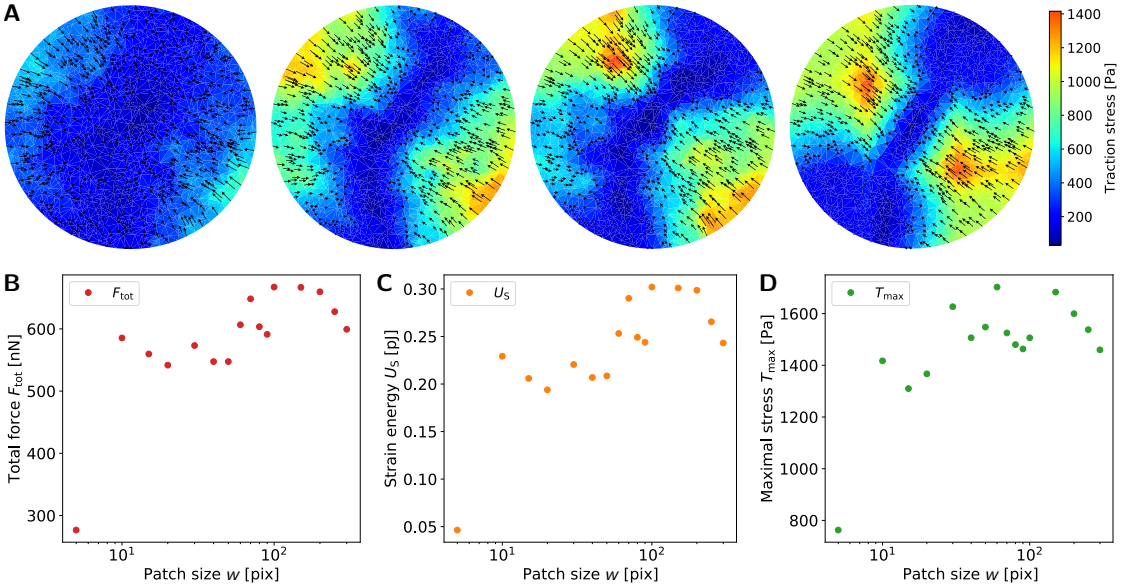

Figure 8.2: Resulting traction stress pattern of the FE simulation as a function of the patch size w. **(A)** Qualitative comparison of traction stresses for patch sizes 5 pix, 15 pix, 40 pix and 300 pix. **(B-D)** Total force F_{tot}, strain energy U_{S} and maximal traction stress T_{max} as a function of the patch size, respectively.

pattern and the global quantities total traction force

$$F_{\mathrm{tot}} = \int_A |\mathbf{T}| \, \mathrm{d}A = \int_A |Y\mathbf{u}| \, \mathrm{d}A \,, \tag{8.18}$$

strain energy

$$U_{\mathrm{S}} = \frac{1}{2} \int_A \mathbf{T}\mathbf{u}_{\mathrm{s}} \, \mathrm{d}A = \frac{1}{2} \int_A Y_{\mathrm{s}} |\mathbf{u}_{\mathrm{s}}|^2 \, \mathrm{d}A = \frac{1}{2} \int_A \frac{Y^2}{Y_{\mathrm{s}}} |\mathbf{u}|^2 \, \mathrm{d}A \,, \tag{8.19}$$

and maximal stress T_{max}, using the actin-stained image from Figure 8.1 and the corresponding traction pattern in Figure 4.2 as benchmark. For a too small patch size w, all quantities decrease significantly as well as the average traction magnitude, suggesting that the contractile fibers operate independently of each other. For a too large patch size w, the overall magnitude of the global quantities does to vary significantly. However, with increasing patch size, the highest traction peaks move towards the interior of the cell, become smoother and resemble each other. This is due to the fact that the homogenization is performed over an increasing area and the contribution of characteristic features of the SF pattern is blurred.
A patch size of $w \approx 40$ pix turns out to be the optimal choice in this case. It allows to average over multiple SFs (about 5 pix for the width of a SF), on the one hand, and is still much smaller than the total image size (600 pix), on the other hand.

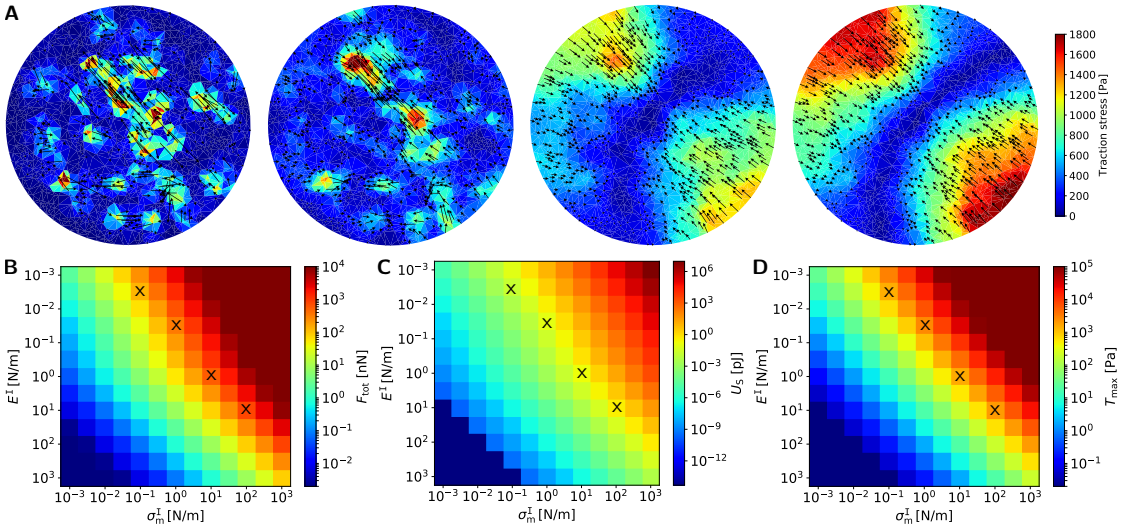

Figure 8.3: Resulting traction stress pattern of the FE simulation as a function of the microscopic stiffness E^{I} and stress $\sigma_{\mathrm{m}}^{\mathrm{I}}$. **(A)** Qualitative comparison of traction stresses for the microscopic stiffnesses and stresses $E^{\mathrm{I}} = 5 \times 10^{-3}\,{}^{N}/_{\mathrm{m}}$ and $\sigma_{\mathrm{m}}^{\mathrm{I}} = 0.1\,{}^{N}/_{\mathrm{m}}$, $E^{\mathrm{I}} = 3.2 \times 10^{-2}\,{}^{N}/_{\mathrm{m}}$ and $\sigma_{\mathrm{m}}^{\mathrm{I}} = 1.0\,{}^{N}/_{\mathrm{m}}$, $E^{\mathrm{I}} = 1.0\,{}^{N}/_{\mathrm{m}}$ and $\sigma_{\mathrm{m}}^{\mathrm{I}} = 10.0\,{}^{N}/_{\mathrm{m}}$, and $E^{\mathrm{I}} = 10.0\,{}^{N}/_{\mathrm{m}}$ and $\sigma_{\mathrm{m}}^{\mathrm{I}} = 100.0\,{}^{N}/_{\mathrm{m}}$, from *left* to *right*. **(B-D)** Total force F_{tot}, strain energy U_{S} and maximal traction stress T_{max} as a function of the microscopic stiffness and stress, respectively. *Black crosses* refer to the traction stress patterns in Panel A. For each simulation, a patch size $w = 40\,\mathrm{pix}$ is used.

Estimation of the Microscopic Material Properties E^{I} and $\sigma_{\mathrm{m}}^{\mathrm{I}}$ Figure 8.3 depicts both qualitatively and quantitatively the influence of the microscopic material properties E^{I} and $\sigma_{\mathrm{m}}^{\mathrm{I}}$ on the resulting traction stress pattern and the global quantities introduced in the previous paragraph.

We find that the microscopic properties have a strong effect on both the traction stress pattern and the global quantities of a cell. Quantitatively, only for a ratio of $\sigma_{\mathrm{m}}^{\mathrm{I}}/E^{\mathrm{I}} \approx 10$, which is highlighted by black crosses in Figure 8.3B-D, we are able to reproduce a total force, strain energy and maximal stress in the range of the experimentally acquired values (compare Figure 4.2), thus effectively reducing the number of free parameters to one.

The absolute values of E^{I} and $\sigma_{\mathrm{m}}^{\mathrm{I}}$ can be deduced from the traction images in Figure 8.3A. For increasing E^{I}, we find that the penetration length of cellular stresses increases, as one would expect from Equation 5.5: For small E^{I}, multiple spatially independent stress spots emerge, while for large E^{I}, all traction sources contribute to two large traction peaks.

We conclude that a microscopic stiffness of $E^{\mathrm{I}} \approx 1\,{}^{N}/_{\mathrm{m}}$, i.e. $E^{\mathrm{II}} \approx 10^{-3}\,{}^{N}/_{\mathrm{m}}$, and $\sigma_{\mathrm{m}}^{\mathrm{I}} \approx 10\,{}^{N}/_{\mathrm{m}}$ yield best results with respect to the traction patterns acquired by means of TFM.

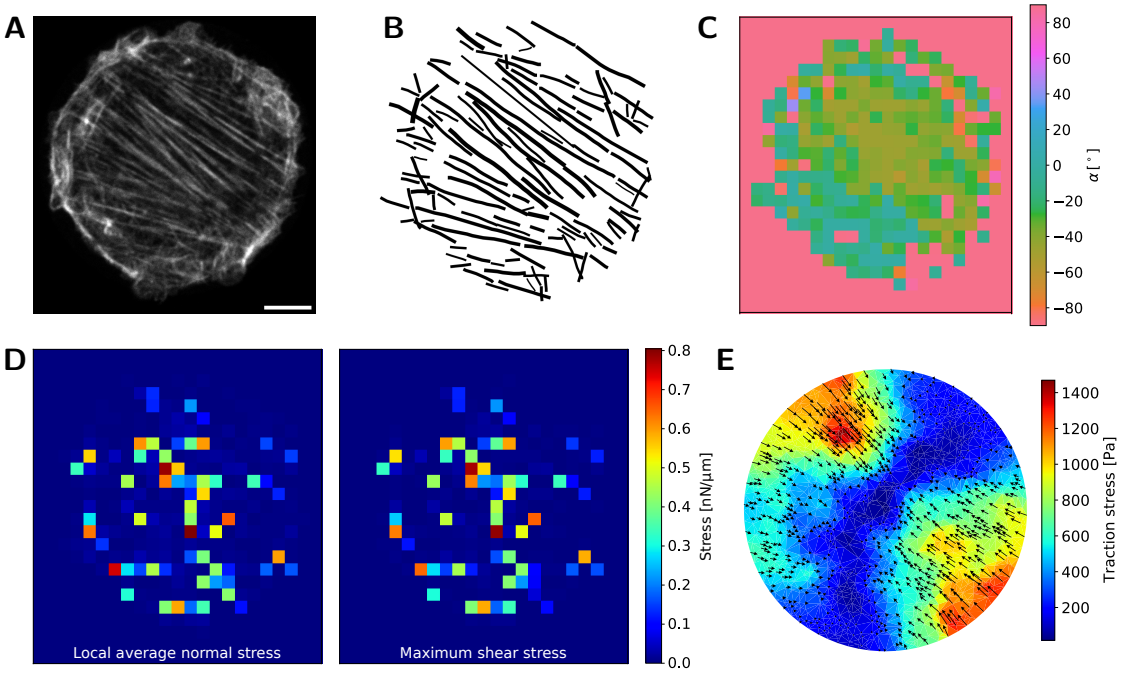

Figure 8.4: Calculation of the traction stress field inferred from the structure of the actin CSK for a cell adhering to a circular fibronectin pattern. **(A)** Representative actin cytoskeleton of a cell which adheres to a circular fibronectin pattern. Scale bar is 100 pix or 7 μm. By courtesy of Tomas Andersen, Université Grenoble Alpes. **(B)** Extracted filamentous structures of the actin cytoskeleton: The actin cytoskeleton is represented via a binary coding. *Black* means "stress fiber", while *white* means "void". **(C)** Principal orientation α of the calculated homogenized stress tensor. **(D)** Local average normal stress and maximum shear stress, respectively. **(E)** Traction stress field $\mathbf{T} = Y\mathbf{u}$ resulting from the FE simulation.

8.2.3 Exemplary Calculation of Cellular Stresses

We can finally use the parameterization from Section 8.2.2 to infer internal and traction stresses for the two compositions of the actin CSK introduced in Chapter 4: *Full circle* and *wheel* pattern. In the following, we will use the same set of parameter values for both patterns which are listed in Table A.8.

Figures 8.4A-C show the raw actin-stained image, segmented SFs and principal orientations of SFs of a typical cell which spread on a full circle pattern, respectively. We find a single predominant orientation of SFs around $-40\,°$.

Figure 8.4D illustrates the negative local average normal stress $-(\sigma_{\max}+\sigma_{\min}/2)$ and the maximum shear stress $\sigma_{\max}-\sigma_{\min}/2$ deduced from the homogenization, with maximal and minimal principal stresses $\sigma_{\max}$ and $\sigma_{\min}$, respectively [*Tambe et al.*, 2011]. The stress fields closely resemble each other, which indicates that $\sigma_{\min} \ll \sigma_{\max}$, i.e. the stress tensor is unidirectional in almost each subpatch of the stress field as one would expect intuitively from the arrangement of SFs. The largest accumulation of internal stresses is found

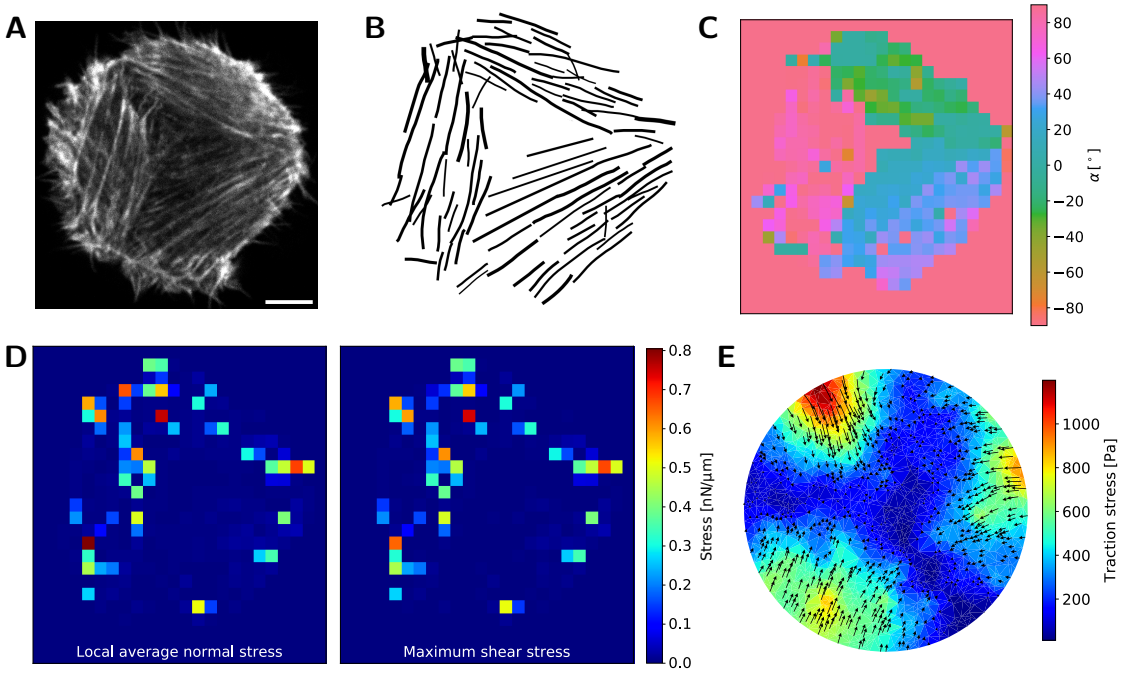

Figure 8.5: Calculation of the traction stress field inferred from the structure of the actin CSK for a cell adhering to a wheel-shaped fibronectin pattern. **(A)** Representative actin cytoskeleton of a cell which adheres to a circular fibronectin pattern. Scale bar is 100 pix or 7 μm. By courtesy of Tomas Andersen, Université Grenoble Alpes. **(B)** Extracted filamentous structures of the actin cytoskeleton: The actin cytoskeleton is represented via a binary coding. *Black* means "stress fiber", while *white* means "void". **(C)** Principal orientation α of the calculated homogenized stress tensor. **(D)** Local average normal stress and maximum shear stress, respectively. **(E)** Traction stress field $\mathbf{T} = Y\mathbf{u}$ resulting from the FE simulation.

in the cell center, where the SF density is highest. Typical internal stresses are about $\sigma_0 h_c \approx 0.5\,{}^{\mathrm{nN}}/_{\mu\mathrm{m}}$, which is in the range of internal stress values of fibroblasts obtained from the simulations in Chapters 3 and 4.

Figure 8.4E finally depicts the predicted traction stress pattern of the cell resulting from the FE simulation. The dominant traction peaks are oriented parallel to the predominant orientation of the actin CSK. Traction stresses further increase with increasing distance from the center of the cell. Qualitatively, we find a good agreement between the simulated traction stress and the experimentally acquired traction stress pattern for circle-patterned cells in Figure 4.2A.

We further conducted the traction inference method for a cell spread on the wheel pattern as depicted in Figure 4.1C. For simplicity, we assumed in the FE simulation that the full circle pattern below the cell is adhesive. Figures 8.5A-C show the raw actin-stained image, segmented SFs and principal orientations of SFs of a typical cell which spread on a wheel pattern, respectively. Here, we find three dominant orientations of SFs with angles

80 °, 30 ° and −20 °, which justifies the design of the actin CSK used in Figure 4.5C.
Figure 8.5D shows the negative local average normal stress and maximum shear stress for the wheel-patterned cell. As in Figure 8.4D, both stress fields closely resemble each other, also indicating that $\sigma_{\min} \ll \sigma_{\max}$. In contrast to Figure 8.4D, the largest internal stresses are located at the periphery of the cell, where the SF density is highest in this case. Typical internal stresses are in the same range as for circle-patterned cells. However, the distribution of stress peaks is sparser, which suggests that fewer SFs are registered by the algorithms.
Finally, Figure 8.5E reveals the predicted traction stress pattern of the cell resulting from the FE simulation. As in the experimental results shown in Figure 4.3A, we find three distinct traction peaks located at the intersection of the SF clusters. Compared with the traction stress pattern in Figure 8.4E, we find that the maximal traction stress, as well as the total force and strain energy, are lower by about 40 % for wheel-patterned cells, a fact that was already observed in Figures 4.2 and 4.3.
Apparently, the difference in terms of traction stresses originates from the composition of the actin CSK in both cases. In particular, for the wheel-patterned cells, two features come into question as compared to the circle-patterned cells: On the one hand, the three clusters of SFs entail different principal directions, which makes them pull into different directions at the intersection points and, with this, eliminate each other to a certain degree. On the other hand, a single cluster of SFs contains only half of the number of parallel SFs as compared to the only cluster in circle-patterned cells. That is why the weaker maximal traction stress of wheel-patterned cells might also originate from the reduced contractile efficiency of the small clusters.
Overall, we find a good agreement between typical internal stress magnitudes and traction stress patterns acquired from the FE simulations and the corresponding TFM results in Chapter 4.

8.3 Conclusion

In this section, we introduced the two-dimensional asymptotic homogenization technique and used the mathematical framework to develop a continuum model-based method, aiming at estimating internal and traction stresses of adhering cells. We constrained the free parameters of the algorithm to meet the requirements set by means of TFM calculations and showed based on exemplary datasets that the traction stress fields predicted by means of our new algorithm are in good qualitative agreement with those determined by means of TFM.
Compared to the MBTFM algorithm introduced by *Soiné et al.* [2015], the new model yields a much faster computation time due to its continuum-based nature, while maintaining the capability to qualitatively infer stresses from the distribution of stress fibers in a cell. Existing continuum models, such as those by *Edwards and Schwarz* [2011] or *Oakes et al.* [2014], which lack information about the internal structure of the CSK, are outperformed by the new model.
Beyond that, the continuum model-based method allows to infer microscopic parameters

from the knowledge of macroscopic mechanical properties of the cell, analogous to Chapter 7. We obtain typical local stiffness values of SFs of $E^{\mathrm{I}}h_{\mathrm{c}} = 10^3\,{}^{\mathrm{nN}}/_{\mu\mathrm{m}}$, which closely resembles the values reported by *Livne and Geiger* [2016], if assuming a typical cell height of $h_{\mathrm{c}} = 1\,\mu\mathrm{m}$. Further, we get local effective stresses in the range of $\sigma_{\mathrm{m}}^{\mathrm{I}}h_{\mathrm{c}} = 10^4\,{}^{\mathrm{nN}}/_{\mu\mathrm{m}}$, which is several orders of magnitude larger than typical stresses exerted by single myosin filaments. The origin of these large stresses might, however, originate from a yet uncovered force-generating mechanism apart from the myosin-induced forces, as discusses in Chapter 7.
In Chapter 10, we will discuss further extensions to the continuum model which will allow to improve its performance towards the precision of discrete model-based TFM.

9 Summary

The combination of Fourier-based traction force microscopy and finite element simulations used in this manuscript has demonstrated the feasibility of using a thermo-viscoelastic continuum model with coupling to a viscoelastic foundation to describe the mechanical properties of the actin cytoskeleton in adhering cells. Beyond that, a mathematical framework has been adapted which allows to interrelate these properties at macro- and microscopic spatial scales and, with this, connect the local composition of the actin cytoskeleton to its global effect. The necessary steps carried out to reach this conclusion are briefly summarized in the following.

As a technical basis for this manuscript, we started in Chapter 2 with an optimization of the regularized Fourier Transform Traction Cytometry (FTTC) algorithm, aiming at enabling both a reliable and, at the same time, automatized estimation of cellular traction stresses. We analytically revealed that regularization is indeed an inevitable step in process of traction force reconstruction from the deformation of an elastic substrate. In the course of reconstructing synthetic traction patterns, we could show that the data-driven Generalized Cross-Validation (GCV) method outperforms other Tikhonov-based estimators used so far. We further demonstrated that, for the idealized case of uncorrelated noise in the experimentally obtained substrate deformation, sparse regularization is preferable to the typical choice of Tikhonov regularization. In a real setting entailing both correlated and uncorrelated noise, however, Tikhonov-based regularization prevails over other regularization norms.

Thereafter, in Chapter 3, we introduced a viscoelastic continuum model of Maxwell type to describe the dynamics of cellular traction stresses and flows of cytoskeletal constituents along stress fibers (SFs) in fibroblast cells, whose RhoA signaling pathway was spatiotemporally controlled by means of optogenetic activation. The continuum model helped to explain the overall stress increase and elastic-like relaxation of single SFs upon introduction and removal of the activating light, respectively, allowing to extract a characteristic relaxation time constant of about $\tau = 50\,\mathrm{min}$ for the transition from solid-like to fluid like behavior of SFs. Moreover, we used the model to identify the protein zyxin as a key regulator of the elasticity of SFs.

In Chapter 4, we extended the continuum model by an anisotropic stress tensor and an inhomogeneous coupling to the elastic substrate to account for the influence of the composition of the fibronectin micropattern on the composition of the actin cytoskeleton and, with this, on the contractility of the cell. We used experimental data of photoactivated cells to constrain the model parameters and to explain why cells reveal a different contractile behavior on differently shaped fibronectin coatings, even if they adopt the same spread area or contour. We were able to reproduce the positive correlation of the contractile energy cells invest and their spread area, yielding typical contractile stresses

in the range of $\sigma_0 h_c = 1\,{}^{\mathrm{nN}}/_{\mu\mathrm{m}}$. The computational investigation of the dynamic force production in cells showed that, on the global scale, the contractile behavior of cells can be best described by a viscoelastic model of Kelvin-Voigt type, which, by design, allows to capture the tensional homeostasis of a cell in the absence of a regulatory signal. Our model finally allowed to determine a photoactivating pulse duration of about 30 ms above which the effect of the CRY2/CIBN dimerizer system on the regulatory RhoA signaling pathway saturates.

We then investigated the dynamics of force generation by human blood platelets spreading onto elastic substrates of variable stiffness in Chapter 5. Traction force reconstruction allowed to identify a force anisotropy, quantified by a dipole ratio of about 2 , and two distinct contractile behaviors of individual platelets, namely oscillating and non-oscillating. Both were found to be uncorrelated with respect to cellular or extracellular properties. We used our continuum model to explain the positive correlation between the maximal force level a platelet reaches and its spread area, revealing a large internal stress of hundreds of kPa, which, with a typical platelet thickness of 100 nm, results in a planar stress in the order of $\sigma_0 h_c = 10\,{}^{\mathrm{nN}}/_{\mu\mathrm{m}}$. Our continuum model moreover allowed to hypothesize that, due to this uniquely small thickness, platelets lack mechanosensitivity in the investigated stiffness range.

In Chapter 6, we turned to multicellular systems and showed for the particular example of a collectively migrating layer of Madin-Darby Canine Kidney (MDCK) cells that the selective emergence of leader cells at the margin of the layer depends on the dynamics of its follower cells and is spatially limited by the length scale of collective force transduction. Despite the diverse mechanical activity of single cells, we were able to use our continuum model to explain the origin, maintenance and splitting of leader cells based on the penetration of forces in elastic solids with elastic coupling, suggesting that the ideal distance between two neighboring leader cells minimizes the total mechanical energy of the cell layer. We finally reduced our model to a single dimension to establish an analytical treatment of the problem, but found out that the above conclusions can not be drawn from a one-dimensional description. This suggests that the mechanical establishment of leader cells is a two-dimensional effect.

Finally, in Chapters 7 and 8, we investigated the relation of the microscopic composition of the actin cytoskeleton and the macroscopic mechanical properties of a cell by adopting the asymptotic homogenization technique to our continuum model.

In Chapter 7, we were able to analytically derive formulae to connect local and global mechanical quantities of a one-dimensional elastic bar with an inhomogeneous stiffness and stress distribution, revealing that the global stiffness depends primarily only on the local stiffness distribution, while the global contractile stress is influenced by both local stiffness and stress at first order. For the particular example of a SF, we found out that only a local metamaterial-like property in the myosin-free region can explain the discrepancy between the comparably low local stresses induced by single myosin filaments and the large global stresses of single SF measured at focal adhesion sites. We referred to possible micromechanical mechanisms which are likely to contribute to this uncommon mechanical behavior.

Finally, in Chapter 8, we applied two-dimensional asymptotic homogenization to infer the

internal and traction stress pattern of a cell from the composition of its actin cytoskeleton. We optimized the involved parameters and verified with the help of experimental data that the resulting algorithm allows to predict cellular contractile behavior in different environments.
The following chapter will provide an overview of tasks which bear the potential to improve the theoretical and computational framework presented so far.

10 Outlook

This manuscript has successfully demonstrated the applicability of a continuum model to describe cellular contractility on multiple spatial scales and the adaptability of the asymptotic homogenization technique to establish a connection between local and global cellular properties in the existing continuum framework. The following discussion contains suggestions for prospective analytical and simulative studies which have the potential to enhance the modeling approach at hand.

Improvement of the Quantification of Cellular Stresses In Chapter 2, we investigated the influence of both the estimation method and the regularization norm on the quality of traction force reconstruction in the context of FTTC and found out, by means of artificial data sets, that Tikhonov regularization with GCV as estimator outperforms other regularization schemes. It remains to be tested whether L_p-based regularization, with $2 < p < \infty$, yields a better overall performance than the Tikhonov norm. We could further use the introduced NCP method to estimate the predominant noise type in advance and, based on this, choose the appropriate regularization algorithm. Also, an investigation of sparse regularization based parameter estimators for the particular example of FTTC is not known so far.
In the context of three-dimensional TFM, a similar methodological comparison of known traction reconstruction methods, like the Green's function based method by *del Álamo et al.* [2013] or the direct method by *Franck et al.* [2011], remains to be accomplished. A precise quantification of cellular traction forces in three dimensions could e.g. uncover the mechanosensitivity of human blood platelets at low substrate stiffnesses hypothesized in Chapter 5. Altogether, the detailed characterization of existing methods to efficiently reconstruct cellular traction stresses would help to extend and improve the software framework introduced in Chapter 2 and, with this, be of great value to the biophysical community.

Improvement of the Continuum Modeling Approach of Cellular Contractility In the course of this manuscript, we found that a continuum modeling approach allows to reproduce fundamental mechanical properties of both single cells and cell assemblies. However, the continuum model is far from being universally applicable. For further improvements, experimental and theoretical methods have to go hand in hand.
In retrospect to Chapters 3 and 4, we could explore the cellular response to two or more simultaneous photoactivation regions. In this case, it is to be expected that the current material model needs to be coupled to a mathematical description of material generation or degradation and requires FE remeshing algorithms in the simulation. Further, one could think of analyzing the optogenetic activation of whole cells in epithelial sheets

to introduce the effect of tissue cohesion and influence of cellular rearrangements in the model. An investigation of cellular behavior upon photoactivation when the cell is confined in micro-engineered three-dimensional scaffolds, as described by *Scheiwe et al.* [2015], would also be a possible direction of future research.
Methods to improve the combined visualization of the actin cytoskeleton, focal adhesions and simultaneous force reconstruction, as conducted e.g. by *Oakes et al.* [2014], could help to enhance both the experimental and theoretical results reported in this manuscript. For example, the correlation of the cytoskeletal architecture and the traction stress pattern of blood platelets could help to explain the force anisotropy measured in Chapter 5. A correlation of this kind could further enable to spot the mechanical characteristics in the context of leader cell selection in Chapter 6. In particular, we could use the homogenization-based ansatz from Chapter 8 to improve the calculation of internal cellular stresses by exploiting the predominant direction of SFs in single cells of a collectively moving epithelial cell layer.
To model the collective dynamics in this particular example, one could use a Cellular Potts Model (CPM), as introduced by *Albert and Schwarz* [2014], and extend the model by an elastic substrate starting from the modeling approach of *van Oers et al.* [2014]. A further integration of discrete elements, like SFs, in the framework of the CPM might improve both the description and prediction capabilities of this stochastic model.
Moreover, the continuum model based TFM approach presented in Chapter 8 can be improved in many respects. First, we could introduce a non-zero spring stiffness density Y only at the exact locations of focal adhesion sites. This would require both precise image segmentation and finite element meshing algorithms, as introduced e.g. in the work of *Soiné et al.* [2015]. Second, we could skip the estimation of the spring stiffness density Y and instead use continuum substrates. The corresponding simulation ansatz could be based on the framework introduced by *Banerjee and Marchetti* [2012] and would require the adoption of either partial integro-differential equations or Fourier transform-based methods in the existing finite element simulation. Third, an extension of the existing homogenization-based algorithm to three dimensions would allow to describe mechanical properties of cells which are spread in three-dimensional micro-scaffolds.
Finally, a closer investigation of the metamaterial-like behavior of SFs showed up in Chapter 7 in terms of both experiments and simulations is required. On the experimental side, the simultaneous quantification of myosin motors along single SFs and reconstruction of traction stresses exerted by these, be it via TFM or molecular force sensors, would help to approve or disprove the hypothesis raised in Chapter 7. On the theoretical side, a microscopic model covering both the mechanics of actin and the biochemistry of the association and dissociation of actin filaments could help to determine or exclude the candidate models formulated in Chapter 7, introduced to explain the apparent local metamaterial-like feature of SFs.

A Appendix

A.1 Acronyms

ADP Adenosine diphosphate

AFM Atomic force microscope

ATP Adenosine triphosphate

BEM Boundary element method

CG Conjugate gradient

CIB1 Cryptochrome-interacting basic-helix-loop-helix 1

CPM Cellular Potts Model

CRY2 Cryptochrome 2

CSK Cytoskeleton

ECM Extracellular matrix

FA Focal adhesion

FCP Full Circle Pattern

FE Finite element

FN Fibronectin

FRET Förster resonance energy transfer

FTTC Fourier Transform Traction Cytometry

GAP GTP-activating proteins

GEF Guanine nucleotide exchange factor

GCV Generalized Cross-Validation

GDP Guanosine diphosphate

GTP Guanosine triphosphate

IRLS	Iteratively reweighted least squares
KLT	Kanade-Lucas-Tomasi
LOV	Light-Oxygen-Voltage
MDCK	Madin-Darby Canine Kidney
MLC	Myosin light chain
MSM	Monolayer Stress Microscopy
NCP	Normalized Cumulative Periodogram
PA	photoactivation
PAA	Polyacrylamide
PDMS	Polydimethylsiloxan
PIV	Particle image velocimetry
PFM	Phase Field Model
SEM	Scanning electron microscope
SIM	Structured illumination microscopy
SF	Stress fiber
SVD	Singular value decomposition
STED	Stimulated-Emission-Depletion
STM	Simple tension model
TEM	Tension elasticity model
TFM	Traction force microscopy
VM	Vertex Model
WP	Wheel Pattern

A.2 Traction Force Reconstruction

Synthetic image parameters	
Image size $i_{\max} = j_{\max}$	$125 - 1000$
Force spot ring radius R	$i_{\max}/5$
Angular range θ of force spot position	$40 - 140\,^\circ$
Number N of force spots	2×5
Standard deviation of spot position	$10.0\,^\circ$
Mean ellipse axes $(a_{\text{small}}, b_{\text{small}})$	$(1, 1.5)\ \% \times i_{\max}$
Mean ellipse axes $(a_{\text{large}}, b_{\text{large}})$	$(2, 2.5)\ \% \times i_{\max}$
Standard deviation of ellipse axes	$75\,\% \times a$
Stress in force spot σ_{spot}	$200.0\,\text{Pa} \times \sqrt{a}$
Standard deviation of white or red noise	$5 - 15\,\% \times u_{\max}$
Elastic modulus of substrate E_{S}	$4000\,\text{Pa}$
Poisson's ratio of substrate ν_{S}	0.5
Sparse regularization parameters	
Maximum number of iterations	200
Convergence criterion ϵ	10^{-3}
Threshold value ξ	10^{-6}

Table A.1: Parameters of the synthetic traction and displacement image generation algorithm and parameters used for the sparse regularization algorithms.

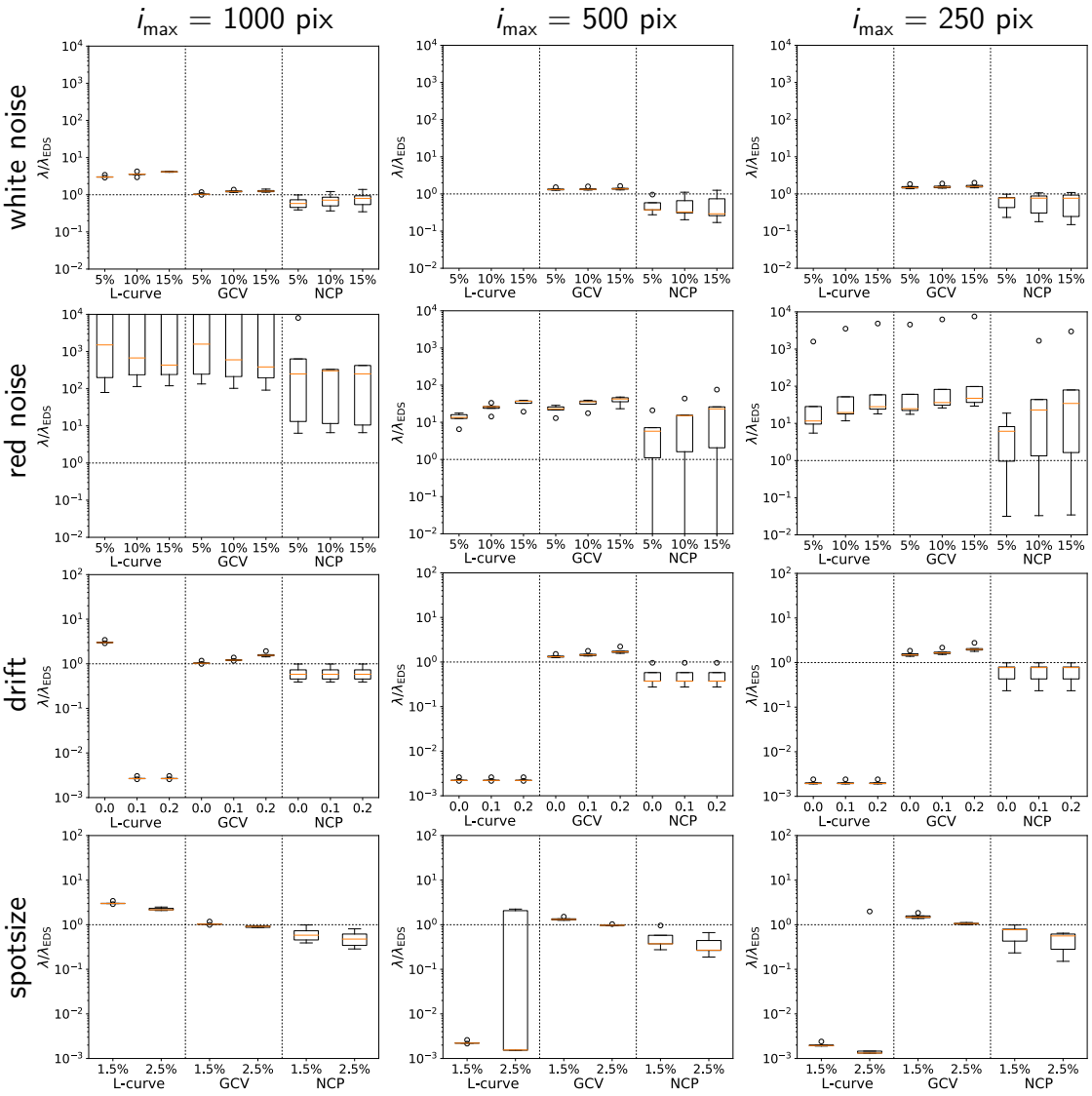

Figure A.1: Comparison of Tikhonov-based regularization protocols as a function of displacement field size i_{max}, noise color and magnitude, average displacement drift and average spot size. The field size is given in pixels, the noise magnitude in percent of maximal displacement, drift is given in pixels and spot size denotes the average size of the long axis of the elliptical force spot as percentile of the field size. Compared to Figure 2.5, the quality measure denotes the ratio of the regularization parameter λ using the respective algorithm and the ideal regularization parameter λ_{EDS} based on the Euclidean distance between original and reconstructed *stress spots*.

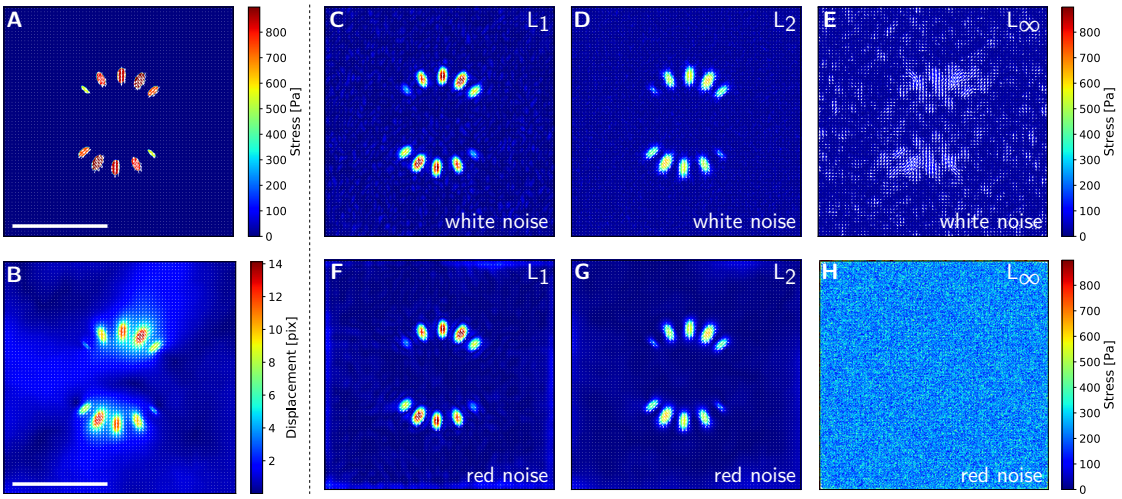

Figure A.2: Different regularizers applied to an exemplary stress field. **(A)** Original stress field. Simulation parameters are: $E_S = 10\,\text{kPa}$, $\nu_S = 0.5\,\text{kPa}$. **(B)** Calculated displacement field with additional red noise with maximal amplitude equaling $1/10$ of the maximal displacement. Panels **C**, **D** and **E** show the optimal reconstructed stress field from the displacement field subjected to white noise with maximal amplitude equaling $1/10$ of the maximal displacement using L_1-, L_2- and L_∞-Regularization, respectively. Panels **F**, **G** and **H** show the same results for a displacement field subjected to *red* noise with maximal amplitude equaling $1/10$ of the maximal displacement.

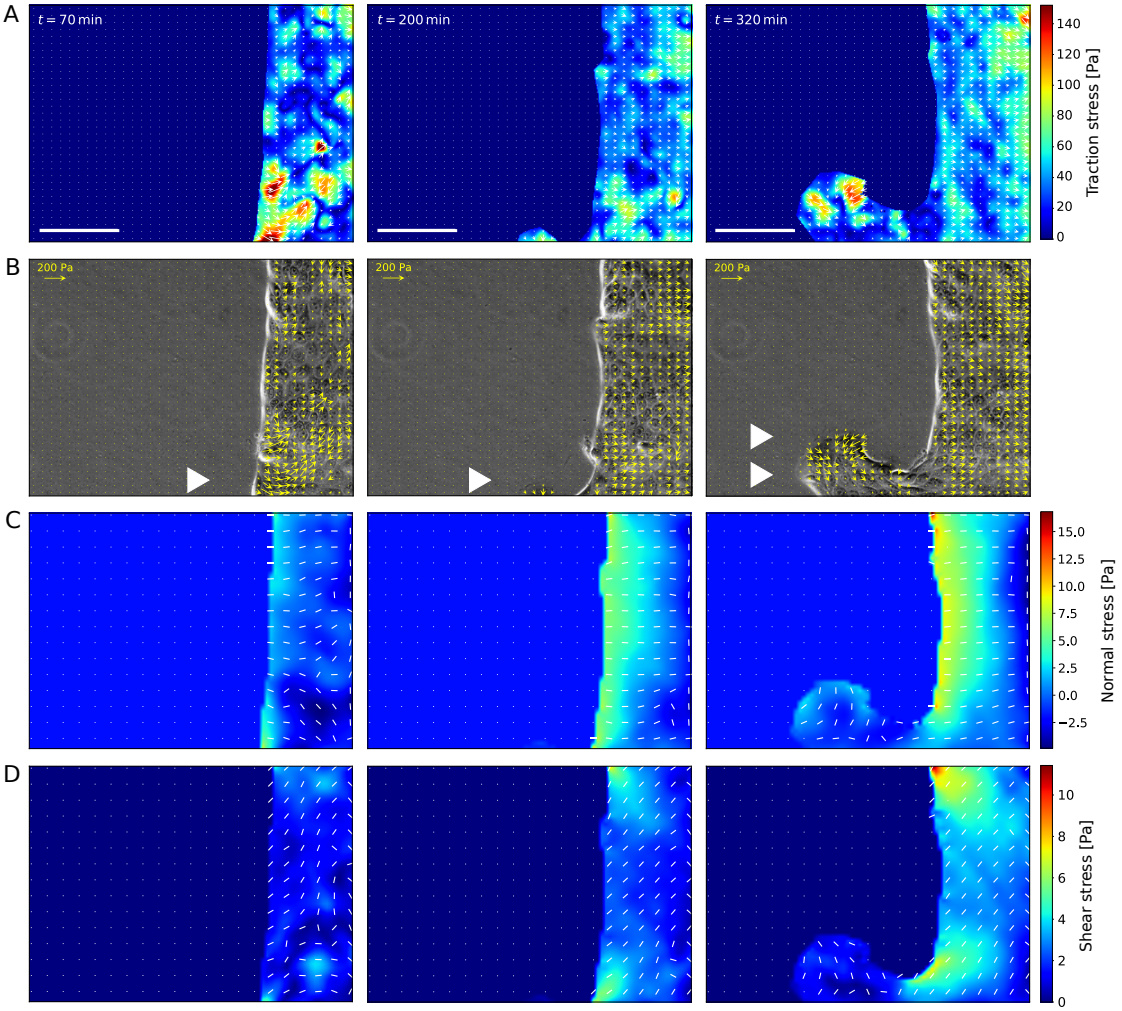

Figure A.3: Only follower cells behind the prospective leader cell exert highest stresses during Phase 0. **(A-D)** Exemplary traction stress magnitudes, traction stresses on top of actin-stained confocal microscopy images, normal and shear stresses, respectively. From *left* to *right*, representative images for Phase 0, 1 and 2 are depicted. In contrast to Figure 6.4, only the non-leader region is emphasized.

A.3 Simulation Results and Parameters

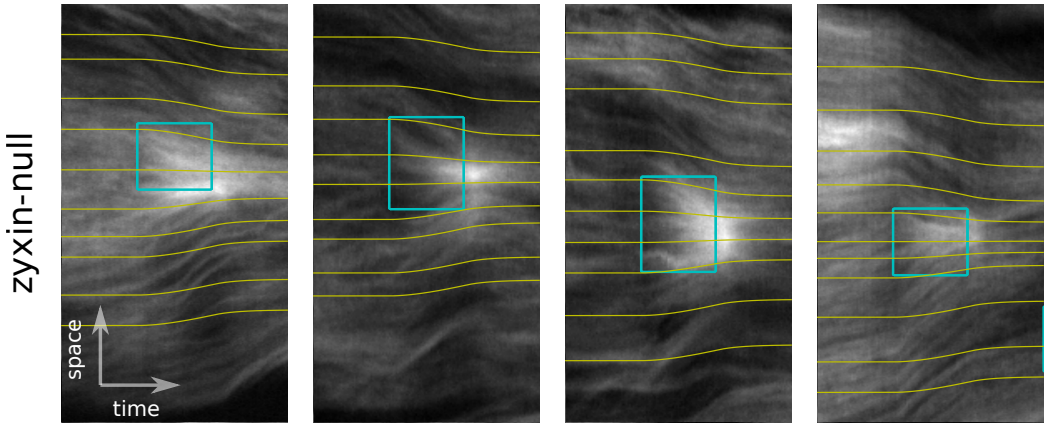

Figure A.4: Kymographs showing the spatiotemporal evolution of fluorescent myosin-II molecules in single stress fibers during activation of RhoA for the zyxin-null experiment. In contrast to Figure 3.9, we inserted the model parameters derived for wild-type cells and turned $E \to \infty$ (*yellow lines*), which, obviously, is not sufficient to describe the zyxin-null case. The system additionally becomes more fluid. As above, *blue boxes* illustrate the activation length ($5\,\mu$m) and duration (900 s).

Fit parameter	**Value in 3.8A**	**Value in 3.8B**
Elastic modulus of the cell E_c	11.19 kPa	1.98 kPa
Viscous modulus of the cell η_c	28.73 MPa · s	1.10 MPa · s
Friction coefficient γ	0.048 $^{kg}/_{s \cdot \mu m^3}$	0.080 $^{kg}/_{s \cdot \mu m^3}$
Background stress σ_{bck}	0.56 kPa	0.67 kPa
Maximal activation stress $\sigma_{0,1}$	0.27 kPa	0.66 kPa
Maximal activation stress $\sigma_{0,2}$	1.66 kPa	0.87 kPa
Maximal activation stress $\sigma_{0,3}$	2.29 kPa	0.72 kPa
Stress activation time τ_{act}	109.39 s	60.02 s
Stress relaxation time τ_{rel}	108.84 s	323.49 s
Strain energy factor α	22.1 kPa	22.1 kPa
Fixed parameter	**Value in 3.8A**	**Value in 3.8B**
Poisson's ratio of the cell ν_c	0.5	
Cell height h_c	1.0 μm	
Cell length L_c	50.0 μm	
Activation length $l_{act,1}$	5.0 μm	5.0 μm
Activation length $l_{act,2}$	5.0 μm	10.0 μm
Activation length $l_{act,3}$	5.0 μm	15.0 μm
Thickness of the substrate h_s	∞	
Poisson's ratio of the substrate ν_s	0.5	
Elastic modulus of the substrate E_s	25.8 kPa	
Parameter from literature	**Value**	**Reference**
Stiffness of focal adhesion bonds k_a	2.5 $^{nN}/_{\mu m}$	*Balaban et al.* [2001]
Length of sarcomeric subunit l_{sarc}	1 μm	*Hu et al.* [2017]
Implicit parameter	**Value in 3.8A**	**Value in 3.8B**
Force localization length l_p	14.39 μm	6.06 μm
Simulation parameter	**Value**	
Spatial resolution Δx	0.0047 μm	
Temporal resolution Δt	10 s	

Table A.2: Fit and fixed parameters of the strain energy fits from Figure 3.8.

Fit parameter	**Wild-type**	**Zyxin-null**	**Zyxin-rescue**
E_c [kPa]	(2.33 ± 1.81)	(9369.66 ± 4490.81)	(1.92 ± 1.38)
η_c [MPa · s]	(6.84 ± 2.97)	(0.53 ± 0.14)	(6.84 ± 5.19)
γ $\left[10^{-2}\,\mathrm{kg/s{\cdot}\mu m^3}\right]$	(3.05 ± 0.54)	(0.02 ± 0.04)	(1.65 ± 0.55)
σ_{bck} [Pa]	(465.55 ± 911.90)	(211.49 ± 65.97)	(4.74 ± 3.53)
σ_0 [kPa]	(4.72 ± 2.56)	(0.98 ± 0.20)	(3.59 ± 1.27)
τ_{act} [s]	(473.15 ± 82.02)	(69.72 ± 40.59)	(240.98 ± 222.37)
τ_{rel} [s]	(215.39 ± 68.88)	(79.82 ± 85.03)	(229.86 ± 74.63)
Implicit parameter	**Wild-type**	**Zyxin-null**	**Zyxin-rescue**
τ_M [min]	(48.93 ± 43.52)	(0.0009 ± 0.0005)	(59.38 ± 62.06)

Table A.3: Fit parameters extracted from the model fits to the myosin kymographs in Figure 3.9. Values are (mean ± standard deviation) of 5, 4 and 5 kymographs of wild-type, zyxin-null and zyxin-rescue cells, respectively.

Fit parameter	**Value in 3.12D**
Elastic modulus of the cell outside PA region E_1	0.64 kPa
Elastic modulus of the cell inside PA region E_2	0 kPa
Viscous modulus of the cell outside PA region η_1	0.15 MPa · s
Viscous modulus of the cell inside PA region η_2	0.08 kPa · s
Friction coefficient γ	2.27 $\frac{\mathrm{kg}}{\mathrm{s{\cdot}\mu m^3}}$
Activation stress σ_{max}	5.73 kPa
Fixed parameter	**Value in 3.12D**
Poisson's ratio of the cell ν_c	0.33
Cell height h_c	1.0 μm
Half-cell length L_x	400.0 μm
Half-cell width L_y	300.0 μm
Length of PA region l_0	50.0 μm
Length of PA region l_1	0.0 μm
Simulation parameter	**Value in 3.12D**
Spatial resolution in x-direction Δx	6.25 μm
Spatial resolution in y-direction Δy	4.69 μm
Temporal resolution Δt	1 s

Table A.4: Fit and fixed parameters of the flow velocity fit from Figure 3.12.

Rectangular stress profile	**Solid**	**Kelvin-Voigt**	**Maxwell**
Elastic modulus of the cell E_c	899.58 Pa	844.62 Pa	1165.22 Pa
Viscous modulus of the cell η_c	–	187.03 kPa · s	229.18 kPa · s
Active stress duration t_{act}	400.62 s	326.29 s	365.03 s
Peak activation stress $\sigma_0^{50\,ms}$	4.85 kPa	6.30 kPa	6.88 kPa
Exponential stress profile	**Solid**	**Kelvin-Voigt**	**Maxwell**
Elastic modulus of the cell E_c	845.48 Pa	796.72 Pa	861.02 Pa
Viscous modulus of the cell η_c	–	187.51 kPa · s	231.49 kPa · s
Stress activation time τ_{act}	61.41 s	56.37 s	56.25 s
Stress relaxation time τ_{rel}	115.16 s	110.61 s	118.29 s
Active stress duration t_{act}	311.59 s	281.04 s	290.23 s
Peak activation stress $\sigma_0^{50\,ms}$	6.01 kPa	7.94 kPa	8.19 kPa
Sigmoid stress profile	**Solid**	**Kelvin-Voigt**	**Maxwell**
Elastic modulus of the cell E_c	762.52 Pa	545.92 Pa	468.83 Pa
Viscous modulus of the cell η_c	–	84.63 kPa · s	68.75 kPa · s
Stress activation time τ_{act}	192.45 s	267.64 s	348.75 s
Stress relaxation time τ_{rel}	206.60 s	340.88 s	363.36 s
Center of activating sigmoid t_{act}	215.00 s	181.64 s	178.43 s
Center of relaxing sigmoid t_{rel}	190.49 s	185.29 s	174.58 s
Peak activation stress $\sigma_0^{50\,ms}$	25.96 kPa	27.65 kPa	31.11 kPa
Fixed parameter		**Value**	
Poisson's ratio of the cell ν_c		0.5	
Cell height h_c		1.0 μm	
Cell radius R_c		17.84 μm	
Thickness of the substrate h_s		50 μm	
Poisson's ratio of the substrate ν_s		0.5	
Elastic modulus of the substrate E_s		4.47 kPa	
Parameter from literature	**Value**		**Reference**
Stiffness of focal adhesion bonds k_a	2.5 nN/μm		*Balaban et al.* [2001]
Length of sarcomeric sub-unit l_{sarc}	1 μm		*Hu et al.* [2017]
Simulation parameter		**Value**	
Spatial resolution in x-direction Δx		0.7 μm	
Spatial resolution in y-direction Δy		0.7 μm	
Temporal resolution Δt		15 s	

Table A.5: Fit and fixed parameters of the strain energy fits from Figures 4.4 as well as default parameters for the Kelvin-Voigt model with sigmoid PA stress profile in Chapter 4.

Fit parameter	**1D model**	**2D model**
Force penetration length l_p	$10.77\,\mu$m	$1.78\,\mu$m
Activation stress σ_0	1.25 MPa	162.70 kPa
Fixed parameter	**1D model**	**2D model**
Platelet length l_0	$10.0\,\mu$m	–
Platelet width w_0	$10.0\,\mu$m	–
Platelet radius r_0	–	$5.0\,\mu$m
Thickness of the substrate h_s	$50\,\mu$m	
Elastic modulus of the substrate E_s	$19 - 83$ kPa	
Parameter from literature	**Value**	**Reference**
Platelet stiffness E_c	5 kPa	*Lam et al.* [2011]
Platelet height h_c	100 nm	*Aquino et al.* [2011]
Poisson's ratio of the cell ν_c	0.3	*Trickey et al.* [2006]
Poisson's ratio of the substrate ν_s	0.3	*Li et al.* [1993]
Implicit parameter	**Value**	
Adhesion layer stiffness density $\frac{N_\mathrm{a} k_\mathrm{a}}{L_\mathrm{c}^2}$	$0.3\,\mathrm{nN}/\mu\mathrm{m}^3$	
Simulation parameter	**2D model**	
Spatial resolution in x-direction Δx	$0.04\,\mu$m	
Spatial resolution in y-direction Δy	$0.04\,\mu$m	

Table A.6: Fit and fixed parameters of the total force vs. cell area fits from Figure 5.8. The adhesion layer stiffness density was estimated from the expression for the penetration length, given our assumed value for E_c, ν_c and h_c.

Default parameter		**Value**
Elastic modulus of the layer E_c		0.7 kPa
Contractile stress of the layer σ_0		1.0 kPa
Gaussian force in leader cells F_L		100 nN
Poisson's ratio of the layer ν_C		0.5
Thickness of the layer h_C		5.0 μm
Thickness of the substrate h_S		50 μm
Poisson's ratio of the substrate ν_S		0.5
Elastic modulus of the substrate E_S		11.0 kPa
Typical layer size L_L		1000 μm
Typical cell size L_C		20 μm
Force localization length l_p		167.4 μm
Fixed parameter (Drugs)	**Blebbistatin**	**Calyculin A**
Elastic modulus of the layer E_c	0.1 kPa	5.0 kPa
Contractile stress of the layer σ_0	0.5 kPa	5.0 kPa
Gaussian force in leader cells F_L	10 nN	400 nN
Force localization length l_p	63.3 μm	447.5 μm
Fixed parameter (Substrates)	$E_s = 4$ kPa	$E_s = 90$ kPa
Elastic modulus of the layer E_c	0.25 kPa	2.0 kPa
Contractile stress of the layer σ_0	0.8 kPa	3.0 kPa
Gaussian force in leader cells F_L	30 nN	200 nN
Force localization length l_p	100.1 μm	283.0 μm
Parameter from literature	**Value**	**Reference**
Stiffness of focal adhesion bonds k_a	2.5 $^{nN}/_{\mu m}$	*Balaban et al.* [2001]
Simulation parameter		**Value**
Layer size in x-direction L_x		550.0 μm
Layer size in y-direction L_y		2.0 mm
Spatial resolution in x-direction Δx		5.0 μm
Spatial resolution in y-direction Δy		5.0 μm

Table A.7: Parameters used to generate the curves from Figures 6.10 and 6.12. Parameters used to generate the curves from Figures 6.10 and 6.12

Filament Sensor parameter	**Value**
Minimal pixel brightness	0
Maximal pixel brightness	230
Factor of 8-neighbor Laplace filter	5
Size of Gaussian filter	2 pix
Size of directed Gaussian filter	2 pix
Minimum mean value of line sensor	30
Minimum filament length	50 pix
Length of straight pieces	10 pix
Tolerance	20
Default image parameter	**Value**
Image size	(600×600) pix
Patch side length	40 pix
Default microscopic material parameter	**Value**
Microscopic stiffness E^{I} of SF region	$1\,{}^{\mu N}/_{\mu \mathrm{m}}$
Microscopic stiffness E^{II} of void	$1\,{}^{nN}/_{\mu \mathrm{m}}$
Microscopic Poisson's ratio ν^{I} of SF region	0.5
Microscopic Poisson's ratio ν^{II} of void	0.5
Microscopic stress $\sigma_{\mathrm{m}}^{\mathrm{I}}$ of SF region	$1\,{}^{\mu N}/_{\mu \mathrm{m}}$
Microscopic stress $\sigma_{\mathrm{m}}^{\mathrm{II}}$ of void	0

Table A.8: Parameters used to establish a continuum model of the cellular actin CSK by exploiting its structural information, as described in Figure 8.1.

A.4 Analytical Calculations

A.4.1 Energy Contributions in the One-Dimensional Model of the Formation of Leader Cells

From Equation 6.52, we can calculate the energy U_Y which is stored in the elastic foundation:

$$
\begin{aligned}
U_\mathrm{Y} &= \frac{Y}{2}\int_{-L}^{L} u^2(x)\,\mathrm{d}x = Y\int_{0}^{L} u^2(x)\,\mathrm{d}x \\
&= \alpha\cdot\left\{\frac{1}{4}\left[\cosh\left(\frac{L-l_1}{l_\mathrm{p}}\right)-\cosh\left(\frac{L-l_2}{l_\mathrm{p}}\right)\right]^2\left[l_\mathrm{p}\sinh\left(\frac{2l_1}{l_\mathrm{p}}\right)-2l_1\right]\right. \\
&\quad+\frac{1}{4}\sinh^2\left(\frac{l_1}{l_\mathrm{p}}\right)\left[l_\mathrm{p}\sinh\left(\frac{2\,(L-l_1)}{l_\mathrm{p}}\right)-l_\mathrm{p}\sinh\left(\frac{2\,(L-l_2)}{l_\mathrm{p}}\right)+2\,(l_1-l_2)\right] \\
&\quad+\frac{1}{4}\cosh^2\left(\frac{L-l_2}{l_\mathrm{p}}\right)\left[l_\mathrm{p}\sinh\left(\frac{2l_2}{l_\mathrm{p}}\right)-l_\mathrm{p}\sinh\left(\frac{2l_1}{l_\mathrm{p}}\right)+2\,(l_1-l_2)\right] \\
&\quad-\frac{1}{2}\sinh\left(\frac{l_1}{l_\mathrm{p}}\right)\cosh\left(\frac{L-l_2}{l_\mathrm{p}}\right)\cdot \\
&\qquad\cdot\left[2\,(l_2-l_1)\sinh\left(\frac{L}{l_\mathrm{p}}\right)+l_\mathrm{p}\cosh\left(\frac{L-2l_2}{l_\mathrm{p}}\right)-l_\mathrm{p}\cosh\left(\frac{L-2l_1}{l_\mathrm{p}}\right)\right] \\
&\quad\left.+\frac{1}{4}\left[\sinh\left(\frac{l_1}{l_\mathrm{p}}\right)-\sinh\left(\frac{l_2}{l_\mathrm{p}}\right)\right]^2\left[l_\mathrm{p}\sinh\left(\frac{2\,(L-l_2)}{l_\mathrm{p}}\right)+2\,(L-l_2)\right]\right\}.
\end{aligned}
$$

The energy U_E which is stored in the elastic bar yields

$$
\begin{aligned}
U_\mathrm{E} &= \frac{E_\mathrm{c}}{2}\int_{-L}^{L} \epsilon^2(x)\,\mathrm{d}x = E_\mathrm{c}\int_{0}^{L} \epsilon^2(x)\,\mathrm{d}x \\
&= \alpha\cdot\left\{\frac{1}{4}\left[\cosh\left(\frac{L-l_1}{l_\mathrm{p}}\right)-\cosh\left(\frac{L-l_2}{l_\mathrm{p}}\right)\right]^2\left[l_\mathrm{p}\sinh\left(\frac{2l_1}{l_\mathrm{p}}\right)+2l_1\right]\right. \\
&\quad+\frac{1}{4}\sinh^2\left(\frac{l_1}{l_\mathrm{p}}\right)\left[l_\mathrm{p}\sinh\left(\frac{2\,(L-l_1)}{l_\mathrm{p}}\right)-l_\mathrm{p}\sinh\left(\frac{2\,(L-l_2)}{l_\mathrm{p}}\right)+2\,(l_2-l_1)\right] \\
&\quad+\frac{1}{4}\cosh^2\left(\frac{L-l_2}{l_\mathrm{p}}\right)\left[l_\mathrm{p}\sinh\left(\frac{2l_2}{l_\mathrm{p}}\right)-l_\mathrm{p}\sinh\left(\frac{2l_1}{l_\mathrm{p}}\right)+2\,(l_2-l_1)\right] \\
&\quad-\frac{1}{2}\sinh\left(\frac{l_1}{l_\mathrm{p}}\right)\cosh\left(\frac{L-l_2}{l_\mathrm{p}}\right)\cdot \\
&\qquad\cdot\left[2\,(l_1-l_2)\sinh\left(\frac{L}{l_\mathrm{p}}\right)+l_\mathrm{p}\cosh\left(\frac{L-2l_2}{l_\mathrm{p}}\right)-l_\mathrm{p}\cosh\left(\frac{L-2l_1}{l_\mathrm{p}}\right)\right] \\
&\quad\left.+\frac{1}{4}\left[\sinh\left(\frac{l_1}{l_\mathrm{p}}\right)-\sinh\left(\frac{l_2}{l_\mathrm{p}}\right)\right]^2\left[l_\mathrm{p}\sinh\left(\frac{2\,(L-l_2)}{l_\mathrm{p}}\right)-2\,(L-l_2)\right]\right\}.
\end{aligned}
$$

By adding U_Y and U_E, we get the total energy

$$
\begin{aligned}
U_\mathrm{tot} &= U_\mathrm{Y} + U_\mathrm{E} \\
&= \alpha l_\mathrm{p} \cdot \left\{ \frac{1}{2}\left[\cosh\left(\frac{L-l_1}{l_\mathrm{p}}\right) - \cosh\left(\frac{L-l_2}{l_\mathrm{p}}\right)\right]^2 \sinh\left(\frac{2l_1}{l_\mathrm{p}}\right) \right. \\
&\qquad + \frac{1}{2}\sinh^2\left(\frac{l_1}{l_\mathrm{p}}\right)\left[\sinh\left(\frac{2\,(L-l_1)}{l_\mathrm{p}}\right) - \sinh\left(\frac{2\,(L-l_2)}{l_\mathrm{p}}\right)\right] \\
&\qquad + \frac{1}{2}\cosh^2\left(\frac{L-l_2}{l_\mathrm{p}}\right)\left[\sinh\left(\frac{2l_2}{l_\mathrm{p}}\right) - \sinh\left(\frac{2l_1}{l_\mathrm{p}}\right)\right] \\
&\qquad - \sinh\left(\frac{l_1}{l_\mathrm{p}}\right)\cosh\left(\frac{L-l_2}{l_\mathrm{p}}\right)\left[\cosh\left(\frac{L-2l_2}{l_\mathrm{p}}\right) - \cosh\left(\frac{L-2l_1}{l_\mathrm{p}}\right)\right] \\
&\qquad \left. + \frac{1}{2}\left[\sinh\left(\frac{l_1}{l_\mathrm{p}}\right) - \sinh\left(\frac{l_2}{l_\mathrm{p}}\right)\right]^2 \sinh\left(\frac{2\,(L-l_2)}{l_\mathrm{p}}\right)\right\} \\
&= \frac{\alpha l_\mathrm{p}}{2} \cdot \left[2\sinh\left(\frac{L}{l_\mathrm{p}}\right) - \sinh\left(\frac{L-2l_1}{l_\mathrm{p}}\right)\right. \\
&\qquad \left. -4\cosh\left(\frac{L-l_2}{l_\mathrm{p}}\right)\sinh\left(\frac{l_1}{l_\mathrm{p}}\right) - \sinh\left(\frac{L-2l_2}{l_\mathrm{p}}\right)\right] \\
&= \sigma\left(l_1^-\right)\cdot u\left(l_1^-\right) - \sigma\left(l_1^+\right)\cdot u\left(l_1^+\right) + \sigma\left(l_2^-\right)\cdot u\left(l_2^-\right) - \sigma\left(l_2^+\right)\cdot u\left(l_2^+\right)\,, \qquad \text{(A.3a)}
\end{aligned}
$$

with the constant $\alpha = \sigma_0^2 / E_\mathrm{c}\cosh^2\left(\frac{L}{l_\mathrm{p}}\right)$ in all three cases.

Bibliography

Abdalrahman, T., L. Dubuis, J. Green, N. Davies, and T. Franz, Cellular mechanosensitivity to substrate stiffness decreases with increasing dissimilarity to cell stiffness, *Biomechanics and Modeling in Mechanobiology*, *16*, 2063–2075, 2017.

Abdessamad, Z., I. Kostin, G. Panasenko, and V. Smyshlyaev, Memory effect in homogenization of a viscoelastic kelvin–voigt model with time-dependent coefficients, *Mathematical Models and Methods in Applied Sciences*, *19*, 1603–1630, 2009.

Adrian, R. J., and J. Westerweel, *Particle image velocimetry*, 30, Cambridge University Press, 2011.

Akhmanova, A., and M. O. Steinmetz, Control of microtubule organization and dynamics: two ends in the limelight, *Nature reviews Molecular cell biology*, *16*, 711, 2015.

Albert, P. J., and U. S. Schwarz, Dynamics of cell shape and forces on micropatterned substrates predicted by a cellular potts model, *Biophysical journal*, *106*, 2340–2352, 2014.

Albert, P. J., and U. S. Schwarz, Dynamics of cell ensembles on adhesive micropatterns: bridging the gap between single cell spreading and collective cell migration, *PLoS computational biology*, *12*, e1004,863, 2016.

Alberts, B., D. Bray, J. Lewis, M. Raff, K. Roberts, and J. Watson, *Molecular Biology of the Cell*, 5th ed., Garland, 2007.

Alberts, B., A. Johnson, J. Lewis, D. Morgan, M. Raff, K. Roberts, and P. Walter, *Molecular Biology of the Cell, Sixth Edition*, Taylor & Francis Group, 2014.

Allen, D. M., The relationship between variable selection and data agumentation and a method for prediction, *Technometrics*, *16*, 125–127, 1974.

Allen, R. D., L. R. Zacharski, S. T. Widirstky, R. Rosenstein, L. M. Zaitlin, and D. R. Burgess, Transformation and motility of human platelets: details of the shape change and release reaction observed by optical and electron microscopy., *The Journal of cell biology*, *83*, 126–142, 1979.

Alnæs, M., et al., The FEniCS Project Version 1.5, *Archive of Numerical Software*, *3*, 9–23, 2015.

Andreassen, E., and C. S. Andreasen, How to determine composite material properties using numerical homogenization, *Computational Materials Science*, *83*, 488–495, 2014.

Aquino, D., A. Schönle, C. Geisler, C. v Middendorff, C. A. Wurm, Y. Okamura, T. Lang, S. W. Hell, and A. Egner, Two-color nanoscopy of three-dimensional volumes by 4pi detection of stochastically switched fluorophores, *Nature methods*, *8*, 353–359, 2011.

Ashkin, A., J. M. Dziedzic, J. Bjorkholm, and S. Chu, Observation of a single-beam gradient force optical trap for dielectric particles, *Optics letters*, *11*, 288–290, 1986.

Auernheimer, V., L. A. Lautscham, M. Leidenberger, O. Friedrich, B. Kappes, B. Fabry, and W. H. Goldmann, Vinculin phosphorylation at residues y100 and y1065 is required for cellular force transmission, *J Cell Sci*, *128*, 3435–3443, 2015.

Balaban, N. Q., et al., Force and focal adhesion assembly: a close relationship studied using elastic micropatterned substrates, *Nature cell biology*, *3*, 466–472, 2001.

Banerjee, S., and M. Marchetti, Contractile stresses in cohesive cell layers on finite-thickness substrates, *Physical review letters*, *109*, 108,101, 2012.

Bar-Ziv, R., T. Tlusty, E. Moses, S. A. Safran, and A. Bershadsky, Pearling in cells: a clue to understanding cell shape, *Proceedings of the National Academy of Sciences*, *96*, 10,140–10,145, 1999.

Barber, C. B., D. P. Dobkin, and H. Huhdanpaa, The quickhull algorithm for convex hulls, *ACM Transactions on Mathematical Software (TOMS)*, *22*, 469–483, 1996.

Barnes, J., and D. Allan, A statistical model of flicker noise, *Proceedings of the IEEE*, *54*, 176–178, 1966.

Bauer, F., and M. A. Lukas, Comparing parameter choice methods for regularization of ill-posed problems, *Mathematics and Computers in Simulation*, *81*, 1795–1841, 2011.

Beach, J. R., L. Shao, K. Remmert, D. Li, E. Betzig, and J. A. Hammer III, Nonmuscle myosin ii isoforms coassemble in living cells, *Current Biology*, *24*, 1160–1166, 2014.

Bensoussan, A., J.-L. Lions, and G. Papanicolaou, Asymptotic methods for periodic structures, *Stud. Math. Appl*, *5*, 1978.

Bergert, M., et al., Confocal reference free traction force microscopy, *Nature communications*, *7*, 12,814, 2016.

Besser, A., J. Colombelli, E. Stelzer, and U. Schwarz, Viscoelastic response of contractile filament bundles, *Physical Review E*, *83*, 051,902, 2011.

Billington, N., A. Wang, J. Mao, R. S. Adelstein, and J. R. Sellers, Characterization of three full-length human nonmuscle myosin ii paralogs, *Journal of Biological Chemistry*, *288*, 33,398–33,410, 2013.

Bischofs, I., F. Klein, D. Lehnert, M. Bastmeyer, and U. Schwarz, Filamentous network mechanics and active contractility determine cell and tissue shape, *Biophysical Journal*, *95*, 3488–3496, 2008.

Bischofs, I. B., S. S. Schmidt, and U. S. Schwarz, Effect of adhesion geometry and rigidity on cellular force distributions, *Physical review letters*, *103*, 048,101, 2009.

Blanch-Mercader, C., R. Vincent, E. Bazellières, X. Serra-Picamal, X. Trepat, and J. Casademunt, Effective viscosity and dynamics of spreading epithelia: a solvable model, *Soft matter*, *13*, 1235–1243, 2017.

Blanchoin, L., R. Boujemaa-Paterski, C. Sykes, and J. Plastino, Actin dynamics, architecture, and mechanics in cell motility, *Physiological reviews*, *94*, 235–263, 2014.

Boal, D., *Mechanics of the Cell*, Cambridge University Press, 2012.

Bouguet, J.-Y., Pyramidal implementation of the affine lucas kanade feature tracker description of the algorithm, *Intel Corporation*, *5*, 4, 2001.

Bradski, G., The OpenCV Library, *Dr. Dobb's Journal of Software Tools*, 2000.

Brand, C. A., Forces and flow of contractile networks, Ph.D. thesis, 2017.

Brand, C. A., M. Linke, K. Weißenbruch, B. Richter, M. Bastmeyer, and U. S. Schwarz, Tension and elasticity contribute to fibroblast cell shape in three dimensions, *Biophysical journal*, *113*, 770–774, 2017.

Brask, J. B., G. Singla-Buxarrais, M. Uroz, R. Vincent, and X. Trepat, Compressed sensing traction force microscopy, *Acta biomaterialia*, *26*, 286–294, 2015.

Brückner, B. R., and A. Janshoff, Elastic properties of epithelial cells probed by atomic force microscopy, *Biochimica et Biophysica Acta (BBA)-Molecular Cell Research*, *1853*, 3075–3082, 2015.

Brugués, A., et al., Forces driving epithelial wound healing, *Nature physics*, *10*, 683–690, 2014.

Burnette, D. T., S. Manley, P. Sengupta, R. Sougrat, M. W. Davidson, B. Kachar, and J. Lippincott-Schwartz, A role for actin arcs in the leading-edge advance of migrating cells, *Nature cell biology*, *13*, 371, 2011.

Burnette, D. T., et al., A contractile and counterbalancing adhesion system controls the 3d shape of crawling cells, *J Cell Biol*, pp. jcb–201311,104, 2014.

Burridge, K., and C. Guilluy, Focal adhesions, stress fibers and mechanical tension, *Experimental cell research*, *343*, 14–20, 2016.

Burridge, K., and E. Wittchen, The tension mounts: stress fibers as force-generating mechanotransducers, *The Journal of cell biology*, *200*, 9–19, 2013.

Butler, J., I. Tolić-Nørrelykke, B. Fabry, and J. Fredberg, Traction fields, moments, and strain energy that cells exert on their surroundings, *American Journal of Physiology-Cell Physiology*, *282*, C595–C605, 2002.

Caillerie, D., A. Mourad, and A. Raoult, Discrete homogenization in graphene sheet modeling, *Journal of Elasticity*, *84*, 33–68, 2006.

Campàs, O., et al., Quantifying cell-generated mechanical forces within living embryonic tissues, *Nature methods*, *11*, 183, 2014.

Capdeville, Y., L. Guillot, and J.-J. Marigo, 1-d non-periodic homogenization for the seismic wave equation, *Geophysical Journal International*, *181*, 897–910, 2010.

Carr, M. E., and S. L. Zekert, Measurement of platelet-mediated force development during plasma clot formation, *The American journal of the medical sciences*, *302*, 13–18, 1991.

Chavarría-Krauser, A., and M. Ptashnyk, Homogenization of long-range auxin transport in plant tissues, *Nonlinear Analysis: Real World Applications*, *11*, 4524–4532, 2010.

Chizhik, A. M., et al., Dual-color metal-induced and förster resonance energy transfer for cell nanoscopy, *Molecular biology of the cell*, *29*, 846–851, 2018.

Chrzanowska-Wodnicka, M., and K. Burridge, Rho-stimulated contractility drives the formation of stress fibers and focal adhesions., *The Journal of cell biology*, *133*, 1403–1415, 1996.

Chu, T., W. Ranson, and M. A. Sutton, Applications of digital-image-correlation techniques to experimental mechanics, *Experimental mechanics*, *25*, 232–244, 1985.

Cioranescu, D., and P. Donato, *An introduction to homogenization*, vol. 8, Oxford University Press Oxford, 1999.

Clough, R. W., and J. L. Tocher, Finite element stiffness matrices for analysis of plate bending(finite element stiffness matrixes for analysis of plate bending), *Conference on Matrix Methods in Structural Mechanics*, pp. 515–545, 1965.

Cohen, J. E., and P. Horowitz, Paradoxical behaviour of mechanical and electrical networks, *Nature*, *352*, 699–701, 1991.

Colin-York, H., D. Shrestha, J. H. Felce, D. Waithe, E. Moeendarbary, S. J. Davis, C. Eggeling, and M. Fritzsche, Super-resolved traction force microscopy (stfm), *Nano letters*, *16*, 2633–2638, 2016.

Colombelli, J., et al., Mechanosensing in actin stress fibers revealed by a close correlation between force and protein localization, *Journal of cell science*, *122*, 1665–1679, 2009.

Coughlin, M. F., and D. Stamenović, A prestressed cable network model of the adherent cell cytoskeleton, *Biophysical journal*, *84*, 1328–1336, 2003.

Crick, F., and A. Hughes, The physical properties of cytoplasm, *Experimental Cell Research*, *1*, 37–80, 1950.

Deguchi, S., T. Ohashi, and M. Sato, Tensile properties of single stress fibers isolated from cultured vascular smooth muscle cells, *Journal of biomechanics*, *39*, 2603–2610, 2006.

del Álamo, J., R. Meili, B. Álvarez-González, B. Alonso-Latorre, E. Bastounis, R. Firtel, and J. Lasheras, Three-dimensional quantification of cellular traction forces and mechanosensing of thin substrata by fourier traction force microscopy, *PloS one*, *8*, e69,850, 2013.

Dembo, M., and Y.-L. Wang, Stresses at the cell-to-substrate interface during locomotion of fibroblasts, *Biophysical journal*, *76*, 2307–2316, 1999.

Deshpande, V., R. McMeeking, and A. Evans, A bio-chemo-mechanical model for cell contractility, *Proceedings of the National Academy of Sciences*, *103*, 14,015–14,020, 2006.

Deshpande, V., R. McMeeking, and A. Evans, A model for the contractility of the cytoskeleton including the effects of stress-fibre formation and dissociation, *Proceedings of the Royal Society A: Mathematical, Physical and Engineering Science*, *463*, 787–815, 2007.

Edwards, C., and U. Schwarz, Force localization in contracting cell layers, *Physical review letters*, *107*, 128,101, 2011.

Eltzner, B., C. Wollnik, C. Gottschlich, S. Huckemann, and F. Rehfeldt, The filament sensor for near real-time detection of cytoskeletal fiber structures, *PloS one*, *10*, e0126,346, 2015.

Engler, A. J., S. Sen, H. L. Sweeney, and D. E. Discher, Matrix elasticity directs stem cell lineage specification, *Cell*, *126*, 677–689, 2006.

Étienne, J., J. Fouchard, D. Mitrossilis, N. Bufi, P. Durand-Smet, and A. Asnacios, Cells as liquid motors: Mechanosensitivity emerges from collective dynamics of actomyosin cortex, *Proceedings of the National Academy of Sciences*, *112*, 2740–2745, 2015.

Fabian, L., J. Troscianczuk, and A. Forer, Calyculin a, an enhancer of myosin, speeds up anaphase chromosome movement, *Cell & chromosome*, *6*, 1, 2007.

Farhadifar, R., J.-C. Röper, B. Aigouy, S. Eaton, and F. Jülicher, The influence of cell mechanics, cell-cell interactions, and proliferation on epithelial packing, *Current Biology*, *17*, 2095–2104, 2007.

Finer, J. T., R. M. Simmons, and J. A. Spudich, Single myosin molecule mechanics: piconewton forces and nanometre steps, *Nature*, *368*, 113, 1994.

Fish, J., P. Nayak, and M. H. Holmes, Microscale reduction error indicators and estimators for a periodic heterogeneous medium, *Computational Mechanics*, *14*, 323–338, 1994.

Fish, J., W. Chen, and G. Nagai, Non-local dispersive model for wave propagation in heterogeneous media: multi-dimensional case, *International Journal for Numerical Methods in Engineering*, *54*, 347–363, 2002.

Fortun, D., P. Bouthemy, and C. Kervrann, Optical flow modeling and computation: a survey, *Computer Vision and Image Understanding*, *134*, 1–21, 2015.

Francfort, G. A., and P. M. Suquet, Homogenization and mechanical dissipation in thermoviscoelasticity, *Archive for Rational Mechanics and Analysis*, *96*, 265–293, 1986.

Franck, C., S. A. Maskarinec, D. A. Tirrell, and G. Ravichandran, Three-dimensional traction force microscopy: a new tool for quantifying cell-matrix interactions, *PloS one*, *6*, e17,833, 2011.

Friedl, P., and D. Gilmour, Collective cell migration in morphogenesis, regeneration and cancer, *Nature reviews Molecular cell biology*, *10*, 445–457, 2009.

Fuchs, J.-J., Spread representations, in *Signals, Systems and Computers (ASILOMAR), 2011 Conference Record of the Forty Fifth Asilomar Conference on*, pp. 814–817, IEEE, 2011.

Fürthauer, S., M. Strempel, S. Grill, and F. Jülicher, Active chiral processes in thin films, *Physical review letters*, *110*, 048,103, 2013.

Geisser, S., The predictive sample reuse method with applications, *Journal of the American statistical Association*, *70*, 320–328, 1975.

Gittes, F., B. Mickey, J. Nettleton, and J. Howard, Flexural rigidity of microtubules and actin filaments measured from thermal fluctuations in shape., *The Journal of cell biology*, *120*, 923–934, 1993.

Golub, G. H., M. Heath, and G. Wahba, Generalized cross-validation as a method for choosing a good ridge parameter, *Technometrics*, *21*, 215–223, 1979.

Golub, G. H., P. C. Hansen, and D. P. O'Leary, Tikhonov regularization and total least squares, *SIAM Journal on Matrix Analysis and Applications*, *21*, 185–194, 1999.

Grashoff, C., et al., Measuring mechanical tension across vinculin reveals regulation of focal adhesion dynamics, *Nature*, *466*, 263, 2010.

Guedes, J., and N. Kikuchi, Preprocessing and postprocessing for materials based on the homogenization method with adaptive finite element methods, *Computer methods in applied mechanics and engineering*, *83*, 143–198, 1990.

Gutzman, J. H., and H. Sive, Epithelial relaxation mediated by the myosin phosphatase regulator mypt1 is required for brain ventricle lumen expansion and hindbrain morphogenesis, *Development*, *137*, 795–804, 2010.

Haeger, A., K. Wolf, M. M. Zegers, and P. Friedl, Collective cell migration: guidance principles and hierarchies, *Trends in cell biology*, *25*, 556–566, 2015.

Haghparast, S. M. A., T. Kihara, and J. Miyake, Distinct mechanical behavior of hek293 cells in adherent and suspended states, *PeerJ*, *3*, e1131, 2015.

Hakim, V., and P. Silberzan, Collective cell migration: a physics perspective, *Reports on progress in physics. Physical Society (Great Britain)*, *80*, 076,601, 2017.

Han, S., Y. Oak, A. Groisman, and G. Danuser, Traction microscopy to identify force modulation in subresolution adhesions, *Nature methods*, *12*, 653–656, 2015.

Hansen, P. C., Analysis of discrete ill-posed problems by means of the l-curve, *SIAM review*, *34*, 561–580, 1992.

Hansen, P. C., Regularization tools: A matlab package for analysis and solution of discrete ill-posed problems, *Numerical algorithms*, *6*, 1–35, 1994.

Hansen, P. C., *The L-curve and its use in the numerical treatment of inverse problems*, IMM, Department of Mathematical Modelling, Technical Universityof Denmark, 1999.

Hansen, P. C., M. E. Kilmer, and R. H. Kjeldsen, Exploiting residual information in the parameter choice for discrete ill-posed problems, *BIT Numerical Mathematics*, *46*, 41–59, 2006.

Harris, A. K., P. Wild, D. Stopak, et al., Silicone rubber substrata: a new wrinkle in the study of cell locomotion, *Science*, *208*, 177–179, 1980.

Harris, F. J., On the use of windows for harmonic analysis with the discrete fourier transform, *Proceedings of the IEEE*, *66*, 51–83, 1978.

Hartsock, A., and W. J. Nelson, Adherens and tight junctions: structure, function and connections to the actin cytoskeleton, *Biochimica et Biophysica Acta (BBA)-Biomembranes*, *1778*, 660–669, 2008.

Hassani, B., and E. Hinton, A review of homogenization and topology opimization ii—analytical and numerical solution of homogenization equations, *Computers & structures*, *69*, 719–738, 1998.

Henriques, S. S., R. Sandmann, A. Strate, and S. Köster, Force field evolution during human blood platelet activation, *J Cell Sci*, *125*, 3914–3920, 2012.

Herrmann, H., H. Bär, L. Kreplak, S. V. Strelkov, and U. Aebi, Intermediate filaments: from cell architecture to nanomechanics, *Nature Reviews Molecular Cell Biology*, *8*, 562, 2007.

Hill, A., The mechanical efficiency of frog's muscle, *Proceedings of the Royal Society of London. Series B, Biological Sciences*, pp. 434–451, 1939.

Hinsch, K. D., Holographic particle image velocimetry, *Measurement Science and Technology*, *13*, R61, 2002.

Hitz, M., J. Grabmeier, E. Kaltofen, and V. Weispfenning, *Computer Algebra Handbook: Foundations · Applications · Systems*, SpringerLink : Bücher, Springer Berlin Heidelberg, 2012.

Hohmann, A., and P. Deuflhard, *Numerical Analysis in Modern Scientific Computing: An Introduction*, Texts in Applied Mathematics, Springer New York, 2003.

Holenstein, C. N., U. Silvan, and J. G. Snedeker, High-resolution traction force microscopy on small focal adhesions-improved accuracy through optimal marker distribution and optical flow tracking, *Scientific Reports*, *7*, 2017.

Hornung, U., *Homogenization and porous media*, vol. 6, Springer Science & Business Media, 1997.

Hotulainen, P., and P. Lappalainen, Stress fibers are generated by two distinct actin assembly mechanisms in motile cells, *The Journal of cell biology*, *173*, 383–394, 2006.

Howell, P., G. Kozyreff, and J. Ockendon, *Applied Solid Mechanics*, Cambridge Texts in Applied Mathematics, Cambridge University Press, 2009.

Hu, S., et al., Long-range self-organization of cytoskeletal myosin ii filament stacks, *Nature cell biology*, *19*, 133–141, 2017.

Huang, J., L. Qin, X. Peng, T. Zhu, C. Xiong, Y. Zhang, and J. Fang, Cellular traction force recovery: An optimal filtering approach in two-dimensional fourier space, *Journal of theoretical biology*, *259*, 811–819, 2009.

Huber, F., A. Boire, M. P. Lopez, and G. H. Koenderink, Cytoskeletal crosstalk: when three different personalities team up, *Current opinion in cell biology*, *32*, 39–47, 2015.

Hufnagel, L., A. A. Teleman, H. Rouault, S. M. Cohen, and B. I. Shraiman, On the mechanism of wing size determination in fly development, *Proceedings of the National Academy of Sciences*, *104*, 3835–3840, 2007.

Hunter, J. D., Matplotlib: A 2d graphics environment, *Computing In Science & Engineering*, *9*, 90–95, 2007.

Iskratsch, T., H. Wolfenson, and M. Sheetz, Appreciating force and shape – the rise of mechanotransduction in cell biology, *Nature reviews. Molecular cell biology*, *15*, 825–833, 2014.

Jégou, H., T. Furon, and J.-J. Fuchs, Anti-sparse coding for approximate nearest neighbor search, *arXiv preprint arXiv:1110.3767*, 2011.

Jen, C. J., and L. V. McIntire, The structural properties and contractile force of a clot, *Cytoskeleton*, *2*, 445–455, 1982.

John, K., D. Caillerie, P. Peyla, A. Raoult, and C. Misbah, Nonlinear elasticity of cross-linked networks, *Physical Review E*, *87*, 042,721, 2013.

Jones, E., T. Oliphant, and P. Peterson, Scipy: open source scientific tools for python, 2014.

Käfer, J., T. Hayashi, A. F. Marée, R. W. Carthew, and F. Graner, Cell adhesion and cortex contractility determine cell patterning in the drosophilaretina, *Proceedings of the National Academy of Sciences*, *104*, 18,549–18,554, 2007.

Kanchanawong, P., G. Shtengel, A. M. Pasapera, E. B. Ramko, M. W. Davidson, H. F. Hess, and C. M. Waterman, Nanoscale architecture of integrin-based cell adhesions, *Nature*, *468*, 580, 2010.

Karunarathne, W. A., P. R. O'Neill, and N. Gautam, Subcellular optogenetics–controlling signaling and single-cell behavior, *J Cell Sci*, *128*, 15–25, 2015.

Kassianidou, E., C. A. Brand, U. S. Schwarz, and S. Kumar, Geometry and network connectivity govern the mechanics of stress fibers, *Proceedings of the National Academy of Sciences*, p. 201606649, 2017.

Kaunas, R., H. Hsu, and S. Deguchi, Sarcomeric model of stretch-induced stress fiber reorganization, *Cell Health Cytoskeleton*, *3*, 13–22, 2011.

Kennedy, M. J., R. M. Hughes, L. A. Peteya, J. W. Schwartz, M. D. Ehlers, and C. L. Tucker, Rapid blue-light-mediated induction of protein interactions in living cells, *Nature methods*, *7*, 973–975, 2010.

Kojima, H., A. Ishijima, and T. Yanagida, Direct measurement of stiffness of single actin filaments with and without tropomyosin by in vitro nanomanipulation, *Proceedings of the National Academy of Sciences*, *91*, 12,962–12,966, 1994.

Kovács, M., J. Tóth, C. Hetényi, A. Málnási-Csizmadia, and J. R. Sellers, Mechanism of blebbistatin inhibition of myosin ii, *Journal of Biological Chemistry*, *279*, 35,557–35,563, 2004.

Kumar, S., I. Z. Maxwell, A. Heisterkamp, T. R. Polte, T. P. Lele, M. Salanga, E. Mazur, and D. E. Ingber, Viscoelastic retraction of single living stress fibers and its impact on cell shape, cytoskeletal organization, and extracellular matrix mechanics, *Biophysical journal*, *90*, 3762–3773, 2006.

Ladoux, B., R.-M. Mège, and X. Trepat, Front–rear polarization by mechanical cues: From single cells to tissues, *Trends in cell biology*, *26*, 420–433, 2016.

Lam, W. A., O. Chaudhuri, A. Crow, K. D. Webster, A. Kita, J. Huang, D. A. Fletcher, et al., Mechanics and contraction dynamics of single platelets and implications for clot stiffening, *Nature materials*, *10*, 61–66, 2011.

Landau, L. D., and E. Lifshitz, Theory of elasticity, vol. 7, *Course of Theoretical Physics*, *3*, 109, 1986.

Langanger, G., M. Moeremans, G. Daneels, A. Sobieszek, M. De Brabander, and J. De Mey, The molecular organization of myosin in stress fibers of cultured cells., *The Journal of cell biology*, *102*, 200–209, 1986.

Legant, W. R., J. S. Miller, B. L. Blakely, D. M. Cohen, G. M. Genin, and C. S. Chen, Measurement of mechanical tractions exerted by cells in three-dimensional matrices, *Nature methods*, *7*, 969, 2010.

Lennon, J. J., Red-shifts and red herrings in geographical ecology, *Ecography*, *23*, 101–113, 2000.

Letort, G., H. Ennomani, L. Gressin, M. Théry, and L. Blanchoin, Dynamic reorganization of the actin cytoskeleton, *F1000Research*, *4*, 2015.

Li, Y., Z. Hu, and C. Li, New method for measuring poisson's ratio in polymer gels, *Journal of Applied Polymer Science*, *50*, 1107–1111, 1993.

Li, Z., E. S. Kim, and E. L. Bearer, Arp2/3 complex is required for actin polymerization during platelet shape change, *Blood*, *99*, 4466–4474, 2002.

Linke, M., Image analysis and modeling of cellular organization in micropatterned environments, Ph.D. thesis, 2017.

Livne, A., and B. Geiger, The inner workings of stress fibers- from contractile machinery to focal adhesions and back, *J Cell Sci*, *129*, 1293–1304, 2016.

Löber, J., F. Ziebert, and I. S. Aranson, Modeling crawling cell movement on soft engineered substrates, *Soft matter*, *10*, 1365–1373, 2014.

Lodish, H., A. Berk, P. Matsudaira, C. A. Kaiser, M. Krieger, and M. P. Scott, *Molecular Cell Biology, Fifth Edition*, Palgrave Macmillan, 2004.

Lourenco, L., and A. Krothapalli, On the accuracy of velocity and vorticity measurements with piv, *Experiments in fluids*, *18*, 421–428, 1995.

Lucas, B. D., T. Kanade, et al., An iterative image registration technique with an application to stereo vision, 1981.

Luo, T., K. Mohan, P. Iglesias, and D. Robinson, Molecular mechanisms of cellular mechanosensing, *Nature materials*, *12*, 1064–1071, 2013.

Marée, A. F., A. Jilkine, A. Dawes, V. A. Grieneisen, and L. Edelstein-Keshet, Polarization and movement of keratocytes: a multiscale modelling approach, *Bulletin of mathematical biology*, *68*, 1169–1211, 2006.

Marée, A. F., V. A. Grieneisen, and L. Edelstein-Keshet, How cells integrate complex stimuli: the effect of feedback from phosphoinositides and cell shape on cell polarization and motility, *PLoS computational biology*, *8*, e1002,402, 2012.

Mark, S., R. Shlomovitz, N. S. Gov, M. Poujade, E. Grasland-Mongrain, and P. Silberzan, Physical model of the dynamic instability in an expanding cell culture, *Biophysical journal*, *98*, 361–370, 2010.

Marti, O., et al., Scanning probe microscopy of biological samples and other surfaces, *Journal of microscopy*, *152*, 803–809, 1988.

Martiel, J.-L., A. Leal, L. Kurzawa, M. Balland, I. Wang, T. Vignaud, Q. Tseng, and M. Théry, Measurement of cell traction forces with imagej, *Methods in cell biology*, *125*, 269–287, 2015.

Maruthamuthu, V., B. Sabass, U. S. Schwarz, and M. L. Gardel, Cell-ecm traction force modulates endogenous tension at cell–cell contacts, *Proceedings of the National Academy of Sciences*, *108*, 4708–4713, 2011.

Maskarinec, S. A., C. Franck, D. A. Tirrell, and G. Ravichandran, Quantifying cellular traction forces in three dimensions, *Proceedings of the National Academy of Sciences*, *106*, 22,108–22,113, 2009.

Mattila, P. K., and P. Lappalainen, Filopodia: molecular architecture and cellular functions, *Nature reviews Molecular cell biology*, *9*, 446–454, 2008.

Mayor, R., and S. Etienne-Manneville, The front and rear of collective cell migration, *Nature Reviews Molecular Cell Biology*, *17*, 97–109, 2016.

Merkel, R., N. Kirchgeßner, C. M. Cesa, and B. Hoffmann, Cell force microscopy on elastic layers of finite thickness, *Biophysical journal*, *93*, 3314–3323, 2007.

Mertz, A. F., et al., Scaling of traction forces with the size of cohesive cell colonies, *Physical review letters*, *108*, 198,101, 2012.

Mertz, A. F., et al., Cadherin-based intercellular adhesions organize epithelial cell–matrix traction forces, *Proceedings of the National Academy of Sciences*, *110*, 842–847, 2013.

Michaelis, L., and M. L. Menten, Die kinetik der inwertinwirkung, *Biochem.*, pp. 333–369, 1913.

Michelson, A., *Platelets*, Academic Press, 2012.

Mitrossilis, D., J. Fouchard, A. Guiroy, N. Desprat, N. Rodriguez, B. Fabry, and A. Asnacios, Single-cell response to stiffness exhibits muscle-like behavior, *Proceedings of the National Academy of Sciences*, *106*, 18,243–18,248, 2009.

Mourad, A., Description topologique de l'architecture fibreuse et modélisation mécanique du myocarde, Ph.D. thesis, Institut National Polytechnique de Grenoble-INPG, 2003.

Nelder, J. A., and R. Mead, A simplex method for function minimization, *The computer journal*, *7*, 308–313, 1965.

Nelson, C. M., R. P. Jean, J. L. Tan, W. F. Liu, N. J. Sniadecki, A. A. Spector, and C. S. Chen, Emergent patterns of growth controlled by multicellular form and mechanics, *Proceedings of the National Academy of Sciences of the United States of America*, *102*, 11,594–11,599, 2005.

Neuman, K. C., and A. Nagy, Single-molecule force spectroscopy: optical tweezers, magnetic tweezers and atomic force microscopy, *Nature methods*, *5*, 491, 2008.

Nicolaou, Z. G., and A. E. Motter, Mechanical metamaterials with negative compressibility transitions, *Nature materials*, *11*, 608, 2012.

Niederman, R., and T. D. Pollard, Human platelet myosin. ii. in vitro assembly and structure of myosin filaments., *The Journal of Cell Biology*, *67*, 72–92, 1975.

Norstrom, M. F., P. A. Smithback, and R. S. Rock, Unconventional processive mechanics of non-muscle myosin iib, *Journal of Biological Chemistry*, *285*, 26,326–26,334, 2010.

Novozhilov, V., Theory of elasticity [in russian], sudpromgiz, leningrad (1958), *Google Scholar*, 1961.

Oakes, P., Y. Beckham, J. Stricker, and M. Gardel, Tension is required but not sufficient for focal adhesion maturation without a stress fiber template, *The Journal of cell biology*, *196*, 363–374, 2012.

Oakes, P., S. Banerjee, M. Marchetti, and M. Gardel, Geometry regulates traction stresses in adherent cells, *Biophysical journal*, *107*, 825–833, 2014.

Oakes, P. W., E. Wagner, C. A. Brand, D. Probst, M. Linke, U. S. Schwarz, M. Glotzer, and M. L. Gardel, Optogenetic control of rhoa reveals zyxin-mediated elasticity of stress fibres, *Nature Communications*, *8*, ncomms15,817, 2017.

Orlik, J., Homogenization for viscoelasticity of the integral type with aging and shrinkage, 1998.

Palencia, E. S., *Non-homogeneous media and vibration theory*, Springer-Verlag, 1980.

Paluch, E. K., et al., Mechanotransduction: use the force (s), *BMC biology*, *13*, 47, 2015.

Papanicolaou, G., and S. Varadhan, Boundary value problems with rapidly oscillating random coefficients, in *Proceedings of Conference of Random Fields, Esztergom, Hungary, 27*, pp. 835–873, Seria Colloquia Mathematica Societatis Janos Bolyai, 1979.

Peterson, L. J., Z. Rajfur, A. S. Maddox, C. D. Freel, Y. Chen, M. Edlund, C. Otey, and K. Burridge, Simultaneous stretching and contraction of stress fibers in vivo, *Molecular biology of the cell*, *15*, 3497–3508, 2004.

Phillips, D. L., A technique for the numerical solution of certain integral equations of the first kind, *Journal of the ACM (JACM)*, *9*, 84–97, 1962.

Pleines, I., et al., Megakaryocyte-specific rhoa deficiency causes macrothrombocytopenia and defective platelet activation in hemostasis and thrombosis, *Blood*, *119*, 1054–1063, 2012.

Plotnikov, S. V., B. Sabass, U. S. Schwarz, and C. M. Waterman, High-resolution traction force microscopy, *Methods in cell biology*, *123*, 367, 2014.

Polacheck, W. J., and C. S. Chen, Measuring cell-generated forces: a guide to the available tools, *Nature methods*, *13*, 415, 2016.

Pollard, T. D., Rate constants for the reactions of atp-and adp-actin with the ends of actin filaments., *The Journal of cell biology*, *103*, 2747–2754, 1986.

Prost, J., F. Jülicher, and J.-F. Joanny, Active gel physics, *Nature Physics*, *11*, 111–117, 2015.

Pulli, K., A. Baksheev, K. Kornyakov, and V. Eruhimov, Real-time computer vision with opencv, *Communications of the ACM*, *55*, 61–69, 2012.

Purves, W., D. Sadava, G. Orians, and H. H.C., *Life: Science of Biology*, Life : The science of biology, W.H. Freeman, 2003.

Qiu, Y., et al., Platelet mechanosensing of substrate stiffness during clot formation mediates adhesion, spreading, and activation, *Proceedings of the National Academy of Sciences*, *111*, 14,430–14,435, 2014.

Raffel, I. M., C. E. Willert, and J. Kompenhans, Image evaluation methods for piv, in *Particle Image Velocimetry*, pp. 105–146, Springer, 1998.

Rausch, S., T. Das, J. R. Soiné, T. W. Hofmann, C. H. Boehm, U. S. Schwarz, H. Boehm, and J. P. Spatz, Polarizing cytoskeletal tension to induce leader cell formation during collective cell migration, *Biointerphases*, *8*, 32, 2013.

Reffay, M., M.-C. Parrini, O. Cochet-Escartin, B. Ladoux, A. Buguin, S. Coscoy, F. Amblard, J. Camonis, and P. Silberzan, Interplay of rhoa and mechanical forces in collective cell migration driven by leader cells, *Nature cell biology*, *16*, 217–223, 2014.

Reinhart-King, C. A., M. Dembo, and D. A. Hammer, The dynamics and mechanics of endothelial cell spreading, *Biophysical journal*, *89*, 676–689, 2005.

Ridley, A. J., and A. Hall, The small gtp-binding protein rho regulates the assembly of focal adhesions and actin stress fibers in response to growth factors, *Cell*, *70*, 389–399, 1992.

Roca-Cusachs, P., V. Conte, and X. Trepat, Quantifying forces in cell biology, *Nature cell biology*, *19*, 742, 2017.

Rozario, T., and D. W. DeSimone, The extracellular matrix in development and morphogenesis: a dynamic view, *Developmental biology*, *341*, 126–140, 2010.

Russell, R. J., A. Y. Grubbs, S. P. Mangroo, S. E. Nakasone, R. B. Dickinson, and T. P. Lele, Sarcomere length fluctuations and flow in capillary endothelial cells, *Cytoskeleton*, *68*, 150–156, 2011.

Sabass, B., M. L. Gardel, C. M. Waterman, and U. S. Schwarz, High resolution traction force microscopy based on experimental and computational advances, *Biophysical Journal*, *94*, 207–220, 2008.

Saha, A., M. Nishikawa, M. Behrndt, C.-P. Heisenberg, F. Jülicher, and S. W. Grill, Determining physical properties of the cell cortex, *Biophysical journal*, *110*, 1421–1429, 2016.

Sánchez-Palencia, E., Non-homogeneous media and vibration theory, *Lecture notes in physics*, *127*, 1980.

Sanchez-Palencia, E., Homogenization method for the study of composite media, in *Asymptotic Analysis II—*, pp. 192–214, Springer, 1983.

Sandmann, R., and S. Köster, Topographic cues reveal two distinct spreading mechanisms in blood platelets, *Scientific reports*, *6*, 22,357, 2016.

Sandmann, R., S. S. G. Henriques, F. Rehfeldt, and S. Köster, Micro-topography influences blood platelet spreading, *Soft Matter*, *10*, 2365–2371, 2014.

Scales, J. A., A. Gersztenkorn, and S. Treitel, Fast ip solution of large, sparse, linear systems: Application to seismic travel time tomography, *Journal of Computational Physics*, *75*, 314–333, 1988.

Scarano, F., and M. L. Riethmuller, Iterative multigrid approach in piv image processing with discrete window offset, *Experiments in Fluids*, *26*, 513–523, 1999.

Scheiwe, A., S. Frank, T. Autenrieth, M. Bastmeyer, and M. Wegener, Subcellular stretch-induced cytoskeletal response of single fibroblasts within 3d designer scaffolds, *Biomaterials*, *44*, 186–194, 2015.

Schillers, H., M. Wälte, K. Urbanova, and H. Oberleithner, Real-time monitoring of cell elasticity reveals oscillating myosin activity, *Biophysical journal*, *99*, 3639–3646, 2010.

Schlosser, F., F. Rehfeldt, and C. F. Schmidt, Force fluctuations in three-dimensional suspended fibroblasts, *Phil. Trans. R. Soc. B*, *370*, 20140,028, 2015.

Schwarz, U., and S. Safran, Physics of adherent cells, *Reviews of Modern Physics*, *85*, 1327, 2013.

Schwarz, U. S., and J. R. Soiné, Traction force microscopy on soft elastic substrates: A guide to recent computational advances, *Biochimica et Biophysica Acta (BBA)-Molecular Cell Research*, *1853*, 3095–3104, 2015.

Schwarz, U. S., N. Q. Balaban, D. Riveline, A. Bershadsky, B. Geiger, and S. Safran, Calculation of forces at focal adhesions from elastic substrate data: the effect of localized force and the need for regularization, *Biophysical journal*, *83*, 1380–1394, 2002.

Seifert, J., J. Rheinlaender, F. Lang, M. Gawaz, and T. E. Schäffer, Thrombin-induced cytoskeleton dynamics in spread human platelets observed with fast scanning ion conductance microscopy, *Scientific Reports*, *7*, 4810, 2017.

Serwane, F., A. Mongera, P. Rowghanian, D. A. Kealhofer, A. A. Lucio, Z. M. Hockenbery, and O. Campàs, In vivo quantification of spatially varying mechanical properties in developing tissues, *Nature methods*, *14*, 181, 2017.

Shao, D., W.-J. Rappel, and H. Levine, Computational model for cell morphodynamics, *Physical review letters*, *105*, 108,104, 2010.

Shi, J., et al., Good features to track, in *Computer Vision and Pattern Recognition, 1994. Proceedings CVPR'94., 1994 IEEE Computer Society Conference on*, pp. 593–600, IEEE, 1994.

Sigmund, O., and S. Torquato, Design of materials with extreme thermal expansion using a three-phase topology optimization method, *Journal of the Mechanics and Physics of Solids*, *45*, 1037–1067, 1997.

Smith, M. A., E. Blankman, M. L. Gardel, L. Luettjohann, C. M. Waterman, and M. C. Beckerle, A zyxin-mediated mechanism for actin stress fiber maintenance and repair, *Developmental cell*, *19*, 365–376, 2010.

Soiné, J., C. Brand, J. Stricker, P. Oakes, M. Gardel, and U. Schwarz, Model-based traction force microscopy reveals differential tension in cellular actin bundles, *PLoS computational biology*, *11*, e1004,076–e1004,076, 2015.

Soiné, J. R., N. Hersch, G. Dreissen, N. Hampe, B. Hoffmann, R. Merkel, and U. S. Schwarz, Measuring cellular traction forces on non-planar substrates, *Interface focus*, *6*, 20160,024, 2016.

Solon, J., I. Levental, K. Sengupta, P. C. Georges, and P. A. Janmey, Fibroblast adaptation and stiffness matching to soft elastic substrates, *Biophysical journal*, *93*, 4453–4461, 2007.

Stam, S., J. Alberts, M. L. Gardel, and E. Munro, Isoforms confer characteristic force generation and mechanosensation by myosin ii filaments, *Biophysical journal*, *108*, 1997–2006, 2015.

Stamhuis, E. J., Basics and principles of particle image velocimetry (piv) for mapping biogenic and biologically relevant flows, *Aquatic Ecology*, *40*, 463–479, 2006.

Steinwachs, J., C. Metzner, K. Skodzek, N. Lang, I. Thievessen, C. Mark, S. Münster, K. E. Aifantis, and B. Fabry, Three-dimensional force microscopy of cells in biopolymer networks, *Nature methods*, *13*, 171, 2016.

Stone, M., Cross-validatory choice and assessment of statistical predictions, *Journal of the royal statistical society. Series B (Methodological)*, pp. 111–147, 1974.

Strickland, D., Y. Lin, E. Wagner, C. Hope, J. Zayner, C. Antoniou, T. Sosnick, E. Weiss, and M. Glotzer, Tulips: Tunable, light-controlled interacting protein tags for cell biology, *Nature methods*, *9*, 379–384, 2012.

Style, R., R. Boltyanskiy, G. German, C. Hyland, C. MacMinn, A. Mertz, L. Wilen, Y. Xu, and E. Dufresne, Traction force microscopy in physics and biology, *Soft Matter*, *10*, 4047–4055, 2014.

Sugimura, K., P.-F. Lenne, and F. Graner, Measuring forces and stresses in situ in living tissues, *Development*, *143*, 186–196, 2016.

Summerfield, M., *Rapid GUI programming with Python and Qt: the definitive guide to PyQt programming*, Pearson Education, 2007.

Tambe, D. T., et al., Collective cell guidance by cooperative intercellular forces, *Nature materials*, *10*, 469–475, 2011.

Tan, J. L., J. Tien, D. M. Pirone, D. S. Gray, K. Bhadriraju, and C. S. Chen, Cells lying on a bed of microneedles: an approach to isolate mechanical force, *Proceedings of the National Academy of Sciences*, *100*, 1484–1489, 2003.

Tanimoto, H., and M. Sano, A simple force-motion relation for migrating cells revealed by multipole analysis of traction stress, *Biophysical journal*, *106*, 16–25, 2014.

Tarle, V., A. Ravasio, V. Hakim, and N. S. Gov, Modeling the finger instability in an expanding cell monolayer, *Integrative Biology*, *7*, 1218–1227, 2015.

Taylor, Z. J., R. Gurka, G. A. Kopp, and A. Liberzon, Long-duration time-resolved piv to study unsteady aerodynamics, *IEEE Transactions on Instrumentation and Measurement*, *59*, 3262–3269, 2010.

Thoresen, T., M. Lenz, and M. L. Gardel, Thick filament length and isoform composition determine self-organized contractile units in actomyosin bundles, *Biophysical journal*, *104*, 655–665, 2013.

Tibshirani, R., Regression shrinkage and selection via the lasso, *Journal of the Royal Statistical Society. Series B (Methodological)*, pp. 267–288, 1996.

Tikhonov, A. N., Solution of incorrectly formulated problems and the regularization method, in *Soviet Mathematics*, vol. 4, pp. 1035–1038, 1963.

Tlili, S., C. Gay, F. Graner, P. Marcq, F. Molino, and P. Saramito, Colloquium: Mechanical formalisms for tissue dynamics, *The European Physical Journal E*, *38*, 1–31, 2015.

Tojkander, S., G. Gateva, and P. Lappalainen, Actin stress fibers–assembly, dynamics and biological roles, *Journal of cell science*, *125*, 1855–1864, 2012.

Tollenaere, H., and D. Caillerie, Continuous modeling of lattice structures by homogenization, *Advances in Engineering Software*, *29*, 699–705, 1998.

Torres, P., Modeling shape and rupture of filament networks, Ph.D. thesis, Heidelberg, Univ., Diss., 2012, 2012.

Torres, P., I. Bischofs, and U. Schwarz, Contractile network models for adherent cells, *Physical Review E*, *85*, 011,913, 2012.

Toyjanova, J., E. Bar-Kochba, C. López-Fagundo, J. Reichner, D. Hoffman-Kim, and C. Franck, High resolution, large deformation 3d traction force microscopy, *PloS one*, *9*, e90,976, 2014a.

Toyjanova, J., E. Hannen, E. Bar-Kochba, E. M. Darling, D. L. Henann, and C. Franck, 3d viscoelastic traction force microscopy, *Soft matter*, *10*, 8095–8106, 2014b.

Trepat, X., M. R. Wasserman, T. E. Angelini, E. Millet, D. A. Weitz, J. P. Butler, and J. J. Fredberg, Physical forces during collective cell migration, *Nature physics*, *5*, 426, 2009.

Trichet, L., J. Le Digabel, R. J. Hawkins, S. R. K. Vedula, M. Gupta, C. Ribrault, P. Hersen, R. Voituriez, and B. Ladoux, Evidence of a large-scale mechanosensing mechanism for cellular adaptation to substrate stiffness, *Proceedings of the National Academy of Sciences*, *109*, 6933–6938, 2012.

Trickey, W. R., F. P. Baaijens, T. A. Laursen, L. G. Alexopoulos, and F. Guilak, Determination of the poisson's ratio of the cell: recovery properties of chondrocytes after release from complete micropipette aspiration, *Journal of biomechanics*, *39*, 78–87, 2006.

Tseng, Q., et al., A new micropatterning method of soft substrates reveals that different tumorigenic signals can promote or reduce cell contraction levels, *Lab on a chip*, *11*, 2231–2240, 2011.

Tsuda, Y., H. Yasutake, A. Ishijima, and T. Yanagida, Torsional rigidity of single actin filaments and actin–actin bond breaking force under torsion measured directly by in vitro micromanipulation, *Proceedings of the National Academy of Sciences*, *93*, 12,937–12,942, 1996.

Tukey, J. W., An introduction to the calculations of numerical spectrum analysis, *Spectral analysis of time series*, *25*, 2546, 1967.

Valon, L., F. Etoc, A. Remorino, F. di Pietro, X. Morin, M. Dahan, and M. Coppey, Predictive spatiotemporal manipulation of signaling perturbations using optogenetics, *Biophysical journal*, *109*, 1785–1797, 2015.

Valon, L., A. Marín-Llauradó, T. Wyatt, G. Charras, and X. Trepat, Optogenetic control of cellular forces and mechanotransduction, *Nature communications*, *8*, 14,396, 2017.

van Oers, R. F., E. G. Rens, D. J. LaValley, C. A. Reinhart-King, and R. M. Merks, Mechanical cell-matrix feedback explains pairwise and collective endothelial cell behavior in vitro, *PLoS computational biology*, *10*, e1003,774, 2014.

Van Rossum, G., et al., Python programming language., in *USENIX Annual Technical Conference*, vol. 41, p. 36, 2007.

Verkhovsky, A. B., and G. G. Borisy, Non-sarcomeric mode of myosin ii organization in the fibroblast lamellum., *The Journal of cell biology*, *123*, 637–652, 1993.

Vernerey, F. J., and M. Farsad, An eulerian/xfem formulation for the large deformation of cortical cell membrane, *Computer methods in biomechanics and biomedical engineering*, *14*, 433–445, 2011.

Vianay, B., J. Käfer, E. Planus, M. Block, F. Graner, and H. Guillou, Single cells spreading on a protein lattice adopt an energy minimizing shape, *Physical review letters*, *105*, 128,101, 2010.

Wagner, E., and M. Glotzer, Local rhoa activation induces cytokinetic furrows independent of spindle position and cell cycle stage, *J Cell Biol*, pp. jcb–201603,025, 2016.

Walt, S. v. d., S. C. Colbert, and G. Varoquaux, The numpy array: a structure for efficient numerical computation, *Computing in Science & Engineering*, *13*, 22–30, 2011.

Weitzman, M., and K. M. Hahn, Optogenetic approaches to cell migration and beyond, *Current opinion in cell biology*, *30*, 112–120, 2014.

Welte, M. A., Bidirectional transport along microtubules, *Current Biology*, *14*, R525–R537, 2004.

Westerweel, J., Fundamentals of digital particle image velocimetry, *Measurement science and technology*, *8*, 1379, 1997.

Westerweel, J., and F. Scarano, Universal outlier detection for piv data, *Experiments in fluids*, *39*, 1096–1100, 2005.

Willert, C. E., and M. Gharib, Digital particle image velocimetry, *Experiments in fluids*, *10*, 181–193, 1991.

Wolf, K., Y. I. Wu, Y. Liu, J. Geiger, E. Tam, C. Overall, M. S. Stack, and P. Friedl, Multi-step pericellular proteolysis controls the transition from individual to collective cancer cell invasion, *Nature cell biology*, *9*, 893, 2007.

Wolfenson, H., A. Bershadsky, Y. I. Henis, and B. Geiger, Actomyosin-generated tension controls the molecular kinetics of focal adhesions, *J Cell Sci*, *124*, 1425–1432, 2011.

Wu, Y. I., D. Frey, O. I. Lungu, A. Jaehrig, I. Schlichting, B. Kuhlman, and K. M. Hahn, A genetically encoded photoactivatable rac controls the motility of living cells, *Nature*, *461*, 104–108, 2009.

Ye, N., D. Verma, F. Meng, M. W. Davidson, K. Suffoletto, and S. Z. Hua, Direct observation of α-actinin tension and recruitment at focal adhesions during contact growth, *Experimental cell research*, *327*, 57–67, 2014.

Yoshigi, M., L. M. Hoffman, C. C. Jensen, H. J. Yost, and M. C. Beckerle, Mechanical force mobilizes zyxin from focal adhesions to actin filaments and regulates cytoskeletal reinforcement, *J Cell Biol*, *171*, 209–215, 2005.

Zaidel-Bar, R., C. Ballestrem, Z. Kam, and B. Geiger, Early molecular events in the assembly of matrix adhesions at the leading edge of migrating cells, *Journal of cell science*, *116*, 4605–4613, 2003.

Zaidel-Bar, R., M. Cohen, L. Addadi, and B. Geiger, Hierarchical assembly of cell–matrix adhesion complexes, 2004.

Zand, M. S., and G. Albrecht-Buehler, What structures, besides adhesions, prevent spread cells from rounding up?, *Cytoskeleton*, *13*, 195–211, 1989.

Ziebert, F., and I. S. Aranson, Effects of adhesion dynamics and substrate compliance on the shape and motility of crawling cells, *PloS one*, *8*, e64,511, 2013.

Ziebert, F., S. Swaminathan, and I. S. Aranson, Model for self-polarization and motility of keratocyte fragments, *Journal of The Royal Society Interface*, p. rsif20110433, 2011.

Zou, H., and T. Hastie, Regularization and variable selection via the elastic net, *Journal of the Royal Statistical Society: Series B (Statistical Methodology)*, *67*, 301–320, 2005.

List of Publications

In the following table, manuscripts are listed which have been written down in the course of this thesis. Reference **6** will be included in the PhD-thesis of Julia Jäger.

1	Patrick W. Oakes, Elizabeth Wagner, Christoph A. Brand, Dimitri Probst, Marco Linke, Ulrich S. Schwarz, Michael Glotzer and Margaret L. Gardel **Optogenetic control of RhoA reveals zyxin-mediated elasticity of stress fibres** *Nature Communications* **8** (2017): ncomms15817.	Chapter 3
2	Tomas Andersen, Dimitri Probst, Ulrich S. Schwarz and Martial Balland **Actin polarity determines efficiency of force production during optogenetic activation** Currently in preparation (2018)	Chapter 4
3	Jana Hanke, Dimitri Probst, Assaf Zemel, Ulrich S. Schwarz and Sarah Köster **Dynamics of force generation by spreading platelets** Currently under revision (2018)	Chapter 5
4	Medhavi Vishwakarma, Jacopo Di Russo, Dimitri Probst, Ulrich S. Schwarz, Tamal Das and Joachim P. Spatz **Group decisions regulate emergence of epithelial leader cells during collective migration** Currently under revision (2018)	Chapter 6
5	Dimitri Probst and Ulrich S. Schwarz **Stress fiber is metamaterial** Currently in preparation (2018)	Chapter 7
6	Elena Kassianidou, Dimitri Probst, Julia Jäger, Ulrich S. Schwarz and Sanjay Kumar **Extracellular matrix geometry determines stress fiber network organization during cell spreading** Currently in preparation (2018)	

Danksagungen

An erster Stelle möchte ich mich bei meinem Betreuer Prof. Dr. Ulrich Schwarz für seine Unterstützung und die Betreuung während der Doktorarbeit bedanken. Ich konnte in der Arbeitsgruppe ein tiefes Verständnis der Biophysik erlangen und die wissenschaftliche Forschung kennenlernen. Insbesondere danke ich für die Möglichkeit, dass ich an internationalen Kollaborationen mitwirken durfte, und auf zahlreichen Konferenzen, sowohl national als auch international, produktive Erfahrungen sammeln durfte.
Ich möchte mich auch bei Prof. Dr. Heinz Horner für das Interesse an meiner Arbeit und die Zweitkorrektur bedanken.
Ein großer Dank geht an die Landesgraduiertenförderung und das Institut für Theoretische Physik, über die ich finanziert wurde.
Vielen Dank den zahlreichen Leuten, mit denen ich in Kollaborationen zusammenarbeiten durfte (chronologisch geordnet): Patrick Oakes, Elisabeth Wagner, Christoph Brand, Marko Linke, Michael Glotzer, Margaret Gardel, Jana Hanke, Assaf Zemel, Sarah Köster, Medhavi Vishwakarma, Jacopo Di Russo, Tamal Das, Joachim Spatz, Elena Kassianidou, Julia Jäger, Sanjay Kumar, Tomas Andersen und Martial Balland.
Besonderer Dank geht an meine Arbeitsgruppe für die gute Zusammenarbeit und das nette Miteinander. Zunächst die Philosophenwegler: Felix Frey danke ich dafür, dass er mich all die Jahre als Arbeitszimmer- und Hotelzimmergenosse ertragen hat und mit mir um die halbe Welt gereist ist. Immer wieder gerne. Auch für die zahlreichen Diskussionen von Biophysik bis Hängebrückenarchitektur. Vielen Dank an Justin Grewe für den wissenschaftlichen und nichtwissenschaftlichen Austausch. Vielen Dank an Falko Ziebert für die Tipps beim Aufschreiben und für das Ermöglichen einer knappen saarländischen Mehrheit. Nun zu den BioQuantlern: Vielen Dank an Nikolas Schnellbächer für die Organisation von Reisen zu Konferenzen und für technische Ratschläge. Vielen Dank an Julia Jäger für die angenehme Zusammenarbeit, die vielen Diskussionen sowie die gute Leistung beim Ruperto Carola Cup. Vielen Dank an Anil Kumar Desanna, vor allem immer mal wieder für den nichtwissenschaftlichen Austausch. Nun noch zu den Alumni: Vielen Dank an Marko Linke und Christoph Brand für die erfolgreiche Zusammenarbeit. Vielen Dank an Philipp Albert für die Hilfe beim Postererstellen. Ebenso ein großes Dankeschön Jérôme Soiné für den wissenschaftlichen Austausch und für die KSC-Besuche. Bitte nicht sauer sein, falls ich jemanden vergessen habe ...
Ein riesengroßer Dank geht an Nina Kraus. Ihr möchte ich für die Unterstützung in allen Lebenslagen, für ihre Motivation und ihre Geduld während des Aufschreibens dieser Arbeit danken. Meiner Familie danke ich für die Finanzierung meines Studiums und für die Unterstützung über viele Jahre.
Großer Dank geht auch an die Fußballgruppen des SSC Karlsruhe und Borussia BioQuant. Selbstverständlich auch besten Dank an die Gräther Kickers 06.